LEVEL III

A050 506

AD A056748

(12)

(6) INVESTIGATION OF LASER PROPULSION. Volume II.

(10) P.K. Chapman, D.H. Douglas—Hamilton, H. Legner, D.A. Reilly and G. Weyl

Avco Everett Research Laboratory, Inc.
Everett, MA 02149

(11) November 1977   (12) 264 p.

(9) Final Technical Report, period 1 March 1976 to 15 November 1977, Volume II

(15) N00014-76-C-0646, DARPA Order-3138

APPROVED FOR PUBLIC RELEASE; DISTRIBUTION UNLIMITED.

D D C
RECEIVED
JUL 28 1978
E

048 450

78 07 21 016

FOREWORD

REPORT DOCUMENTATION PAGE		READ INSTRUCTIONS BEFORE COMPLETING FORM
1. REPORT NUMBER	2. GOVT ACCESSION NO.	3. RECIPIENT'S CATALOG NUMBER
4. TITLE (and Subtitle) INVESTIGATION OF LASER PROPULSION VOLUME II		5. TYPE OF REPORT & PERIOD COVERED Final Technical Report 1 March 1976 - 15 Nov. 1977
		6. PERFORMING ORG. REPORT NUMBER
7. AUTHOR(s) P. K. Chapman, D. H. Douglas-Hamilton and H. Legner, D.A. Reilly, G. Weyl		8. CONTRACT OR GRANT NUMBER(s) N00014-76-C-0646
9. PERFORMING ORGANIZATION NAME AND ADDRESS Avco Everett Research Laboratory, Inc. 2385 Revere Beach Parkway Everett, Massachusetts 02149		10. PROGRAM ELEMENT, PROJECT, TASK AREA & WORK UNIT NUMBERS 6E20 7E20
11. CONTROLLING OFFICE NAME AND ADDRESS Defense Advanced Research Projects Agency DARPA Order No. 3138		12. REPORT DATE November 1977
		13. NUMBER OF PAGES 267
14. MONITORING AGENCY NAME & ADDRESS(if different from Controlling Office) Office of Naval Research Department of the Navy Arlington, Virginia 22217		15. SECURITY CLASS. (of this report) Unclassified
		15a. DECLASSIFICATION/DOWNGRADING SCHEDULE

16. DISTRIBUTION STATEMENT (of this Report)

Approved for public release; distribution unlimited

17. DISTRIBUTION STATEMENT (of the abstract entered in Block 20, if different from Report)

18. SUPPLEMENTARY NOTES

19. KEY WORDS (Continue on reverse side if necessary and identify by block number)

Laser
Rocket Engine
Propulsion

20. ABSTRACT (Continue on reverse side if necessary and identify by block number)

The use of large ground based lasers to radiate power into a rocket engine allows arbitrary choice of propellant and specific impulse. The case of launch of one ton payload from near ground to geosynchronous transfer ellipse appears to be feasible using stacked carbon dioxide repetitive pulse lasers. Atmospheric propagation is enhanced by bleaching out CO_2 absorption and using phase correction of the thermal blooming generated we expect that 1 microradian beam spreading can be achieved. The use of pulsed lasers permits an engine based on the laser detonation wave, in which laser

DD FORM 1473 EDITION OF 1 NOV 65 IS OBSOLETE
1 JAN 73

20. Abstract (Continued)

energy is efficiently absorbed by inverse Bremsstrahlung in the propellant, which then expands out of the engine and provides thrust. Continuous use costs in the order of $20/lb to GEO are anticipated.

ACCESSION for

NTIS	White Section	X
DDC	Buff Section	☐
UNANNOUNCED		☐
JUSTIFICATION		

BY
DISTRIBUTION/AVAILABILITY CODES

| Dist. | AVAIL and/or SPECIAL | |
| A | | |

TABLE OF CONTENTS

VOLUME II

LIST OF ILLUSTRATIONS

VOLUME II

7

V. CW LASER ROCKET ENGINE

1. INTRODUCTION AND ENGINE CONFIGURATIONS

Two basic engine configurations have evolved for CW laser propulsion. The character of the designs depends significantly upon the manner in which the laser radiation is introduced into the absorption chamber. In one case the laser beam enters the chamber passing through the rocket exhaust plume without having its energy absorbed in the plume or nozzle (see Section V.3). This concept comprises the single port engine. In the other configuration the beam enters the chamber through a window (solid or aerodynamic) with all of the absorption occurring in the chamber. The nozzle and plume part of this so-called two-port engine rocket are not different from conventional chemical rocketry.

a. Single-Port Engine; Bleaching

In Figure 33 we see the schematic of a single-port CW laser propulsion engine. The laser beam enters through the nozzle which also serves as a collector for the beam. The propellant used with this scheme is fed from a tank into the absorption chamber where it absorbs laser radiation via molecular or inverse bremstrahlung absorption. Some quantitative estimates of laser absorption waves and the absorption zone structure are given in Section V.3.

A propellant that does not absorb in the plume or nozzle but does absorb in the chamber to raise the stagnation enthalpy is required. Furthermore, a nearly step function behavior of the absorption coefficient between

11

PAYLOAD

PROPELLANT

ABSORPTION
CHAMBER

NOZZLE/
COLLECTOR
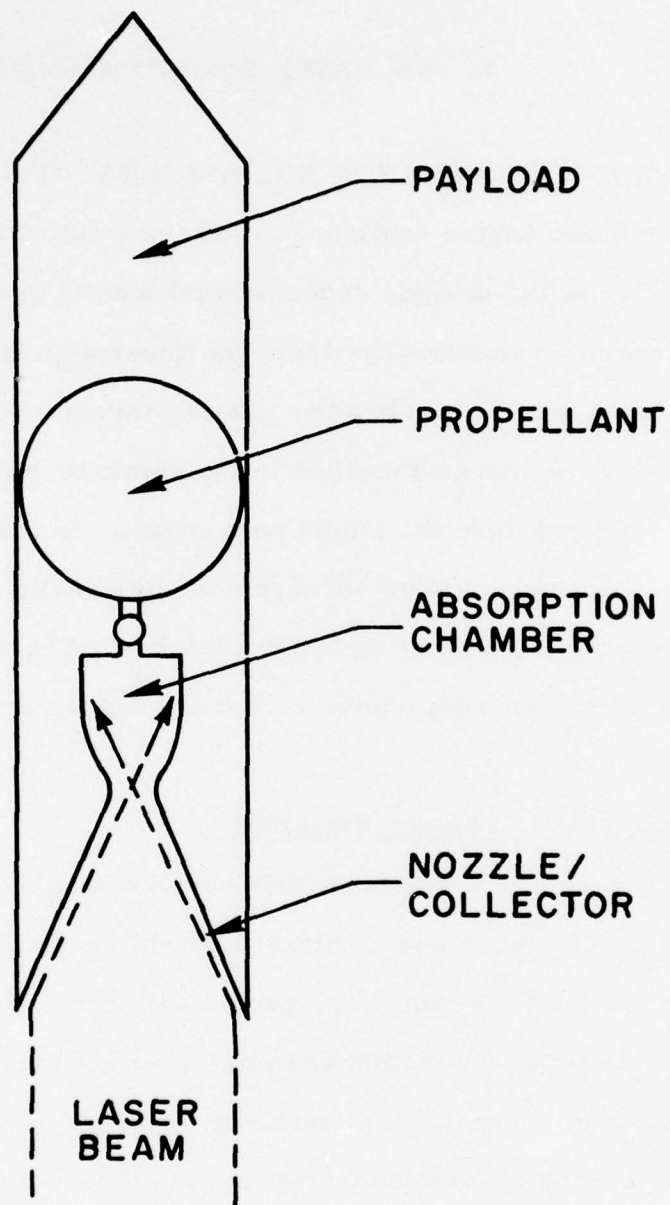
LASER
BEAM

H 4253

Figure 33   Single-Port CW Laser Propulsion Rocket Configuration

12

the chamber and the nozzle is preferred. In general, the temperature will not have a step function variation with engine location and bleaching will not occur. The temperature variation will depend upon the nozzle geometry and on the kinetic processes (dissociation and recombination). A slow temperature variation, for example, would keep the absorption coefficient high in the nozzle. This would only permit a fraction of the radiation to reach the chamber and hence alter the entire absorption process upon which the engine was originally designed. Critical experiments for the single-port configuration are proposed in Section V.5.

b. Two-Port Engine

In Figure 34 there is a schematic of a two-port cw laser propulsion engine. The laser beam enters through a side port onto a focusing mirror which deflects the beam through an aerodynamic window. The propellant and the aerodynamic window source flow medium are the same. Here, as in the single-port device, selected seedants can be added to enhance or suitably modify the absorptive characteristics of the flow. Note again the need for an absorption coefficient that absorbs the radiation in the chamber under high pressure conditions. In the next section the thermodynamics of various candidate propellants is discussed.

The two key areas of research needed for the single-port engine are also needed for the two-port scheme. In addition there is a third important area of concern - the aerodynamic window flow. A supersonic aerodynamic window flow can be designed to operate at a practically infinite pressure ratio between the high pressure chamber and the low pressure ambient. The precise flow characteristics in the vicinity of the aerodynamic window are rather complex; further downstream approaching the focus of the laser

13

PAYLOAD

PROPELLANT

FOCUSSING
MIRROR

LASER
BEAM

AERO WINDOW

ABSORPTION
CHAMBER

NOZZLE
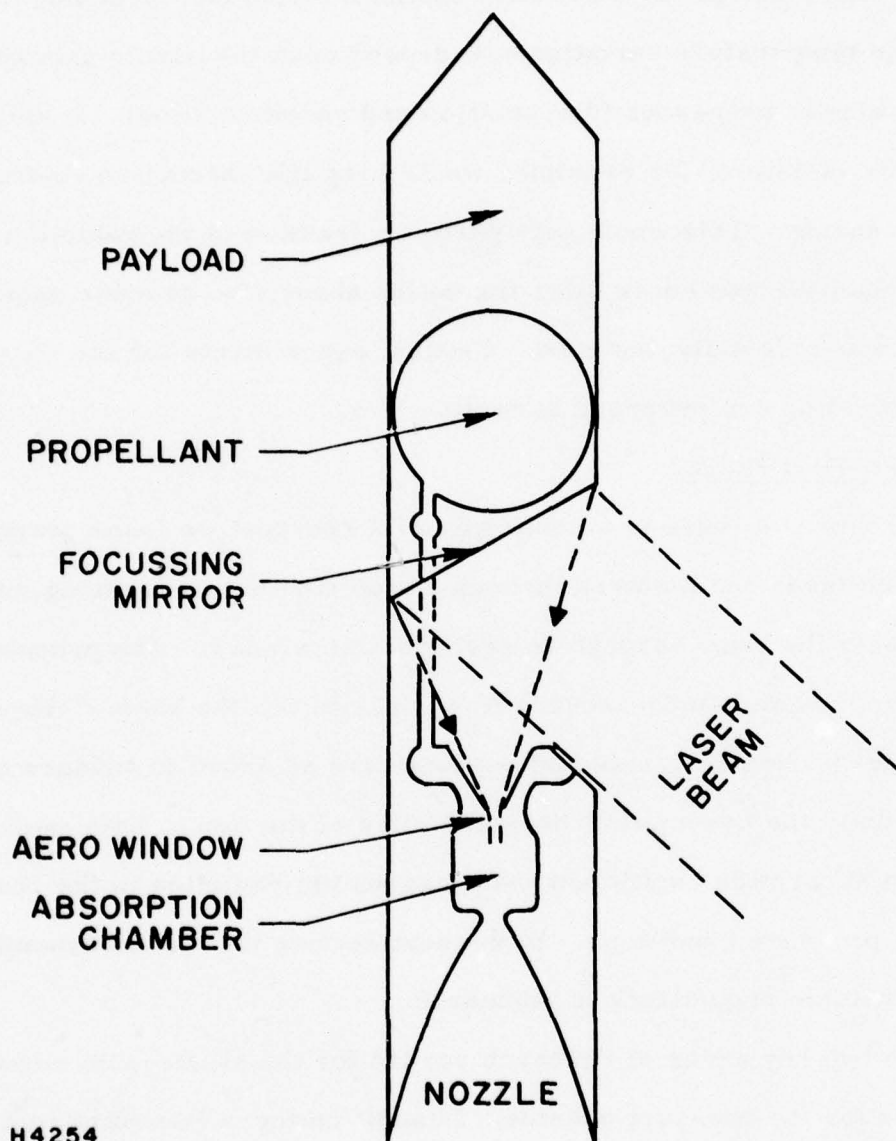
H4254

Figure 34   Two-Port CW Laser Propulsion Rocket Configuration

14

beam and the absorption chamber, there is a supersonic flow which must be decelerated to subsonic velocities via a normal shock. The focus of the beam (absorption zone) is in the subsonic portion of the chamber flow. The energetics of the essentially constant pressure heating is then completely analogous to the processes occurring in chemical propulsion systems. Since the absorption processes will induce laser absorption waves in the chamber that will travel toward the beam, the aerodynamic-window flow configuration will be perturbed.

It is obvious that problems remain to be solved for the two-port configuration. We have examined some of the matters described above. In Section V.4 we describe the gasdynamic matching analysis for the two-port system with the purpose of obtaining scaling maps that size experimental engines for various power levels. In Section V.5 we describe a burner experiment that can potentially address many of the questions we have posed in the present discussions. We must add that most of our attention has been paid to the two-port engine. This reflects our view that the increased flexibility of this configuration, as contrasted to the inflexible need for absorption coefficient tailoring with the single-port engine, has more promise for early success. We must add that whatever is learned regarding the physics of the absorption process will be applicable to both CW laser propulsion engine configurations.

2. THERMODYNAMICS

The thermodynamics of addition of energy to the flowing medium in the absorption chamber will be discussed. There are a number of connected areas of interest. Firstly, we define the enthalpy increase required to provide a certain specific impulse (for a specified mission). A laser system must be capable of delivering the enthalpy increase to the propellant of interest. Secondly, several propellants will be described and assessments regarding their applicability will be made. High temperature water appears to be a particularly interesting propellant. Thirdly, certain practical aspects of the thermodynamic efficiency of propellants as well as loss mechanisms will be discussed.

a. Specific Impulse

An important measure of a propulsion system is its specific impulse. Under uniform exhaust flow conditions, i.e., all the fluid particles are leaving the rocket nozzle exit plane at the same velocity, the specific impulse is defined[*] as

$$I_{sp} = U_7/g \text{ (seconds)} \tag{277}$$

where U_7 is the constant exit speed and g is the acceleration of gravity. Since the chamber speed is typically a fraction ($\sim 1/10$) of the sound speed, the kinetic energy per unit mass in the chamber will be small compared to the thermal energy introduced via laser radiation. Hence the energy equation between the absorption chamber and the nozzle exit is

$$U_7 = \sqrt{2(h_5 - h_7)} \tag{278}$$

---

[*] The subscript numbering system refers to the stations in a configured two-port laser propulsion engine (see Figure 52 and Table 4).

16

where h_5 is the chamber enthalpy and h_7 is the exhaust nozzle enthalpy.
The expansion of the flow in the nozzle will reduce the thermal energy
continually. Hence, to maximize the exit velocity h_7 is set to zero. Then
the maximum specific impulse I_{sp} is related to the enthalpy change by:

$$\Delta h_5 = \frac{g^2 I_{sp}^2}{2} \qquad (279)$$

Note that h_5 is replaced by Δh_5 since enthalpy differences from some
common reference state are always considered. Relation (279) is plotted
in Figure 35. Chemical rockets have propulsion systems that are theo-
retically capable of about 500 seconds as shown in Table 3. The chemical
regime is shaded on the figure. Laser propulsion rockets are not confined
to the chemical energy of reaction between fuel and oxidizer as a limiting
factor for Δh_5. Conceivably, it should be possible to attain specific im-
pulses in the thousands of seconds. Mission analysis studies (see Section II)
have shown, however, that specific impulses between 500 and 1000 seconds
are of considerable interest. Laser propulsion is needed because there are
no existing systems that operate in this range.

Based upon Figure 35 it is evident that one requires an enthalpy
increase of at least 10^4 J/gm to obtain a specific impulse of $\sim$500 seconds.
This statement reflects a perfectly efficient process. If one factors in the
potential losses, then one must supply something like 30 or 40% excess
Δh_5 to achieve the specific impulses indicated. Note that LH_2-LO_2 chemical
rockets are $\sim$60% efficient. Loss terms will be itemized in a subsequent
subsection; they are dominated by the heat transfer to the walls in the ab-
sorption chamber.

b. Propellants

The specific impulse variation with Δh_5 shown in Figure 35 defines
a criterion for the selection of a propellant. We must provide at least 10^4

17
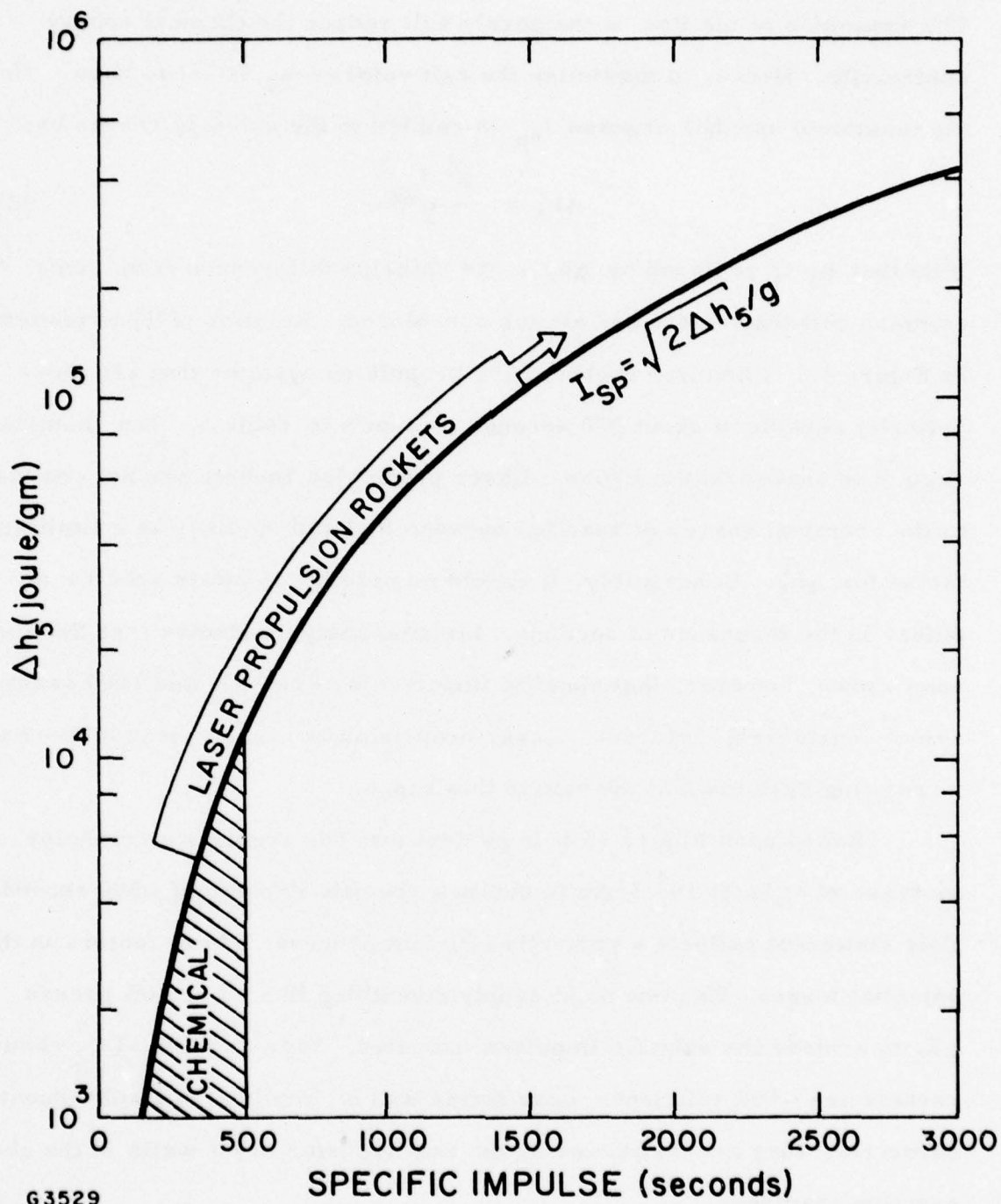
Figure 35   Enthalpy Increase Required to Attain Ideal Impulse

18

TABLE 3. THEORETICAL MAXIMUM SPECIFIC IMPULSE
FOR SELECTED CHEMICAL ROCKETS (Ref. Wilkins (1963))

(CHAMBER PRESSURE = 68.03 atm)

System	Weight % Oxidizer	Specific Impulse (Sec)	Chamber Temperature (°K)	Exit Pressure (atm)
H_2 - OF_2	85.5	411	3591	1
	87	458	3756	0.136
	91	491	4149	0.0136
H_2 - F_2	89	410	3964	1
	92	457	4462	0.136
	94	489	4809	0.136
B_5H_9 - OF_2	80	367	5169	1
	80	422	5169	0.136
	81.5	466	5215	0.0136
BeH_2 - F_2	80.5	395	5331	1
	80.5	453	5331	0.136
	79	501	5194	0.0136
LiH - F_2	82	363	4886	1
	82	410	4886	0.136
	82	445	4886	0.0136
H_2 - O_2	78	391	2769	1
	82	437	3182	0.136
	84	470	3374	0.0136

19

J/gm to a laser propulsion rocket absorption chamber to exceed specific impulses achievable by chemical propulsive systems.

This statement is significant from a number of points of view.

(i) Any propellant conceivable will have as much enthalpy as desired if one is willing to operate over large temperature and pressure ranges.

(ii) Large (temperature and/or pressure) excursions will not be a favorable circumstance from the point of view of the absorption process since the absorption coefficients (for molecular or Inverse Bremstrahlung) depend critically upon the temperature and pressure.

(iii) The extraction (or efficient use) of the available enthalpy Δh_5 is an additional important factor influencing propellant choice. Practical rocket nozzle expansion bells have area ratios that are perhaps between 10 and 100; typically the ratio is near 40. Improvement in the state-of-the-art may perhaps permit an area ratio of up to 10^3 or even higher, but there will eventually be a practical limitation.

(iv) Enthalpy extraction from the heated gas may be restricted due to dissociation and vibrational specific heat lag. Thermodynamic properties of propellants are most usually displayed in Mollier charts, in which enthalpy is plotted against entropy.

c. H_2O Mollier Chart

In Figure 36 a Mollier Chart for H_2O is illustrated. Enthalpy and entropy are the ordinate and abscissa on the Mollier Chart; the thermodynamic variables illustrated in Figure 36 are the pressure, p in atmospheres, the temperature, T in °K and the compressibility factor Z which is defined by the gas law $p = Z\rho R_o T$ where ρ is the density and R_o is the universal gas constant. Z is a measure of the dissociation of

20
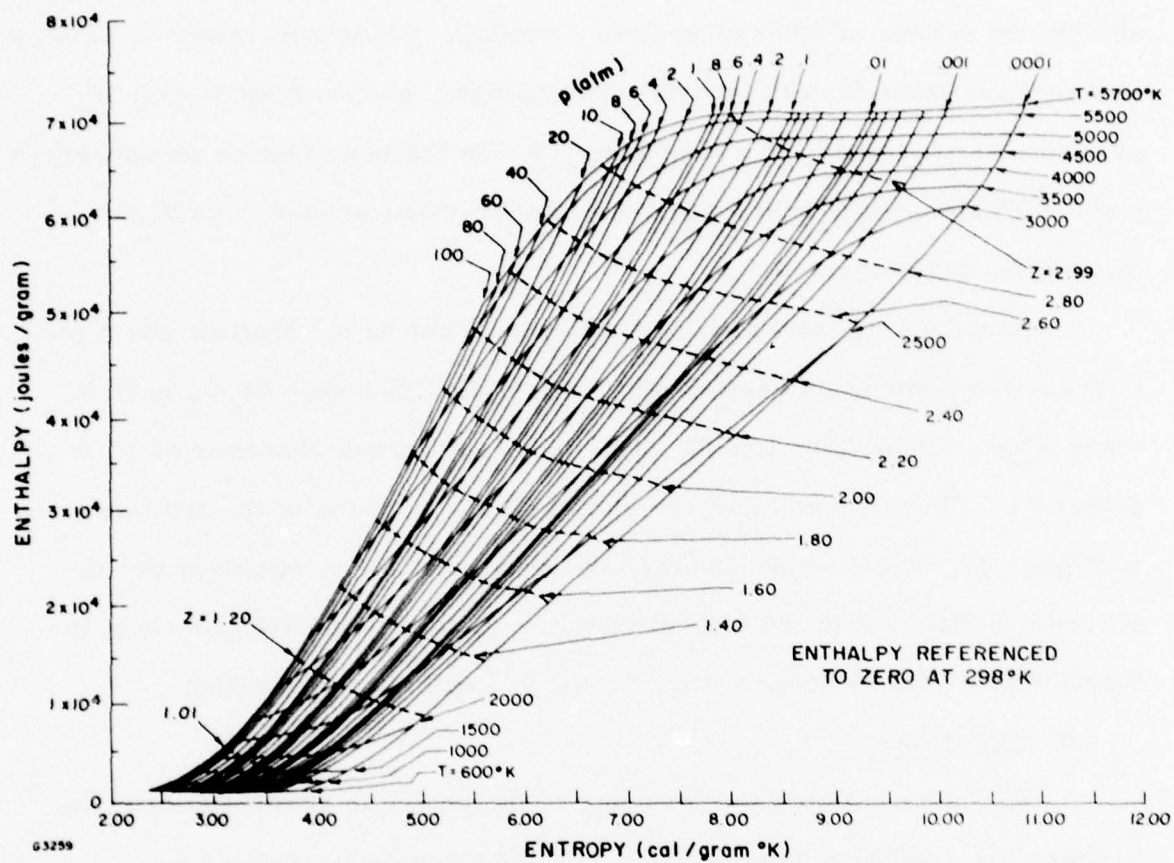
Figure 36   Mollier Chart for Water

the gas. The chart was generated utilizing the AERL equilibrium chemistry program. Note immediately that there is sufficient available enthalpy to achieve an excess of 500 sec specific impulse. Obviously, there is sufficient enthalpy available for all candidate propellants, however for H_2O it is available at <u>reasonably low temperatures</u>. In the next section one observes that a 60% efficient process requires temperatures around $5000^{\circ}K$ for interesting pressures.

Particularly interesting boundaries to put on the Mollier chart for H_2O are the absorption coefficient contours for 1% molar Al_2O_3 in H_2O, since Al_2O_3 dissociates to AlO which is a very strong absorber of 10.6 μm radiation. These boundaries are shown on the skeleton of the Mollier chart in Figure 37. Note, in particular, the nesting of large values of the absorption coefficient in the high pressure region of the chart, which is fortunate since initial high pressure facilitates enthalpy extraction.

d. Efficiency

We now evaluate the efficiency of the chamber absorption (heating) process for candidate propellants. The efficiency ϵ is defined as

$$\epsilon = \frac{\Delta h_5 - \Delta h_7}{\Delta h_5} \tag{280}$$

where Δh_7 is the nozzle exit enthalpy. If the exit enthalpy is zero, this means that the exhaust products in the nozzle are at the same state that they were prior to the absorption of laser radiation - hence the process is perfectly efficient. Let us now relate the efficiency to the specific impulse, by using Eq. (278). Thus,

$$\frac{g^2 I_{sp}^2}{2 \Delta h_5} = 1 - \frac{\Delta h_7}{\Delta h_5} = \epsilon \tag{281}$$

22
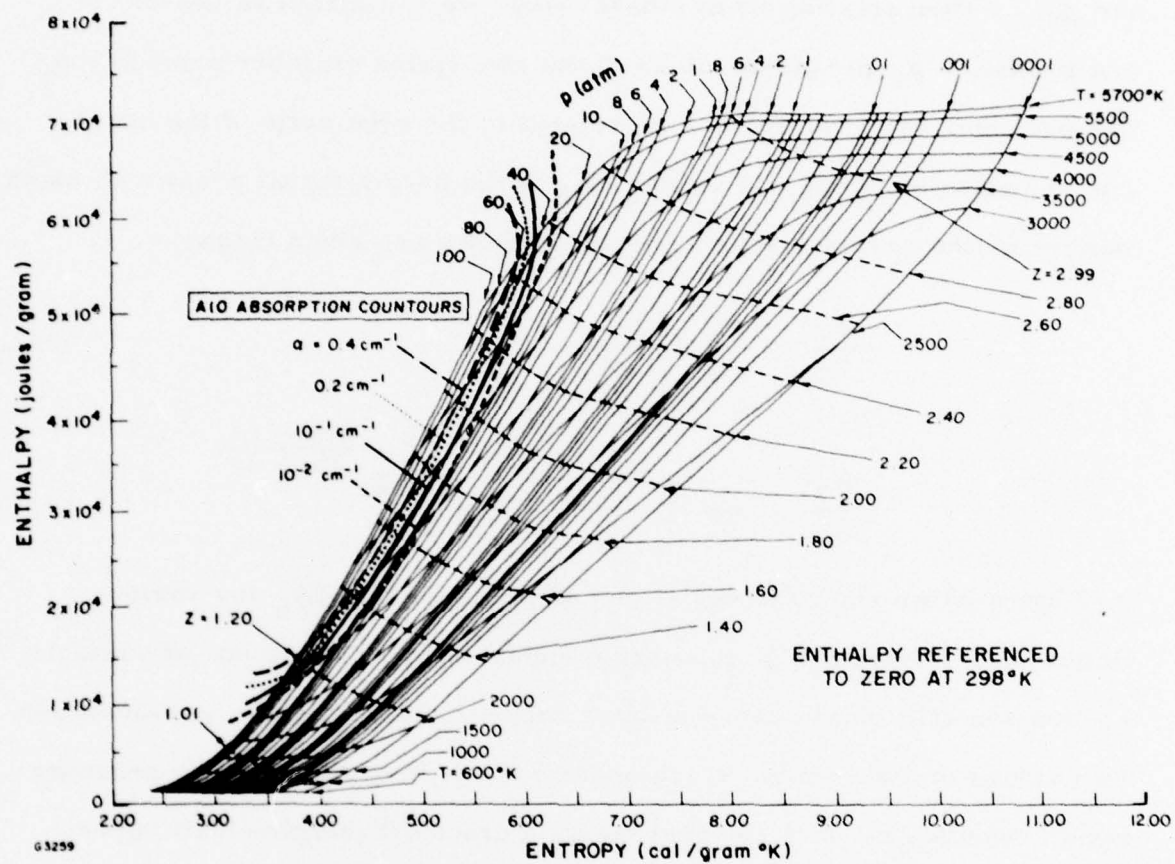
Figure 37   Molecular Absorption Contours for AlO

23

From Eq. (281) we observe that specifying I_{sp} and ϵ determines Δh_5 and Δh_7. Then starting from a base level, we can obtain values of the exit pressure p_7 for given values of the absorption chamber pressure p_5. The pressure ratio can further be related to the area ratio of the nozzle. The variation of p_7/p_5 and A_7/A_6 (A_6 is the nozzle throat area) with Mach number as the parameter for constant γ flows are given below:

$$\frac{p_7}{p_5} = \left(1 + \frac{\gamma - 1}{2} M^2\right)^{\gamma/1 - \gamma} \tag{282}$$

$$\frac{A_7}{A_6} = \frac{1}{M} \left[\frac{2\left(1 + \frac{\gamma - 1}{2} M^2\right)}{\gamma + 1}\right]^{\frac{\gamma + 1}{2(\gamma - 1)}} \tag{283}$$

On Figure 38 we show the variations of p_7/p_5 and A_7/A_6 for various values of γ. Even though the nozzle expansion process is one of variable γ, one can still obtain valuable information from a constant γ calculation. Two values of the area ratio are of interest as they relate to the pressure ratio. An area ratio of 10^3 represents a practical (nonphysical) upper bound to that ratio. Rocket nozzles just become too long. (Note the wide variation of p_5/p_7 depending upon γ.) Another interesting value is for an area ratio of 40 which represents a typical high performance rocket expansion bell area ratio.

e. Efficiency of Water Rocket

We apply the preceding ideas to the water rocket, i.e., the H_2O Mollier chart described in the previous section. A specific impulse of 700 sec is selected. This alters the Δh_5 depending upon the efficiency; however, the difference between Δh_5 and Δh_7 is constant, to provide the 700 sec of specific impulse. The cases of 30%, 60% and 90% efficiency

24
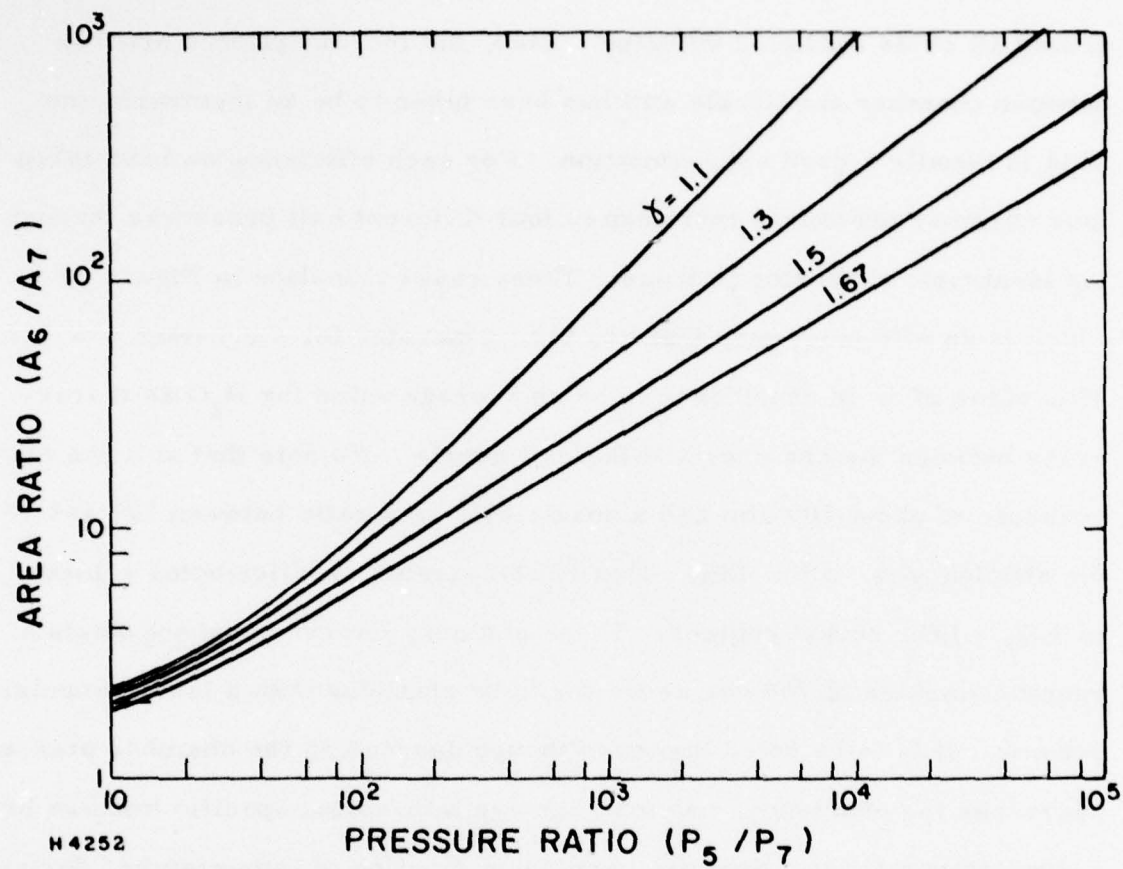
Figure 38   Expansion Pressure Ratio Related to Area Ratio

H 4252

are shown on the skeletal H_2O Mollier chart in Figure 39. The cycle base-line has been taken as $1000^\circ K$. Note that the 90% efficiency case utilizes nearly all of its available enthalpy. Also, the thermodynamic process between chamber and nozzle exit has been taken to be an isentropic one. This is usually a good approximation. For each efficiency we have taken four chamber pressures that drop to four different exit pressures through the isentropic expansion process. These cases translate to Figure 40 which is an efficiency map that has been generated for a constant $\gamma = 1.3$. This value of γ is considered to be an average value for H_2O as it trav-erses between the chamber and the exit nozzle. We note that at a chamber pressure of about 100 atm and a nozzle bell area ratio between 10^2 and 10^3 the efficiency is 55 to 75%. This is comparable to efficiencies achieved in LH_2 - LO_2 rocket engines. These engines, however, cannot obtain a specific impulse of 700 sec as we would be obtaining with a laser propulsion scheme. It is to be noted that even though decreasing the chamber pressure decreases the efficiency, one may achieve interesting specific impulse levels at low temperatures. Specific impulse as function of temperature, derived from the Mollier chart, is shown in Figure 41.

    f. Losses

The propellant enthalpy is reduced by heat transfer losses to the confining walls of the engine. A good discussion of heat transfer in the rocket chamber environment is given by Summerfield.[4]

(4) Summerfield, M., "The Liquid Propellant Rocket Engine in Princeton Aeronautical Paperbacks," Number 1, Liquid Propellant Rockets, Princeton University Press (1960).

26
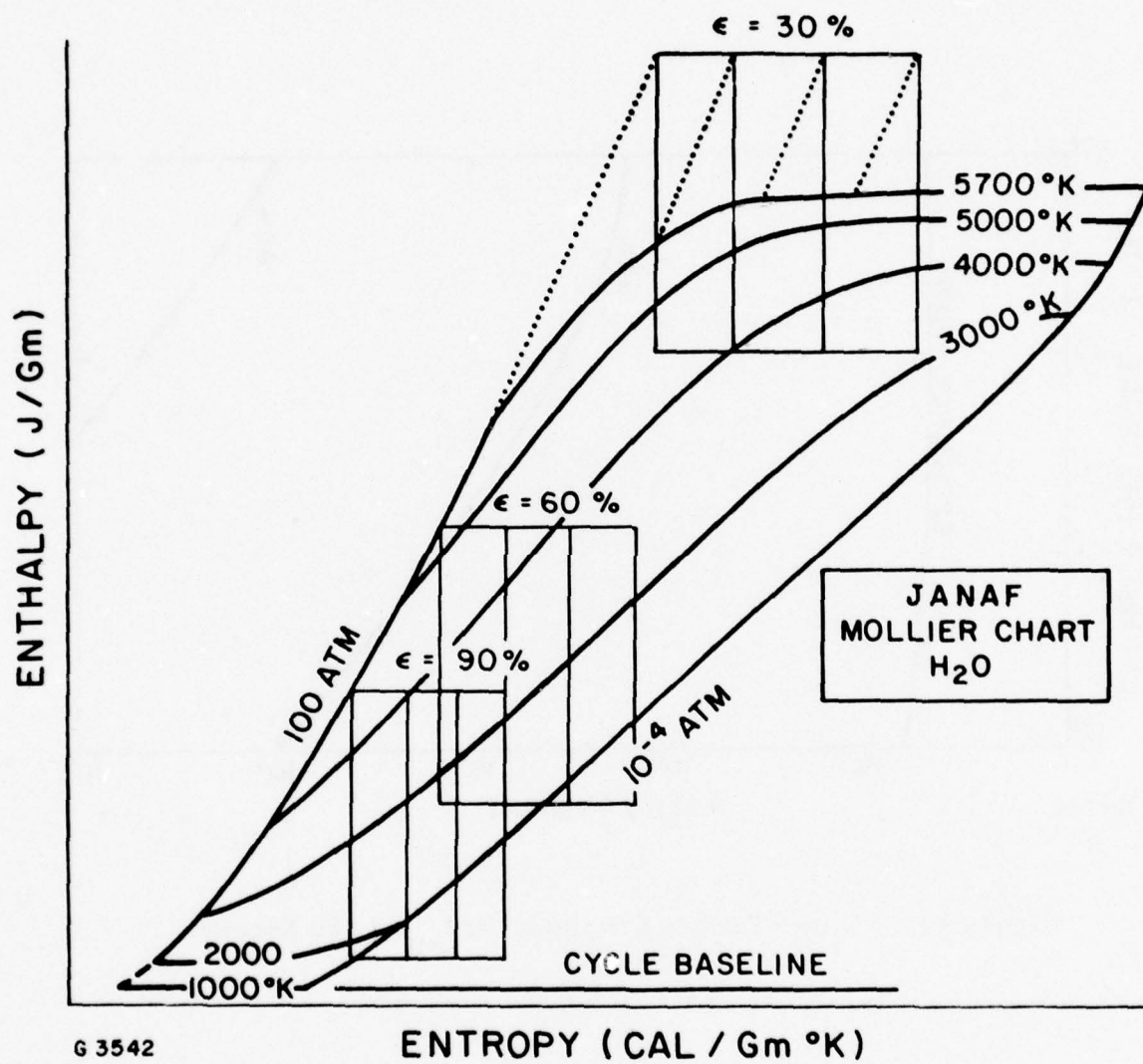
Figure 39   Operating Regimes for H_2O Rocket at I_{sp} of 700 Seconds
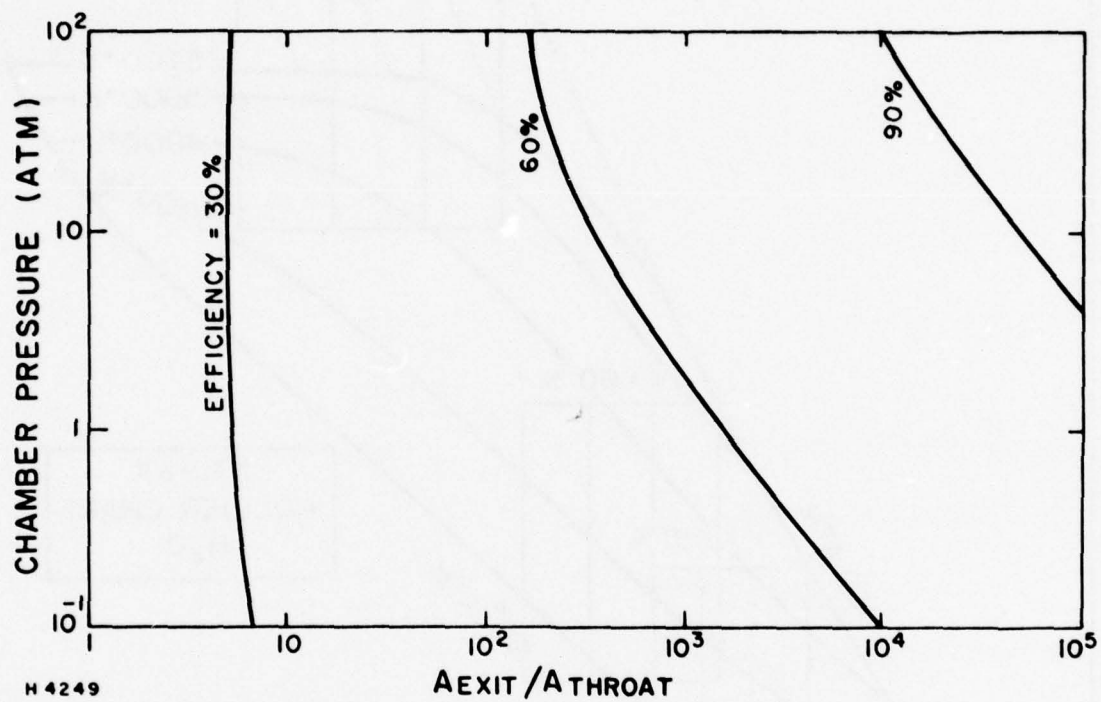
Figure 40   Water Rocket Efficiency at I_{sp} of 700 Seconds

28
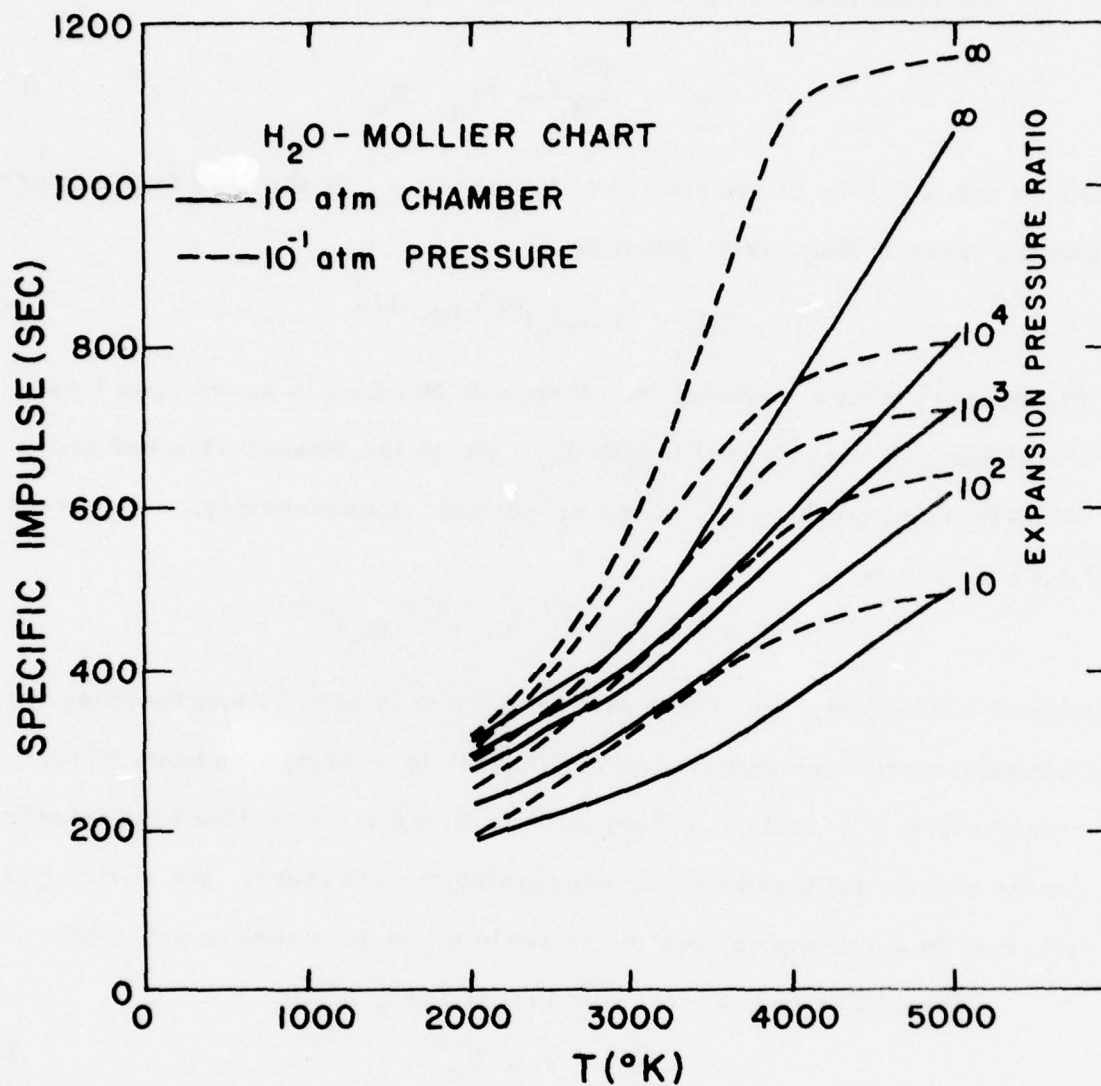
Figure 41   Water Mollier Chart Specific Impulse

29

He finds that the convective heat transfer is given by the expression

$$q_c = \frac{Nu_x\, k}{L_x} (T_x - T_w) \tag{284}$$

where sub x refers to the station of interest, T_w is the wall temperature and the Nusselt Number is given by

$$Nu_x = a\, (Re_x)^{4/5} (Pr)^{1/3} \tag{285}$$

The quantity a is a constant, the Reynolds Number is based upon local conditions and the relevant length L_x. Pr is the Prandtl Number and k is the thermal conductivity of the propellant. Consequently, the convective heat transfer is

$$q_c = K\, (L_x)^{-1/5} (T_x)^{4/5} (p_x)^{4/5} \tag{286}$$

with K a constant. The transport properties (viscosity and thermal conductivity) were approximated to be linearly increasing functions of the temperature T_x. Relation (286) implies that the convective heat transfer can be significantly reduced by decreasing the pressure. We utilize this behavior in a subsequent section to scale a low-pressure experiment.

The radiative heat transfer losses are given by

$$q_r = \epsilon\, \sigma\, T_x^4 \tag{287}$$

where the emissivity can approach unity for gases under high temperature conditions. Typical chemical rocket chambers experience 75% of their losses via convective heat transfer and 25% via radiative heat transfer, but they operate above atmospheric pressure. Subatmospheric pressure operation would reduce q_c and therefore make q_r dominant. Effective chamber design might be employed to capture some of the radiant heat loss.

30

Other losses to the system arise due to heating and flow nonuniform-ities. Heating nonuniformities arise due to nonuniform absorption of the laser radiation leading to "hot spots" that must "mix" with relatively cold propellant. Such mixing will more than likely be turbulent and it will be entropy producing. These thermal effects must be considered in addition to the nonuniform velocity effects produced by the boundary layer and heat transfer losses during the nozzle expansion processes.

All of the effects discussed above lead to a reduction of the equi-librium thermodynamic efficiencies described in the preceding subsections.

3. FLUID DYNAMICS

The absorption of laser radiation by a fluid whether stationary or in motion leads to the dynamic change of that fluid medium. In general, laser absorption fluid mechanics is very complex; phenomenon may be steady or unsteady, explosive or simply due to volumetric heating.

The physics of any particular scheme is strongly governed by the absorption process. Laser-supported waves, whether they are detonation waves or deflagration waves, are closely linked to the absorption process. Furthermore, the structure of the steady wave phenomenon is likewise dominated by the absorption of laser radiation. A gas may absorb laser radiation at a specific wavelength via molecular absorption in some temperature range. With increasing temperature the absorption co-efficient typically decreases as the absorbing specie dissociates until inverse bremstrahlung leads to a rapid increase of absorption. The transition between the two types of absorption will have an important effect on the type of absorption wave produced.

In the sections that follow, one-dimensional laser absorption wave phenomenon, i.e., the complete* Hugoniot curve, and the structure of quasi-one-dimensional absorption zones, are calculated.

a. Hugoniot Curve for One-Dimensional Laser-Supported Waves

Raizer[5] obtained a relation for the laser-supported detonation wave velocity under the "zero counter pressure" limit. His expression is apparently only valid in the upper (detonation) branch of the Hugoniot curve

---

* The word complete refers to the calculation of both the upper (detonation) and lower (deflagration) branches of the Hugoniot curve for one-dimensional flow with energy addition through laser radiation. Raizer (Ref. 5) computed the detonation wave branch in his classic paper.

(5) Raizer, Yu. P., (1965) "Heating of a Gas by a Powerful Light Pulse," Soviet JETP, 21, No. 5, 1009.

relating pressure to density. If one attempts to evaluate his relation on the lower branch of the Hugoniot, one obtains a square root singularity. This difficulty will be highlighted when we reexamine the Raizer[5] analysis in order to obtain an equation which admits a solution on the deflagration branch.

The one-dimensional gasdynamic equations with laser energy absorption read as follows for steady flow (where $(\ )_x$ indicates differentiation), ρ is the density, u is the velocity, I is the radiation intensity (W/cm^2), and α is the absorption coefficient.

$$(\rho u)_x = 0 \tag{288}$$

$$(\rho u)\, u_x = -p_x \tag{289}$$

$$\left[(\rho u)\,(h + u^2/2)\right]_x + I_x = 0 \tag{290}$$

$$I_x = \delta \alpha I \quad \text{where } \delta = \begin{cases} -1 & \text{laser radiation parallel} \\ & \text{to flow} \\ \\ +1 & \text{laser radiation antiparallel} \\ & \text{to flow} \end{cases} \tag{291}$$

$$h = h\,(p, \rho) \tag{292}$$

$$p = Z\,(T, \rho)\, \rho\, R_o T \tag{293}$$

$$\alpha = \alpha\,(\rho, T) \tag{294}$$

33

The implicit approximation made in writing down these equations
is that we are excluding diffusive effects. Diffusive effects are also
neglected when deriving the shock adiabatic and the Hugoniot curve when
chemical energy is released into the flow.

Suppose there is a discontinuity zone somewhere in the flow. This
is depicted in Figure 42. Conditions on either side of the zone are ex-
amined. The frame of reference considered makes the discontinuity zone
(DZ) fixed in space. Across DZ from Eq. (288)

$$\rho u \;=\; constant \;=\; m \tag{295}$$

or

$$\rho_1 u_1 \;=\; \rho_2 u_2 \tag{296}$$

Furthermore, utilizing Eq. (295) in Eq. (289) provides

$$p_1 \;+\; m u_1 \;=\; p_2 \;+\; m u_2 \tag{297}$$

across DZ. Finally, the energy Eq. (290) integrated and evaluated away
from the DZ gives

$$m\,(h_1 + u_1{}^2/2) + I_1 \;=\; m\,(h_2 + u_2{}^2/2) + I_2 \tag{298}$$

The light intensity on one side of the DZ is known (i. e., either I_1 or I_2);
the intensity on the other side of the DZ depends upon the absorption pro-
cesses. In turn the absorption physics (absorption coefficient) is coupled

34

$$\ldots \ldots \ldots \ldots \ldots \ldots \ldots$$
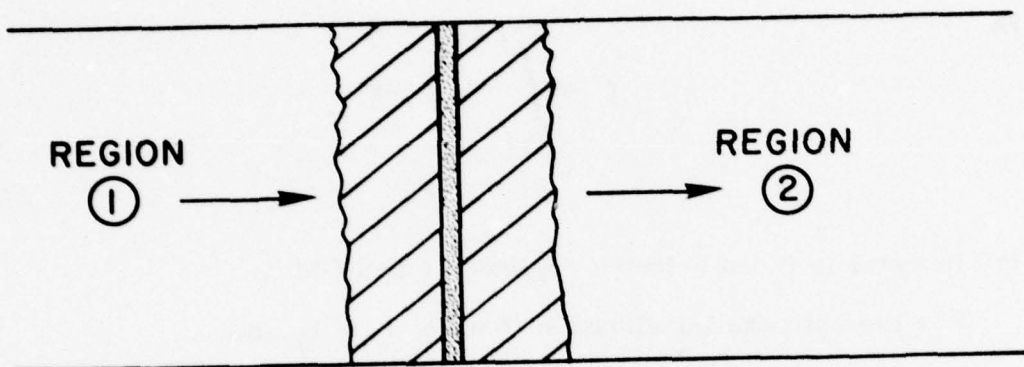
REGION ① → **REGION ②**

H 4250

Figure 42   Discontinuity Zone

35

to the dynamics (flowfield) as well as the thermodynamics. We now consider Eq. (291). For the case with $\delta = -1$ and taking the laser flux $I_o = I_1$

$$I_1 - I_2 = I_o \left[1 - \exp(-\zeta) \right] \qquad (299)$$

where

$$\zeta \equiv \int_{[1]}^{[2]} \alpha \, dx \qquad (300)$$

and the integral is taken between region [1] and [2].

For the antiparallel situation ($\delta = 1$), $I_2 = I_0$ and

$$I_2 - I_1 = I_0 \left(1 - \exp(-\zeta) \right) \qquad (301)$$

If we consider the parallel situation ($\delta = -1$) with the direction of the laser radiation the same as the flow direction, then Eq. (298) reads

$$h_2 + u_2^2/2 = h_1 + u_1^2/2 + \frac{I_0}{m} \qquad (302)$$

for the complete absorption of laser radiation in DZ. Region 1 is the unperturbed state with ρ_1, p_1, h_1 known. The wave velocity (of DZ) is $u_1 \equiv W$. The Hugoniot conditions then read

$$\rho_2 u_2 = \rho_1 W = m \qquad (303)$$

$$P_2 + m u_2 = p_1 + m W \tag{304}$$

$$h_2 + u_2^2/2 = h_1 + W^2/2 + I_0/\rho_1 W \tag{305}$$

In order to proceed further, the perfect gas relation with constant γ is employed.

$$h = \frac{\gamma}{\gamma - 1} \frac{p}{\rho} \tag{306}$$

Raizer[5] used the same relationship in his analysis.

It is more convenient to manipulate the equations after defining new variables. Let

$$\eta \equiv \rho_1/\rho_2 \tag{307}$$

$$P \equiv p_2/p_1 \tag{308}$$

Equation (304) reads

$$W^2 = \frac{(P-1) \dfrac{p_1}{\rho_1}}{1-\eta} \tag{309}$$

Substitution of Eq. (309) into the square of Eq. (205) after using Eq. (306) provides the following relationship between $P-1 \equiv \zeta$ and $(\eta-1)/\eta \equiv \sigma$:

$$\zeta^3 \, (\Gamma - 1 + \sigma/2)^2 \; + \; \zeta^2 \, 2\Gamma\sigma \, (\Gamma - 1 + \sigma/2)$$

$$+ \; \zeta \, \Gamma^2 \sigma^2 \; + \; H_0^2 \, \sigma \; = \; 0 \tag{310}$$

where

$$\Gamma \equiv \gamma/(\gamma - 1) \quad \text{and} \quad H_0^2 \equiv I_0^2 \, \rho_1/p_1^3 \tag{311}$$

Equation (310) is a cubic equation for ζ (pressure) as a function of the σ (density). This relation is more general than the Raizer[5] - derived relation. The Raizer formula is obtained from our basic equations by substituting Eq. (309) into Eq. (306) (without squaring); he obtains

$$\zeta = \left[\frac{\frac{2\gamma}{\gamma - 1} \, (1-\eta) \; + \; 2(1-\eta)^{1/2} \, H_0}{\left(\frac{\gamma+1}{\gamma-1}\right) \eta - 1} \right]^{2/3} \tag{312}$$

Raizer omitted the first term in the numerator by making the "zero counter pressure" approximation. We include this term for completeness. The difficulty in Eq. (312) is the square root term $(1-\eta)^{1/2}$. On the detonation branch with $\eta < 1$ $(\rho_1 < \rho_2)$ an acceptable value for the pressure can be obtained; however, on the deflagration branch $\eta > 1$ $(\rho_1 > \rho_2)$ we would be forced to take accept an imaginary pressure if we used Eq. (312). The use of our Eq. (310) circumvents this difficulty and permits the calculation of the deflagration branch.

Prior to describing solutions for the generalized Hugoniot curve we must specify the physical limits of the parameters.

38

(i)   The density is a positive finite quantity: $0 < \eta < \infty$

(ii) The pressure is a positive finite quantity: $0 < P < \infty$

(iii) A solution for Eq. (310) is given by $\xi = 0$, $\sigma = 0$ independent of the value of H_o. This point corresponds to $W^2 = 0$ since $P_1 = P_2$ and $\rho_1 = \rho_2$ for this situation.

(iv) The Hugoniot curve exists in the second and fourth quadrants of the coordinate system formed by the intersection of the $\xi = 0$ line and $\eta = 1$ line. This conclusion is reached from Eq. (309) which states that all solution points on the Hugoniot curve must have negative slopes in the ξ-η plane.

The forbidden regions are shown shaded in Figure 43 along with solutions curves obtained by solving Eq. (310). The Hugoniot curves on the deflagration branch lead to negative pressures at values of η that depend upon the laser radiation intensity. Note how rapidly negative pressures are realized for $H_o = 10$ whereas a gentle approach at nearly constant pressure is found for $H_o = 1$. The variation of the value of η whence the pressure first becomes negative, i.e., η_{cr} can be found vs H_o from Eq. (310) by setting $\xi = -1$. We obtain a parabolic equation for $\sigma_{cr} = (\eta_{cr} - 1)/\eta_{cr}$. This algebraic equation can be readily solved. In particular for $\gamma = 1.40$,

$$\sigma_{cr} = 5/6 + H_o^2/18 - \sqrt{(H_o^4 + 30 H_o^2)/324} \qquad (313)$$

A plot of η_{cr} vs H_o is shown in Figure 44. Note that the slowest variation of η_{cr} with H_o occurs in the neighborhood of $H_o \approx 1$. Furthermore, as H_o becomes excessively large $\eta_{cr} \to 1$ and as H_o becomes very small $\eta_{cr} \to 6$.
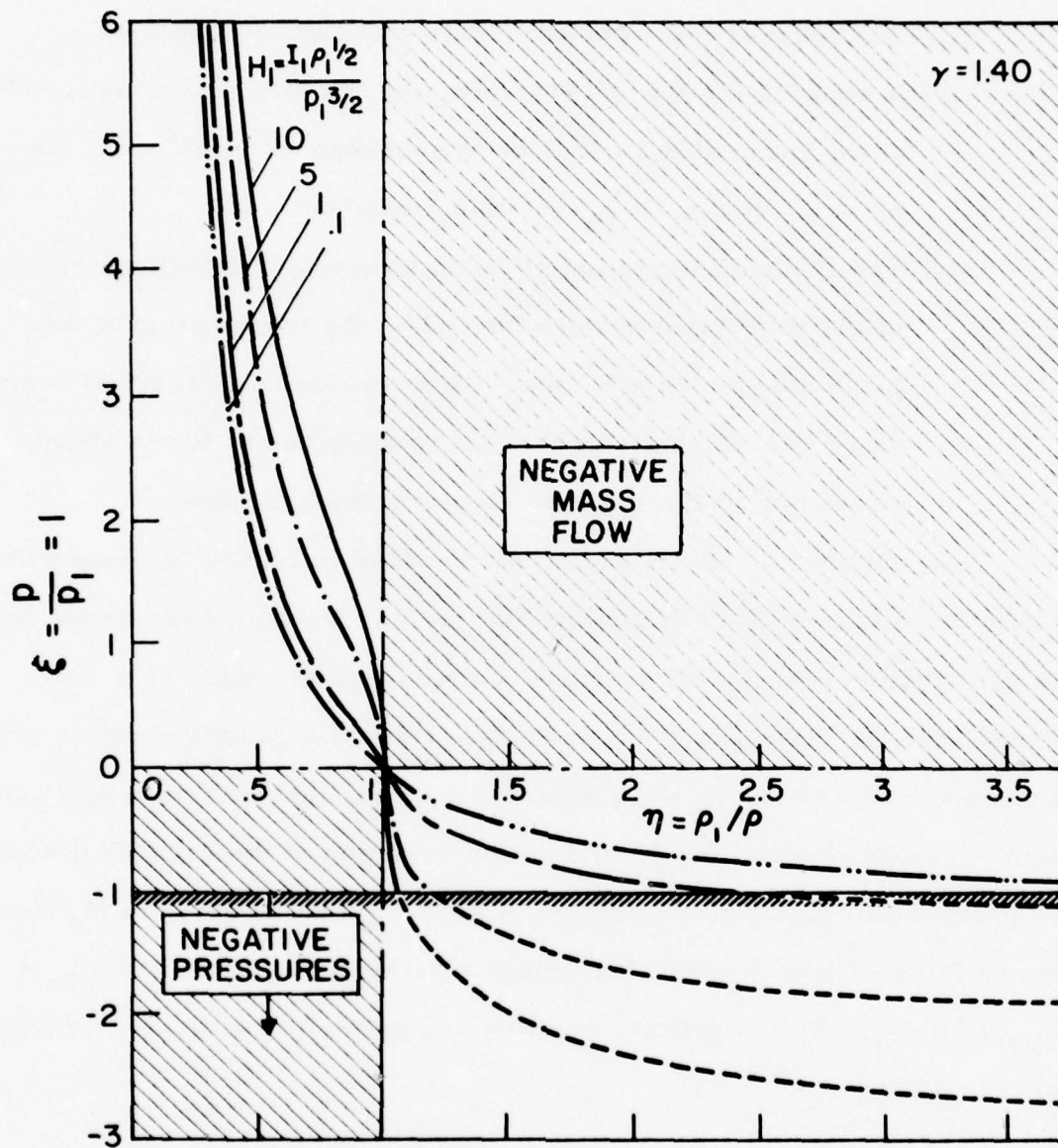
39

Figure 43   Laser Absorption Hugoniot Curves ($\gamma = 1.40$)

40
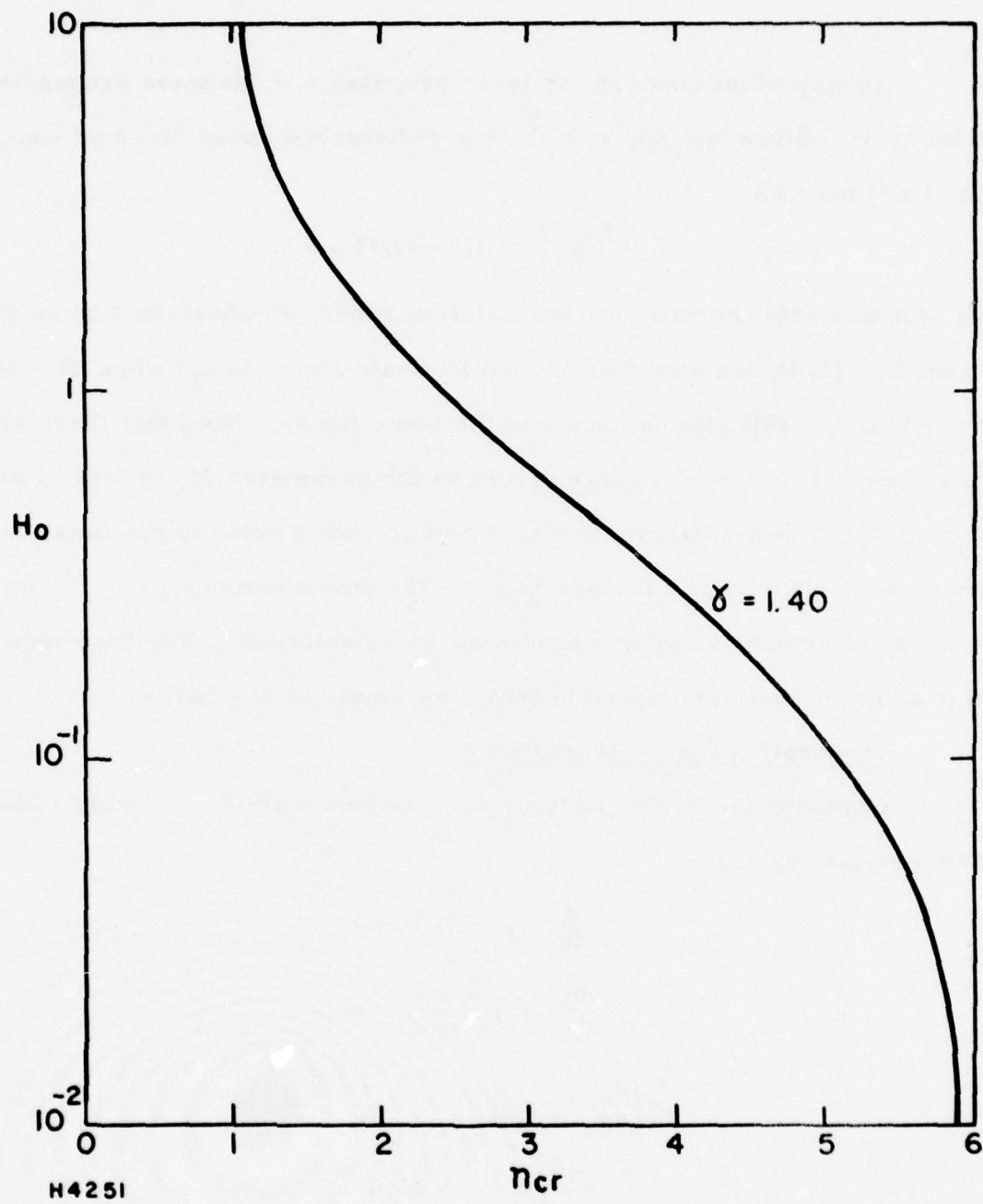
Figure 44   Variation of Critical Density Ratio with Input Radiation
(γ = 1.40)

41

An important concern for laser propulsion is the wave propagation velocity W. Since $\gamma p_1/\rho_1 = a_1^2$, the undisturbed speed of sound squared, Eq. (309) becomes

$$\gamma \ W^2/a_1^2 = (P - 1)/(1 - \eta) \tag{314}$$

We plot this velocity ratio for our solution curves as shown in Figure 45. From Eq. (314), we note that W will be sonic (equal to a_1) when $(P - 1)/(1 - \eta)$ is γ. This line is shown on the same figure. Note that there are no subsonic solutions for large values of the parameter H_o (= 10). For $H_o = 1$ there is a small regime of subsonic waves prior to the negative pressure limit. As one further reduces the power number ($H_o = 1/10$), there is an extensive region of subsonic wave solutions. For the range of η's shown, the wave speed becomes as small as one-half a_1.

b. Absorption Zone Gasdynamics

Consider the basic gasdynamic equations with laser energy addition. These equations read:

$$\frac{d}{dx} (\rho u A) = 0 \tag{315}$$

$$\frac{dp}{dx} + \rho u \frac{du}{dx} = 0 \tag{316}$$

$$\rho u \left(\frac{dh}{dx} + u \frac{du}{dx} \right) = -\frac{1}{A} \frac{d(IA)}{dx} \tag{317}$$

$$\frac{d(IA)}{dx} = -IA \alpha \tag{318}$$

$$h = h(p, \rho) \tag{319}$$

$$T = T(h, p) \tag{320}$$

$$H = h + \tfrac{1}{2} u^2 \tag{321}$$

where A is the area variation of the channel.

42
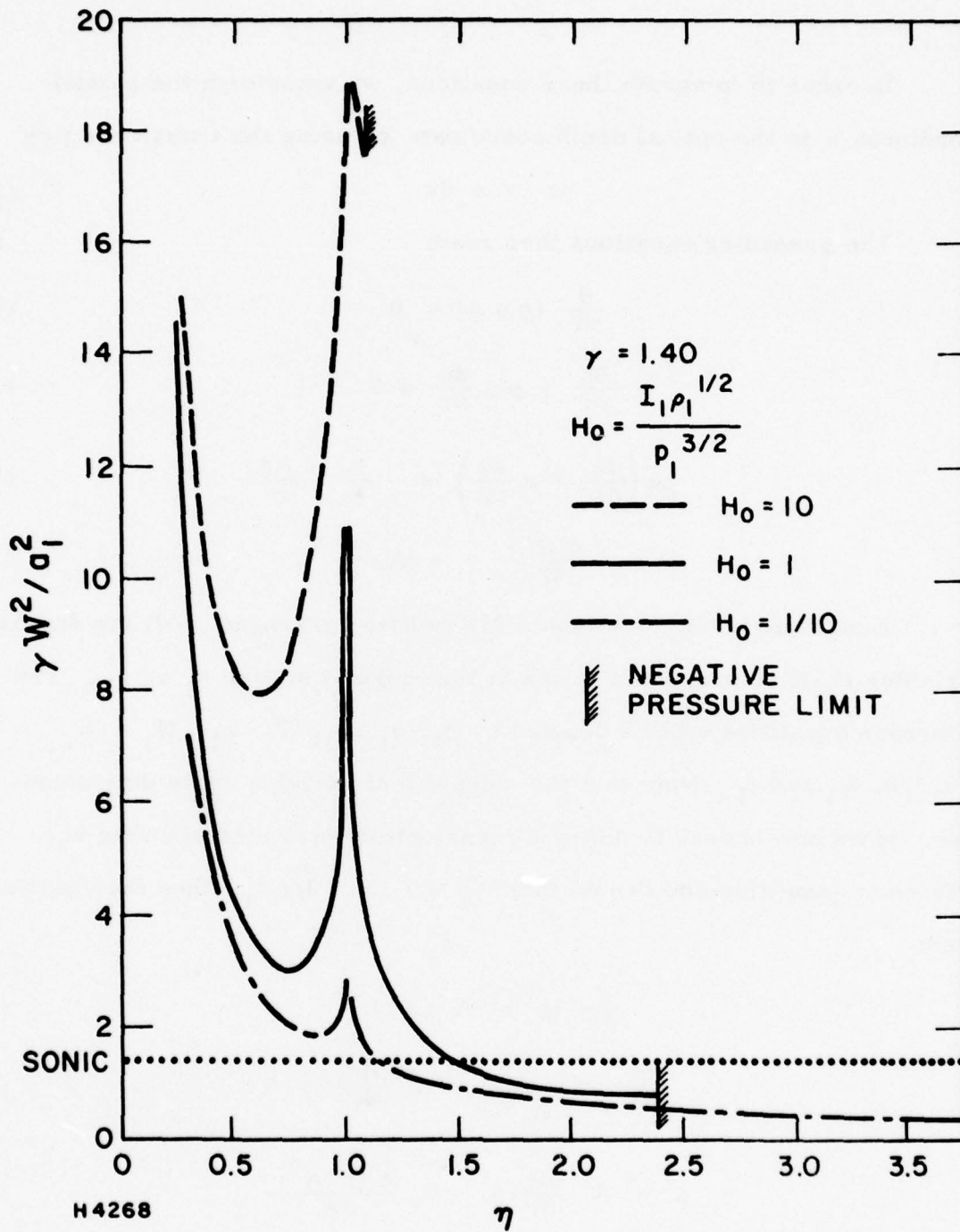
Figure 45   Wave Velocities on Hugoniot Curve ($\gamma = 1.40$)

43

In order to integrate these equations, we transform the spatial coordinate x to the optical depth coordinate τ using the transformation

$$d\tau \equiv a \ dx \tag{322}$$

The preceding equations then read:

$$\frac{d}{d\tau} \ (\rho \ u \ A) = 0 \tag{323}$$

$$\frac{dp}{d\tau} + \rho \ u \ \frac{du}{d\tau} = 0 \tag{324}$$

$$\rho u \left(\frac{dh}{d\tau} + u \ \frac{du}{d\tau}\right) = - \ \frac{1}{A} \ \frac{d \ (IA)}{d\tau} \tag{325}$$

$$\frac{d \ (IA)}{d\tau} = - \ IA \tag{326}$$

Equations (319), (320) and (321) remain unchanged. All the dependent variables shall be presumed known at the original station x_1 or τ_1. The reference quantities will be denoted by ρ_1, u_1, p_1, T_1, h_1, $H_1 = h_1 + u_1^2/2$, A_1 and I_1. Note that the independent variable τ is dimensionless. If we now choose to define dimensionless variables utilizing our reference quantities and denote them by $(\ )^* \equiv (\ )/(\ )_1$, then the equations read:

$$\frac{d}{d\tau} \ (\rho^* \ u^* \ A^*) = 0 \tag{327}$$

$$\frac{dp^*}{d\tau} + \frac{1}{C_1^2} \ \rho^* \ u^* \ \frac{du^*}{d\tau} = 0 \tag{328}$$

$$\rho^* \ u^* \ A^* \ \frac{dH^*}{d\tau} = - \ P_1 \ \frac{d \ (I^* \ A^*)}{d\tau} \tag{329}$$

$$H^* = \left(1 - \frac{u_1^2}{2H_1}\right) h^* + \left(\frac{u_1^2}{2H_1}\right) u^{*2} \tag{330}$$

$$\frac{d \ (I^* \ A^*)}{d\tau} = - \ I^* \ A^* \tag{331}$$

44

where a compressibility number

$$C_1^2 \equiv p_1/\rho_1 u_1^2 \tag{332}$$

a power ratio

$$P_1 \equiv I_1 A_1/\rho_1 u_1 A_1 H_1 \tag{333}$$

and the ratio $(u_1^2/2H_1)$ contained in Eq. (350) characterizes the laser energy addition problem.

Equation (327) simply integrates to

$$\rho^* u^* A^* = 1 \tag{334}$$

The transformation to the optical depth coordinate τ makes it easy to integrate Eq. (331). The solution reads

$$I^* A^* = e^{(\tau_1 - \tau)} \tag{335}$$

The use of Eqs. (334) and (335) in Eq. (329) permits the integration of the equation. The solution for the stagnation enthalpy becomes

$$H^* = 1 + P_1 (1 - e^{\tau_1 - \tau}) \tag{336}$$

We also have a thermodynamic relationship (319) which may in general be a complex function

$$h^* = h^* (p^*, \rho^*) \tag{337}$$

It now remains to solve the momentum equation relating the variation of pressure to the velocity variation. We begin by multiplying Eq. (328) by A^* and utilizing Eq. (334) to find

$$\frac{1}{C_1^2} \frac{du^*}{d\tau} = p^* \frac{dA^*}{d\tau} - \frac{d (A^* p^*)}{d\tau} \tag{338}$$

We can integrate Eq. (338) to the implicit form

$$\frac{1}{C_1^2} u^* = F(\tau) - F(\tau_1) + \frac{1}{C_1^2} u_1^* - A^* p^* + A_1^* p_1^* \tag{339}$$

45

where

$$F(\tau) - F(\tau_1) = \int_{\tau_1}^{\tau} p^*(\tau) \frac{dA^*}{d\tau} \, d\tau \qquad (340)$$

The system of equations can be solved algebraiclly for some idealized situations. In general, one must resort to a numerical calculation in order to solve the system.

c. Constant Pressure Approximation

From Eq. (328) note that if the flow is nearly incompressible $(C_1^2 \gg 1)$, $p \approx p_1 = $ constant. Upon making this approximation, one can solve Eqs. (334), (336) and (337) simultaneously or we can obtain a single equation for the density h^*. Equation (336) and the definition of H^* by Eq. (330) implies

$$\left(1 - \frac{u_1^2}{2H_1}\right) h^* + \left(\frac{u_1^2}{2H_1}\right) u^{*2} = 1 + P_1 \left(1 - e^{\tau_1 - \tau}\right)$$

Equation (334) gives

$$\left(1 - \frac{u_1^2}{2H_1}\right) h^* + \left(\frac{u_1^2}{2H_1}\right) \frac{1}{\rho^{*2} A^{*2}} = 1 + P_1 \left(1 - e^{\tau_1 - \tau}\right)$$

On the initial condition isobar $(p_1^* = 1)$ in relation (337) we have $h^* = h_1^*(p_1^* = 1, \rho^*)$. Hence

$$\left(1 - \frac{u_1^2}{2H_1}\right) h_1^*(p_1^* = 1, \rho^*) + \left(\frac{u_1^2}{2H_1}\right) \frac{1}{\rho^{*2} A^{*2}} = 1 + P_1 \left(1 - e^{\tau_1 - \tau}\right) \qquad (341)$$

For a perfect gas,

$$h = \frac{\gamma}{\gamma - 1} \frac{p}{\rho} \qquad (342)$$

or in dimensionless form

$$h^* = p^*/\rho^* \qquad (343)$$

46

and for the $p_1^* = 1$ isobar,

$$h_1^* = \rho^{*-1}$$

Therefore using Eq. (343) in Eq. (341) and defining $R^* \equiv \rho^{*-1}$, we get a quadratic relation for R^*, i.e.,

$$a R^{*2} + b R^* + c = 0 \tag{344}$$

where

$$a = \left(\frac{u_1^2}{2H_1}\right) \frac{1}{A^{*2}}$$

$$b = 1 - \frac{u_1^2}{2H_1}$$

$$- c = 1 + P_1 \left(1 - e^{\tau_1 - \tau}\right)$$

The solution is therefore

$$R^* = \frac{-b + \sqrt{b^2 - 4ac}}{2a} \tag{345}$$

We further note that the ratio of $u_1^2/2H_1$ will be small for our low speed high pressure environment. Consequently $a \approx 0$, $b \approx 1$. Then Eq. (344) simply gives

$$R^* = 1 + P_1 \left(1 - e^{\tau_1 - \tau}\right) \tag{346}$$

or

$$\rho^* = \frac{1}{1 + P_1 \left(1 - e^{\tau_1 - \tau}\right)} \tag{347}$$

The selection of the perfect gas law made it easy to solve Eq. (342). If we do not make this approximation, but let a and b be zero and one respectively (equivalent to zero velocity), then the equation for the density reads

47

$$h_1^*(1, \rho^*) = 1 + P_1(1 - e^{\tau_1 - \tau}) \qquad (348)$$

A curve fit for $h_1^*(1, \rho^*)$ e.g., from a Mollier diagram could be used to obtain an explicit analytical relationship for ρ^*. The inversion of Eq. (348) gives, in general,

$$\rho^* = \rho^* \left[1 + P_1(1 - e^{\tau_1 - \tau}) \right] \qquad (349)$$

whence ρ^* is a function of the argument in brackets.

At constant pressure we can obtain an approximate form for the enthalpy variation with density, i.e., $h_1^*(1, \rho^*)$ under nonideal conditions. We no this for high-temperature water - both as an example and as a potentially important practical case. An examination of the H_2O Mollier chart shows that at a high pressure (50 atm), the variation of enthalpy is approximately

$$h_1^*(1, \rho^*) = (\rho^*)^{-5/4} \qquad (350)$$

in the temperature range of 3500°K to 5500°K. Expression (350) differs from Eq. (343) because of dissociation effects. Calculations for the ideal gas Eq. (343) and the real gas Eq. (350) will be described in the subsequent section on the molecular absorption of AlO.

d. Molecular Absorption of AlO

The absorption coefficient of 1% Al_2O_3 molar in H_2O at a pressure of 50 atm peaks at an interesting (from a mission point of view) temperature and value as calculated by Douglas-Hamilton.[6] The curves obtained may be fitted quite well to be parabolas in the semi-log plot of α (cm^{-1}) vs T(°K). A curve fit of the 50 atm case was made (c. f. Figure 46) and the

(6) Douglas-Hamilton, D. H., AERL private communication (1976).

48
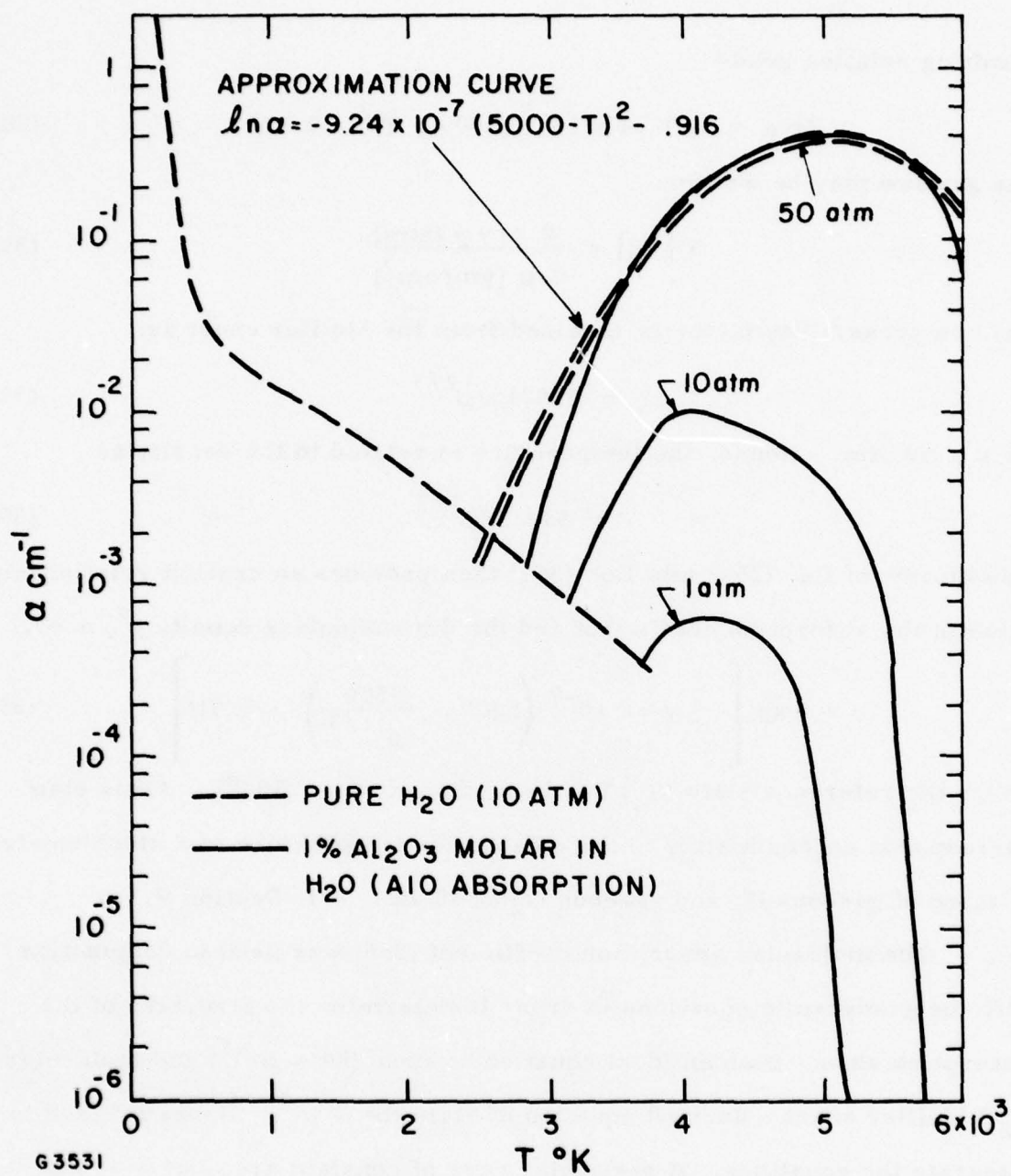
Figure 46   Absorption Coefficient of 1% Al_2O_3 Molar in H_2O

49

resulting relation reads

$$\ln a = -9.24 \times 10^{-7} (5000 - T)^2 - 0.916 \qquad (351)$$

The gas law may be written:

$$T\,[^{\circ}K] = \frac{0.219\ p\ [atm]}{Z\ \rho\ [gm/cm^3]} \qquad (352)$$

The compressibility factor is obtained from the Mollier chart as:

$$Z = 0.0213/\rho^{2/3} \qquad (353)$$

for p = 50 atm. Hence, the temperature is related to the density as

$$T = 514.1/\rho^{1/3} \qquad (354)$$

Substitution of Eq. (354) into Eq. (351) then provides an explicit relationship between the absorption coefficient and the dimensionless density ρ^*, i.e.,

$$a = \exp\left[-9.24 \times 10^{-7} \left(5000 - \frac{3500}{\rho^{*1/3}}\right) - 0.916\right] \qquad (355)$$

where the reference state (T_1) has been chosen to be $3500^{\circ}K$. (This state corresponds approximately to the combustion temperature of a stochiometric mixture of gaseous H_2 and gaseous O_2 at 50 atm, c.f. Section V.5.)

The molecular absorption coefficient (355) was used in conjunction with the gasdynamic equations in order to determine the structure of the absorption zone. Both an ideal equation of state ($h^* \sim \rho^{*-1}$) and molecular H_2O Mollier chart - derived equation of state ($h^* \sim \rho^{*-5/4}$) was utilized to integrate the equations. A particular case of constant area ($A^* = 1$) was selected. Hence the solution for the intensity is merely a decaying exponential in the τ plane as given by Eq. (335). This is plotted in Figure 47; note that I/I_1 is 1% of its initial value at $\tau \approx 4.6$.

The calculations presented below correspond to the dimensionless compressibility number, $C_1 = 8.66$ and power ratio $P_1 = 2.9, 23.7$. Since

50

G6045
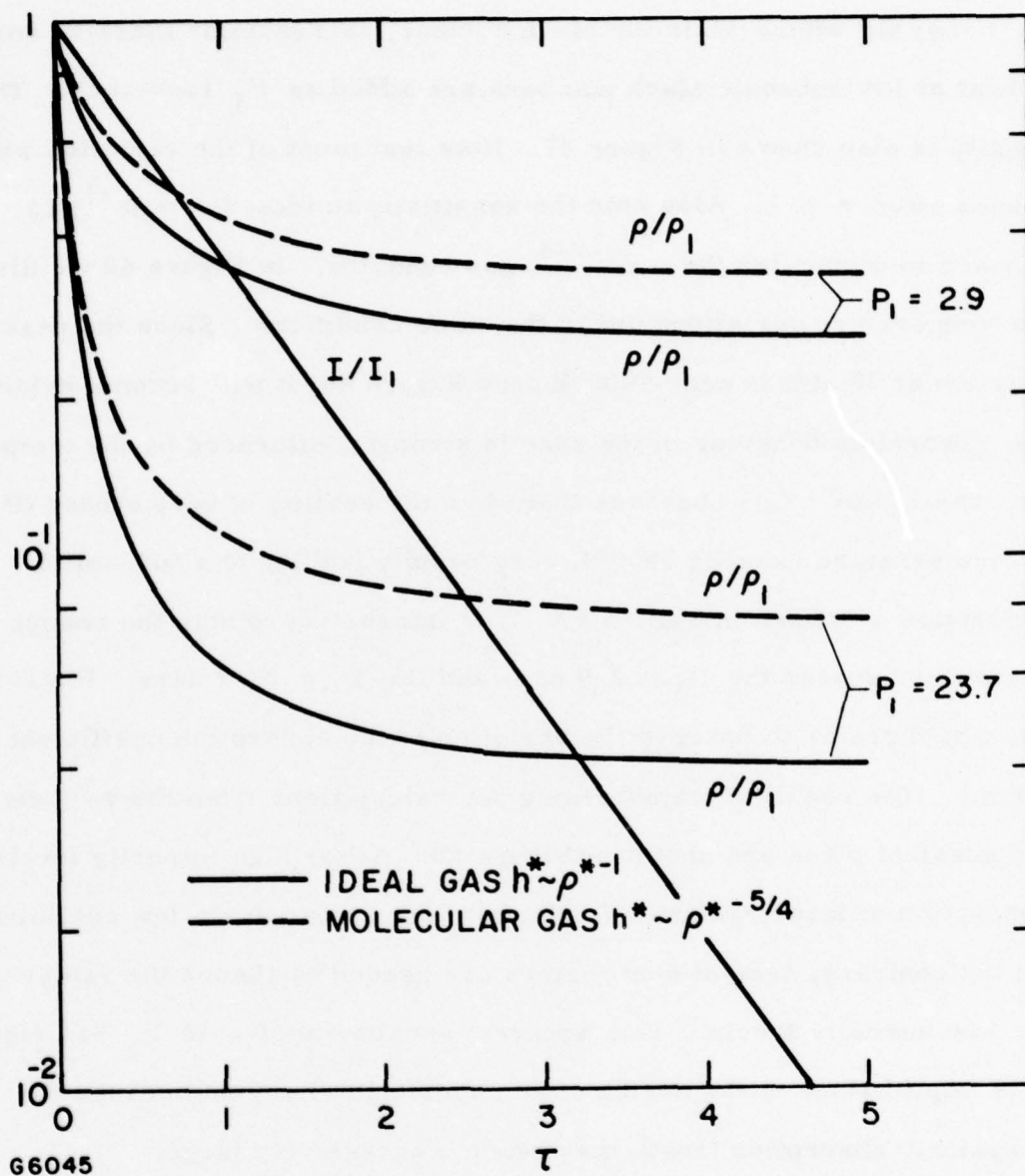
Figure 47   Density and Intensity Variation in Optical Depth Plane

51

$C_1 = \sqrt{\gamma/M}$, where M is the Mach number, increasingly massive amounts of heat at low subsonic Mach numbers are added as P_1 increases. The density is also shown in Figure 47. Note that most of the variation with τ ceases after $\tau > 2$. Also note the sensitivity to ideal $(h* \sim \rho*^{-1})$ as opposed to molecular $(h* \sim \rho*^{-5/4})$ gas behavior. In Figure 48 we illustrate the temperature variations under the same conditions. Since the peak absorption at 50 atm is near $5000^\circ K$ (see Figure 46) it will become evident that absorption behavior in the zone is strongly influenced by the temperature variations. One observes that when the heating is very strong $(P_1 \gg 1)$, the temperature exceeds $5000^\circ K$ very rapidly leading to a turn-off of absorption as shown in Figure 49. It is interesting to note the change in character between the $P_1 = 2.9$ case and the $P_1 = 23.7$ case. Physically one would prefer to observe the variation of the absorption coefficient with x (cm). The result of transforming our calculations from the τ-plane to the physical plane are shown in Figure 50. At the high intensity levels, the absorption of laser radiation is virtually complete after a few centimeters. On the contrary, tens of centimeters are needed to absorb the radiation at the low intensity levels. This apparent sensitivity of α to P_1 has significant implications in the design of an experimental engine because the "physical" absorption length may become excessively large.

e. Absorption Stability

The stability of laser-heated flows is an important concern for any absorption scheme. Wu and Pirri[7] examined the "local" stability of a laser heated flow in a geometry representative of a typical rocket motor

(7) Wu, P. and Pirri, A.N., AIAA J. 14, No. 3, 390 (1976).

$P_I = 23.7$

$P_I = 2.9$

10^4

T
(°K)

IDEAL GAS $h \sim \rho^{-1}$ ——————

MOLECULAR GAS $h \sim \rho^{-5/4}$ — — — —

10^3

0   1   2   3   4   5

τ

G 6039
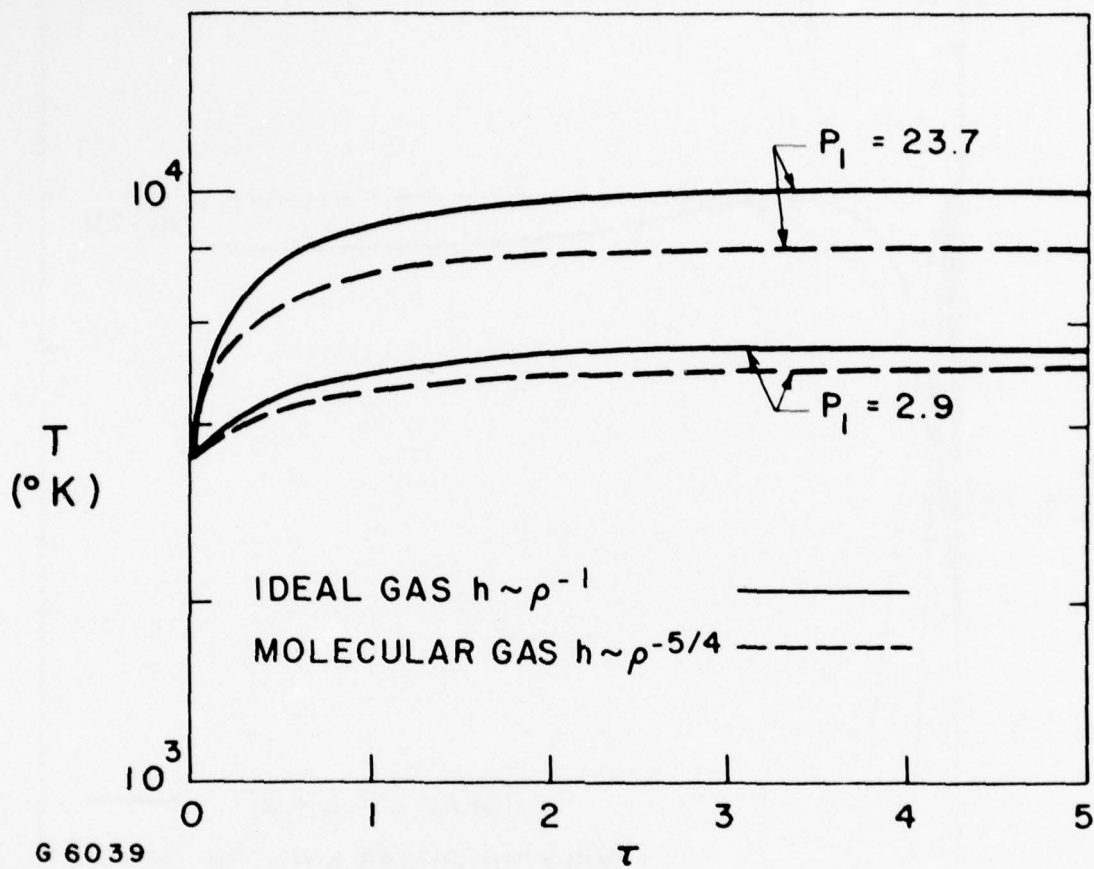
Figure 48   Temperature Variation in Optical Depth Plane

53
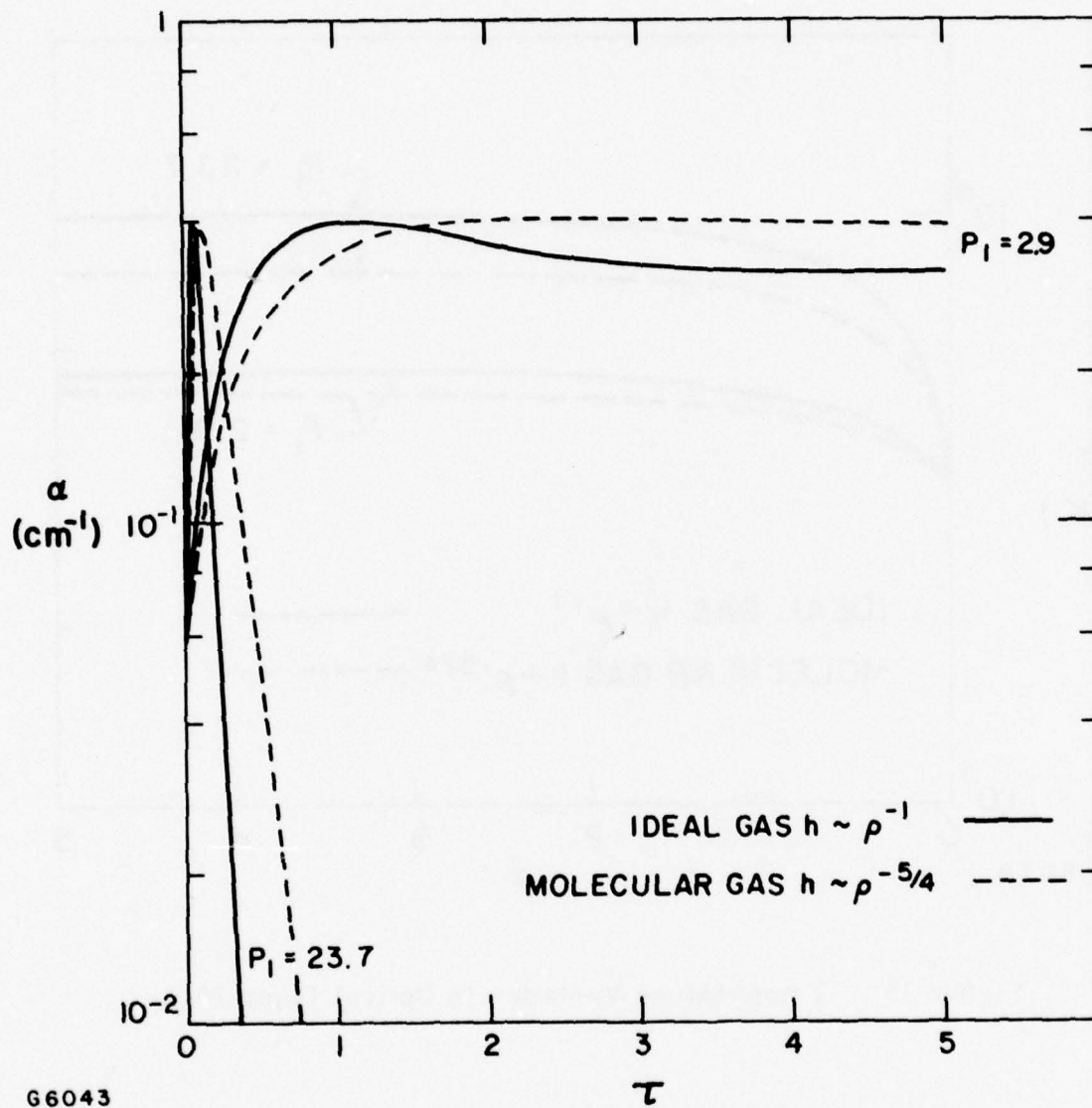
Figure 49   Absorption Coefficient in Optical Depth Plane

G6043
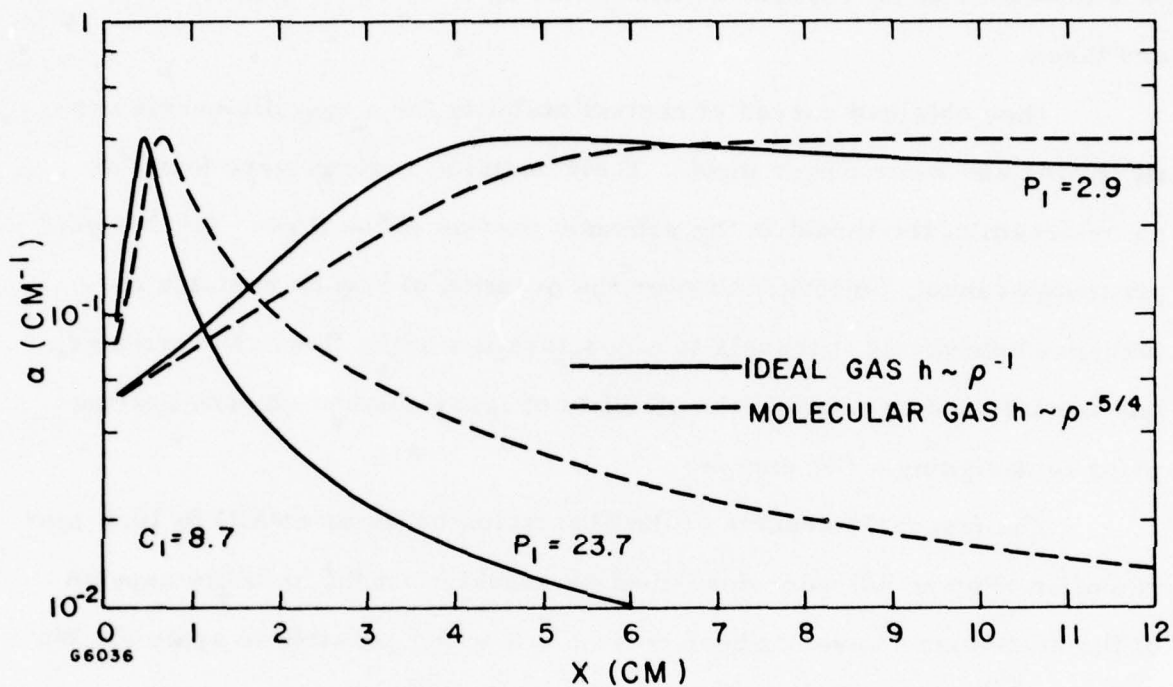
Figure 50   Absorption Coefficient in Physical Plane

with an absorption chamber followed by a throat and then an expansion nozzle. The absorption coefficient was modeled as $K_c \rho^n T^m$ where K_c is a constant and the Inverse Bremsstrahlung values $n = 2$, $m = -3/2$ are taken.

They obtained curves of neutral stability for a specific nozzle configuration and laser power input. Their unstable regions were found to be upstream of the throat in the subsonic portion of the flow. The analysis presented cannot, however, answer the question of how an unstable disturbance behaves as it travels to a new location in the flow. Nevertheless, one is cautioned to examine the stability of laser absorption zone heating prior to designing a CW engine.

The favorable aspects of the absorption behavior of AlO to 10.6 μm radiation (Figure 50) were described previously; but the stability aspects of the heated zone have not been treated. It is not possible to apply the Wu and Pirri[7] stability calculations to the molecular absorption situation. Since the stability of the laser-heated zone as treated by Wu and Pirri[7] is dependent upon so many aspects of the physical problem such as absorption mechanism, channel area variation, real gas phenomena, beam direction (relative to flow direction) etc., it would appear to be fruitful to address the stability question from a more global point of view. That is, one could hope to answer the question: What type of absorption coefficient behavior in the flowing environment would lead to complete stability? Such an investigation will be patterned after the work of Jacob and Mani. [8]

---

(8) Jacob, J. and Mani, S. "Thermal Instability in High Power Laser Discharges" (1975).

56

4. SCALING STUDIES FOR TWO-PORT CW ENGINE

In the past experimental CW laser propulsion engines have been very small due in part to the lack of sufficient laser power available. We will confirm these features of laser rockets in detail for various rockets characterized by a constant ratio of specific heats.

a. Nozzle Throat Size

The cross-sectional area of the sonic nozzle throat following the laser absorption section is given by the following expression:

$$A_6 = \frac{\dot{m} \, T_5^{1/2}}{p_5} \left(\frac{R_o}{W_5} \right)^{1/2} \sqrt{\frac{1}{\gamma_5} \left(\frac{\gamma_5 + 1}{2} \right)^{\frac{\gamma_5 + 1}{\gamma_5 - 1}}} \tag{356}$$

where sub-6 refers to the nozzle throat and sub-5 refers to the absorption chamber; $\dot{m}$ is the mass flow, T_o is the stagnation temperature, p_o is the stagnation pressure, R_o is the gas constant, W is the molecular weight, and γ is the ratio of specific heats.

Under ideal conditions the maximum attainable exit velocity is given as:

$$u_7^2 = \frac{2 \gamma_5}{\gamma_5 - 1} \frac{R_o}{W_5} T_5 \tag{357}$$

The specific impulse is simply given by u_7/g, hence, a mission-derived value for I_{sp} defines the right hand side of Eq. (357). A relation between $T_5(^oK)$ and $I_{sp}(sec)$ is given below where W_5 is given in gm/gm-mole.

$$T_5(^oK) = 5.78 \times 10^{-3} \left(\frac{\gamma_5 - 1}{\gamma_5} \right) W_5 \, I_{sp}^2 \tag{358}$$

57

substitution of Eq. (358) into Eq. (356) provides:

$$A_6 = \frac{\dot{m} g I_{sp}}{p_{05}} \Gamma(\gamma_5)$$ (359)

where

$$\Gamma(\gamma_5) \equiv \left[\frac{\gamma_5 - 1}{2\gamma_5^2} \left(\frac{\gamma_5 + 1}{2} \right)^{\frac{\gamma_5 + 1}{\gamma_5 - 1}} \right]^{1/2}$$ (360)

$\Gamma(\gamma_5)$ varies monotonically from 0.339 ($\gamma_5 = 1.1$) to 0.616 ($\gamma_5 = 1.67$). The primary variation of A_6 in Eq. (359) is therefore due to $\dot{m} I_{sp}/p_{05}$. If we select an I_{sp} of 1000 sec, then

$$A_6(cm^2) = 0.967 \, \Gamma \, \frac{\dot{m}(gm/sec)}{p_{05}(atm)}$$ (361)

This relation is plotted in Figure 51 with the nozzle throat area as the parameter. In addition, we have added the laser power scale on the left hand side of the figure assuming all of the laser power goes into heating the gas, i.e.,

$$\dot{m} = \frac{2 \, IP}{g^2 I_{sp}^2}$$ (362)

where IP is the laser power. We have gone through this relatively simple exercise to highlight the observation that low pressure operation is favorable from the point of view of increasing the geometry of candidate CW engine configurations. For example, a laser power of 10 kW absorbed into a flowing gas at 0.2 gm/sec and 10^{-1} atm pressure would have a throat area of 7.5 cm^2 or a throat radius of 1.5 cm. The remainder of the scaled-up engine would be a nice laboratory device, i.e., a nozzle area ratio of 100

58
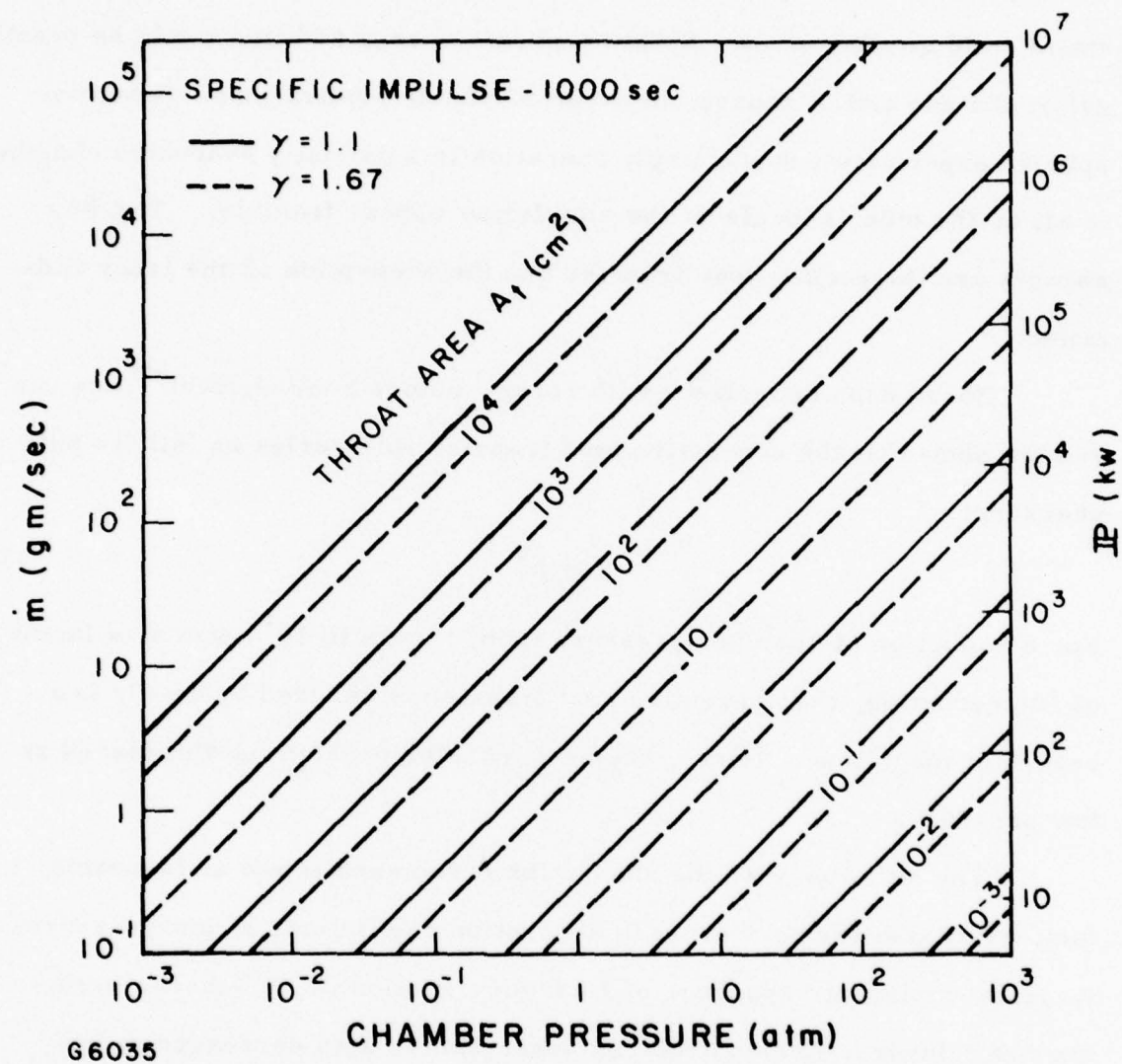
Figure 51   Throat Area for I_{sp} = 1000 sec

G6035

would provide an exit radius of 15 cm. The energy addition in the chamber would yield similar sizes. Subatmospheric energy addition would be practical at altitude and of course, in exoatmospheric applications. Subatmospheric experiments would imply operation in a partially evacuated chamber if all of the other aspects of the simulation appear feasible. Two key aspects are the rocket heat transfer and the absorption of the laser radiation.

Based upon experience with rocket motors Summerfield[4] one can readily show that the convective heat transfer rate varies as follows with pressure:

$$q \sim P_5^{0.9} \tag{363}$$

For a reduction of chamber pressure from 10 atm to 10^{-1} atm or a factor of 100 reduction, the convective heat transfer is reduced by nearly two orders of magnitude. Hence, the heat transfer problem is diminished at low pressures.

The situation with the absorption phenomena is not as favorable; in fact, most gases have decreased absorption coefficients at low pressures. A typical molecular absorber of 10.6 μm radiation (AlO) behaves in this manner. Inverse Bremsstrahlung absorption is also decreased at low pressures. This may imply the use of very long absorption chambers in low pressure rockets - but this is not a critical concern for the proof of principle simulation suggested in Section V.5.

b. Two-Port Rocket Scaling Considerations

The analysis of the two-port rocket considers nine different station locations. These stations are defined in the schematic two-port engine in Figure 52 and described in Table 4. One can calculate the relative sizes

60
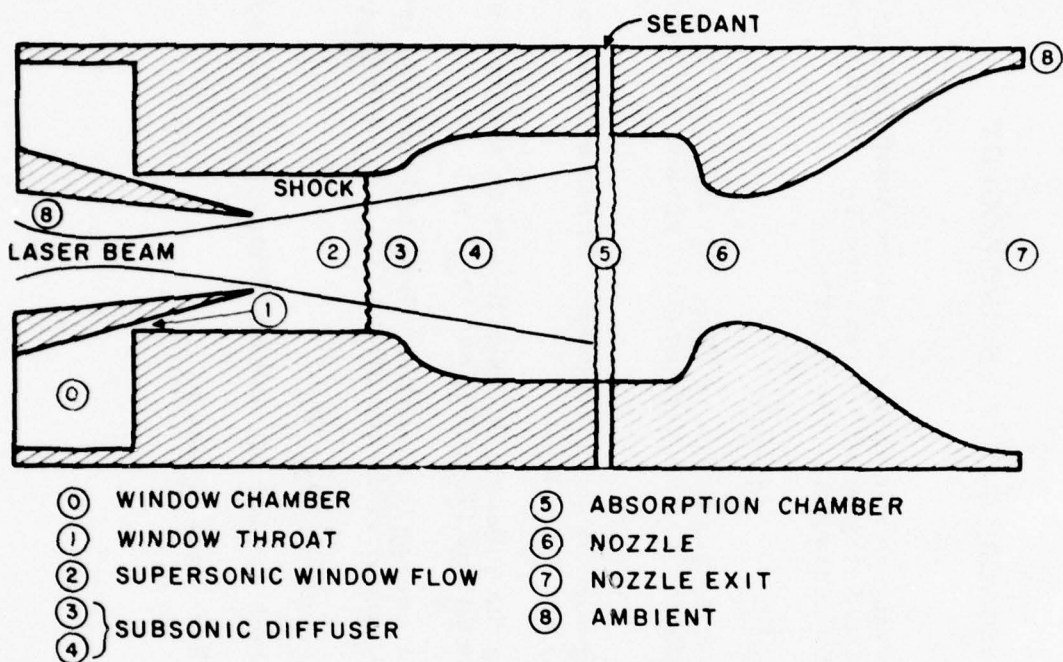
Figure 52   Schematic Two-Port CW Laser Engine

TABLE 4. STATIONS IN TWO-PORT LASER ENGINE ROCKET

⓪ Window Plenum: Plenum chamber containing an aerodynamic window/propellant gas at a stagnation pressure p_o and stagnation temperature T_o. Conditions should be sufficient to avoid condensation in the stream.

① Window Throat: Sonic throat with (T_{01}, T_1) and (p_{01}, p_1).

② Window Flow: Flow with Mach number M_2 at conditions (T_{02}, T_2) and (p_{02}, p_2). M_2 and the window geometry insure that the aerodynamic window will operate successfully.

③ Subsonic Flow: (Normal Shock) Subsonic flow following normal shock recovery. It has a Mach number M_3 at conditions (T_{03}, T_3) and (p_{03}, p_3).

④ Subsonic Flow: (Diffuser) Subsonic flow following the subsonic diffuser flow to an absorption chamber Mach number M_4 at conditions (T_{04}, T_4) and (p_{04}, p_4).

⑤ Absorption Zone: Zone in which the laser energy is absorbed. Heat addition will increase the Mach number to M_5 and provide conditions (T_{05}, T_5) and (p_{05}, p_5).

⑥ Nozzle Throat: Sonic throat with (T_{06}, T_6) and (p_{06}, p_6).

⑦ Nozzle Exit: Supersonic flow at a Mach number M_7 and conditions (T_{07}, T_7) and (p_{07}, p_7).

⑧ Ambient: Static ambient atmosphere with T_8 and p_8.

62

of such an engine once a specific mission requirement has been established. A specific impulse of 1000 sec is chosen. This corresponds to an interesting mission as defined in the trajectories section. The maps developed will provide indications of the physical size of two-port engines as a function of laser power level.

The maps are derived by considering the one dimensional gasdynamic heat addition problem using gas tables. Constant-γ calculations are performed even though the ratio of specific heats varies considerably for the thermodynamic states of interest. (See Appendix C).

As configured in Figure 52, the engine consists of three key elements that provide for the sizing of the engine; aerodynamic window, absorption chamber, and rocket nozzle. The nozzle throat sets the "level" of the rocket geometry - and thereby is a key aspect of the scaling. The elements are discussed in turn.

c. Aerodynamic Window

In Figure 53 we see an exploded view of a simply wedge supersonic aerodynamic window. The interior wedge angle θ is chosen such that the flow does not turn upstream (antiparallel) to the incoming laser radiation. This aerodynamic window must operate under pressure conditions that vary from 1 atm at sea level to essentially vacuum when operating exoatmospherically. The maximum flow deflection angle $\omega_{max}-\omega$(degrees) is given by an infinite pressure ratio (for the vacuum case). The variation of $\omega_{max}-\omega$ and θ is given in Figure 54 for various values of M_2 and the γ of the window flow gas. Note that we have indicated the minimum M_2 required to achieve the desired turning of the flow for each γ - this corresponds to $\theta = 0^o$. The

63
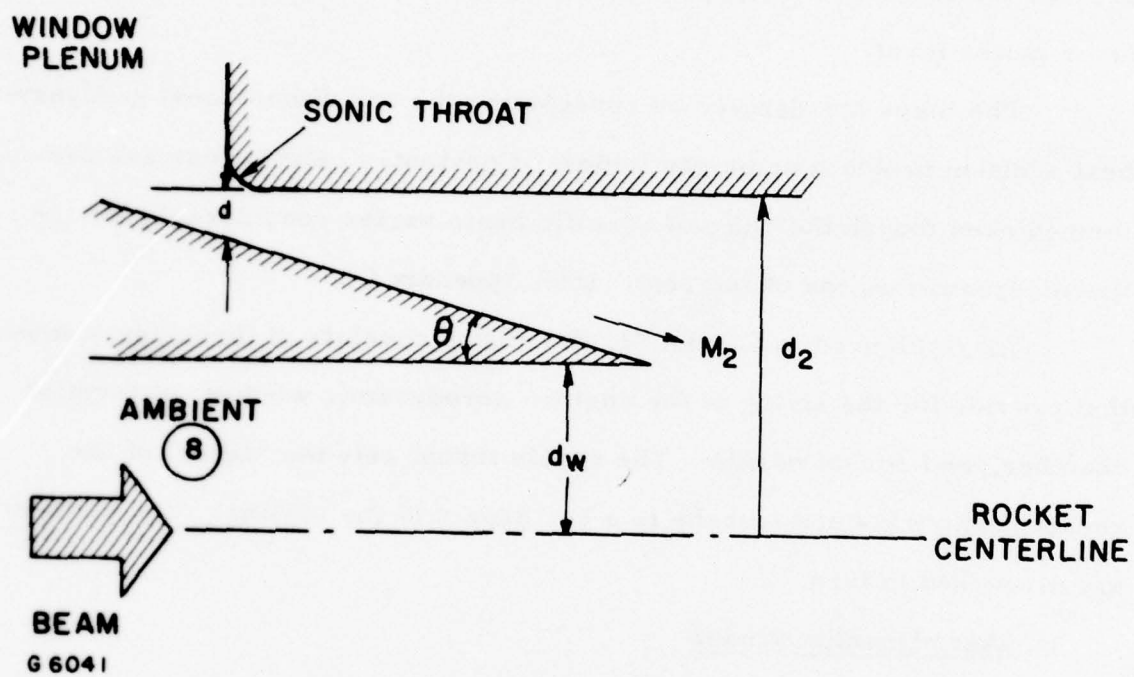
Figure 53   Wedge Supersonic Aerodynamic Window
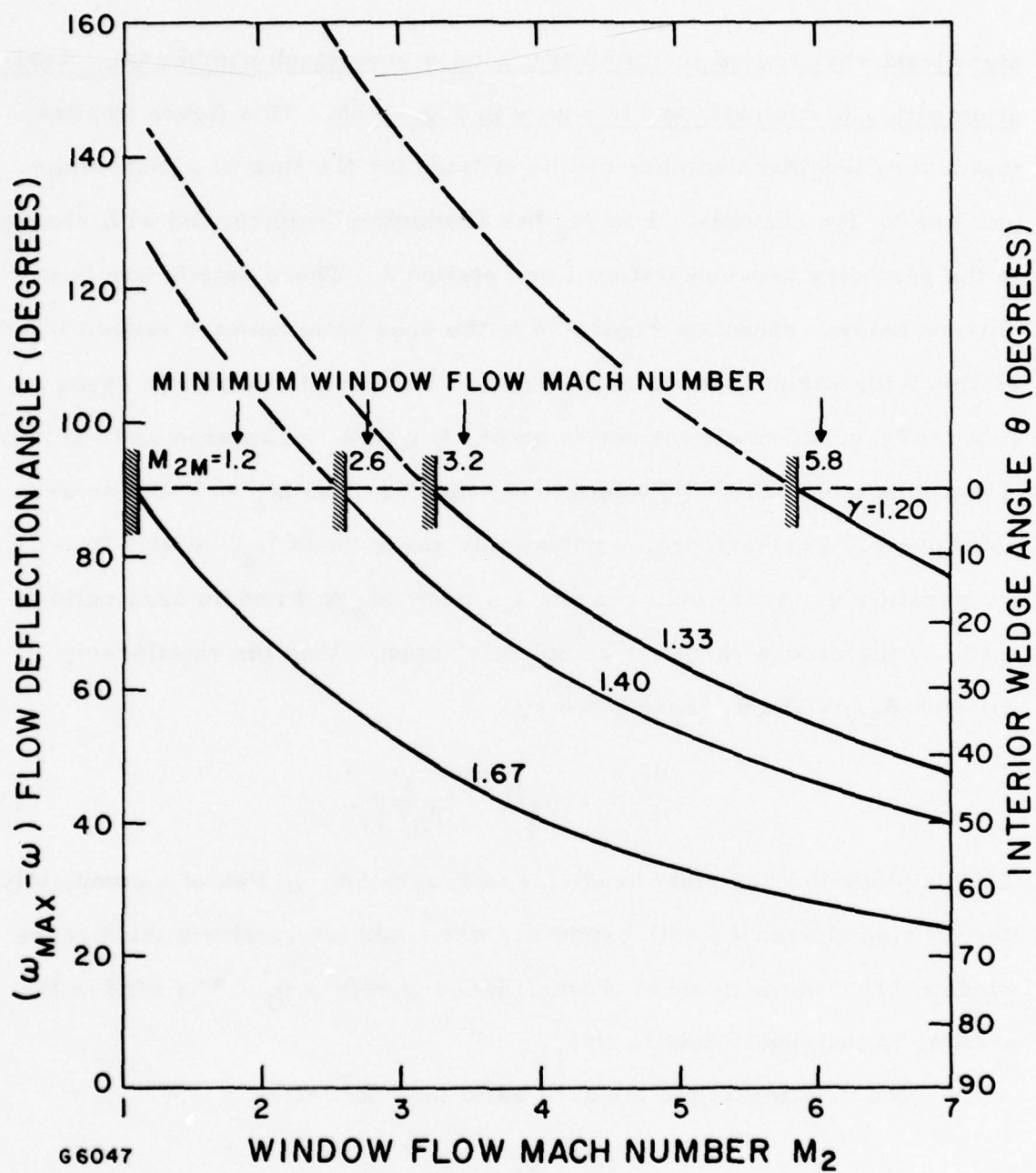
Figure 54   Flow Deflection Angle Variation with M_2 and θ

significant variation of the minimum window flow Mach number M_{2m} variation with γ is dramatic and is shown in Figure 55. This figure implies that a very low Mach number can be utilized for the flow of a monatomic gas like H_e for example. Low M_2 has immediate implications with respect to the geometry between station 1 and station 2. These details are considered below. Shown on Figure 56 is the area ratio between station 1 and station 2 for various values of M_2 and γ. The use of monatomic gases ($\gamma = 1.67$), would imply the use of an $M_2 \approx 2$ flow and an area ratio of ~ 2. A diatomic gas such as N_2 would imply the use of an $M_2 \approx 3$ with an area ratio of ~ 5. Furthermore, a polyatomic gas such as H_2O (with a low-temperature $\gamma = 4/3$) would require a window $M_2 \approx 4$ and an area ratio of > 10. If the window throat is completely "open," then the relationship between A_2/A_1 and d_1/d_2 is given by

$$\frac{d_1}{d_2} = 1 - \sqrt{1 - \frac{1}{(A_2/A_1)}} \tag{364}$$

This is plotted on the right hand side of Figure 56. In lieu of a completely "open" ring of area A_1 with height d_1, one could alternatively think of the window throat as made up of N small holes of radius δ_1. The window throat area A_1 is then equivalent to $N\pi\delta_1^2$.

The relationship to the area ratio then becomes

$$\frac{N^{1/2} \delta_1}{d_2} = \frac{A_1^{1/2}}{A_2} \tag{365}$$

This relationship is also plotted on Figure 56. We will utilize these quantities shortly when we specify the geometry of a particular engine. Previous rough scaling efforts have shown that the smallest dimension of the rocket configuration shown will be the window throat dimension - d_1 or δ_1.

66
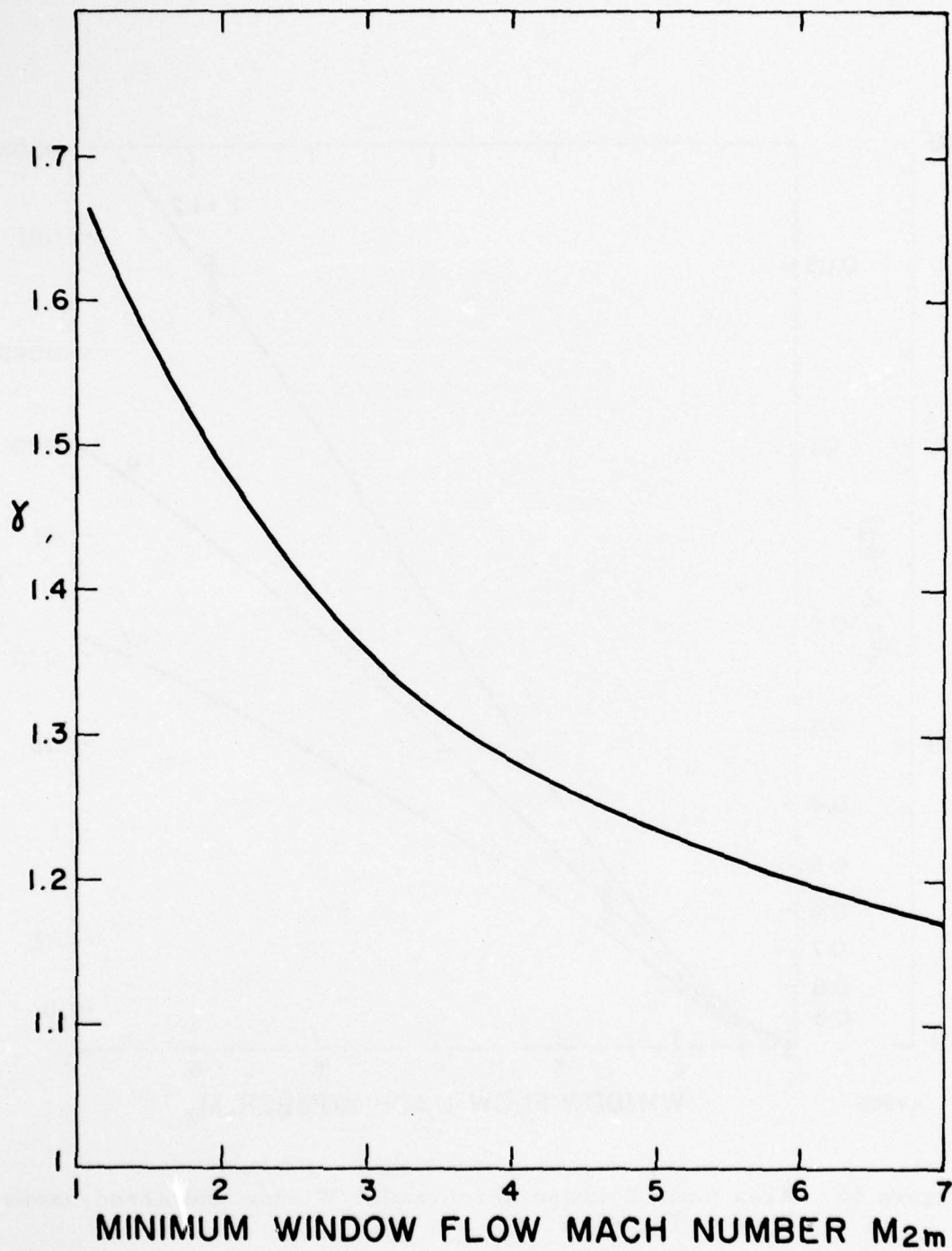
Figure 55   Minimum Window Flow Mach Number M_{2m}

H4263

67
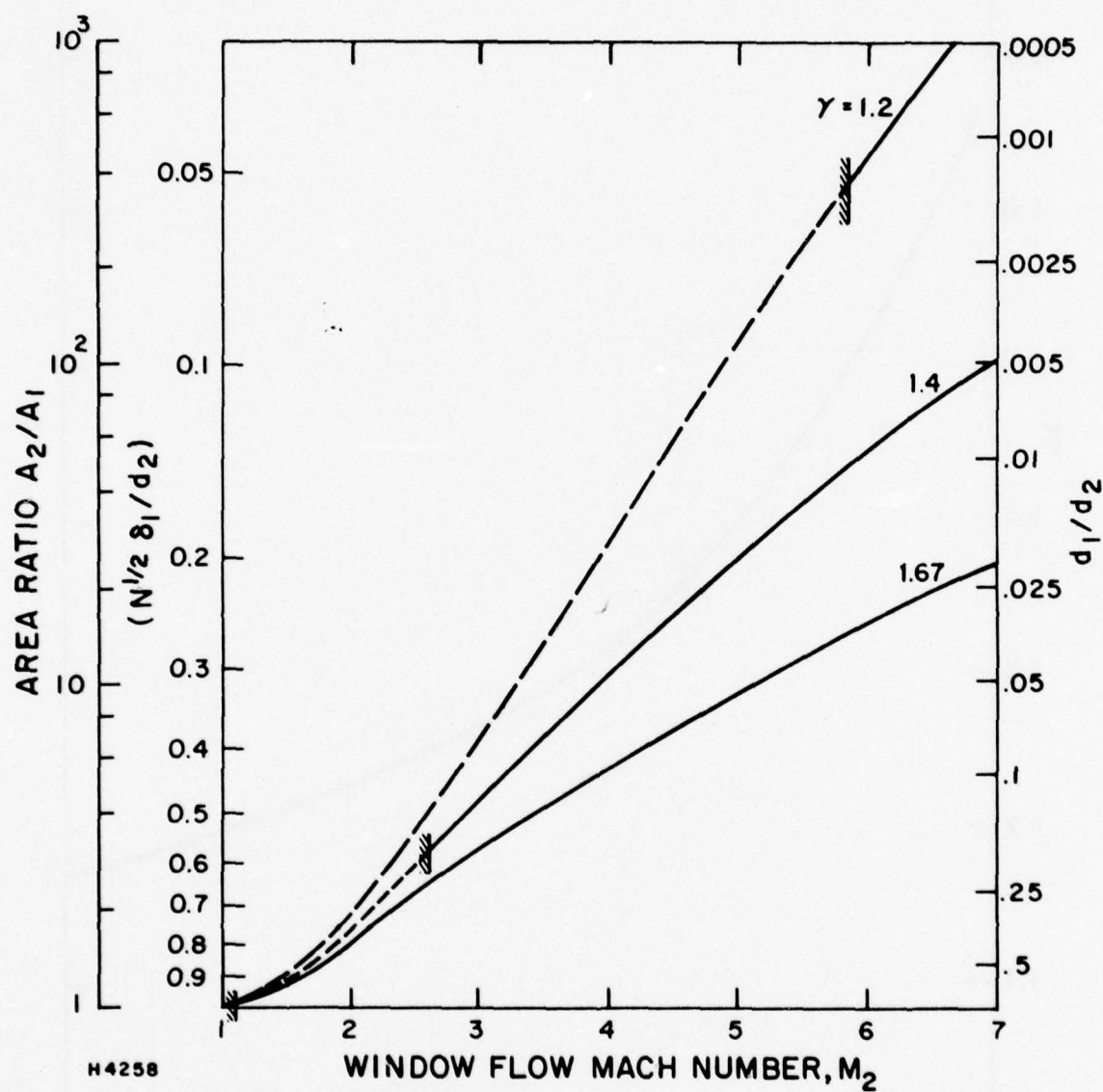
Figure 56   Area Ratio Between Aerodynamic Window and Aerodynamic
Window Throat

68

The window area which permits the entrance of the laser beam into the engine is defined by the radius d_w as shown on the schematic Figure 53. This area is sized by the breakdown limits of the laser radiation. A good number for "dirty air" breakdown is 10^3 kW/cm^2. The breakdown limit defines a minimum d_w for a particular power level. Breakdown limitations reveal that a practical engine would be meters in diameters whereas a laboratory device would be centimeter size.

d. Absorption Chamber

The absorption chamber is between the rocket nozzle and the aerodynamic window. Figure 57 gives the area ratio $A_3/A_6 = A_2/A_6$ as a function of the window Mach number M_2 and δ. Two other inputs needed to generate this figure are the absorption chamber initial Mach number, taken as $M_4 = 1/10$, and the ratio of stagnation temperatures before and after absorption, i.e., T_{05}/T_{04}. Note how insensitive this ratio A_3/A_6 is to M_2 and γ. A value of between 2/10 and 6/10 is reasonable.

The region between station 3, the subsonic flow downstream of normal shock, and station 4, the preabsorption $M_4 = 1/10$ flow, is a subsonic diffuser with a slight inclination ($\approx 6^o$) to avoid flow separation and the concomittant losses. The subsonic diffuser separates the two constant area sections: supersonic diffuser section and the absorption section. The addition of heat in a constant area duct neglecting friction (Rayleigh line) leads to the determination of the ratio A_5/A_6 as shown in Figure 58. Note the slow variation with γ for the various levels of T_{05}/T_{04}. Furthermore, the area ratio between the absorption chamber and the nozzle throat is < 3 for all values of $T_{05}/T_{04} > 4$.
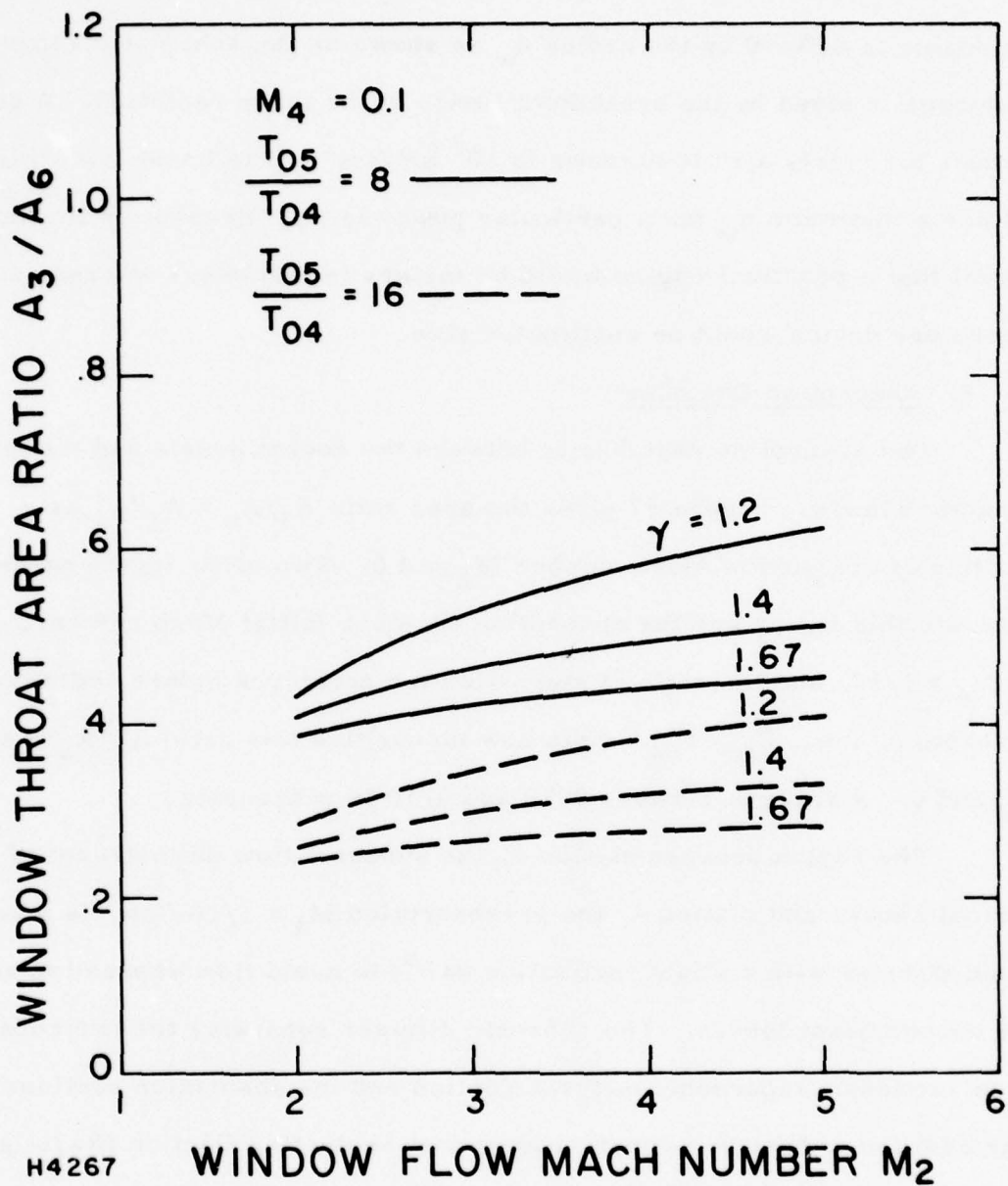
Figure 57   Subsonic Diffuser Dimensions

70
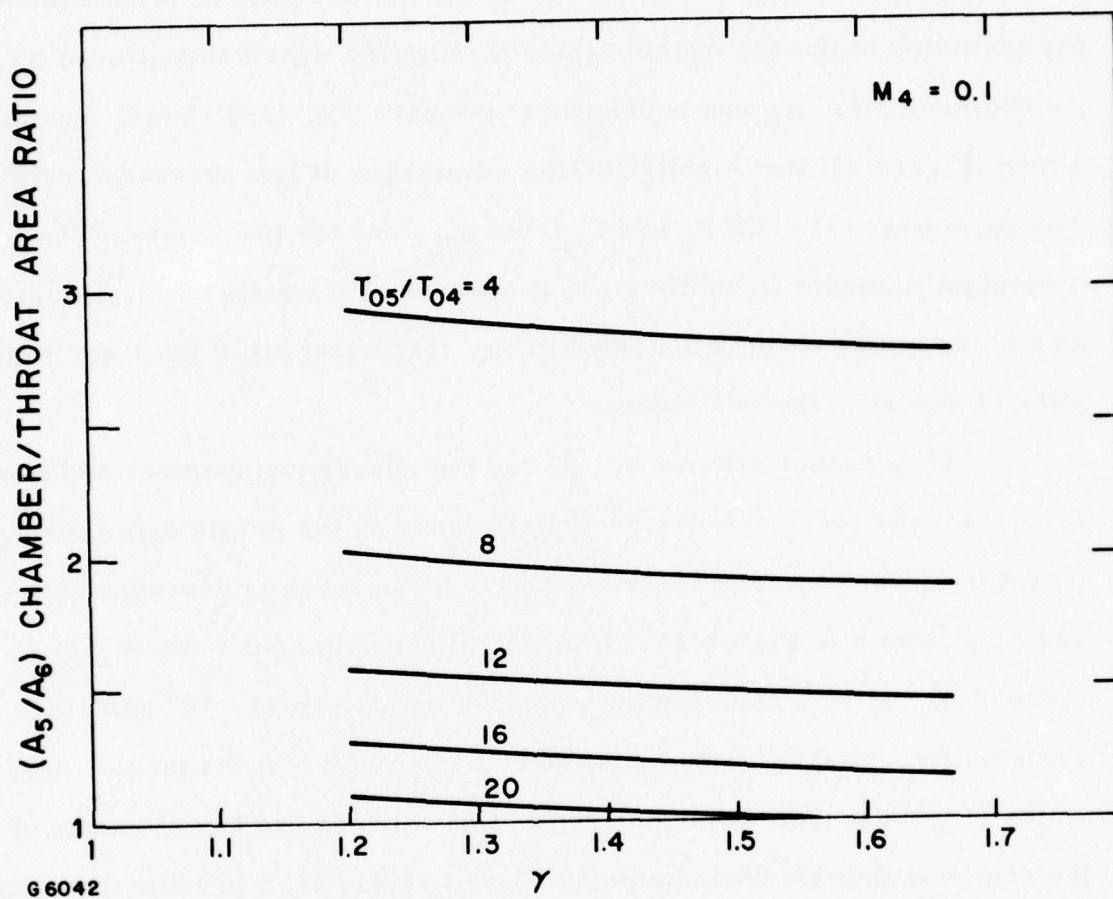
Figure 58   Absorption Chamber Dimensions

G 6042

71

e. Expansion Nozzle

It is evident from Figures 57 and 58 that the nozzle throat scales the geometry of the absorption region through the nozzle throat area A_6. An expression for A_6 was developed previously (Eq. (359)) which developed a map (Figure 51) that highlighted the advantages of low pressure operation. The parameters that fix A_6 are I_{sp}, IP, p_{05}, and the propellant. The propellant influence is subtle since it appears in the ratio of specific heats as well as in our assumption (used in Eq. (362)) that all of the laser radiation is absorbed in the medium.

The pressure difference between the absorption chamber and nozzle exit plane will accelerate the propellant gases as the nozzle exit area A_7 is increased from A_6. The variation over a large range of pressure ratios and γ are shown in Figure 38. A practical range of area ratio A_7/A_6 is between 10 and 10^3; this implies pressure ratios between 10^2 and 10^6. Furthermore, a significant variation of A_7/A_6 with γ at the largest area ratios is to be noted. A further connection between two key elements of the engine is provided by combining Figure 56 and 58 to provide the ratio of throat areas A_1/A_6. This ratio is given in Figure 59. It varies significantly with γ and M_2.

f. Scaling Maps

The considerations of the preceding section indicate that the specification of a "general engine concept" would necessitate the construction of a multidimensional map. In order to reduce the number of variables, three interesting cases are chosen. These cases are defined in Table 5. Some remarks relating to the choice of various parameters are now given. The three cases are distinguished primarily by the selection of γ; based upon

72
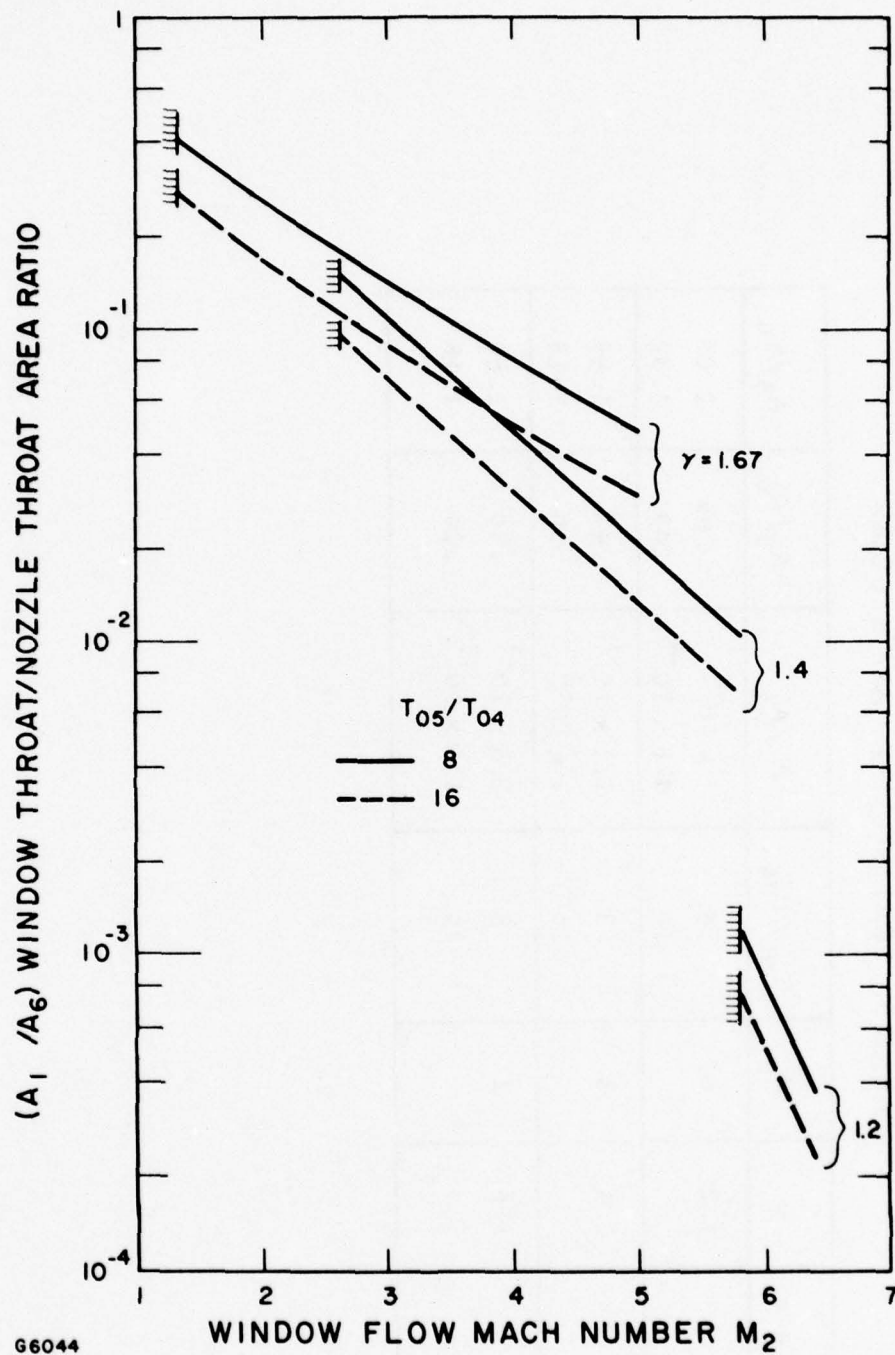
Figure 59   Window Throat/Nozzle Throat Area Ratio

73

TABLE 5. SCALING MAP CASE STUDIES

Case	γ	M_2	T_{05}/T_{04}	A_1/A_6	A_3/A_6	A_5/A_6
1	1.2	6	8 16	7×10^{-4} 4.5×10^{-4}	.65 .43	2.05 1.32
2	1.4	3	8 16	1.1×10^{-1} 7×10^{-2}	.47 .30	1.95 1.25
3	1.67	2	8 16	2.5×10^{-1} 1.6×10^{-1}	.39 .24	1.88 1.18

Figure 55 the choice of γ prescribes a minimum M_2. We have selected such an M_2. The stagnation temperature ratio allows for a significant range of temperature; specifically, if preheating is necessary to avoid condensation, T_{05} can reach $10,000^{\circ}$K. The area ratios in Table 5 are then taken from previously developed figures.

All three cases are considered to develop a specific impulse of 1000 sec, but at two different chamber pressures: $p_{05} = 10$ atm and $p_{05} = 1/10$ atm. One map has been drawn for each of the three cases; since there is a relatively small difference between the cases $T_{05}/T_{04} = 8$ and 16, we display only the $T_{05}/T_{04} = 8$ case. The 10 atm situation is described: the 1/10 atm on the maps are simply shifted to the right by two orders of magnitude. The scaling maps are given in Figures 60, 61 and 62. Case 1 ($\gamma = 1.20$) is interesting from the standpoint that the window throat area A_1 is rather small compared to the other dimensions. Case 2 ($\gamma = 1.40$) brings the dimensions closer together. Finally, Case 3 ($\gamma = 1.67$) indicates that all the dimensions in the rocket are less than order of magnitude apart.

We also show the minimum window area $A_2 \equiv \pi d_w^2$ which results from the use of 10^6 W/cm^2 as the breakdown limit.

75
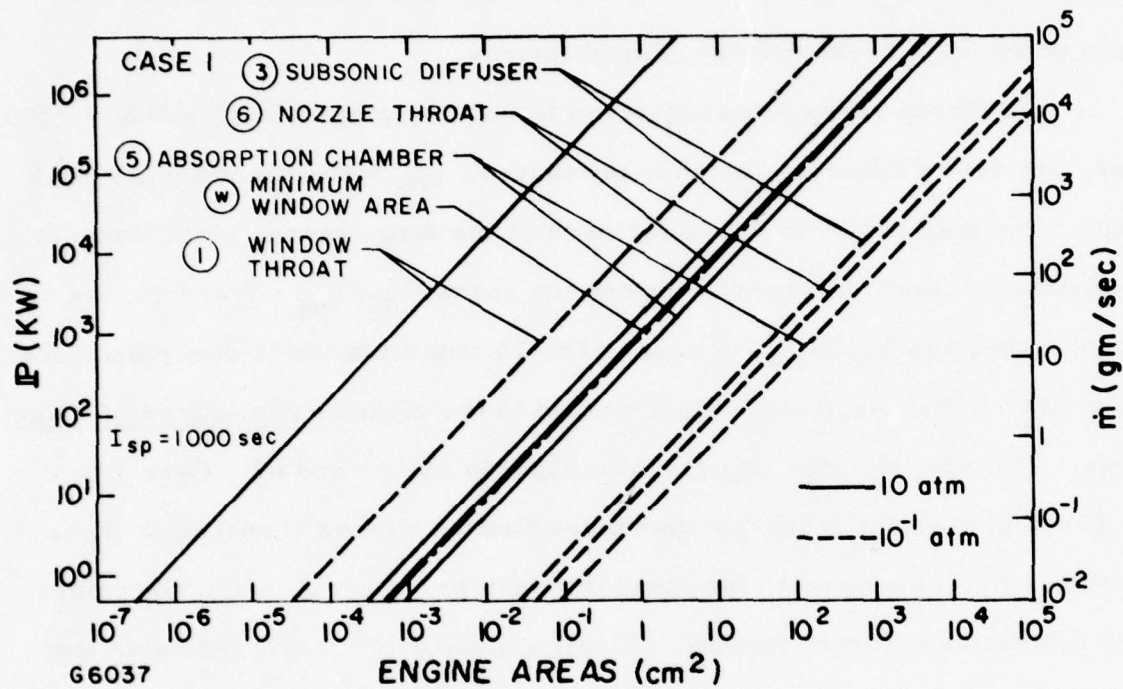
Figure 60   Two-Port Scaling Map (Case 1)
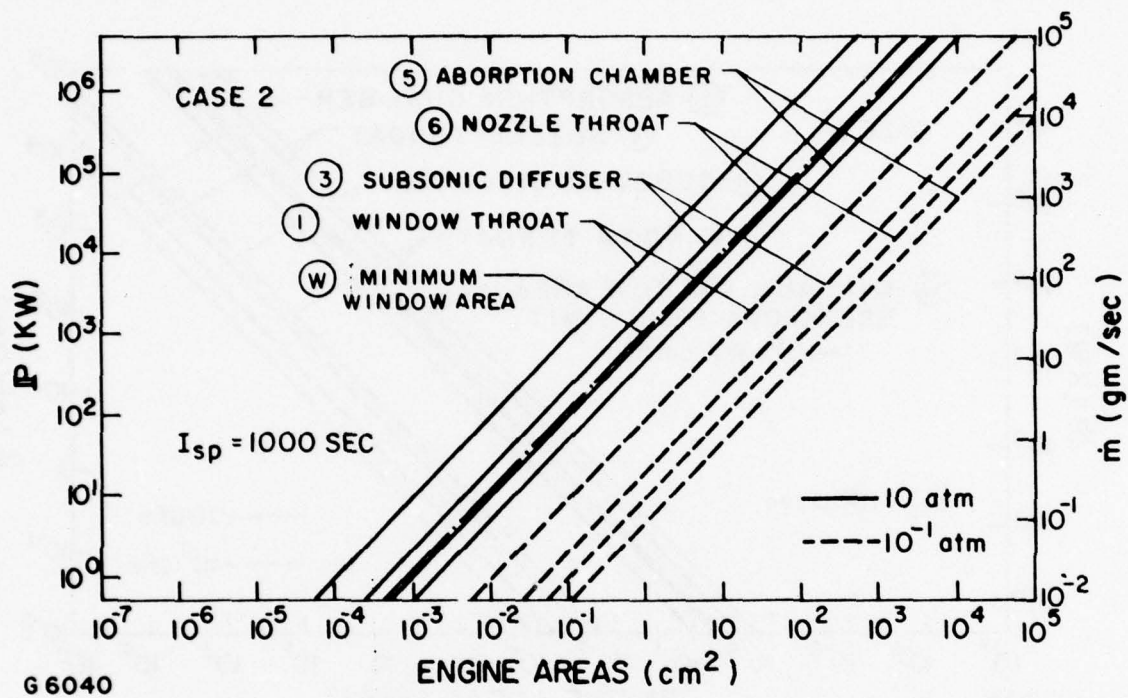
Figure 61   Two-Port Scaling Map (Case 2)

77
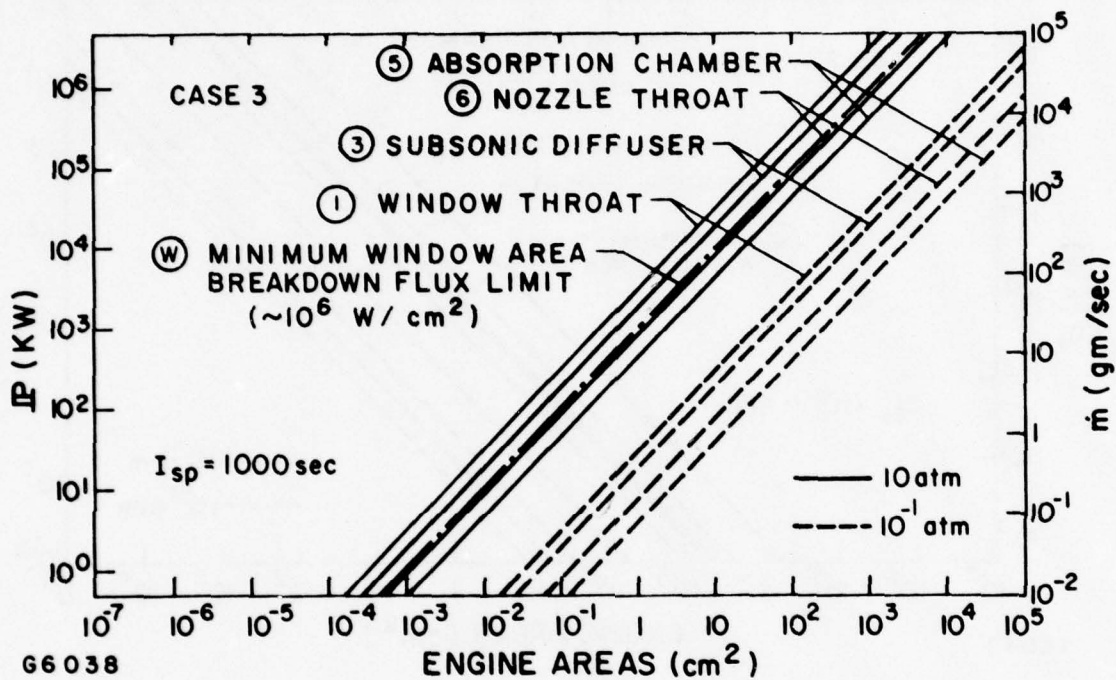
Figure 62   Two-Port Scaling Map (Case 3)

78

5. EXPERIMENTS FOR CW LASER PROPULSION

In order to propel a vehicle efficiently utilizing laser radiation the absorption mechanism must be understood. This section defines a number of experiments that could potentially aid in establishing the practicality of CW laser propulsion.

Absorption phenomena (I) are most fundamental. There are physical properties of gases that must be known - to as yet an unspecified tolerance - in order to design a two-port engine. It is obvious as observed in Section V.3 that the theoretical modeling of the absorption region depends strongly upon the absorption coefficient behavior. Whether the absorption zone is one diameter in width or a hundred meters in width is an important concern. The important differences between molecular and Inverse Bremsstrahlung are also very important to chamber design. And in view of the fact that a_ν can have a behavior that differs in character for an individual propellant as well as for a propellant with a modifying seedant, experimental measurements of the absorption coefficient are much needed. (The following section describes Type I experiments.)

Absorption gas dynamics (II) involves Type I absorption phenomena in a flowing environment. The key question from a practical point of view is can one control the laser-supported waves; a secondary question relates to the behavior of laser-supported waves as one modifies the absorption phenomenon through the "null" between molecular absorption and absorption by Inverse Bremsstrahlung.

The two-port propulsion system (III) involves Type I and Type II phenomenon in addition to the aerodynamic window flow region and the

79

nozzle expansion flow that are respectively fore and aft of the absorption chamber. An experiment of Type III involves most of the elements of a real rocket system and is therefore the most complex type of experiment. The selection of a Type III experiment obviously depends upon the information of Type I and Type II measurements.

A number of Type I absorption experiments are described in the next section. This discussion is followed by the description of a high-pressure burner experiment that consists of perturbing and modifying an H_2O flame produced by the stochiometric mixing of gaseous H_2 with gaseous O_2. This is essentially a Type II experiment with Type I and Type III cases also possible; the limitation of the burner experiment is the restriction to H_2O or seeded H_2O as the propellant. The last section outlines what is primarily a Type III experiment: low-pressure two-port simulation.

a. Absorption Measurements

The design of the cw laser propulsion engine depends critically upon the absorptive characteristics of candidate propellants. In this section we describe shock-tube experiments that can be utilized to make absorption measurements. For this experiment one is singularly interested in laser beam transmission through the propellant medium which will typically be at high temperature and high pressure. The shock tube is ideally suited for the investigation because (1) the thermodynamic conditions (T, p) can be controlled and (2) wide range of propellants (fuel and seed) can be examined. Some initial assessments have been made of utilizing shock tube to measure the absorption characteristics of H_2O (and seeded H_2O).

The shock tube configuration limits the temperature range of H_2O to approximately $3500^{\circ}K$ in the pressure range of 2 - 10 atm. This

80

operating range is shown on Figure 63 where the curves at 3, 5, and 8 torr correspond to the initial pressure of H_2O at $298^{\circ}K$. Specific calculations for the 3 torr case are shown on Table 6.

The proposed shock tube configuration and diagnostics are shown on Figure 64. Typical shock tube conditions of $330^{\circ}K$, 4 atm H_2O can be obtained with a 30 atm H_2 driver pressure and saturated water vapor ($-5^{\circ}C$) providing a driven H_2O pressure of 3 torr. Higher temperature and pressures can be achieved using an inert gas filler, e.g., Argon.

The diagnostics for the experiment are shown on Figure 64. A Schlieren setup would be utilized to examine the boundary layer and observe the position of the shock wave. The boundary layer characteristics of interest are the thickness and the thermal characteristics. The primary diagnostics would be $10.6 \mu m$ transmission measurements employing a CO_2 laser. The windows would be made of ZnSe (Irtran 4). Temperature probes along the tube and at the end of the tube would be employed to determine the shock velocity. Both pure H_2O and seeded H_2O would be examined. The physical shock tube would be approximately 8 feet long and 1 1/2 in. in diameter. The windows would be one centimeter from the end wall.

Note that the possibility of absorption of the laser radiation in the shock tube boundary layer was investigated and found to be insignificant.

b. High-Pressure Burner Experiment

A potentially attractive means of laser propulsion is by means of a two-port rocket configuration utilizing a CW laser. However, scaling studies have shown that an experimental two-port system would be extremely small unless very high power lasers were used. In order to avoid the problems associated with such small systems, a CW simulation experiment was
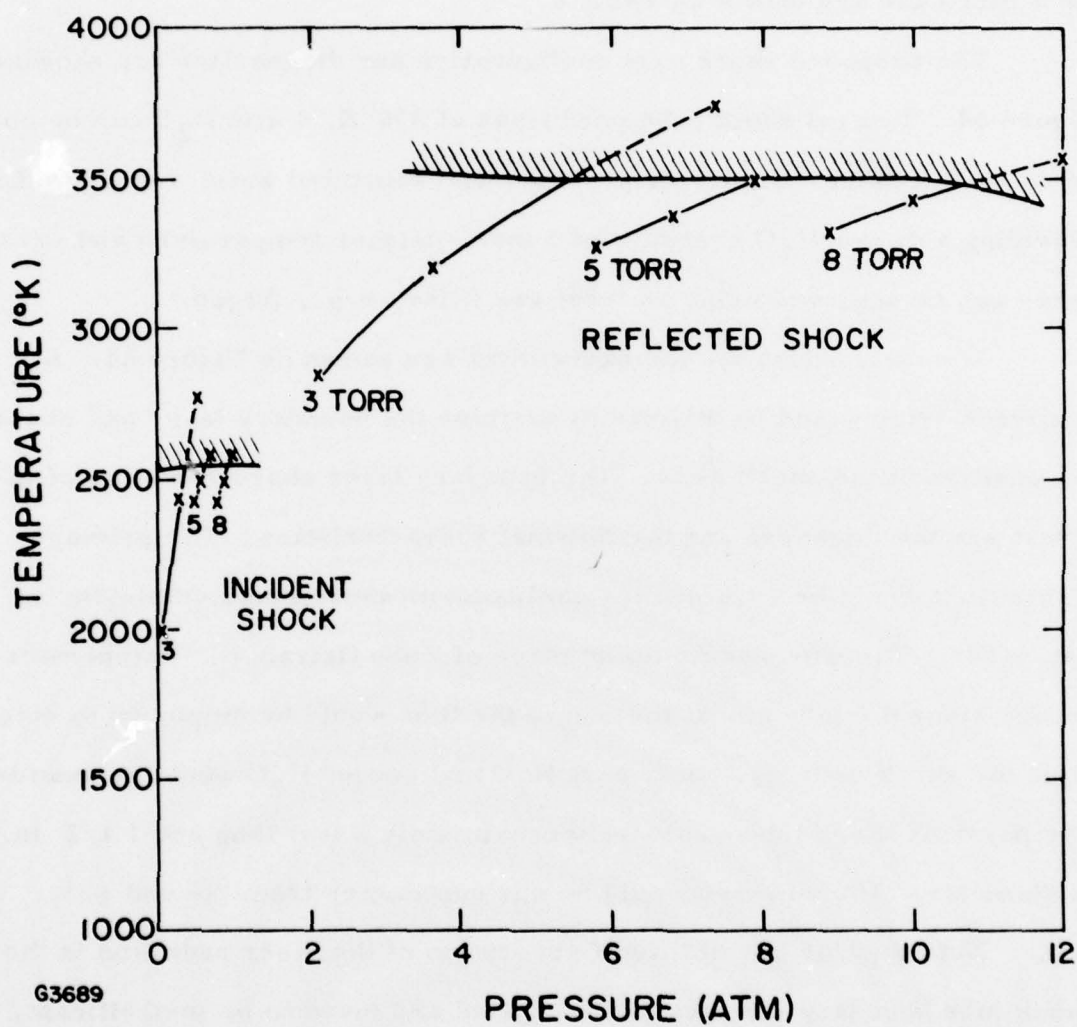
Figure 63 H_2O Absorption Measurements Regime in Shock Tube

TABLE 6. H_2O SHOCK TUBE CALCULATIONS

Initial Conditions
(pure H_2O)

$T_1 = 298°K$
$P_1 = 3$ torr
$C_1 = 427$ m/sec

SHOCK VELOCITY km/sec	M_1	INCIDENT SHOCK P_2(atm)	$T_2(°K)$	REFLECTED SHOCK P_5(atm)	$T_5(°K)$	DRIVER PRESSURE P_{H_2} (atm)	P_5/P_1 ρ_5/ρ_1
2.923	6.85	0.219	2000	2.07	2830	6.8	50
3.534	8.28	0.326	2400	3.66	3217	31.6	73
4.46	10.44	0.53	2800	7.53	3724	468	120

*Subscripts refer to typical shock tube configuration
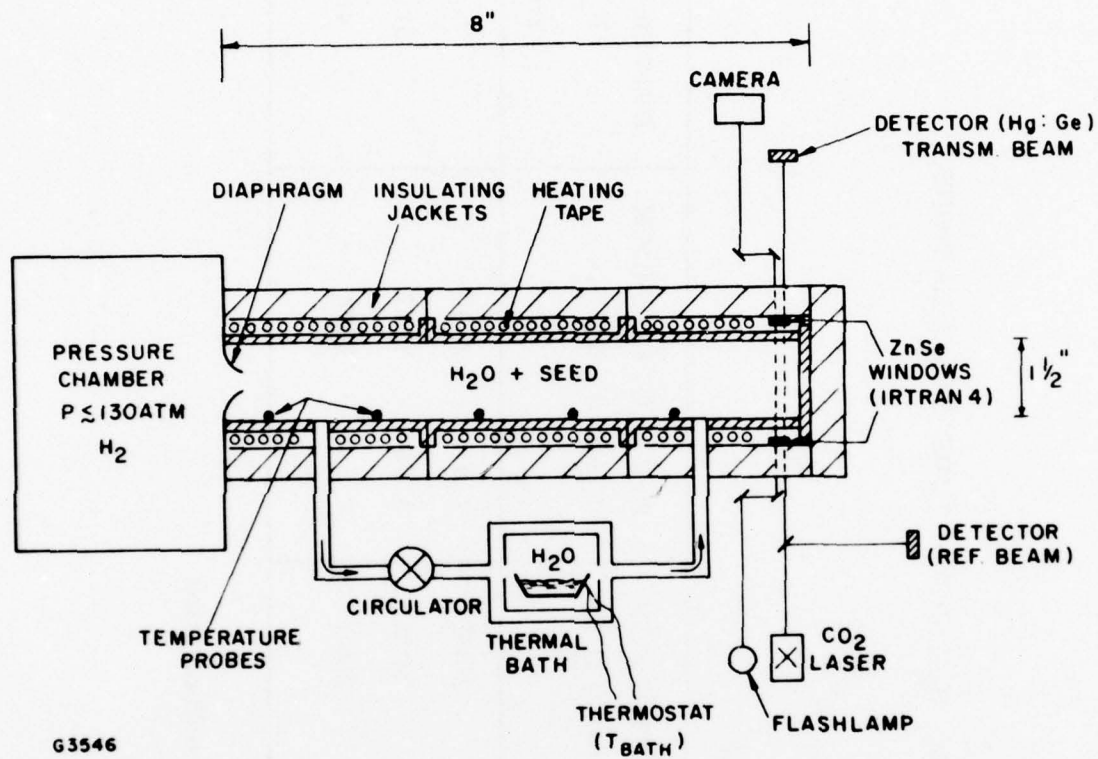
Figure 64   Shock Tube Configuration and Diagnostics (Illustrated for H_2O)

conceived. In principle this system uses the combustion energy of H_2 and O_2 to heat the resultant H_2O to temperatures high enough to be close to the laser-heated rocket range. Consequently the optical properties of the heated gas can be investigated without using a very hig power laser. We are primarily interested in determining the absorption characteristics at high temperatures, the interaction between laser-absorption waves and the flow field, the operation of an aerodynamic window for the laser absorption-flow problem; and the coupled radiation-gas dynamics phenomenon in two-port rockets.

In order to obtain enthalpies representative of laser propulsion applications, we will use the High Enthalpy Absorption Test - Cell [HEAT-Cell] which is an experiment that utilizes the laser to perturb an existing high temperature environment to a larger enthalpy environment. Since one of our candidate propellants is H_2O, it is appropriate to use a gH_2/gO_2 motor since the combustion products are predominantly H_2O, [6] see Figure 65. The mixture of gaseous H_2 and gaseous O_2 at super atmospheric pressures provides combustion at high chamber temperatures. The adiabatic flame (chamber) temperature for a pressure of 34.01 atm is shown in Figure 66 vs the O_2/H_2 mixture ratio (by weight). [9] The stochiometric mixture ratio of 8 gives the highest temperature of approximately $3500^{\circ}K$. In this preliminary analysis we will consider the burner flame to be a homogeneous one from the temperature point of view. The actual structure of the flame fronts will be studied subsequently. We will consider this state to

(9) Wilkins, R.L., "Theoretical Evaluation of Chemical Propellants," Prentice-Hall, Inc., Englewood Cliffs, N.J. (1963) p. 181.
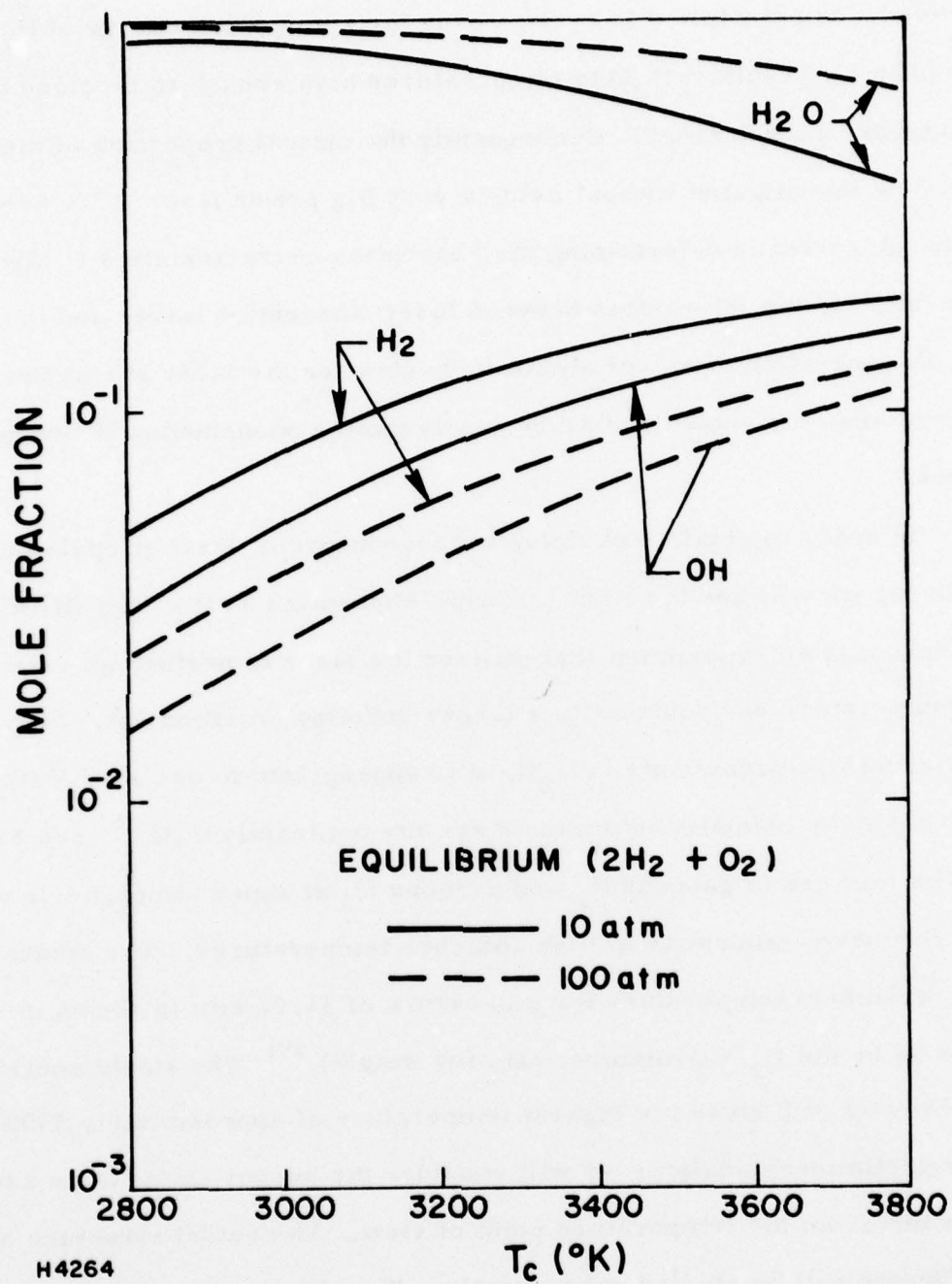
Figure 65   Mole Fraction of Primary Constituents in High
Temperature Water
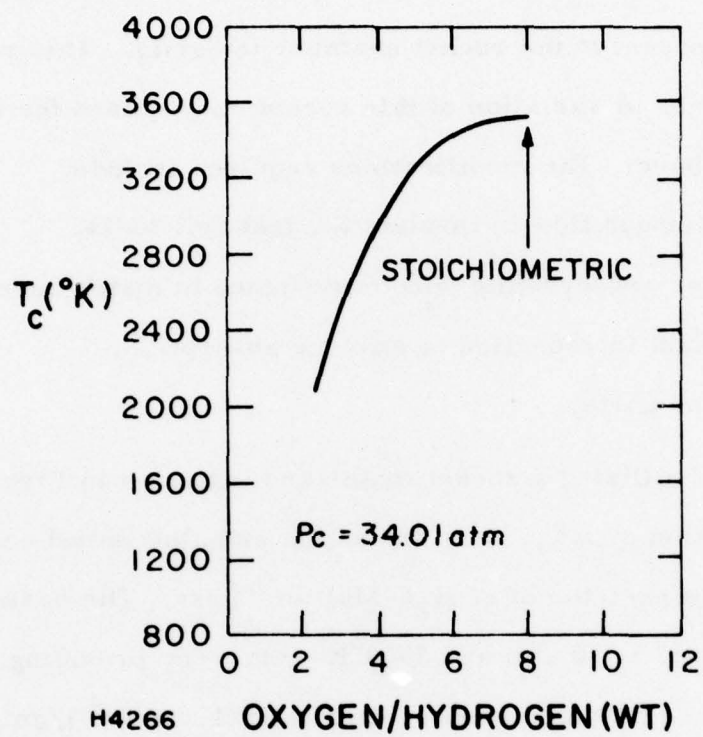
Figure 66   Chamber Temperature vs O_2/H_2 Mixture Ratio

be the initial condition in our test cell. This high temperature - high pressure environment is a severe one from the materials point of view. A small 160 lb thrust H_2/O_2 rocket described by Ferriso[10] et al., utilizes water cooling to preserve the rocket chamber integrity. This rocket is shown in Figure 67. A variation of this rocket can be used for the investigations discussed above. The modifications required include:

    (i)   Buffer gas flow to insulate the test cell walls.

    (ii)   Laser aerodynamic window designed to match burner flow.

    (iii)   Seedant introduction to enhance absorption.

    (iv)   Probe ports.

The advantages of utilizing a rocket motor are indicated in Figure 68. First the combustion process provides a high enthalpy initial condition. We can see this on the skeleton of an H_2O Mollier Chart. The basic combustion state is isolated at 10 atm and $3500°K$ — thereby providing an increase in enthalpy over room temperature H_2O of about 1.6×10^4 j/gm. Absorption characteristics of steam at these temperatures are of interest by themselves. However, we would like to obtain higher temperatures to simulate realistic laser propulsion missions. Hence, to obtain an interesting temperature of $4500°K$, the laser absorption of only 2.7×10^4 j/gm would be needed as shown on Figure 68. The Ferriso rocket mass flow of 0.2 kg/sec implies the use of a 5.4 MW laser power source to achieve the indicated Δh. This total Δh change from room temperature conditions would yield a total $\Delta h \sim 4.3 \times 10^4$ j/gm. It corresponds to an ideal specific

(10) Ferriso, C., et al., "High Temperature Infrared Emission and Absorption Studies," General Dynamics/Astronautics. Scientific Report AE61-0910, (1961).

WATER OUT

WATER IN

O₂

H₂O

O₂ H₂

H₂O

O₂

PROPELLANT INJECTOR

CHAMBER-NOZZLE ASSEMBLY

COOLING JACKET

NOZZLE BLOCK

STATIC PRESSURE TAP

H4265
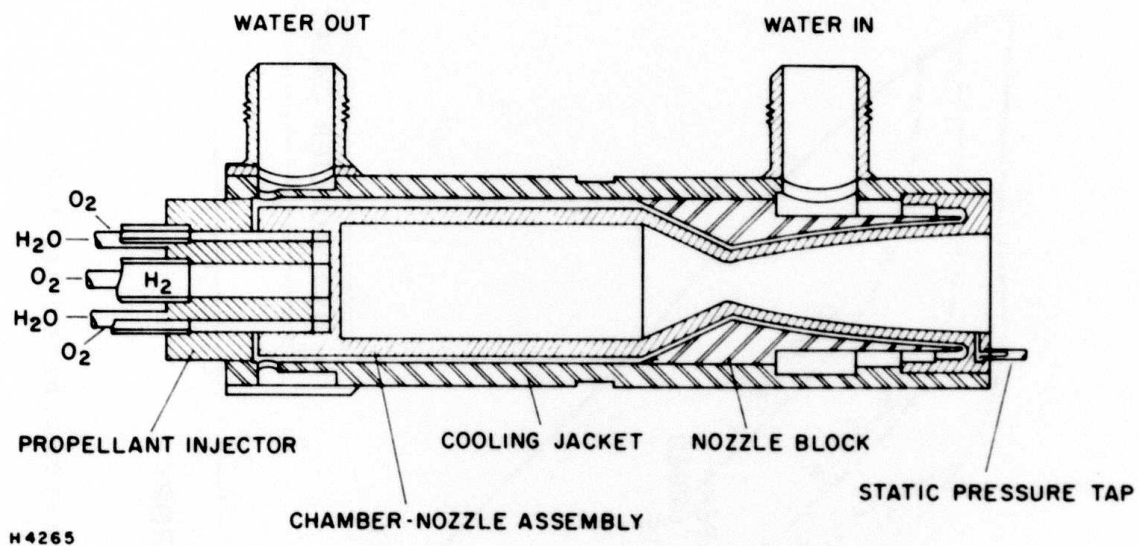
Figure 67   160# Thrust Rocket Burner
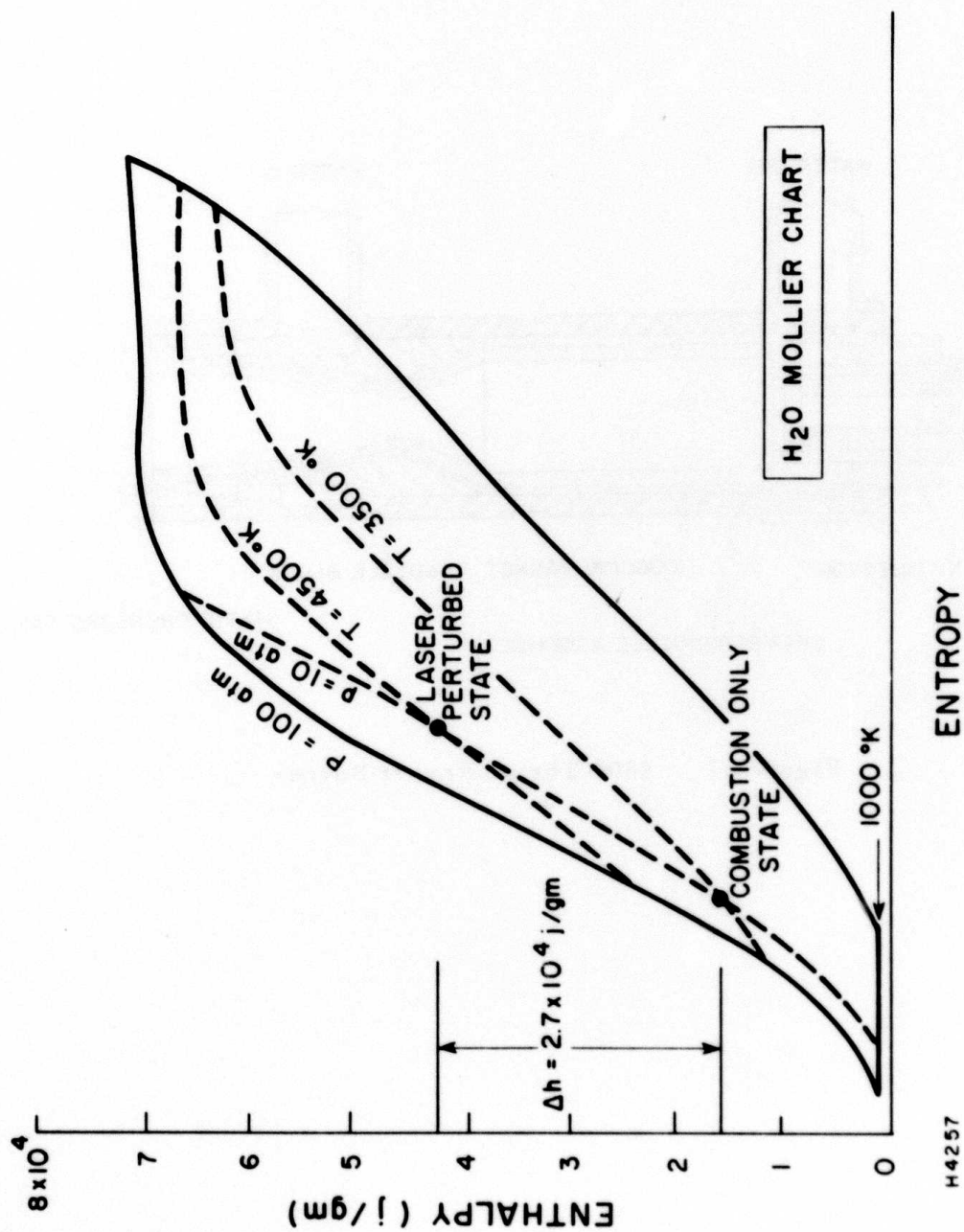
Figure 68   Laser Perturbed State on H_2O Mollier Chart

H4257

90

impulse of about 920 seconds, (see Figure 41) and if realistic nozzle expansion pressure ratios (10^2) are considered one would still obtain a useful I_{sp} of something like 550 seconds. The <u>perturbation</u> to 4500°K at constant pressure is an interesting one, but it requires a high power laser to achieve the high temperature state. The skeletal Mollier chart (Figure 68) leads one to conclude that high pressure operation is favorable for laser propulsion applications because the enthalpy change Δh required to increase the chamber temperature from 3500°K to 4500°K decreases as the pressure increases.

The various HEAT-Cell simulation possibilities are outlined in Table 7. These possible experiments are illustrated in Figure 69.

Experiment 1 is a combustion only experiment. The main purpose of this experimental configuration is to measure the absorption properties of water at high temperatures and pressures. Pressure levels up to 50 atm would be investigated and peak temperatures around 3500°K would be achieved. A low power (10 W) probe laser transverse to the burner flame would be utilized to measure the absorptance of the medium. The combustion only experiment would thus provide $a_\nu = a_\nu(p, T)$ for H_2O. In addition to H_2O, one could study the properties of seeded H_2O by introducing a separate inlet port or by adding the seedant to one of the burner propellants. Water cooling was quite satisfactory for the General Dynamics rocket motor discussed above. Water cooling could be used and the increase in temperature of the water could be measured to gain some understanding of wall heat transfer.

Experiment 2 would add CW laser radiation to the "combustion-generated inferno" at a relatively low power level (e.g., 10 KW from the

91

TABLE 7. HEAT-CELL EXPERIMENTS FOR H_2O

INVESTIGATION \ EXPERIMENT	ABSORPTION	ENGINE CONFIGURATION	HEAT TRANSFER	PROPULSION PARAMETERS
COMBUSTION ONLY	MODE TRANSITION SEEDANT CHAMBER PLUME			
COMBUSTION AND 10 kW LASER	TRANSVERSE PROBE BEAM PARALLEL ANTI-PARALLEL		WATER COOLING	
COMBUSTION AND 100 kW LASER	PARALLEL ANTI-PARALLEL	SINGLE-PORT TWO-PORT AEROWINDOW	WATER COOLING HIGH ENTHALPY INSULATION	
HIGH POWER LASER ONLY	PARALLEL ANTI-PARALLEL	SINGLE-PORT TWO-PORT AEROWINDOW	HIGH ENTHALPY INSULATION	SPECIFIC IMPULSE EFFICIENCY

EXPERIMENT 1
COMBUSTION ONLY
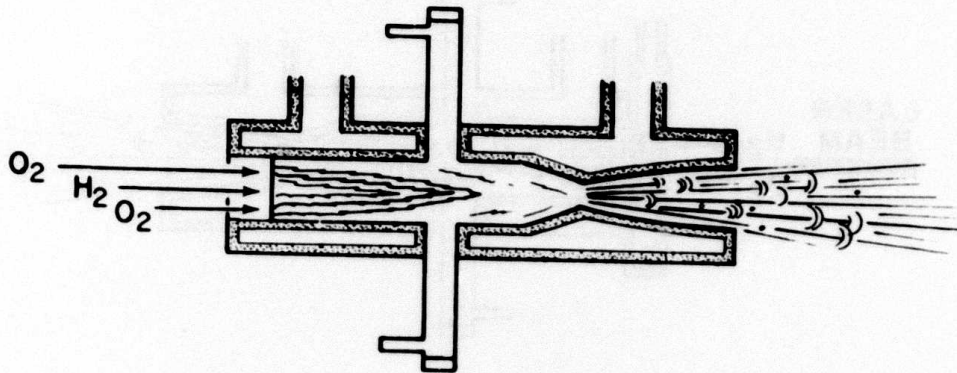
EXPERIMENT 2
COMBUSTION AND LASER

H4260
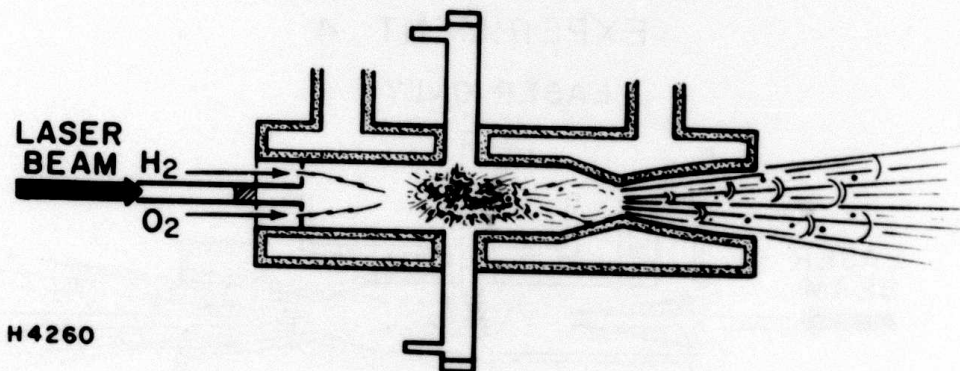
Figure 69   Heat-Cell Experimental Options

93

EXPERIMENT 3
COMBUSTION AND LASER
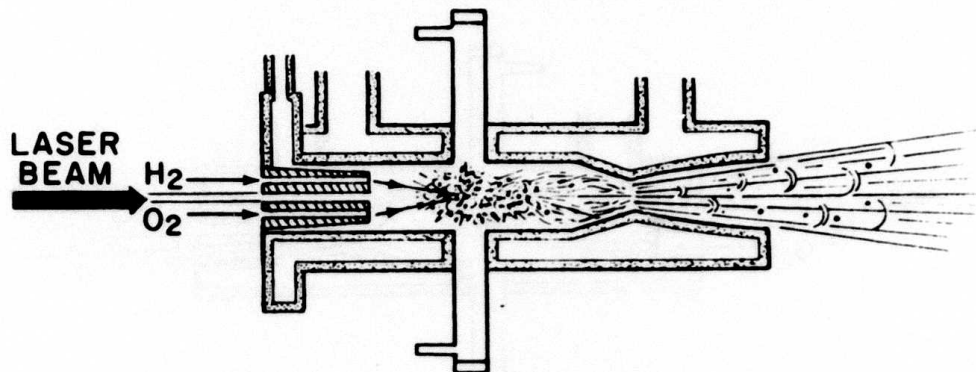
EXPERIMENT 4
LASER ONLY
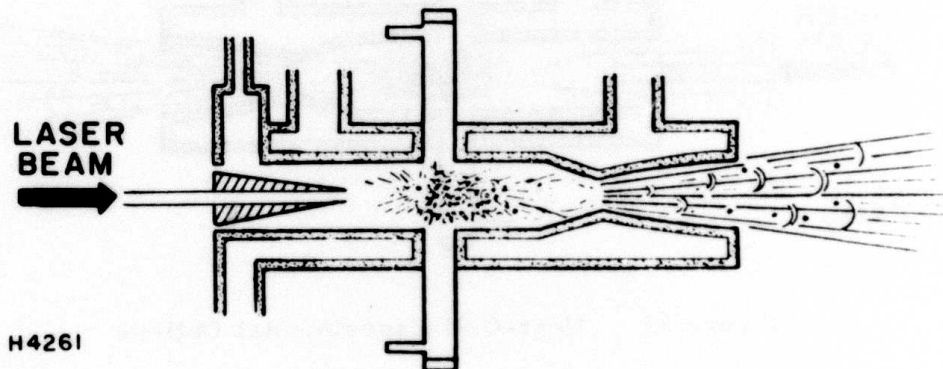
H4261

Figure 69   Continued

94

AERL, Inc. HPL). This perturbation of the rocket scheme would provide

valuable information beyond that gained in Experiment 1. First, the absorp-

tion of laser radiation increases the chamber temperature level so the probe

laser could extend the range of absorption coefficient information. Second,

the perturbing beam could be sent in parallel to the burner flow as shown

in Figure 69 or it could be sent in through the plume (anti-parallel). Axial

absorption would be monitored. The transition from molecular to inverse

Bremsstrahlung absorption would be investigated. The stability of laser

heating problem would also be assessed. The heat transfer problem would

be more acute here; however, water cooling would still maintain the integrity

of the rocket motor.

Experiment 3 differs from Experiment 2 in that the increase in per-

turbing laser power necessitates the use of an aerodynamic window to get

the beam into the chamber. Employing a laser and an aerodynamic window

in concert with a rocket motor situation requires a clever design for the in-

let region. The solution of this problem then provides a more interesting

experiment than that of Experiment 2. The absorption coefficient can be

mapped out further and the mating of the aerowindow with "absorption"

chamber would be tested. The increase in laser power would further in-

crease the heat transfer to the rocket chamber walls. The window flow of

hot steam as well as the rocket flame would to some extent protect the walls

from the laser-absorbed enthalpies.

Experiment 4 begins to resemble the prototype. The rocket motor

aspect of the HEAT-Cell is now completely eliminated. All the enthalpy

needed to raise the high pressure water to $4500^{\circ}K$ now comes from the laser

(which is not a perturbing laser). Further absorption coefficient measurements can thus be made, and transition from molecular to Inverse Bremsstrahlung can be studied. Propulsive thrust and efficiency can be measured and the viability of two-port laser propulsion can be assessed.

Note that the single port concept can be investigated in Experiment 3 and Experiment 4 by turning the aerodynamic window flow off and only flowing propellant into the rocket chamber. It is rather obvious that the series of experiments described are very flexible; additional experiments could be mated to the HEAT-Cell.

c. Low-Pressure Two-Port Simulation

The advantages of operating a CW engine at low (absorption chamber) pressures have been mentioned previously. In Figure 70 we illustrate a scaled drawing of a CW engine operating at 10^{-1} atm pressure. The characteristics of the engine were determined from the scaling maps of Section V.4. One of our purposes in designing the engine was to make it as large as possible in all its elements. For a specific impulse of 1000 sec, Figure 51 provides the throat area A_6 when a laser power level is chosen. If we select 10 KW as the laser power, then A_6 varies between 8.3 and 14.9 cm^2 for γ between $\gamma = 1.1$ and 1.67 respectively. Aerodynamic window calculations (in particular Figure 59) indicate that one obtains the largest sizes at low M_2 and $\gamma = 1.67$. The choice of $M_2 = 2$ selects case 3 (Table 5) which is illustrated in Figure 62. The length (14.6 cm) of the subsonic diffuser is obtained by making the diffuser diverge at 7°.

The length of the absorption chamber has somewhat arbitrarily been selected to be equal to its diameter. Rockets motors typically have square
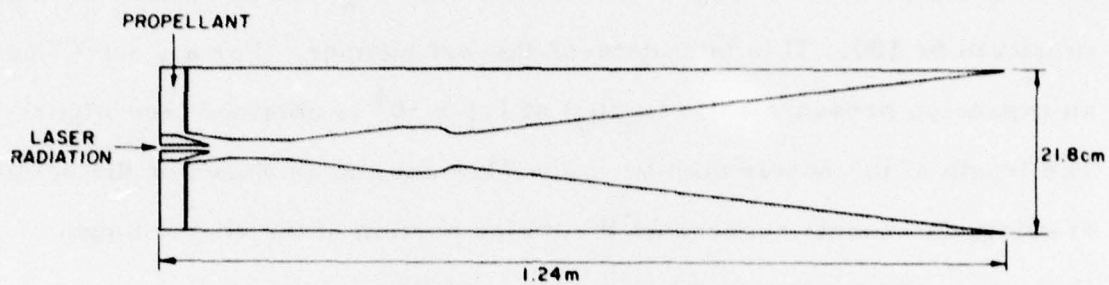
96

PROPELLANT

LASER
RADIATION

21.8cm

1.24m

I_{sp} = 1000 sec A_m > 10^{-2} cm^2

P = 10 KW To_5 / To_4 = 8

Po_5 = 10^{-1} atm A_7/A_6 = 100

γ = 1.67 p_5/p_7 = 1.5 x 10^4

G6049

M_2 = 2

Figure 70   Scaled Low-Pressure Two-Port Engine

dimensions. The length of this chamber is the weakest part of the design; more specifically, since absorption at low pressures may require large absorption lengths, the absorption chamber may have to be "stretched" out. The use of a short-absorption-length seedant would keep the chamber geometry square. An area ratio between the throat (A_6) and the nozzle exit was chosen to be 100. This is a state-of-the-art number. For a $\gamma = 1.67$ gas, an expansion pressure ratio (p_5/p_7) of 1.5×10^4 is obtained (see Figure 38). The length of the nozzle then becomes 73.2 cm and as shown on the scaled drawing, the nozzle represents the major portion of the engine length (1.24 m). The system mass flow is 0.2 gm/sec.

It now becomes evident that the low-pressure engine is well suited to laboratory experiments. Most significantly, at low pressures available high-power lasers, e.g., AERL, Inc's HPL would provide the requisite laser radiation. The mass flows are not excessive and the heat transfer rates will be significantly reduced from the high-pressure simulation. The experimentation would focus upon the use of a seeded-monatomic-like gas $(\gamma = 1.67)$. Since the operation is at sub-atmospheric pressure levels, the experiment would be performed in an evacuated environment. The ambient pressure level would have to be less than 6×10^{-6} atm $(5.1 \times 10^{-3}$ torr). The primary diagnostic for the experiment would be the measurement of thrust — and hence specific impulse.

The goal of the experiment would be "proof of principle". Scaling to high chamber pressures might, however, be difficult due to different absorption behavior even if the low-pressure simulation were successful. We would then view the low-pressure engine as useful for exoatmospheric applications.

98

VI. BEAM TRANSMISSION

1. INTRODUCTION

We wish to find the conditions under which a beam of power in the order of 10^9 W can be transmitted through the atmosphere. We will confine the discussion to a CO_2 laser beam at 10.6 μm, making an angle with the vertical of 60° or less.

The only significant absorbers present in the atmosphere are CO_2 and H_2O. The first of these absorbs by the inverse of the CO_2 laser transition, CO_2 (100) + hν → CO_2 (001). This transition is capable of being saturated or bleached, and when the molecule is bleached absorption becomes effectively negligible. The potential for bleaching out the CO_2 absorption component[11,12] is extremely important for propagation of pulsed CO_2 laser beams, especially those directed near to the vertical, as in the case of laser propulsion applications. We will derive the conditions under which this effect is significant below. We note that CO_2 is present in the atmosphere at a molar concentration of 330×10^{-6}. The second absorber is H_2O; there is some indication that absorption takes place in the continuum of a weakly bound H_2O dimer.[13] The extremely rapid vibrational

(11) Wood, A.D., Camac, M., and Gerry, A.E., Appl. Optics <u>10</u>, 1877 (1971).

(12) Avizonis, P.V., Butts, R., and Hegge, B., Appl. Optics <u>14</u>, 1911 (1975).

(13) Adiks, T., Arefyev, V., and Dianovklokov, V., Sov. JQE 5, 481 (1975).

99

readjustments of the H_2O molecule imply that the molecule cannot be bleached, and the absorption it produces must be added to that of the CO_2 molecule. The H_2O content of the atmosphere is extremely variable, and in order to estimate transmission we have adopted the values for the U.S. standard atmosphere given by Valley, [14] which correspond to 1% molar H_2O at sea level.

The absorption coefficients obtained will then be used to calculate the degree of distortion (thermal blooming) produced in the beam; the phase corrections required to reduce this phenomenon and the maximum correction obtainable will then be computed. These two calculations have been performed on the Lincoln Laboratory propagation code, [15] kindly arranged by J. Herrmann. We proceed to a more detailed discussion.

2. CO_2 ABSORPTION BLEACHING

The CO_2 molecule absorbs 10.6 μm radiation on the resonant $(100) \rightarrow (001)$ transition. The molecular vibrational energy level diagram is shown in Figure 71, in which the major energy transfer processes are indicated. The photon absorption transfers the molecule to the (001) state. There are four possible loss modes from this state; transfer to a nitrogen molecule in the reaction

$$CO_2 (001) + N_2 (0) \rightarrow CO_2 (000) + N_2 (1); \tag{366}$$
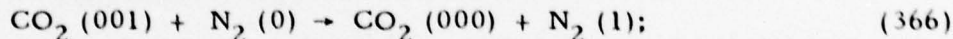
collisional deactivation to the bending mode in the reaction
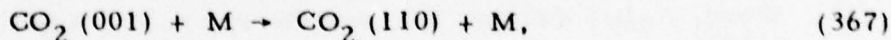
$$CO_2 (001) + M \rightarrow CO_2 (110) + M, \tag{367}$$

(14) Valley, S. L. , Atmospheric Temperature, Density, Pressure and Moisture. Handbook of Geophysics and Space Environments, AFCRL, Office of Aerospace Res. , U.S.A.F. 1965.

(15) Hermann, J. , private communication.

ENERGY LEVEL DIAGRAM
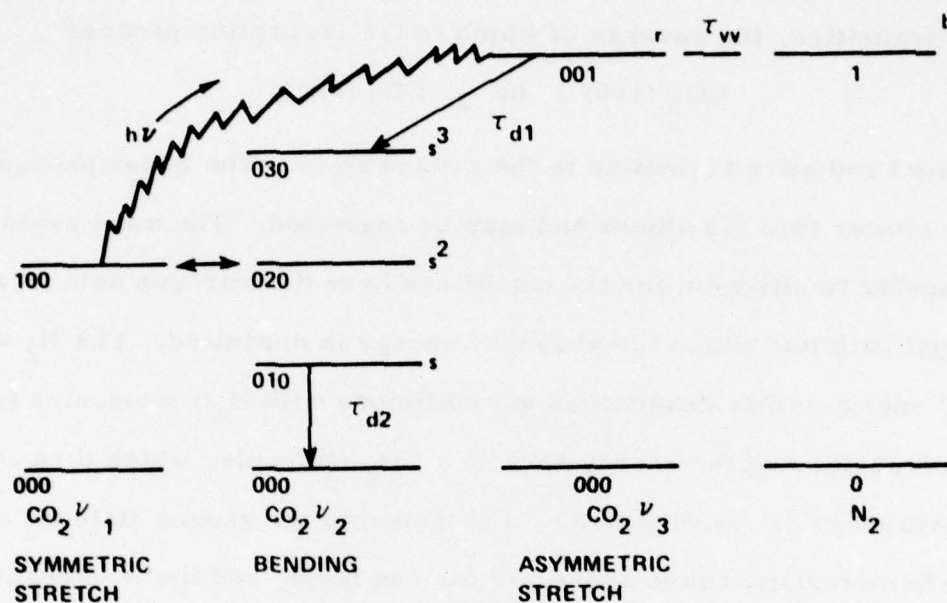
ASSEMPTIONS

1. SYMMETRIC STRETCH & BENDING IN EQUILIBRIUM
2. DURING PULSE r >> b
3. 001 LOSS: VV TRANSFER TO N_2 τ_{vv}
            VV TRANSFER TO 030 τ_{d1}
4. 010 LOSS: VT TRANSFER TO KINETIC τ_{d2}
5. ATMOSPHERIC CO_2 CONTENT: 330 ppm MOLAR
6. ONLY CO_2 ABSORPTION IS CONSIDERED
7. ONLY N_2, O_2 AND H_2O EFFECT ON τ_{d1} AND τ_{d2} CONSIDERED

H 4256

Figure 71 CO_2 - N_2 Kinetic Model

where M is N_2, O_2 or H_2O; stimulated emission by another photon in the laser transition, the reverse of which is the absorption process

$$CO_2 (100) + h\nu \rightleftharpoons CO_2 (001); \tag{368}$$
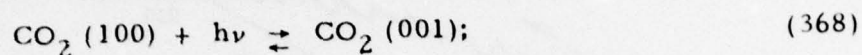
or direct radiative transition to the ground state. The latter process is very much slower than the others and may be neglected. The most rapid process is transfer to nitrogen; for the conditions here the nitrogen acts as a vast thermal bath into which the absorbed energy is deposited. The N_2 vibrational energy either deactivates via collisions with H_2O molecules ($\tau_c \sim 30$ ms) or by transferring the energy back to a CO_2 molecule, which then collisionally deactivates to the bending mode, and thence to the ground state ($\tau_c \sim 16$ ms). The characteristic times above are for sea level, and the H_2O deactivation decreases much more rapidly with height than that due to CO_2 transfer and deactivation; we therefore neglect deactivation of N_2 by H_2O. The characteristic times may be obtained from the rate constants,[16] and we find that process (366) is ~ 100 times faster than process (367), and thus dominates the loss processes from CO_2 (001). The time for process (366) is labelled τ_{VV}, and that for (367) is τ_{d1}; these are shown as functions of altitude in Figure 72.

Simultaneously, depletion of the (100) state by photon absorption results in its repopulation via collisional transfer from the bending mode, which is extremely rapid, and this leads to repopulation of the bending mode from the ground state. This process is strongly catalyzed by H_2O, and the characteristic time for (010) $\rightarrow$ (000) transfer, labelled τ_{d2} in Figure 71 and shown as function of altitude in Figure 72, is dependent on H_2O concentration. Thus the fourth process important for bleaching is:

$$CO_2 (000) + M \rightarrow CO_2 (010) + M. \tag{369}$$

---
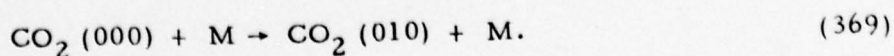
(16) Lewis, P.F. and Trainor, D.W., AERL AMP 422 (Nov. 1974).
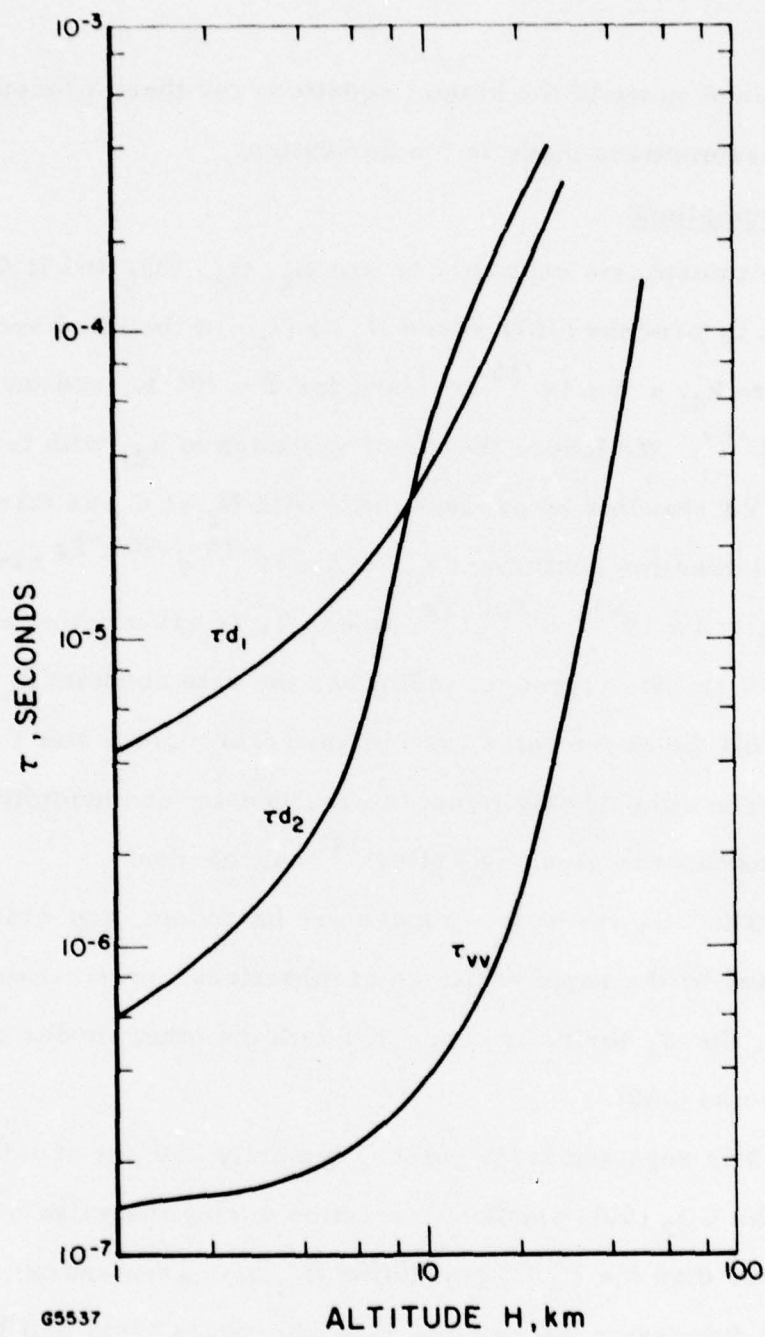
Figure 72 CO_2 Kinetic Times vs Altitude

103

We now proceed to write the kinetic equations for these processes, first listing the assumptions made in the derivation.

a. Assumptions

1. Atmospheric constituents are N_2, O_2, CO_2 and H_2O. Collisional deactivation by process (367) where N_2 or O_2 are the third body have the identical rate $k_{d1} = 3 \times 10^{-15}$ cm^3/sec for $T \sim 300^\circ K$, and for H_2O $k_{d1} = 4 \times 10^{-13}$. We ignore the small variation of k_{d1} with temperature. Collisional VT transfer by process (369) with N_2 or O_2 as third body have the identical reaction coefficient $k_{d2} = 3 \times 10^{-15} e^{-960/Tg}$ cm^3/sec, while for H_2O $k_{d2} = 2 \times 10^{-11} e^{-960/Tg}$, where Tg is gas kinetic temperature. CO_2 - N_2 VV transfer (process (366)) has the rate constant $k_{VV} = 5.8 \times 10^{-13}$ cm^3/sec. All the above rates are obtained from Lewis and Trainor.[16]

2. The atmospheric temperature, density and humidity for the standard U.S. atmosphere given by Valley[14] will be used.

3. The CO_2 vibrational modes are harmonic, and while ν_1 and ν_2 are connected by the rapid exchange of vibrational information between the two modes, the ν_3 series is connected with the other modes only by processes (367) and (368).

4. For repeated laser pulses, typically 250 pps of ~ 10 μs pulse duration, the CO_2 (001) population fraction during the pulse will always be much greater than the N_2 (1) population (N_2 bath assumption), so that for the present discussion the reverse rate of process (366) will be negligibly slow compared to the forward rate.

5. Gas temperature change will affect the molecular kinetics insignificantly, and constant temperature may be assumed during the absorption process.

b. Kinetic Equations

The rate equation for the CO_2 (001) population may be written:

$$\frac{d}{dt} [CO_2\ (001)] = -k_{VV} \{[N_2\ (0)]\ [CO_2\ (001)] - [N_2\ (1)]\ [CO_2\ (000)]\}$$

$$- [CO_2\ (001)]/\tau_{d1} + \frac{\alpha\phi}{h\nu} .$$

where molar concentrations per cubic centimeter are shown in square brackets, ϕ is flux density at 10.6 μm, $h\nu$ is photon energy at 10.6 μm, and α is the absorption coefficient. The above equation may be simplified by defining $r = [CO_2\ (001)]/[CO_2\ (000)]$ and $b = [N_2\ (1)]/[N_2\ (0)]$. Then $r = e^{-3380/T_3}$ where T_3 is the ν_3 vibrational temperature, and $b = e^{-3395/T_N}$, where T_N is N_2 vibrational temperature. Due to the photon pumping $T_3 \gg T_N$, and hence $r \gg b$; we neglect b. Using the definition of τ_{VV} we have

$$\frac{dr}{dt} = -r \left[\frac{1}{\tau_{VV}} + \frac{1}{\tau_{d1}}\right] + \frac{\alpha\phi}{h\nu\ \psi_c\ N_T} \tag{370}$$

where ψ is CO_2 molar fraction and N_T is total gas number density. Ground state depletion may be neglected since $r \ll 1$. At this point we note that α is given by[17]

$$\alpha = F\ (s^2 - r) \tag{371}$$

where

$$F = \sqrt{\frac{M_c}{2\pi k n_o}}\ \frac{\lambda_o^2\ \theta_r}{4\tau_{21}}\ \frac{\psi_c\ N_T\ (2J + 1)\ e^{-J\ (J+1)\ \theta_r/T_g}}{T_g^{3/2}\ \sum N_j\ \sigma_j\ (1 + M_c/M_j)^{1/2}}\ , \tag{372}$$

_____

(17) Douglas-Hamilton, D.H. and Lowder, R.S., AERL CO_2 Laser Kinetics Handbook, 1974.

for small r and s, and the quantities have the following meaning and values for P (20):

M_c	CO_2 mol wt	44
M_N	N_2 mol wt	28
k	Boltzman const.	1.38054×10^{-16}
n_o	Avogadro const.	6.023×10^{-23}
λ_o	Wavelength	$10.59\ \mu m$
J	Upperstate Rotational Quantum Number	19 for P (20)
θ_r	Rotational Spacing	$0.53^{\circ}K$
T_g	Gas temperature	
N_j	Number density of species j $(N_2 + O_2)$	$N_j = \psi_N N_T + \psi_o N_T = N_T$
σ_j	Collisional Cross Section for j $(N_2 + O_2)$	$8.7 \times 10^{-15}\ cm^2$
τ_{21}	Inverse Einstein transition probability	5.38 sec

and $s = CO_2 (010) / CO_2 (000)$, so s^2 is the lower state population fraction.

Substituting the appropriate values for air in Eq. (372) yields the numerical value for the P (20) transition:

$$F = \frac{7.39}{T_g^{3/2}}\ e^{-201/T_g} \tag{373}$$

For constant s, the characteristic time for r to reach the steady state value r_{ss}, from Eq. (370), will be:

$$\tau_c = \tau'_{VV} \left[1 + \phi / \phi_V \right]^{-1}\ ,$$

106

where

$$\tau'_{VV} = \left[\tau^{-1}_{VV} + \tau^{-1}_{d1}\right]^{-1}$$

and

$$\phi_V = h\nu \, \psi_c \, N_T / (F \tau'_{VV})$$

The term ϕ_V is then a saturation flux for vibrational transfer to N_2, and defines the flux at which photon pumping into CO_2 (001) becomes as rapid as vibrational transfer out of CO_2 (001). The numerical value of ϕ_v in the atmosphere is shown in Figure 73. Numerical values for the characteristic time are shown in Figure 74 as function of altitude, and we see that for fluxes greater than 10^4 W/cm^2 the characteristic time is always less than 1 μsec.

We also see from Eq. (370) that, using the definition of ϕ_V, the steady-state value of (001) population fraction will be

$$r_{ss} = \frac{s^2}{1 + \phi_V/\phi} \tag{374}$$

so that the absorption coefficient when the upper state has reached steady state will be

$$\alpha = \frac{\bar{\alpha}}{1 + \phi/\phi_V}$$

where $\bar{\alpha} = F(\bar{r} - \bar{s}^2)$ is the unperturbed value of α, with $\bar{r} = e^{-3380/T_g}$ and $\bar{s} = e^{-960/T_g}$.

We conclude that the value of α given by Eq. (375) will be reached in the times given in Figure 74, i.e., very rapidly compared with pulse durations of 10-20 μsec. We also note that depletion of CO_2 (100) will result in a further decrease in the absorption coefficient on a longer time scale. The kinetic equation for CO_2 (100), allowing for the double
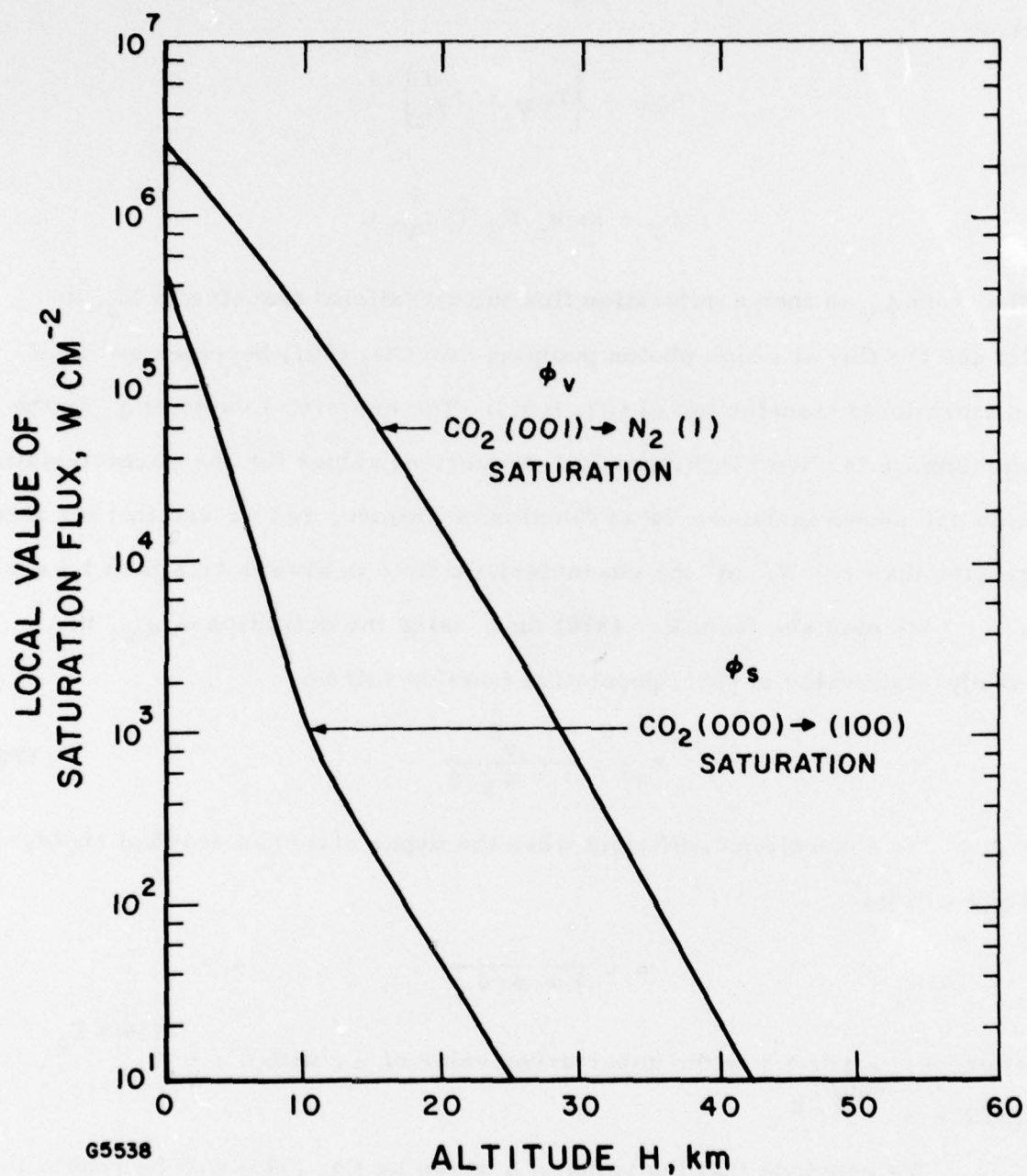
Figure 73 CO_2 Kinetic Saturation Fluxes vs Altitude

CO_2 (001) → N_2 (1) Corresponds to ϕ_v in Test, and

CO_2 (000) → (100) Corresponds to ϕ_s

108
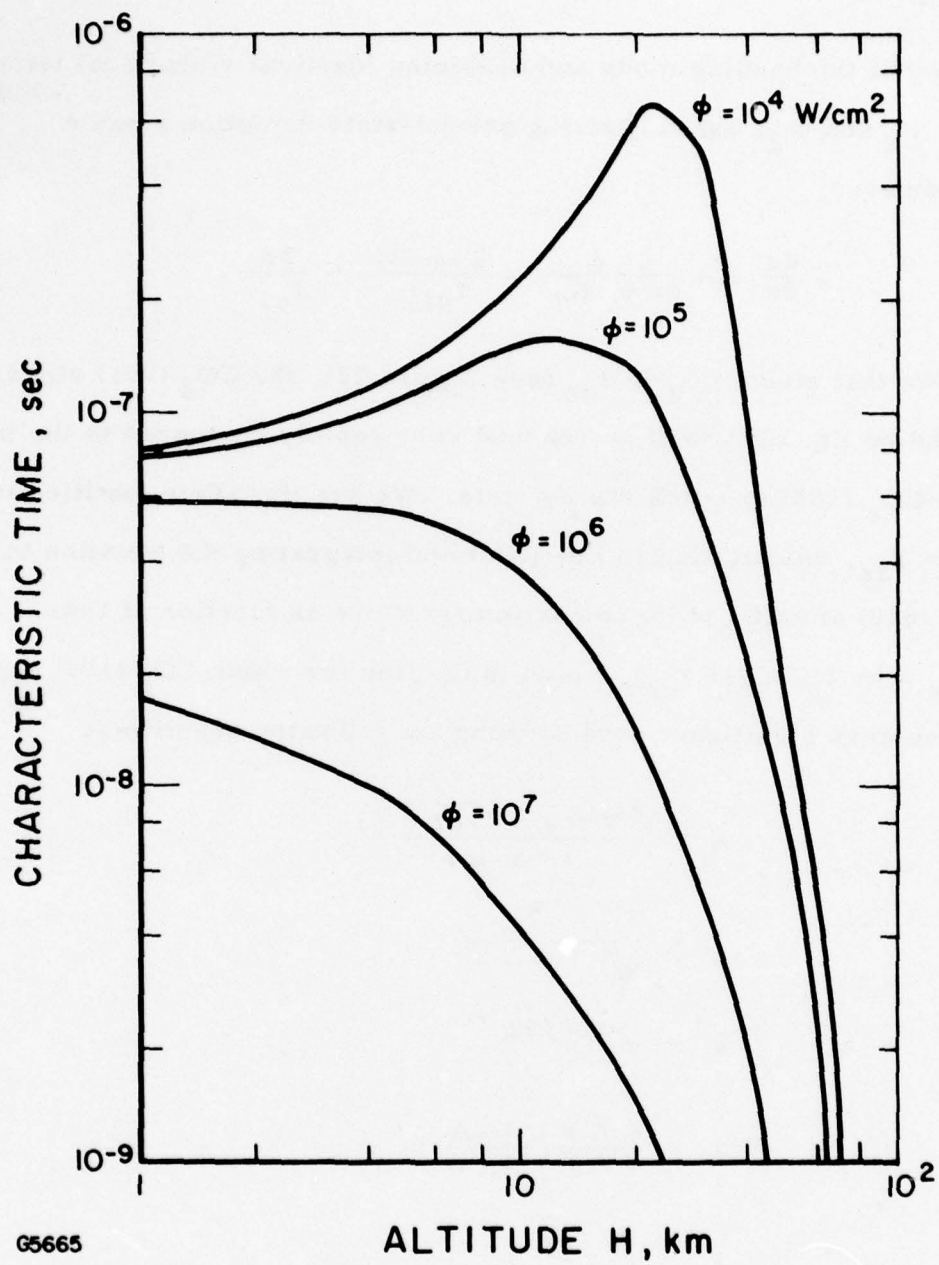
Figure 74   Characteristic Times for CO_2 (001) to Reach Steady
State (Upper State BottleNeck)

degeneracy of the bending mode and assuming identical vibrational tempera-
tures for ν_1 and ν_2, again ignoring ground-state depletion since $e^{-960/T_g} \ll 1$, becomes:

$$2 \frac{ds}{dt} = - \frac{2a\phi}{h\nu \, \psi_c \, N_T} - \frac{2(s-s)}{\tau_{d2}} + \frac{3r}{\tau_{d1}} . \qquad (376)$$

We observe that since $\tau_{VV} \ll \tau_{d2}$ (see Figure 72), the CO_2 (001) steady state given by Eq. (374) will be reached very rapidly compared to the time taken for CO_2 (100) to reach steady state. We are therefore justified in taking $r = r_{ss}$, substituting in Eq. (376) and integrating the equation to obtain CO_2 (010) and CO_2 (100) population fractions as function of time. Defining $\phi_s = h\nu \, \psi_c \, N_T/(F\tau_{d2})$, which is the flux for which CO_2 (100) depopulation becomes significant, and defining the following quantities:

$$A = \frac{\phi_V/\phi_s - 3\tau_{d2}/\tau_{d1}}{1 + \phi_V/\phi}$$

$$\Delta = \sqrt{1 + 4A\bar{s}}$$

$$\bar{s} = e^{-960/Tg}$$

$$a = \frac{2A\bar{s} + 1 - \Delta}{2A\bar{s} + 1 + \Delta}$$

$$c = \Delta/\tau_{d2}$$

the solution of Eq. (376) becomes:

$$a = \frac{\bar{a}}{1 + \phi/\phi_V} \cdot \frac{(\Delta-1)^2}{4A^2\bar{s}^2} \left[\frac{1 + \frac{\Delta+1}{\Delta-1} \, ae^{-ct}}{1 - ae^{-ct}} \right]^2 \qquad (377)$$

110

Here again the important point is that the steady-state value (for $t \to \infty$) is

$$a = \frac{\bar{a}}{4A^2 \bar{s}^2} \cdot \frac{(\Delta - 1)^2}{(1 + \phi/\phi_v)} , \tag{378}$$

which is reached in a characteristic time

$$\tau_c = \tau_{d2}/\Delta \tag{379}$$

We conclude therefore that the absorption coefficient will rapidly drop, in times given in Figure 74, to the values given by Eq. (375). It will continue to drop, in times given by Eq. (379), to the values given by Eq. (378). We therefore plot the Upper State Bottleneck (Eq. (375)), Lower State Bottleneck (Eq. (378)), and characteristic time for moving from the first condition to the second (Eq. (379)) in Figure 75, as functions of altitude. We notice that the important contribution comes from the upper state bottleneck, and that subsequent lower-state depletion decreases the absorption coefficient by factors from 2 to 4. At 3 km altitude the transition between these absorption modes takes only 1 μsec; but at 10 km it takes 10 μsec, and at 20 km about 100 μsec. We conclude that it will be conservative to assume that only the upper state bottleneck will be important for the laser propulsion case. We will proceed therefore to calculate the absorption integrated over distance $\int_x^R a\, dz$, ignoring the time dependence and taking absorptance as given by Eq. (375).

c. Absorption Integral and Beam Distortion

The Distortion Number N, which is a measure of the beam phase distortion produced by thermal blooming, is defined as

$$N = \frac{k\, IP \int_x^R a\, dz}{J D (V + \overline{R \bar{\omega}})} \tag{380}$$

111
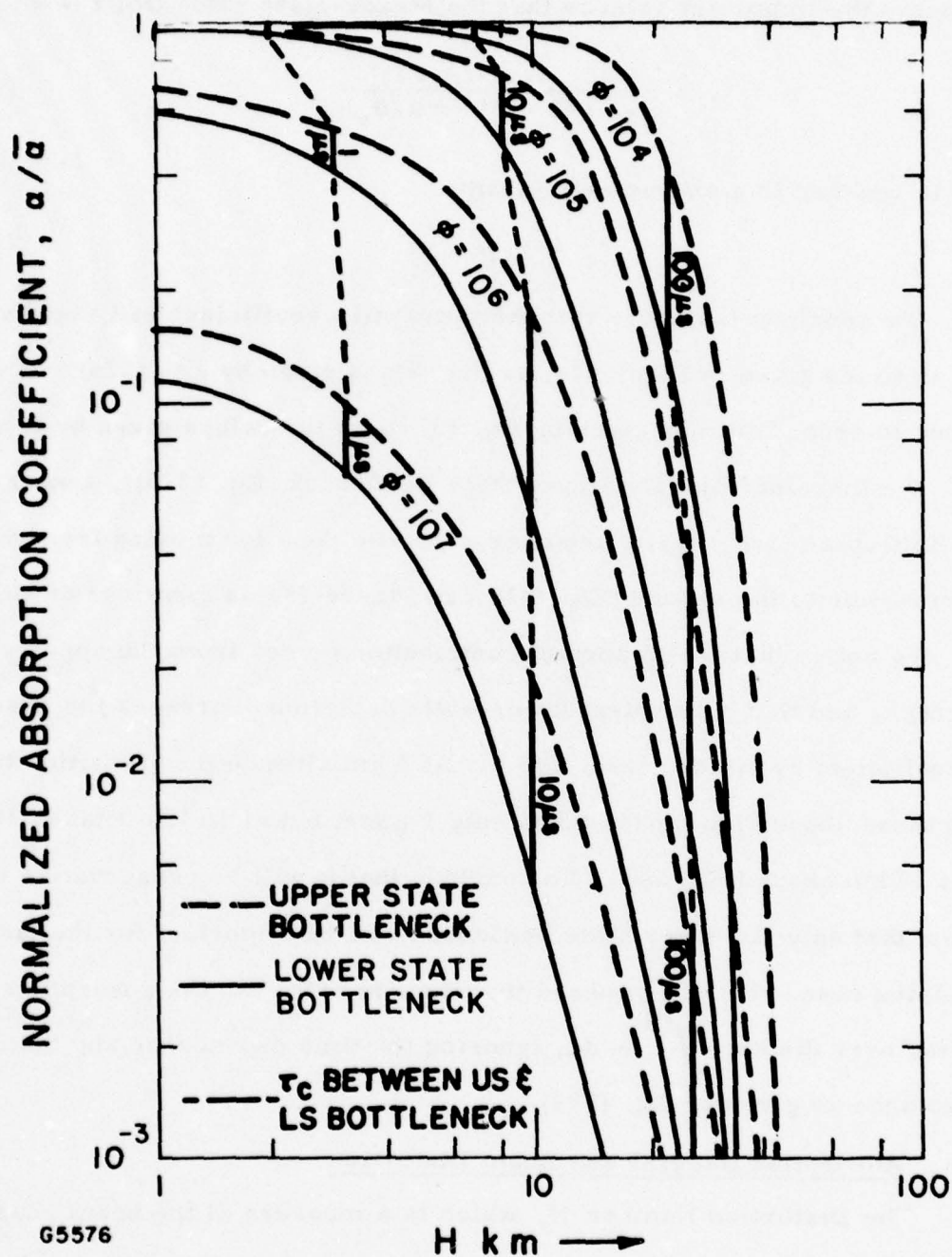
Figure 75   Upper State and Lower State Bleaching Bottlenecks.
The dashed lines are reached in ~10^{-7} sec.
Transition to the solid lines takes place in the times
indicated.

112

where k is the wave number, $\mathbb{P}$ and D the beam power and diameter, x is the initial height and R is the range, V the wind velocity transverse to the beam, $\overline{R\dot{\omega}}$ is the averaged slew velocity and J is constant. We note that α enters only as an integral over the range. For vertical propagation, absorption of CO_2 P(20) radiation is unimportant after about 20 km, and the beam will not become further distorted thereafter. We will therefore calculate the absorptance integral from height x to 20 km, based (as discussed above) on the upper-state bottleneck. Using the standard atmosphere values we obtain the absorbed fraction of the beam shown in Figure 76, in which the effects of H_2O as an absorber and as a vibrational deactivant have been included. For comparison the bed absorption at height H is shown in Figure 76a as function of flux and time into pulse. Thus starting from a height of 3 km, with neglible flux about 43% of the beam is absorbed and 57% transmitted (this ratio is less favorable in more humid atmospheres). A flux of 10^6 W/cm^2, however, which should still be above the aerosol breakdown limit, would only be 12% absorbed; 88% transmitted. We would expect the distortion number to be a factor of 4 lower than in the unbleached case. Consequently bleaching has a significant effect on beam transmission.

113
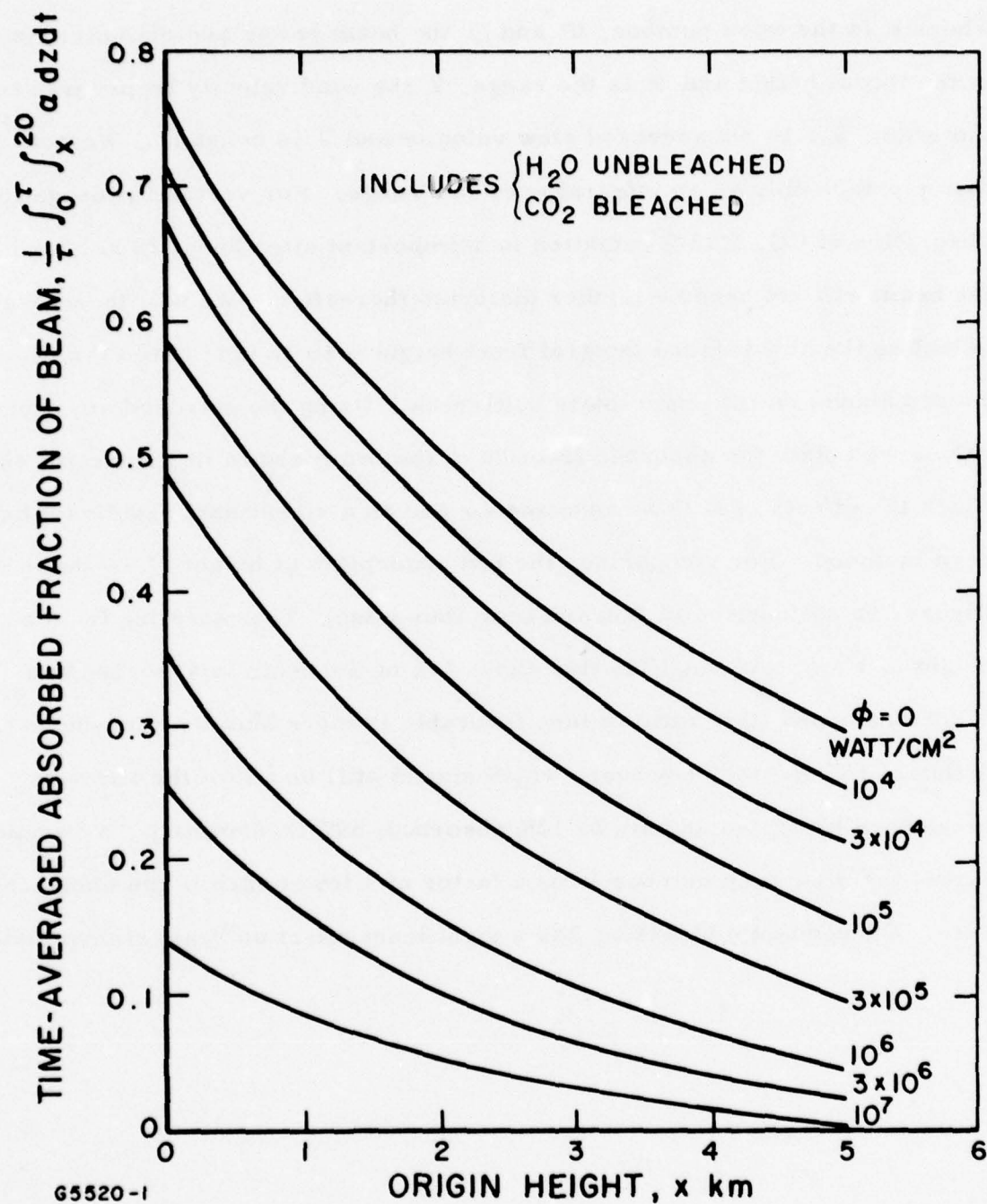
Figure 76   Integrated Absorption Averaged Overtime for 20 μsec
CO_2 P(20) Laser Pulse Propagating Vertically from
Height x to 20 km.   Both CO_2 and H_2O absorption are
included.   Standard U. S. atmosphere is used.

114
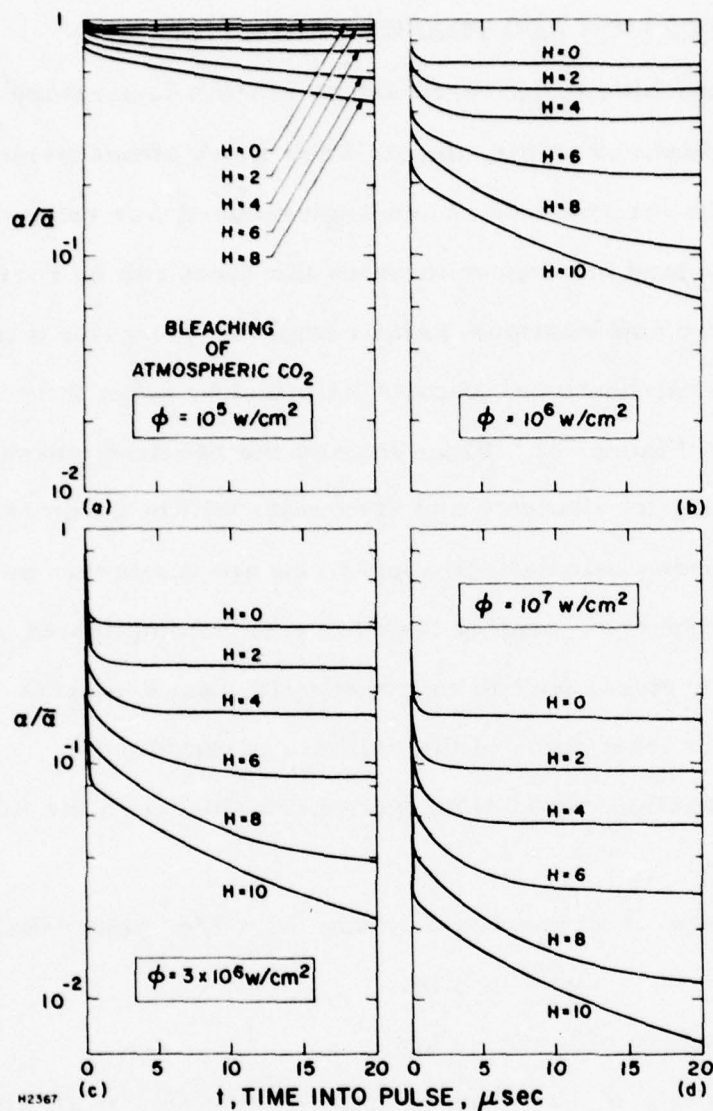
Figure 76a   Bleaching Atmospheric CO_2
Local absorption coefficent a normalized to local unbleached
value $\bar{a}$, as a function of time τ into pulse at constant flux
level ϕ and at constant altitude.   Altitude H is in kilometers.
This absorption coefficient must be added to that due to local
water vapor content.

(a) $\phi = 10^5$ W/cm^2 (b) $\phi = 10^6$ W/cm^2

(c) $\phi = 3 \times 10^6$ W/cm^2 (d) $\phi = 10^7$ W/cm^2

115

3. PHASE DISTORTION AND PHASE CORRECTION

We are indebted to J. Herrmann at Lincoln Laboratory[18,19] for performing calculations on the Lincoln Laboratory atmospheric phase distortion code in which the amount of blooming produced was estimated, and the phase correction (and the degree to which the beam can be corrected) were calculated. In the computations so far completed bleaching was not taken into account; we can however estimate its effect by using the corrected value of $\int_x^R adz$ (see Figure 76). Blooming and the requisite phase corrections calculated for various diameter and slew rates will be summarized below.

The following calculations apply to cw and mp lasers pointing upward through the atmosphere. Scaling laws for such a complicated scenario are not available; therefore, we had to run specific cases in order to explore the influence of at least some of the relevant parameters.

All propagation calculations were performed with the following parameters fixed:

Beam shape = truncated Gaussian with $1/e^2$ power diameter
     equal to 2 m,

Initial altitude of laser = 3 km,

Wind velocity = 10 m/sec of uniform direction at all altitudes.

Two wavelengths were used: 10.6 μ (CO_2) and 4.8 μ (CO), for calculations with diffraction-limited beams. For each of the two wavelengths, an appropriate altitude-dependent absorption coefficient was used, corresponding to mid-latitude summer conditions. For the CO_2 the effect of kinetic cooling is included.

---

(18) J. Herrmann, D.P. Greenwood, P. Kafalas. Anticipated Propagation Conditions for High Energy Lasers at White Sands Missile Range, Contract DAAH01-75-C-1272.

(19) J. Herrmann, Private Communication.

The parameters range, slewing rate, elevation angle, and the over-lap number (for multi-pulse mode) were partially explored.

The results are presented as relative area increase as a function of average power, where the area of a beam is defined as the area containing 63.2% of the total power. In some cases, a diameter of an aperture re-ceiving this fraction of power is used.

Effects due to aerosols and turbulence are not included.

For some cases, a predictive phase correction of thermal blooming was performed.

We give a summary of the principal results.

a. Range Dependence

The relative area increase is only a weak function of the range, as shown in Figure 77, where we plot the area increase as a function of power for two ranges, for cw and multipulse (MP) beams, with pulse overlap num-ber N_o = 2. (N_o is number of laser pulses passing through given volume of gas at laser exit.) The results show that the effective atmospheric bloom-ing lens is a thin lens located near the transmitter. We performed there-fore most of the calculations for the 200-km range.

b. Slewing Rate Dependence

The relative area increase is shown in Figure 78 for two slewing rates for a cw and MP (N_o = 8) beam. The area increase is roughly pro-portional to the slewing rate; therefore, we limited our calculations to a slewing rate of 40 mrad/sec.

c. Elevation Angle Dependence

For cw beams without slewing, the effective lens at an elevation angle of 30° is twice the effective lens at 90°. But the presence of slewing

117
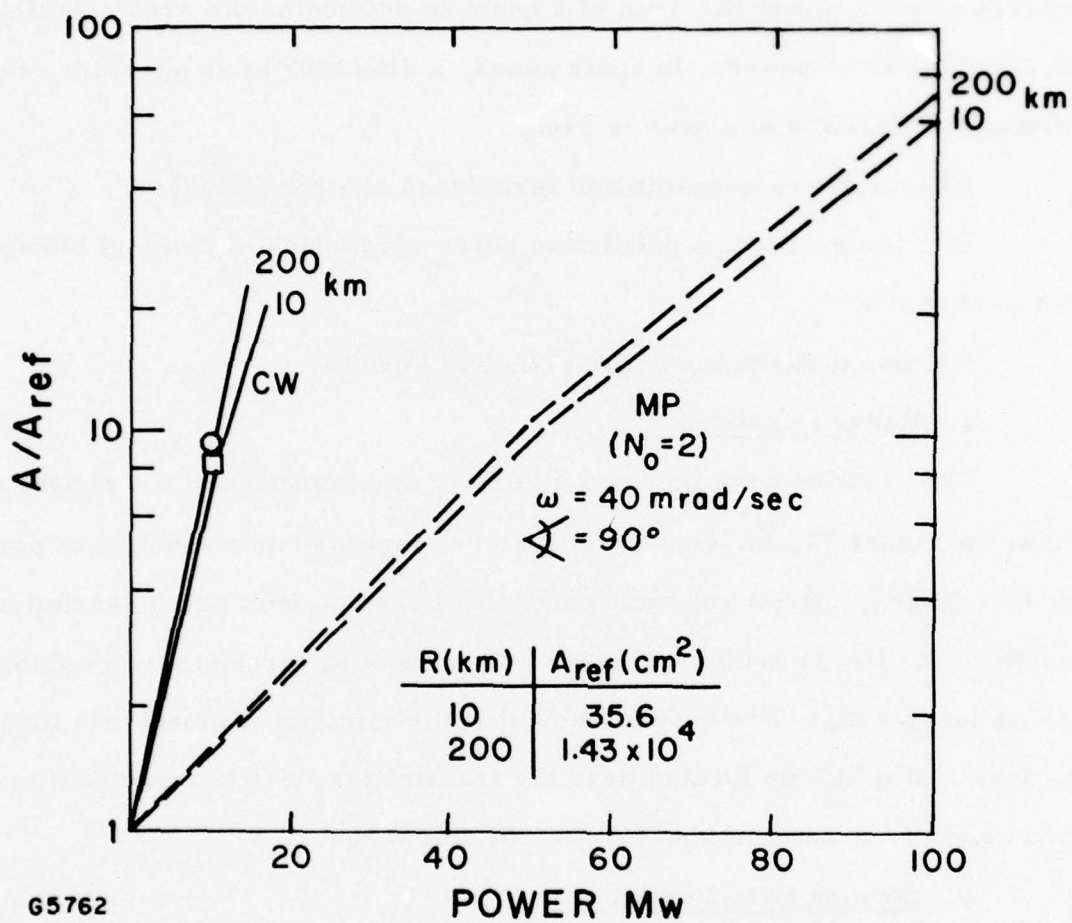
Figure 77   Effect of Range on Multipulse CO_2 Thermal Blooming

G5759
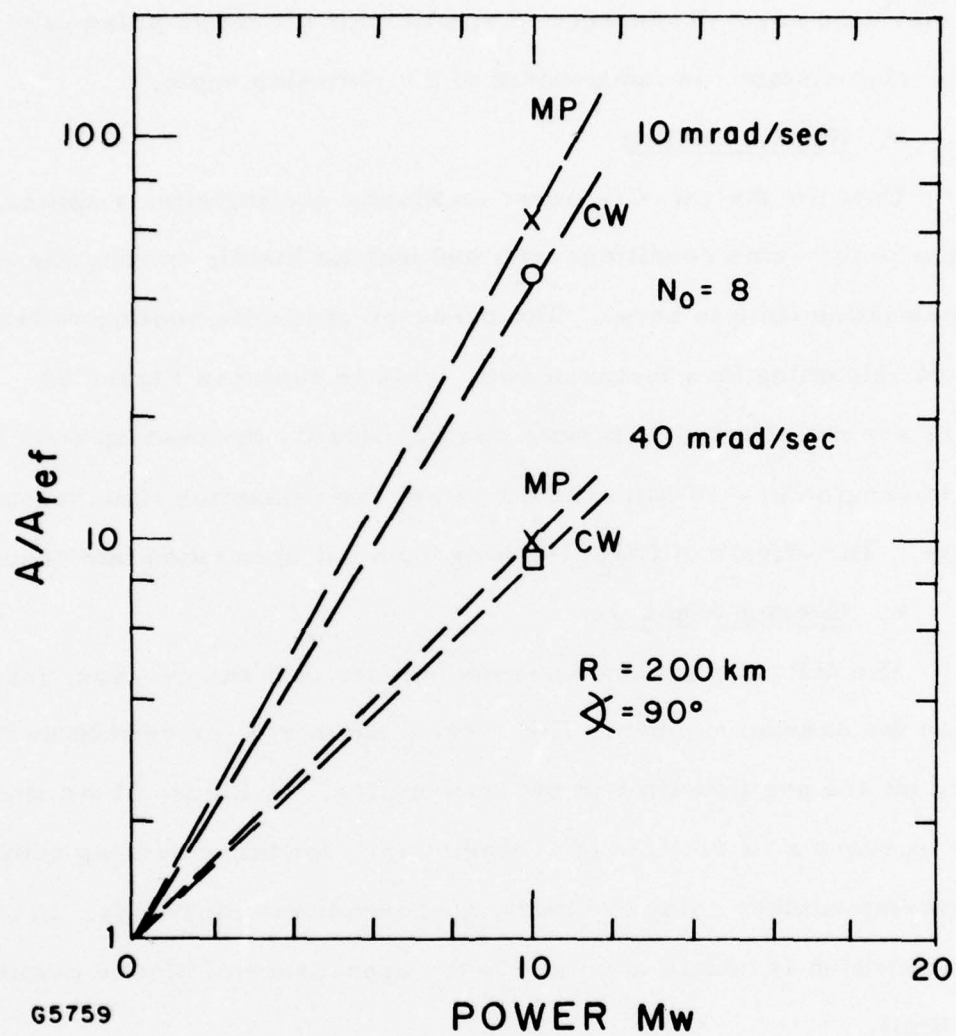
Figure 78   Effect of Slew-Rate for CW and MP CO_2 Laser Beams

119

reduces this effect, as shown in Figure 79 for a 40-mrad/sec slewing rate.
The elevation angle dependence is smaller for the multi-pulse case because
the overlap distance is independent of the elevation angle.

d. Kinetic Cooling

Only for the $cw-CO_2$ laser do kinetic cooling effects appear. We
compared the same conditions with and without kinetic cooling (by reducing
the relaxation time to zero). The presence of kinetic cooling reduces the
thermal blooming by a factor of two. This is shown in Figure 80. The MP
lasers are not affected by kinetic cooling because the overlap does not reach
into the region (6 - 10-km altitude) where the relaxation time becomes ef-
fective. The effects of CO_2 bleaching have not been taken into account here.

e. Overlap Number

The MP case has one parameter more than the cw case, for which
we use the overlap number. The overlap number N_o is defined as the num-
ber of pulses per flow time at the transmitter. In Figure 81 we show the
area increase as a function of average power for three overlap numbers.
An overlap number going to infinity approaches cw conditions. In our case,
this transition is complicated due to the appearance of kinetic cooling for
this limit.

f. Blooming for CO

Thermal blooming for CO wavelengths and absorptions is shown in
Figure 82 for cw and two MP cases. The integrated absorption coefficient
smaller for CO than for CO_2 (0.242 vs 0.541), but the absorption is more
concentrated near the transmitter. Slewing will therefore reduce CO_2
blooming more than CO blooming. The reference area is smaller for CO;
therefore, we get a larger relative blooming effect for CO than for CO_2.

120
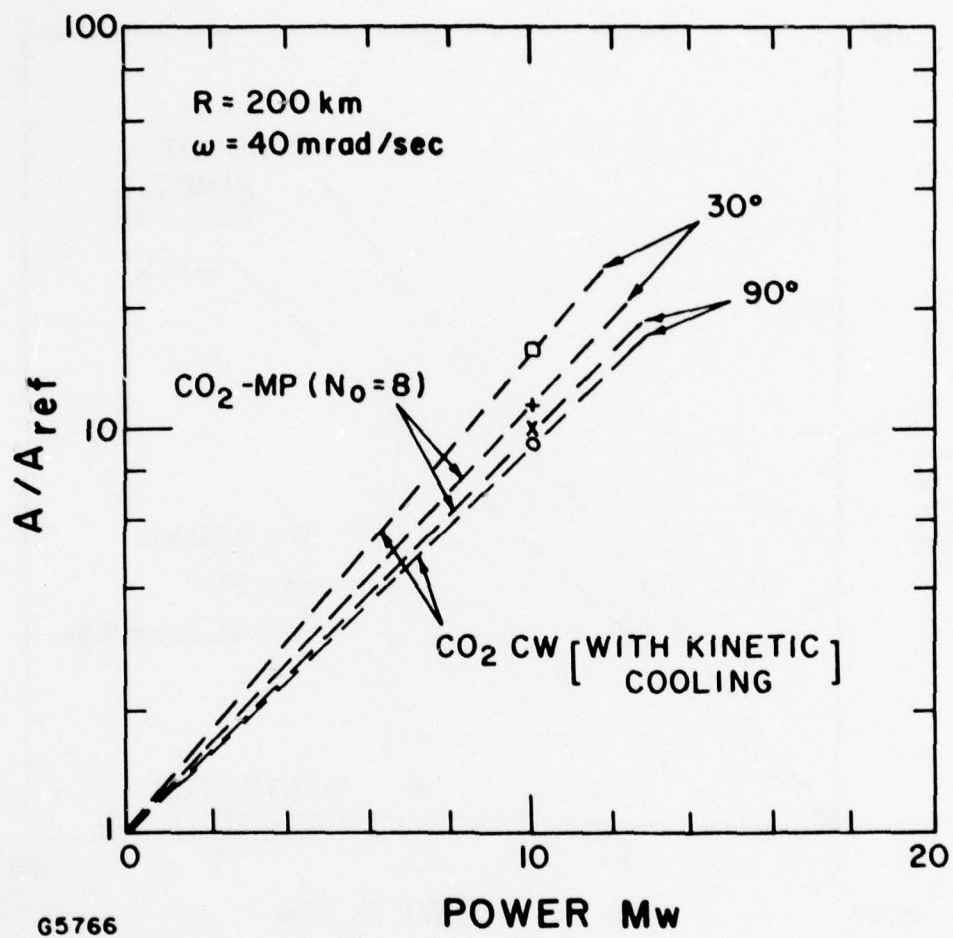
Figure 79   Elevation Angle Dependence of Thermal Blooming for
             CO_2; Multipulse and CW

100

WITHOUT
KINETIC
COOLING

WITH

A/A_{ref}

10

$R = 200\,km$
$\sphericalangle = 90°$
$\omega = 40\,mrad/sec$

CORRECTED

1

0   5   10   15   20

POWER Mw

G5757
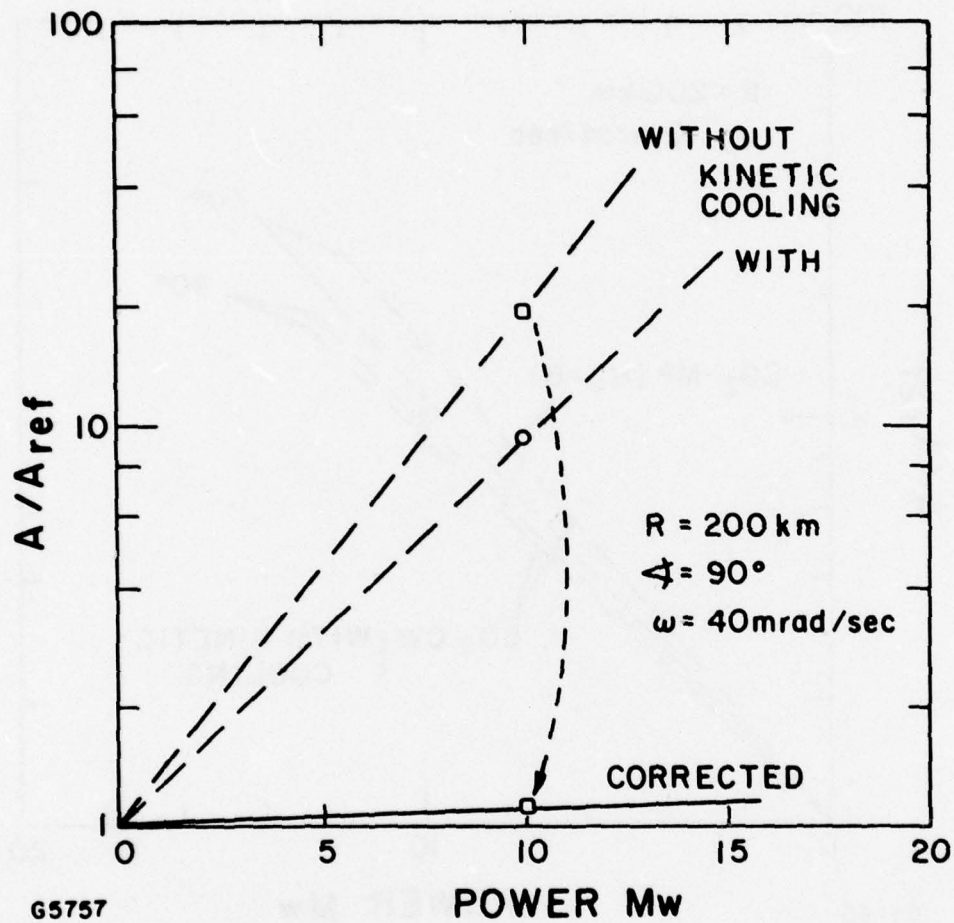
Figure 80   Effect of Kinetic Cooling on CO_2 CW Laser Thermal
Blooming.   Effect of applying phase corrections is
also shown.

122
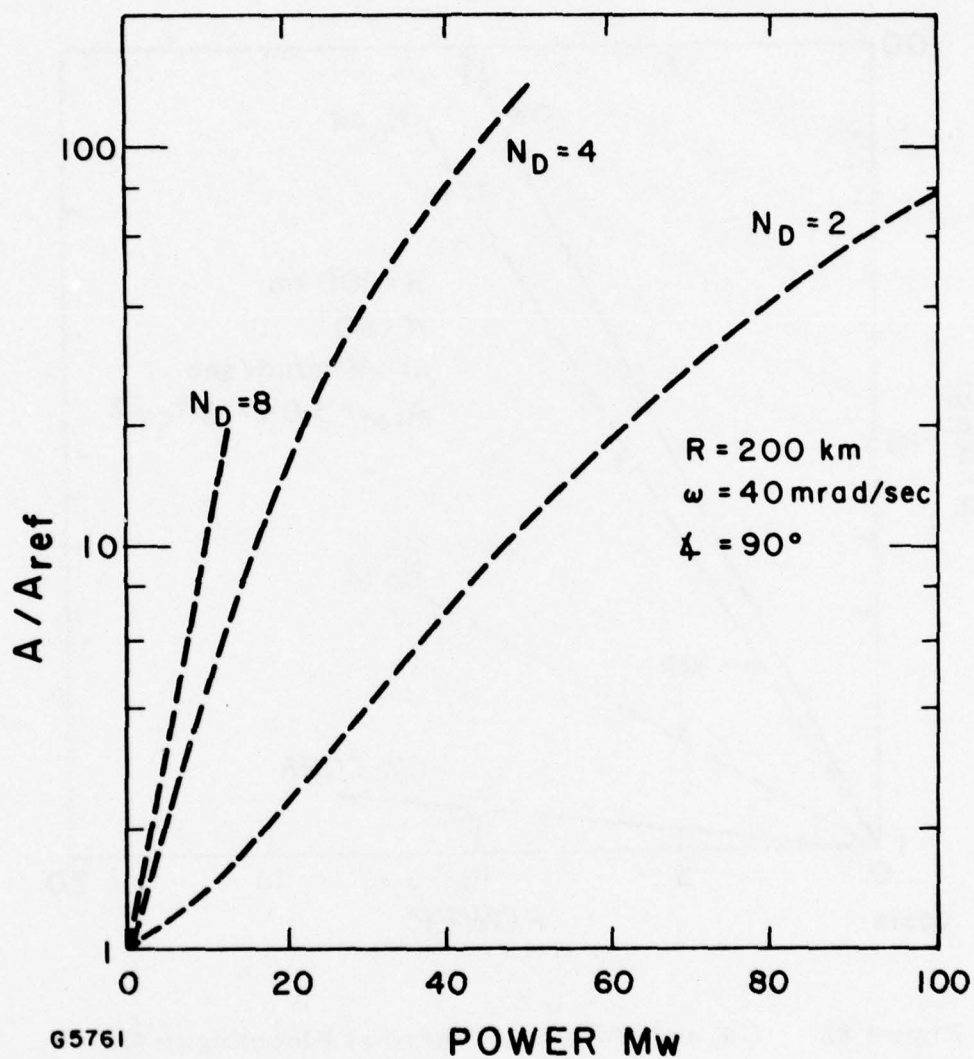
Figure 81   Thermal Blooming Dependence on Overlap Number for CO_2 Multipulse
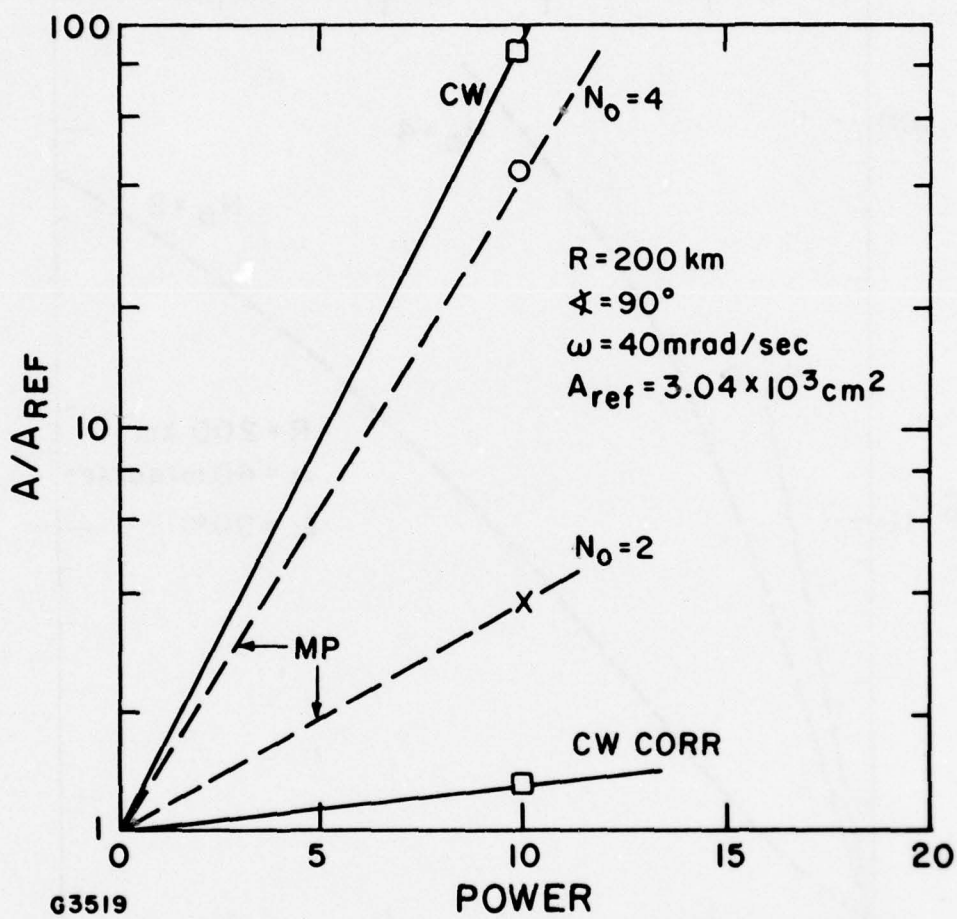
Figure 82   CW and Multipulse Thermal Blooming in CO

124

g. Comparison of CO_2 and CO

In order to compare the thermal blooming for CO_2 and CO, we plot in Figure 83 the diameter (of the 63.2% flux area) in absolute units as a function of power. The difference in the blooming effects is then properly compared.

h. Phase Correction

We can perform different phase corrections for thermal blooming. Our present cw code can be used with the simple predictive correction, which does not permit a proper inclusion of kinetic cooling. We performed therefore the cw phase correction without kinetic cooling effects. Our MP code can be used with the iterative, predictive phase correction. Adaptive corrections were not made.

i. Search for the Phase Corrections (CO_2 - cw)

Phase corrections for the CO_2 - cw laser were performed for two altitudes, 10 and 200 km, and they are presented in Figure 84, where we plot the relative area increase as a function of the scale parameter. The correction for 10 km is not as good as it is for 200 km, because the effective thermal-blooming lens is less thin than for the 200 km case (but it is still thin).

j. Phase Correction for CO_2 - cw

In Figure 85 we plot the relative area increase as a function of power for the CO_2 - cw beam for two altitudes, uncorrected and corrected.

k. Comparison of Corrections

The correction for the 10 km range is less complete than for the 200 km range, but the reference beam is smaller. We plot, therefore, the diameter in absolute units for both cases in Figure 86. If the criterion

125
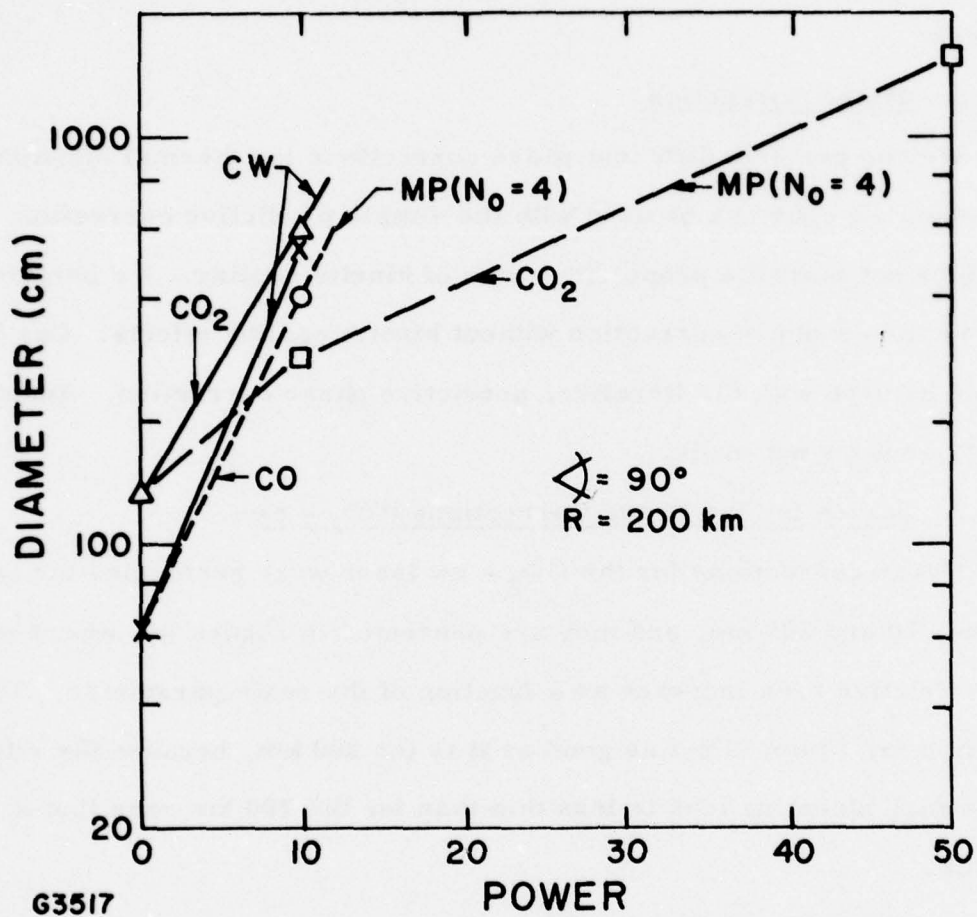
Figure 83   Comparison Between CO and CO_2 Thermal Blooming, for CW and Multipulse (No = 4).   Note that CO blooming increases more rapidly with power than CO_2.

126
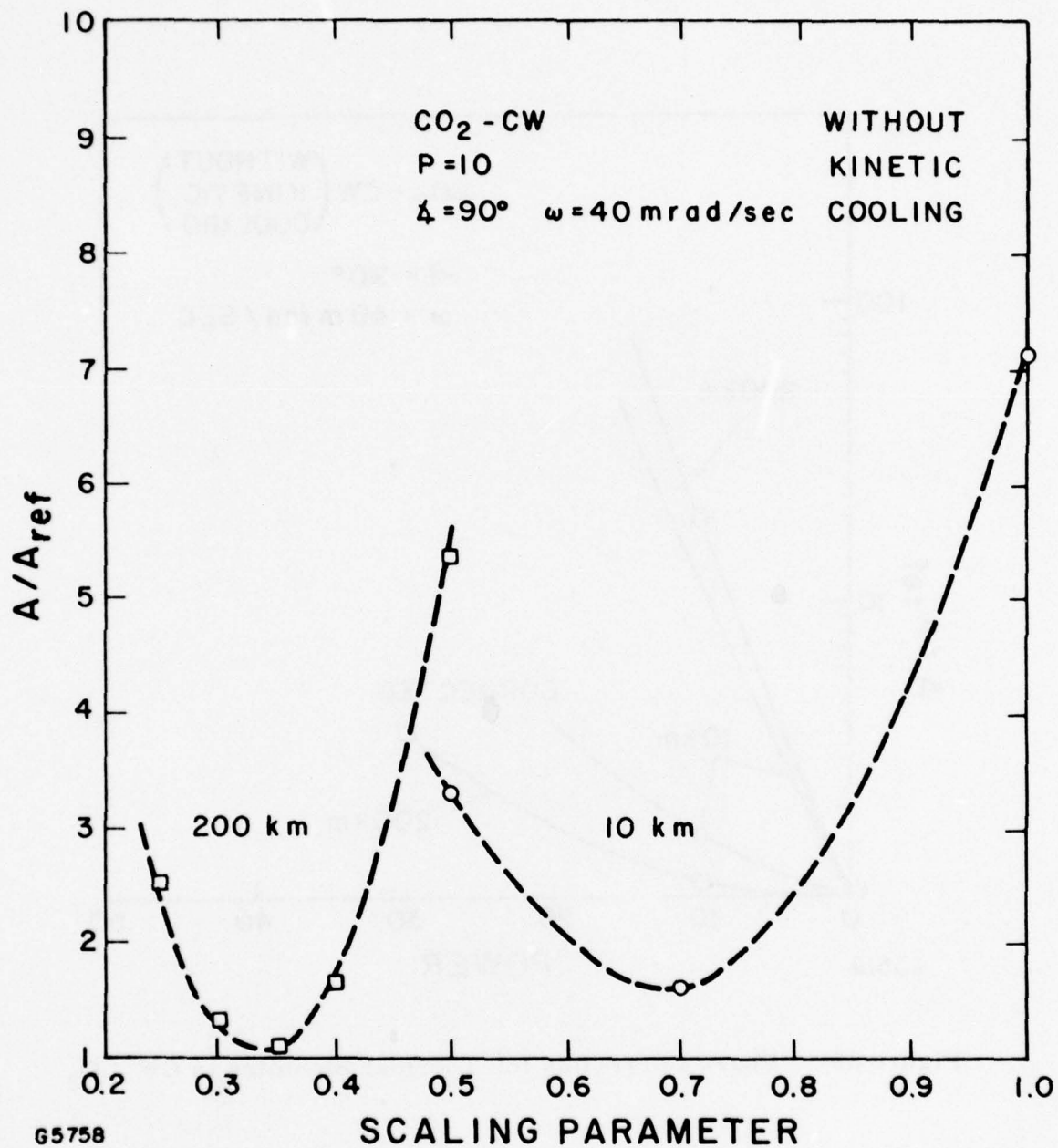
Figure 84   Optimization of the Predictive Corrective for CW CO_2, with 2 Meter Diameter Mirror
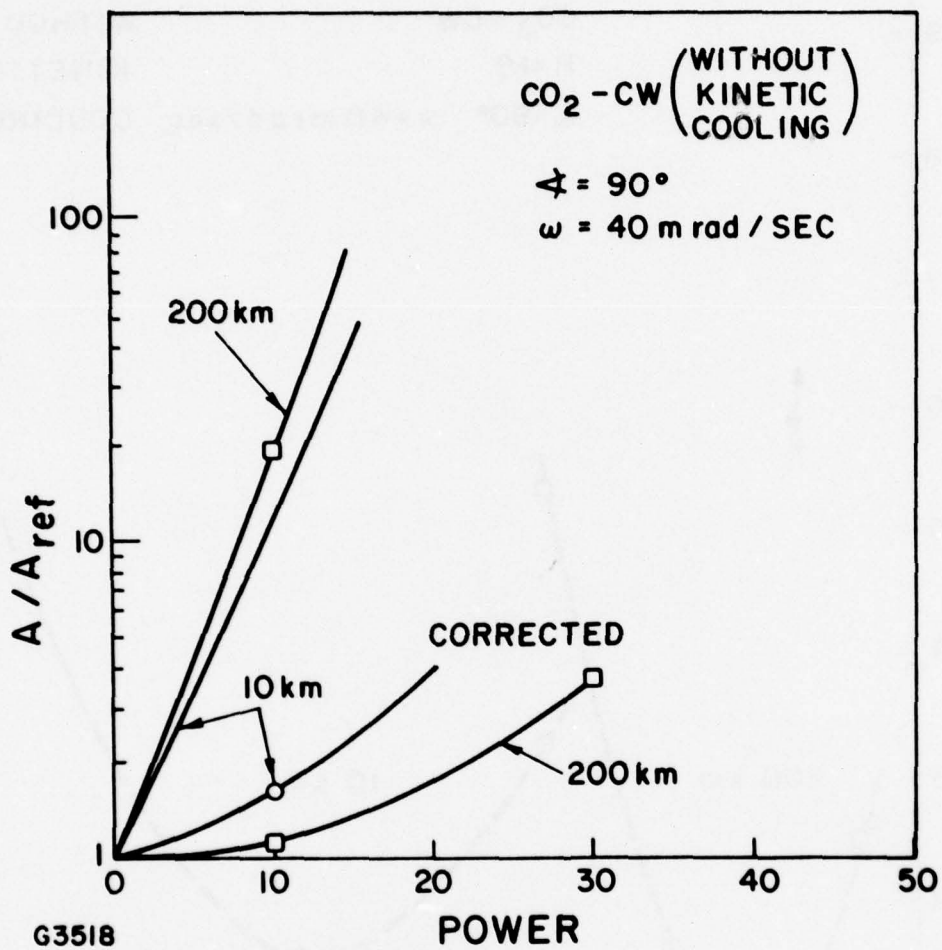
Figure 85   Phase Correction for Thermal Blooming in CW CO_2

128
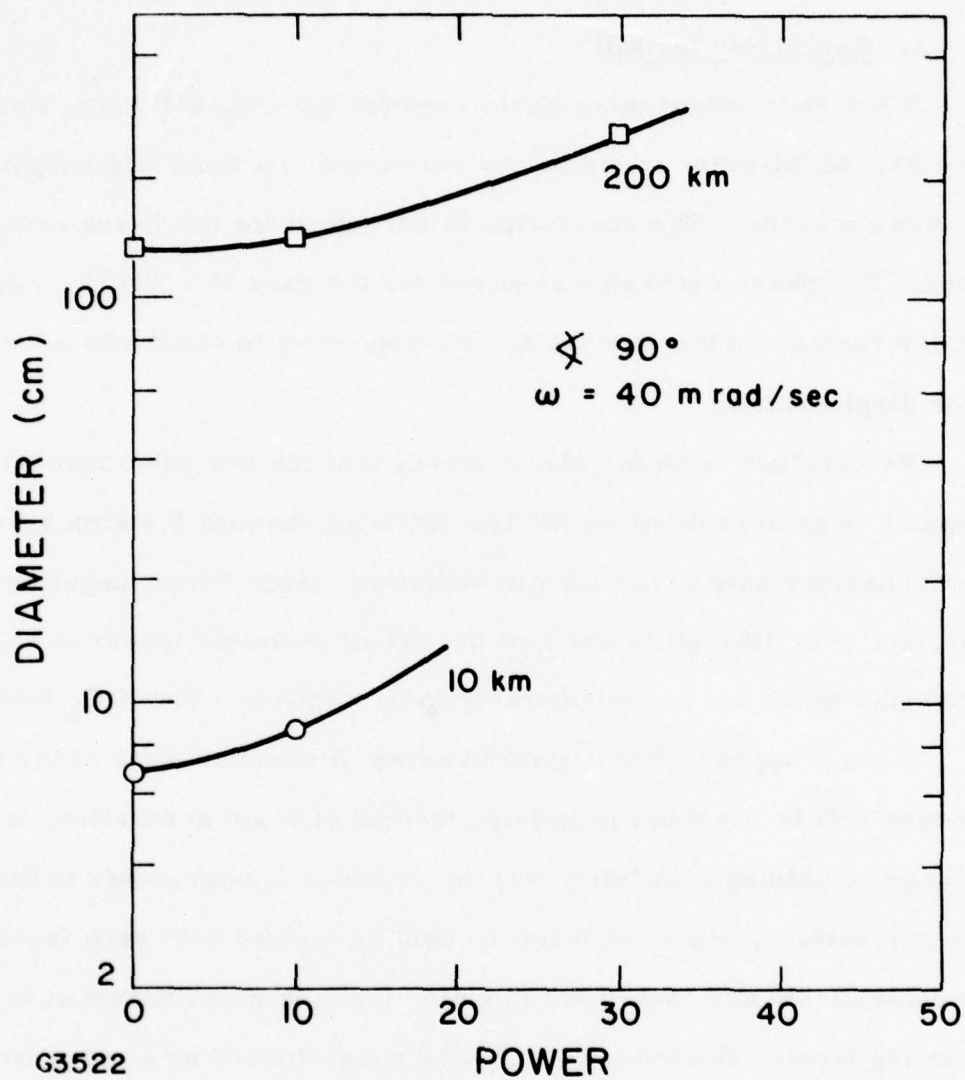
Figure 86   Corrected Beam Diameter at 10 km and 20 km for CO_2 CW

129

of usefulness is a given target size, then the lesser is a given target
size, then the lesser correction of 10 km is not important.

1. Correction for MP

A few corrections were performed for the CO_2-MP case, shown in
Figure 87. Multi-pulse cases can be corrected to a much higher power
level than cw cases. The correction is very good for the lower overlap
number. The phase excursion required for the case $P = 300$ ($N_o = 2$) is
about 100 radians on the wavefront, corresponding to about 100 microns
mirror displacement.

We conclude from the above survey that for low pulse numbers
multipulse is preferable to cw for transmission through the atmosphere.
We will consider only CO_2 10.6 μm radiation, since CO propagation is in-
ferior, and it is difficult to see how the use of chemical lasers at shorter
wavelengths would not be considerably more expensive than CO_2 lasers.

Since it appears that a stacked array of modular units of the CO_2
laser type will be the most promising method of beam generation, the use
of a large combining chandelier mirror provides a natural way to impose
phase corrections, since the mirror could be faceted with each facet separ-
ately controllable and each laser module directing its radiation at the cor-
responding facet. The modules would be phase-locked by a pulse from a
low-power pulse-initiating laser, so that phase corrections to the combined
beam could be provided by independently adjusting each facet on the chande-
lier mirror. An alternate scheme would be to provide phase modulation of
the low power pulse initiating laser, which would produce the required phase
correction in the high power amplified beam. This would have the advantage
of manipulating the beam while at low power.

130
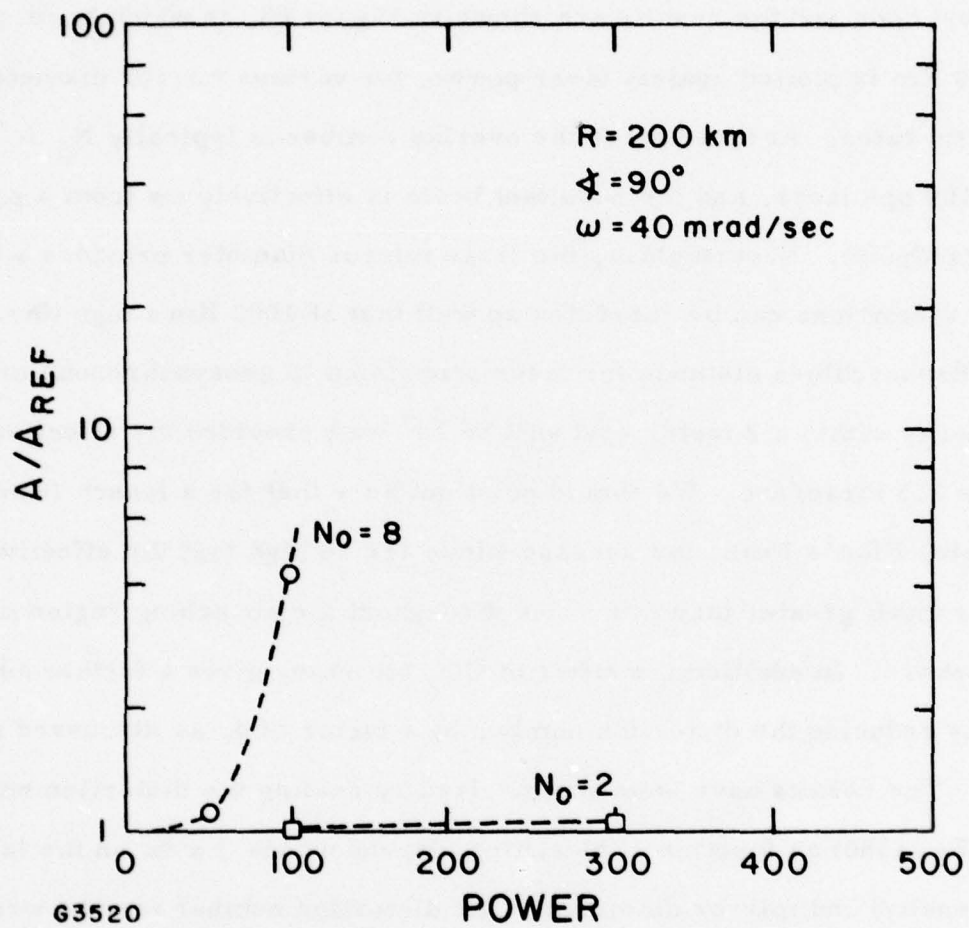
Figure 87   Multipulse Thermal Blooming and Phase Correlation
for CO_2

131

We are therefore interested in the propagation and phase correction of a large pulsed beam, between 10 and 30 meters in diameter. Accordingly calculations have been performed on the Lincoln Laboratory (Herrmann-Bradley) code and the results are shown in Figure 88, in which beam area at 1000 Km is plotted against laser power, for various mirror diameters and slew rates. At these sizes the overlap number is typically $N_o \approx 100\text{--}300$, for a 100 pps laser, and the resultant beam is effectively cw from a propagation standpoint. Nevertheless, the large mirror diameter provides a beam whose distortions can be corrected so well that at 1000 Km range (the maximum Brennschluss distance for laser propulsion to geosynchronous orbit) the energy within a 2 meter spot will be 10^9 watt provided the effective slew rate is 2.5 mrad/sec. We should point out here that for a launch from, for example, Pike's Peak, the average winds are so high that the effective slew rate is much greater than this value throughout the absorbing region of the atmosphere. In addition the effect of CO_2 bleaching gives a further advantage by reducing the distortion number by a factor of 4, as discussed above.

The results have been summarized by scaling the distortion number from Eq. (380) as function of bleaching (dependent via $\int a\, dx$ on the laser flux density) and mirror diameter. The distortion number may be written as:

$$N_D = 9 \; \frac{(\gamma - 1)}{C_s^2} \; \frac{\mathbb{P}}{VD\lambda} \int_X^R a\, dz.$$

where γ is the adiabatic exponent for air and C_s is the sound speed, $\mathbb{P}$ is the laser power, V the wind velocity (including slew rate, D the mirror diameter and λ the optical wavelength. Thus for constant power and

132
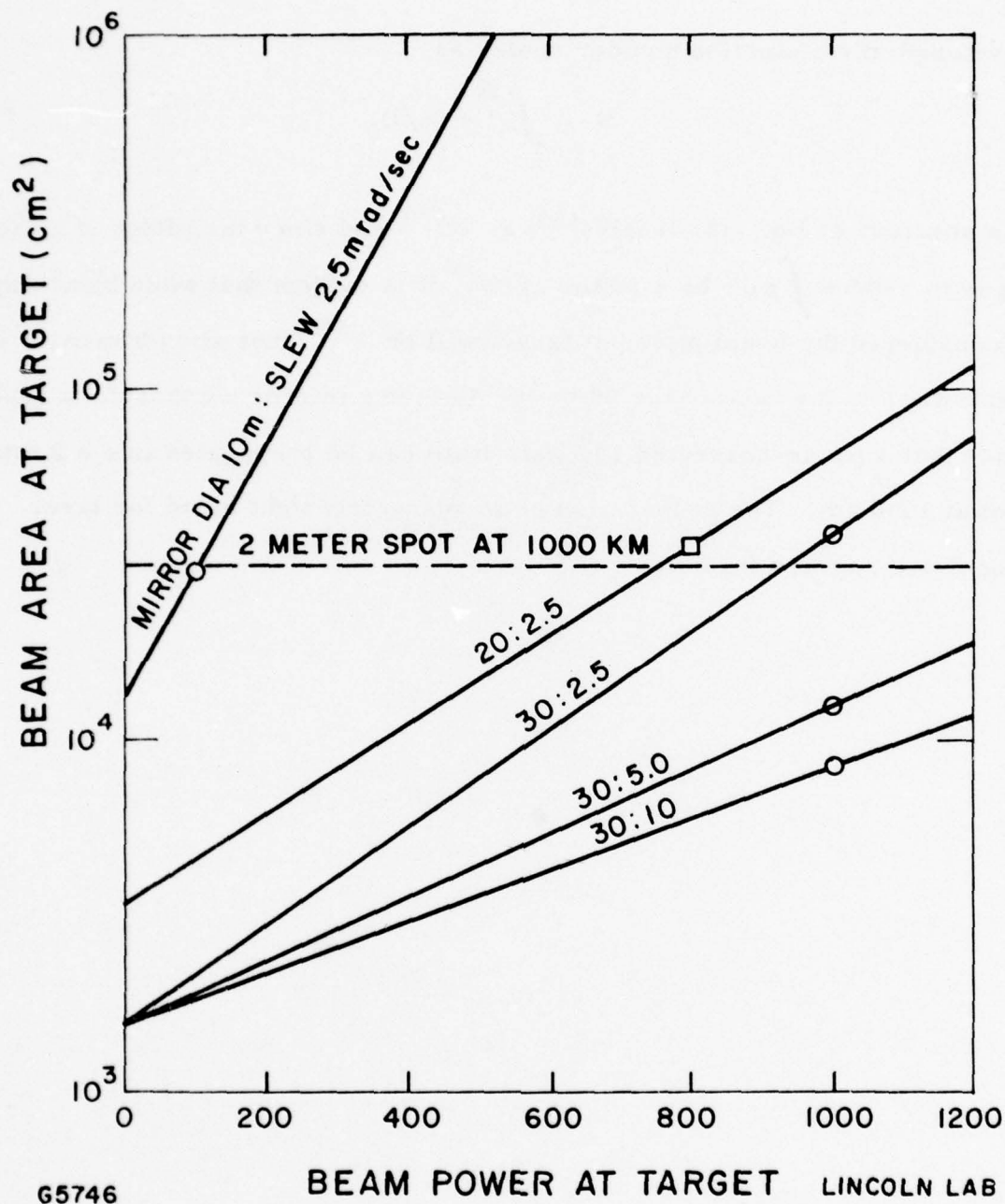
Figure 88   Phase Corrected Area of Laser Beam at Target 1000 km
Distant, vs Laser Power for Various Mirror Diameter
and Slew Rates. At these diameters CW and MP lasers
propagation is indistinguishable.

133

wavelength the distortion number scales as

$$N \propto \int_X^R a \, dz / D. \tag{381}$$

The abscissa of Eq. (381) scales[20] as $N^{3/2}$ and since the effect of bleaching is to reduce $\int a \, dz$ by a factor of two, it is evident that when bleaching is considered the beam power at target will be $2^{3/2}$ that when bleaching is ignored. For the case of the 20 meter diameter mirror we therefore conclude that a phase-corrected 10^9 watt beam can be propagated into a 2 meter spot at 1000 km. The propagation of an adequately tight beam for laser propulsion appears feasible.

---

[20] Alan Phillips, S.A.I., private communication

134

4. PROPAGATION THROUGH H_2O PLUME

Water (or ice) appears to be an ideal fuel for laser propelled
vehicles because a) it is cheap, b) it does not pollute, and c) it has a low
molecular mass in the vapor phase and high density under ambient con-
ditions (as opposed to N_2, H_2, etc. which have to be cooled).

A drawback to the use of water as opposed to liquid N_2 for example,
is the condensation that will occur in the plume and the deleterious effect
that condensation may have on laser propagation. Also, high temperature
H_2O is an absorber of 10.6 μm radiation. We will examine the effect of
water vapor transmission and water condensation on laser propagation in
three regimes.

     a) High altitude plume which expands into vacuum.

     b) Plume at 20 km altitude.

     c) Low altitude plume near sea level.

In Section VI.4.a. we summarize the data on absorption by water vapor in
the 10.6 μm window. In Section VI.4.b. we calculate the exit conditions
at the nozzle for a typical vehicle with mass 8 tons, acceleration a g
$(a \simeq 3)$ and specific impulse 800 sec. The high altitude plume condensation
is calculated in Section VI.4.c. and low and intermediate altitude plumes
in Section VI.4.a. The absorption of the laser beam in these plumes is
also considered in these sections. We present our conclusion in Section
VI.4.e.

a. Absorption by Water Vapor

At low temperatures the absorption by water vapor in the region
near 10.6 μm is small and is of the continuum type. The variation of

135

absorption with wavelength is consistent with the interpretation that the absorption is due to wings of lines originating from the pure rotation band of H_2O beyond 15 μm and of lines from the 6.3 μm vibration-rotation band. A theoretical estimate of absorption made by Kaplan[21] due to the wings of distant lines,

$$k(\nu) \simeq \frac{4.1 \times 10^4}{(\nu - 200)^2} + \frac{3.7 \times 10^3}{(\nu - 1550)^2} \quad g^{-1} \, cm^2, \tag{382}$$

where ν is the wavenumber in cm^{-1}, is in fair agreement with measurements of continuum absorption in the atmosphere made by Bignall et al.[22] and Roach and Goody.[23]

Analyses[24, 25] of more recent measurements by Burch[26], McCoy et al[27] and Arafev[25] indicate that continuum absorption is due to a water vapor dimer, the absorption coefficient being given by (for $\lambda = 10.6 \, \mu$m)

$$\alpha = 4.3 \times 10^{-6} \, p \, (P + 139 \, p) \, km^{-1} \tag{383}$$

(21) This theoretical estimate is quoted in the experimental paper by Bignell et al., next reference.

(22) Bignell, K., Saiedy, F. and Sheppard, P., J. Opt. Soc. Am. 53, 466 (1963).

(23) Roach, W., and Goody, R., Quart. J. Roy. Meteorol. Soc. (London) 84, 319 (1958).

(24) Roberts, R., Selby, J., and Biberman, L., Appl. Optics 15, 2085 (1976).

(25) Adiks, T., Aref'ev, V., and Dianov-Klokov, V.; Sov. J. Quant. Electron, 5, 481 (1975).

(26) Burch, D., "Investigation of the Absorption of Infrared Radiation by Atmospheric Gases," Semi-Annual Technical Report, Aeronutronic Division, Philco Ford Corporation, Report U-4784 (January 1971).

(27) McCoy, J., Rensch, D., and Long, R., Appl. Opt. 8, 1471 (1969).

where p is the partial pressure of water vapor (in Torr) and P the ambient pressure (in Torr), or, equivalently, by

$$\alpha = 1.76 \times 10^{-3} \rho + 1.42 \times 10^{-6} \rho^2 \exp(-\Delta H/RT) \quad km^{-1} \quad (384)$$

where ρ is the water vapor concentration in g/m^3 and $\Delta H = -4,500$ cal/mole. The second term in Eq. (384) is due to the water vapor dimer and dominates over the first term for $\rho > 2.3 \, g/m^3$ at sea level (12% relative humidity at $20^{\circ}C$). The term ΔH in the exponent correlates well with the estimated binding energy of the water vapor dimer. If absorption at $10.6\mu m$ is due entirely to a fundamental band of the water vapor dimer then the absorption coefficient at higher temperatures should be given by the second term of Eq. (384). A plot of the absorption length $L = 1/k$ as given by Eq. (384) as a function of temperature and water vapor pressure (or concentration) is shown in Figure 89.

Experimental measurements of water vapor absorption at temperatures $T \simeq 2000^{\circ}C$ and pressure $p \simeq 1$ atm were reported by Ludwig et al.[28] At high temperatures, vibration-rotation lines, due to high lying levels, appear in the $10 \, \mu m$ window and are the main cause for absorption. Unfortunately, the measurements of Ref. 28 were taken with a resolution of $25 \, cm^{-1}$ and the absorption coefficient at the location of the CO_2 laser lines is unknown. We have used the compilation of spectral information on H_2O made by McClatchey[29] to estimate the

(28) Ludwig, C., Ferriso, L., and Abeyta, C., J. Quant. Spectr. and Rad. Transfer 5, 281 (1965).

(29) McClatchey, R.A., et al., "AFCRL Atmospheric Absorption Line Parameters Compilation," Air Force Cambridge Research Laboratory, AFCRL-TR-73-0096, January 1973.
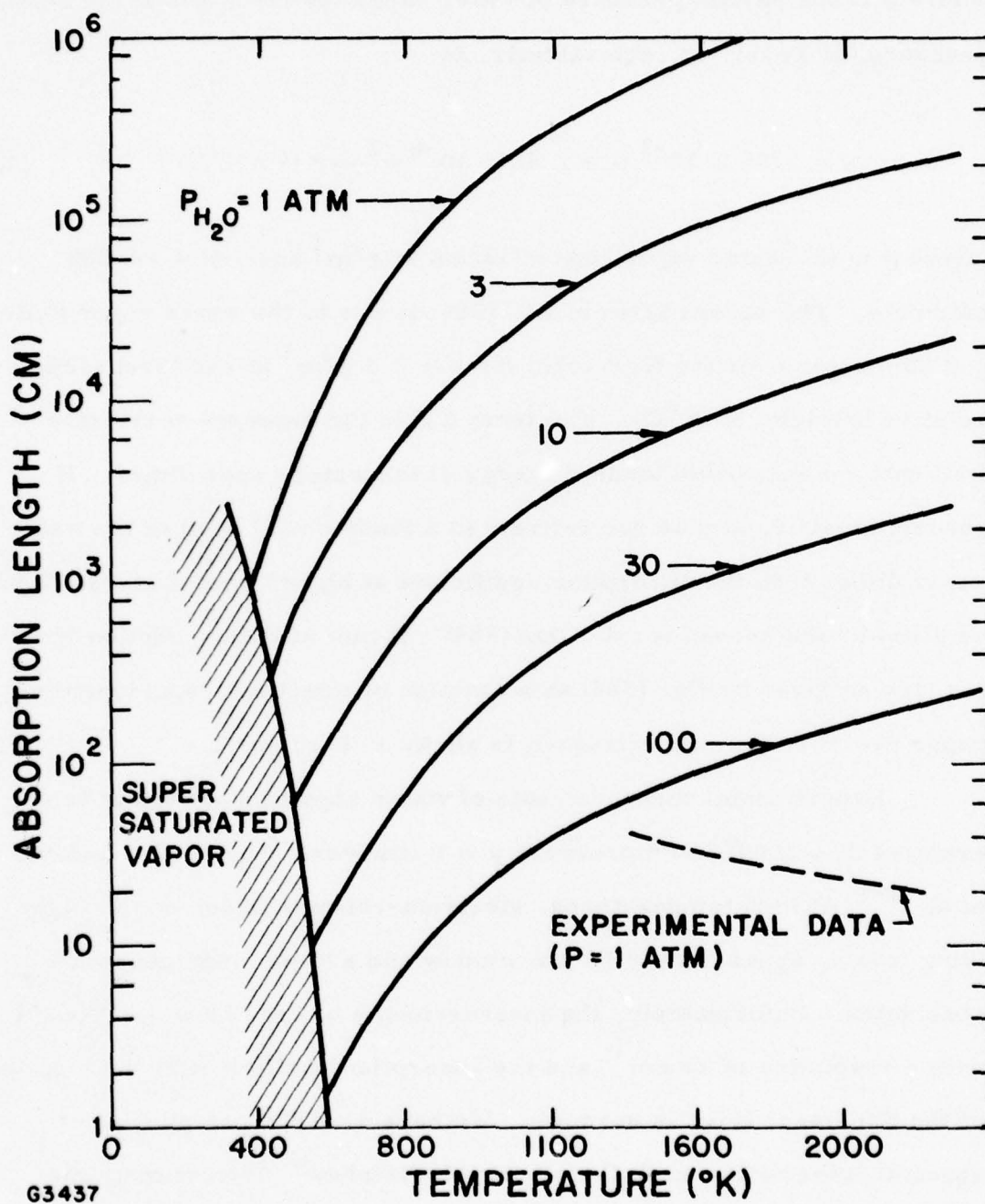
Figure 89   Absorption Length at 10 μm Due to the Water Vapor
             Dimer (The experimental data were taken from Ref. 8)

absorption coefficient at the specific wavelengths of the CO_2 laser. The McClatchey tape[29] contains information on H_2O lines that appear at *room* temperature only, and represents a lower bound on H_2O absorption, since other lines may become important at higher temperatures. Calculations of the absorption coefficient at two pressures are presented in Table 8. Absorption is the largest for the P (20) line of CO_2, this line falling only 0.18 cm^{-1} away from a line of H_2O. The line shape due to collision broadening is given by

$$S(\nu) = \frac{S_o(T) \, \gamma}{\pi [(\nu - \nu_o)^2 + \gamma^2]} \qquad (385)$$

where ν_o is in the position of the line center and γ, the line width, is proportional to pressure and varies inversely with the square root of temperature. The variation of line intensity per atom with temperature is given by

$$S_o(T) = \frac{S_o}{Q_V Q_R} \, \exp - \left(\frac{\epsilon}{kT} \right) \qquad (386)$$

where ϵ is the energy of the lower state of the vibration rotation transition considered and Q_V and Q_R are the vibrational and rotational partition functions. For water vapor at temperatures below 3000°K, $Q_R \propto T^{3/2}$ and $Q_V \simeq (1 - \exp - \theta/T)^{-1}$ where $\theta = 2290$°K (corresponding to the 6.3 μm band of H_2O). At standard temperature and pressure, the line width of an H_2O line is estimated to be[30] ~ 0.07 cm^{-1}, so that at pressures less than atmospheric, the CO_2 lines fall well into the wings of the H_2O lines compiled by McClatchey. The absorption coefficient

(30) Goody, R., Atmospheric Radiation, Vol. I Theoretical Basis, Oxford University Press (1964), p. 115.

139

TABLE 8. ABSORPTION COEFFICENT OF PURE H_2O VAPOR AT ν (cm^{-1})

CO$_2$ Line	ν (cm^{-1})	Temperature ($^\circ$K) 500	1000	1500	2000	2500	3000
				$P = 1$ Atmosphere			
P16	947.74	2.82^{-4}	2.170^{-4}	1.00^{-4}	4.50^{-5}	2.09^{-5}	1.039^{-5}
P18	945.98	9.59^{-5}	2.35^{-4}	1.51^{-4}	7.74^{-5}	3.85^{-5}	1.96^{-5}
P20	944.20	3.54^{-4}	2.07^{-3}	1.29^{-3}	7.33^{-4}	3.88^{-4}	2.06^{-4}
P22	942.38	5.36^{-5}	1.68^{-4}	1.23^{-4}	6.68^{-5}	3.45^{-5}	1.80^{-5}
P24	940.55	1.02^{-4}	2.57^{-4}	1.75^{-4}	9.36^{-5}	4.8^{-5}	2.50^{-5}
CO$_2$ Line	ν						
				$P = 0.06$ Atmosphere			
P16	947.74	1.08^{-6}	8.03^{-7}	3.66^{-7}	1.64^{-7}	7.60^{-8}	3.72^{-8}
P18	945.98	3.52^{-7}	7.65^{-7}	5.47^{-7}	2.80^{-7}	1.39^{-7}	7.08^{-8}
P20	944.20	1.84^{-6}	6.85^{-6}	5.16^{-6}	2.85^{-6}	1.49^{-6}	7.81^{-7}
P22	942.38	1.96^{-7}	6.11^{-6}	4.42^{-7}	2.41^{-7}	1.25^{-7}	6.52^{-8}
P24	940.55	5.84^{-7}	9.38^{-7}	6.37^{-7}	3.40^{-7}	1.73^{-7}	9.05^{-8}

α at temperature T and pressure P is obtained from the absorption coefficient α at a reference temperature T_o and pressure P_o by combining Eqs. (385) and (386). We find

$$\frac{\alpha}{\alpha_o} = \left(\frac{P}{P_o}\right)^2 \left(\frac{T_o}{T}\right)^3 \exp\left[-\frac{\epsilon}{k}\left(\frac{1}{T} - \frac{1}{T_o}\right)\right]\frac{1 - \exp(-\theta/T)}{1 - \exp(-\theta/T_o)} \qquad (387)$$

where one factor $(P/P_o)(T_o/T)$ takes into account the varying amount of absorber (assumed pure) in the path, another factor $(P/P_o)(T_o/T)^{1/2}$ takes into account the pressure broadening of the lines and the remaining factors are due to the partition functions. Absorption of the P(16)-P(24) lines of CO_2 by the H_2O vapor were found to follow Eq. (387) fairly well in the range 300 to 2500°K and can be represented with an accuracy better than 30% by

$$\alpha = A\frac{P^2}{T^3} \exp\left[-(\epsilon/kT)\right][1 - \exp(-2290/T)] \text{ cm}^{-1} \qquad (388)$$

where P is in atmospheres and A and ϵ are given by Table 9.

TABLE 9. PARAMETERS ENTERING IN EQ. (388)

Line	P(16)	P(18)	P(20)	P(22)	P(24)
A(cm^{-1} Atm^{-2} (°K)^3)	1.53×10^6	4.48×10^6	5.55×10^7	4.1×10^6	5.5×10^6
ϵ/k (°K)	1870	2950	3330	3150	3010

A comparison of Eq. (388) and Table 9 for the P(20) line of CO_2 is shown in Figure 90.

b. Exit Conditions for the Study of Plume Behavior

We assume for generality a pulsed device where the expansion time of the vapor in the nozzle is τ (note $\tau \gg \tau_{laser}$) and the repetition rate is f. We define:

141
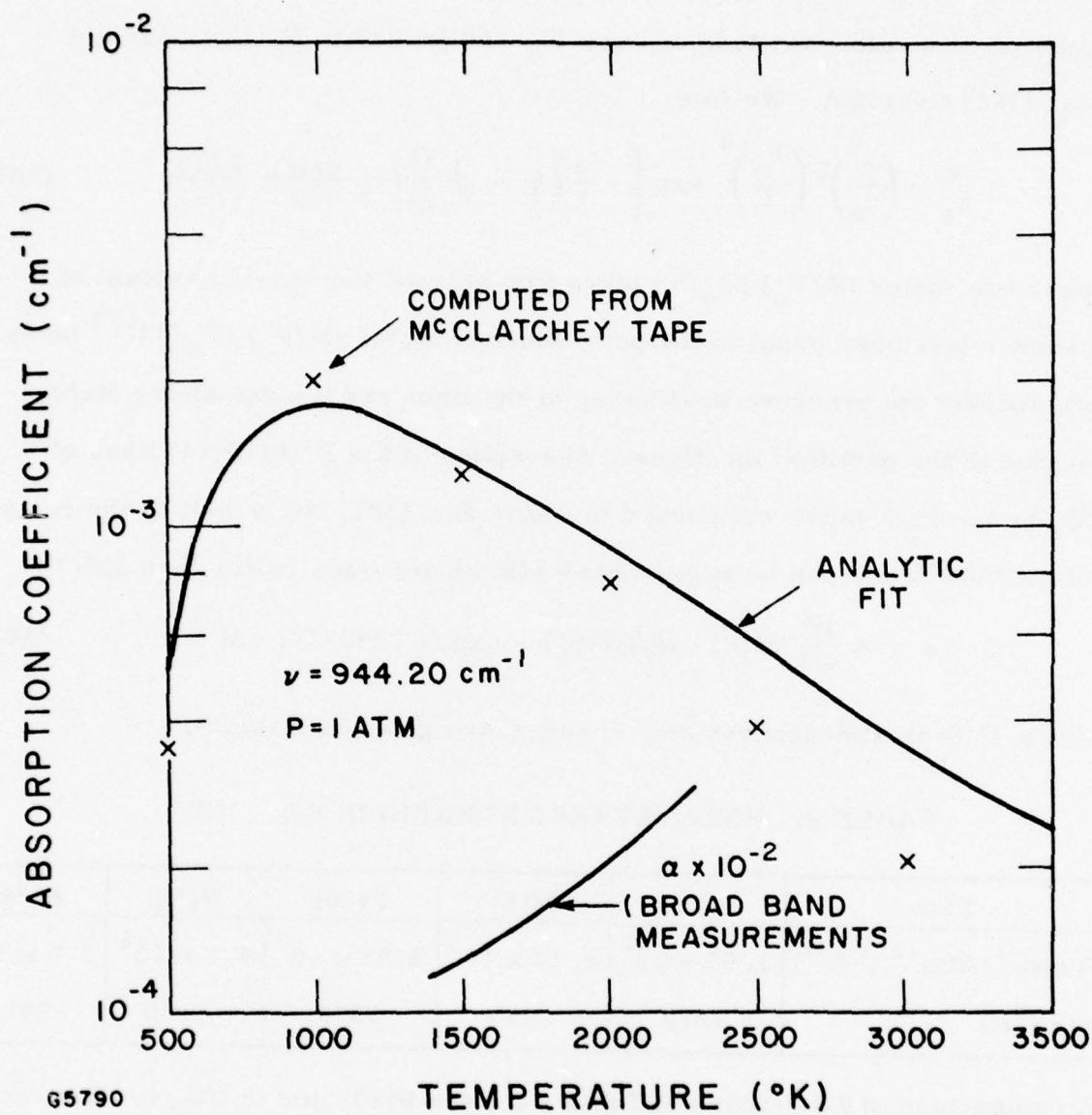
Figure 90   Absorption Coefficient for the P (20) Line of CO_2

I = Specific impulse (800 sec) = V_e/g

T = Temperature

m = Mass of vehicle (8 tons)

μ = Molecular mass of fuel (3×10^{-23} g)

g = Acceleration of gravity (1000 cm sec^{-2})

z = Compressibility factor

u = Velocity of gas with respect to vehicle

A = Nozzle area

ρ = Vapor density

$\dot{m}$ = Mass flow rate

e = Subscript referring to exhaust conditions

s = Subscript referring to stagnation conditions

The equation of motion of the vehicle averaged over many pulses is:

$$m \frac{dV}{dt} = \dot{m} u_e = (\rho_e u_e A_e) \tau f u_e$$

We require, furthermore,

$$m \frac{dV}{dt} = a m g$$

Where typically $a \simeq 3$.

Solving for ρ_e we get

$$\rho_e = \frac{a m}{I^2 g \tau f A} \tag{389}$$

We supplement Eq. (389) with the condition that the efficiency of the engine is η.

The ratio of exit enthalpy h_e to stagnation enthalpy h_s is given by

$$\frac{h_e}{h_s} = 1 - \eta \tag{390}$$

143

also

$$h_s - h_e = \frac{u_e^2}{2} = \frac{I^2 g^2}{2} \tag{391}$$

For I and η given, h_e and h_s are uniquely determined by solving Eqs. (390) and (391). We use the Mollier diagram for H_2O presented in Figure 91.

We assume isentropic expansion in the nozzle. This means that the stagnation and exit conditions lie on a vertical line s = const. in the Mollier diagram. In order to be definite, we choose the reasonable (but somewhat arbitrary) stagnation conditions.

$$\left. \begin{array}{l} p_s = 80 \text{ atm} \\[2mm] T_s = 5700^{\circ}K \\[2mm] h_s = 5.3 \times 10^4 \text{ J/g} \end{array} \right\} \text{Stagnation Conditions}$$

We then calculate that for a 50% efficient engine (η = 0.5)

$$\left. \begin{array}{l} p_e = 0.06 \text{ atm} \\[2mm] T_e = 3000^{\circ}K \\[2mm] h_e = 2.65 \times 10^4 \\[2mm] z_e = 1.6 \\[2mm] I = 760 \end{array} \right\} \begin{array}{l} \text{Exit Conditions} \\ \text{(point of B of Figure 91)} \end{array}$$

The above conditions seem reasonable for operation at high altitudes where $p < 0.06$ atm, but would give a very inefficient engine at sea level. One would get flow separation in the nozzle and shock formation that would bring the exhaust pressure up to atmospheric. The computation of the exit conditions for an over-expanded jet taking into account all these effects is a major task. We will here make the drastic assumption that the fluid in the nozzle expands up to the point p = 1 atm and then forms a parallel jet which

144
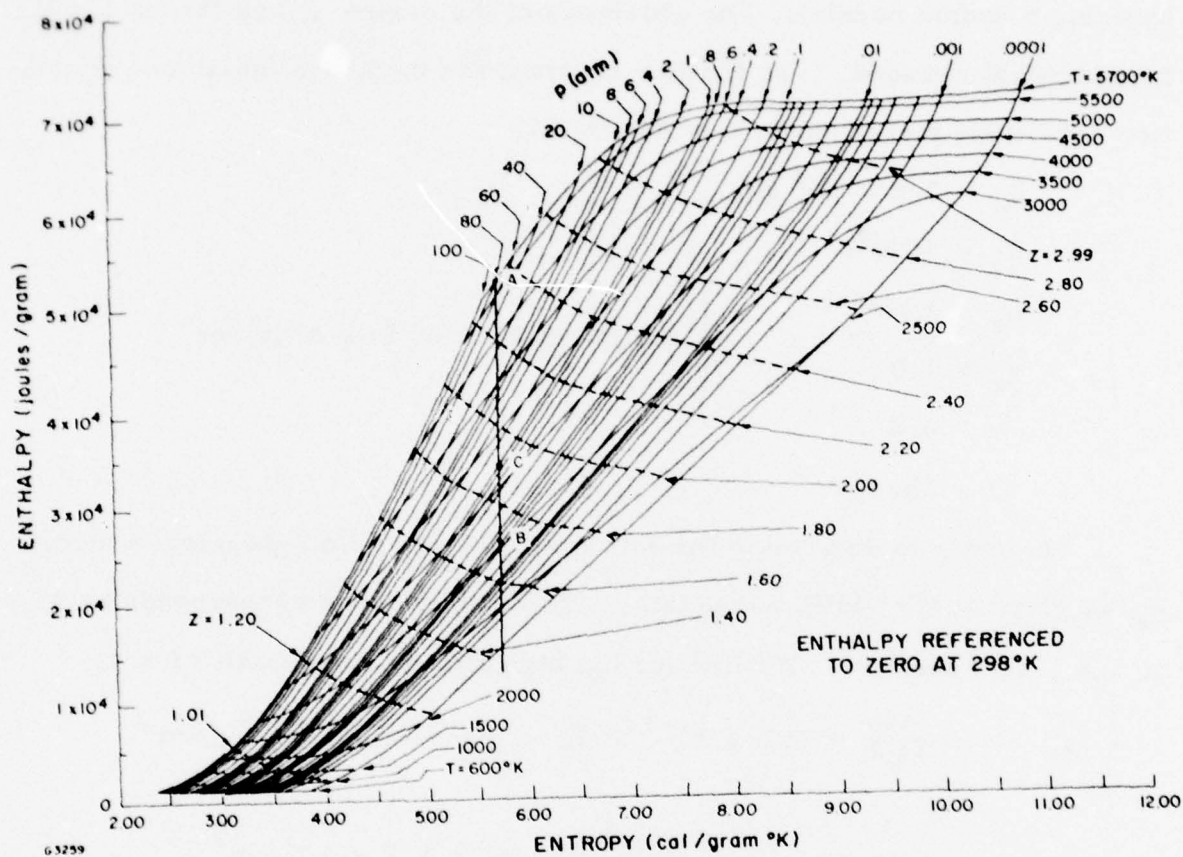
Figure 91   Mollier Chart for H_2O

145

eventually mixes with the atmosphere. This will result in a jet cross section that is much less than the nozzle cross section (such a jet can be realized by using a double nozzle). The efficiency of the engine η and thrust I will be somewhat reduced. The Mollier diagram for the above mentioned stagnation conditions yields (point C of Figure 91).

$$h_e = 3.2 \times 10^4 \text{ J/g}$$
$$T_e = 3600^\circ K$$
$$p_e = 1 \text{ atm}$$
$$z_e = 1.9$$
$$\eta = 0.4$$
$$I = 650 \text{ sec}$$

Exit Conditions at Low Altitudes

In order to determine the exit area, we solve Eq. (389) for A using ρ_e as given by the Mollier diagram. The smallest area corresponds to $\tau f = 1$, i.e., cw operation. We find for the high altitude case (with $\tau f = 1$)

$$\rho_e = 1 \times \frac{300}{3600} \times 1.2 \times 10^{-3} \times \frac{18}{29} \times \frac{1}{1.9} = 3.2 \times 10^{-5} \text{ g/cm}^3$$

$$A_e = \frac{3 \times 8 \times 10^6}{(650)^2 \times (1000) \times 3.2 \times 10^{-5}} = 1.7 \times 10^3 \text{ cm}^2$$

The exit conditions calculated above for the two cases are listed in Table 10. We look at condensation in the plume and its effect on laser propagation in the next sections.

c. Absorption in High Altitude Plumes

For the high altitude case we assume that the plume is expanding into vacuum, that the chemistry is frozen and make a constant $\gamma = 1.33$ assumption for the gas (frozen vibration, 3 degrees of freedom for rotation of H_2O).

TABLE 10. PLUME CONDITIONS

M_e	A_e cm^2	u_e cm/sec	T_e °K	ρ_e g/cm^3	P_e atm	Z_e	I sec
High Altitude Plume							
4.45	1.5×10^4	7.6×10^5	3000	2.8×10^{-6}	0.06	1.6	760
Low Altitude Plume							
3.17	1.78×10^3	6.48×10^5	3600	3.2×10^{-5}	1	1.9	650

The structure of highly under expanded jets has been investigated by many authors[31] and we summarize the results relevant to this research below. The jet geometry is shown in Figure 92. Sufficiently far away from the nozzle the flow is practically radial and the density varies as r^{-2}. Also at a given radial position the density varies as $[\cos (\frac{\pi}{2}\frac{\theta}{\theta_\infty})]^{2/(\gamma - 1)}$ where θ_∞ is the Prandtl Mayer expansion angle and θ the polar angle with respect to the axis of the vehicle. The results quoted above do not take into account the effect of condensation. Since the enthalpy of condensation (11 kcal/mole $\approx$ 3×10^3 J/g) is ten times less than the kinetic energy of the expanding plume $(u_e^2/2 \simeq 3 \times 10^4$ J/g) we expect that condensation will affect the flow in a negligible way.

(1) Study of Condensation and its Effect on Laser Propagation

The characteristic time in our system is $\tau = \sqrt{A_e}/u_e \simeq 10^{-4}$ sec and condensation will start occurring when the condensation rate is high enough so that an appreciable fraction of the flow would condense over the time τ.

The rate of formation of condensation nuclei of critical radius r^*, following condensation theory, is given by

$$J = \frac{\Gamma}{\rho_w} \frac{\rho^2}{\mu^2} \left(\frac{2\mu\sigma}{\pi}\right)^{1/2} X \exp\left[-\frac{4\pi(r^*)^2\sigma}{3 kT}\right] \text{ nuclei cm}^{-3} \text{ sec}^{-1} \qquad (392)$$

where ρ_w is the density of condensed phase (1 g/cc), σ is the surface tension for ice (96 dyne/cm) and where the critical radius of a condensation nucleus is related to the supersaturation ratio as follows

---

(31) H. Ashkenas and F. Sherman in Experimental Methods in Rarefied Gasdynamics, J. H. de Leeuw, Academic Press, New York (1966) Vol. 2, p. 84; F. Albini, AIAA J., 3, 1535 (1965); F. Boynton, AIAA J., 5, 1703 (1967).
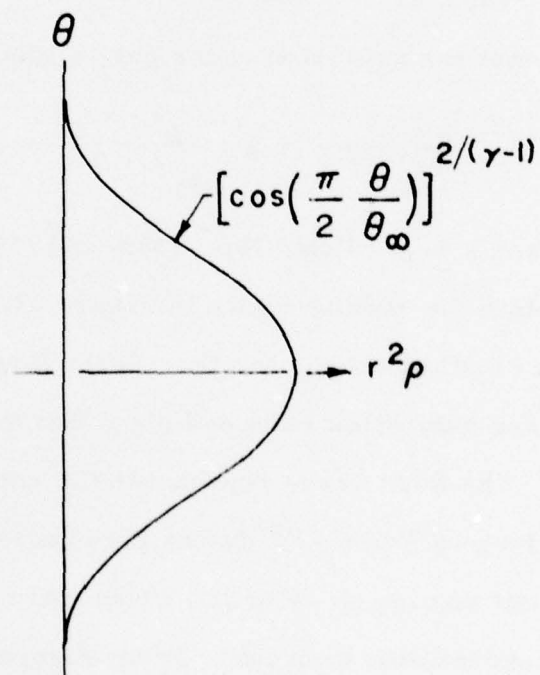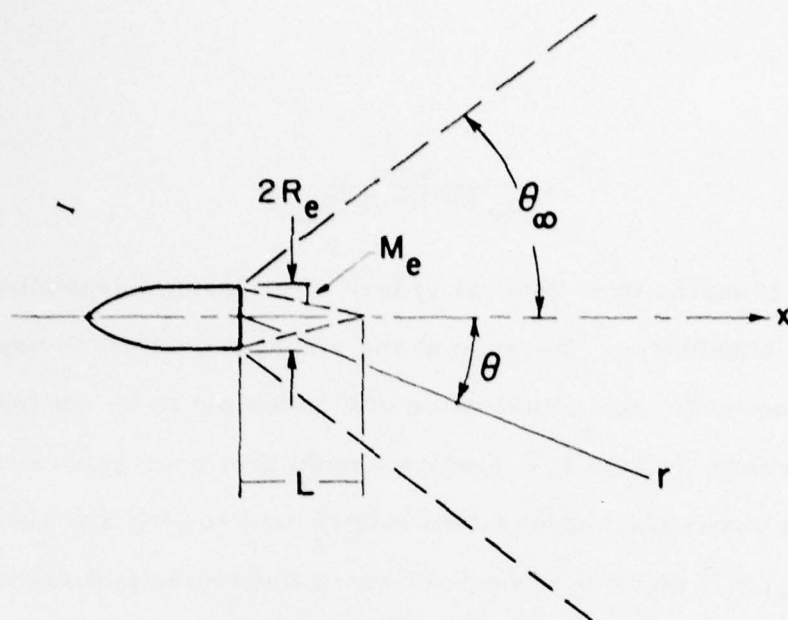
G5791

Figure 92   Geometry for Jet Expansion Into Vacuum

149

$$r^* = \frac{2\mu\sigma}{\rho_w \, kT \, \ell n \, (p/p_{sat})} \qquad (393)$$

The factor Γ varies over several orders of magnitude depending on the nucleation theory considered. Because of the strong temperature dependence of the exponent, however, the actual value of Γ turns out to be not too important. In our calculations we take $\Gamma = 1$ which should be a good approximation for water vapor. We obtain the condensation rate by multiplying Eq. (392) by the factor $4\pi/3 \, (\rho_w/\mu) \, r^{*3}$ which is number of water molecules in a critical condensation nucleus. The saturated vapor pressure of ice is approximately given by

$$p_{sat} = 4 \times 10^7 \, \exp \, (-6170/T) \, \text{atm} \qquad (394)$$

Assuming that the expansion of the gas is adiabatic, i.e.,

$$\frac{p\rho^{-\gamma}}{p_e \rho_e^{-\gamma}} = 1 = \frac{\rho^{1-\gamma} T}{\rho_e^{1-\gamma} T_e} \qquad (395)$$

we can relate T and p to ρ. Using Eqs. (392) and (393) and the exit condition of Table 10 we obtain the results shown in Figure 93. We plotted in Figure 93 three curves as a function of Mach number in the flow. The first two curves are temperature and saturation ratio and show that the flow becomes saturated when $T = 200°K$. The third curve represents the ratio of mass condensed per unit volume [as given by Eq. (392)] during the characteristic time $\tau = \sqrt{A_e}/u_e^*$ to the mass per unit volume ρ. Whenever this ratio reaches a number of order unity we expect condensation to occur. From Figure 93 we see that condensation occurs at $T = 150°K$, i.e., $50°K$ below the saturation temperature. We therefore take $r = r_c$ as the radial position where $T = 150°K$ and $\rho_c = 3.5 \times 10^{-10}$ g/cm^3. In order to make calculations of transmission we assume that all the

---

*More precisely, one should use $\tau = r_c/u_c$, see discussion next page.
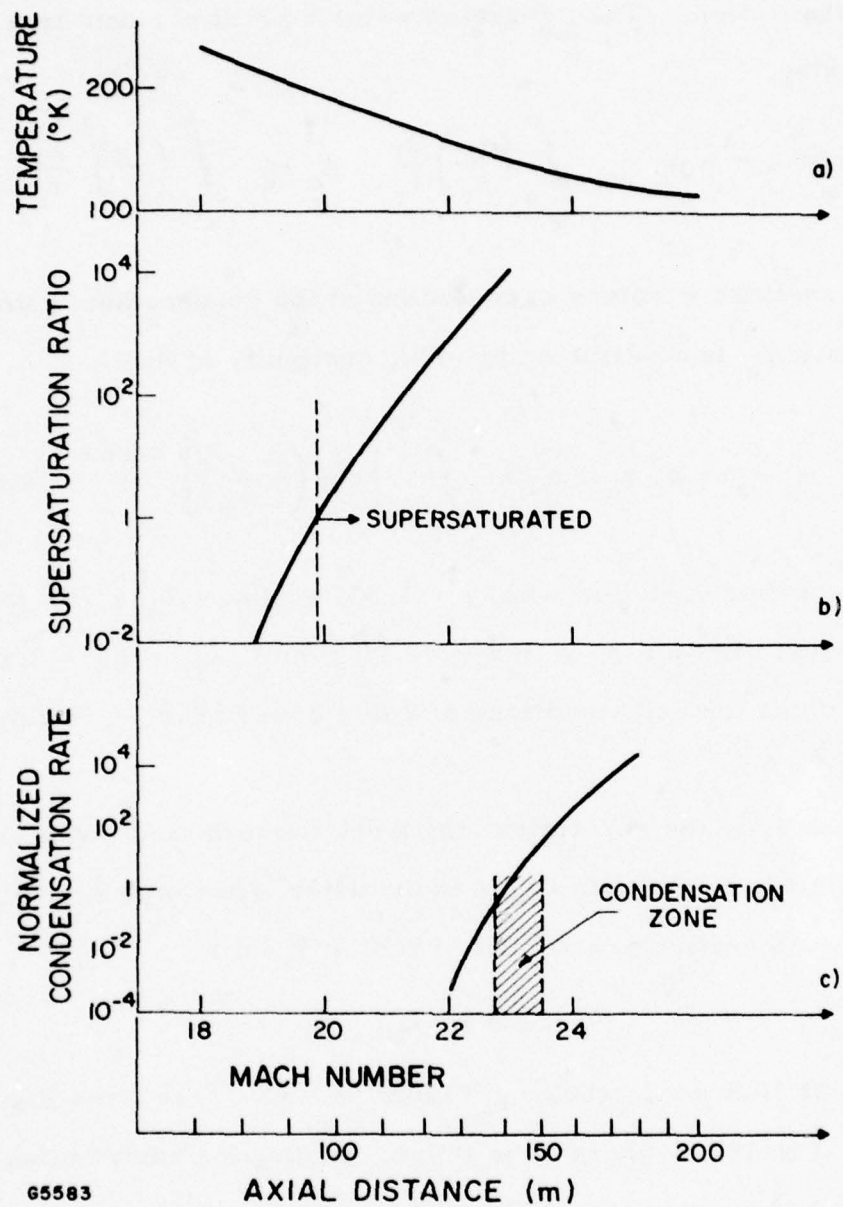
Figure 93   Condensation in High Altitude Plume
a) Temperature vs Mach Number
b) Supersaturation Ratio vs Mach Number
c) Normalized Condensation Rate vs Mach Number

vapor is condensed for $r > r_c$. This should yield an upper bound on absorption by the plume. Absorption will be maximum for a beam traveling along the axis of the vehicle. The integrated water content per unit area along the axis is given by

$$w = \int_{r_c}^{\infty} \rho(r)\, dr = \rho_c\, r_c \int_{r_c}^{\infty} \left(\frac{\rho}{\rho_c}\right) \frac{dr}{r_c} = \rho_c\, r_c \int_{r_c}^{\infty} \left(\frac{r_c}{r}\right)^2 \frac{dr}{r_c} = \rho_c\, r_c$$

where the subscript c refers to conditions at the condensation point. The radial distance r_e is determined by using continuity of flow

$$\rho_e\, u_e\, A_e = \rho_c\, u_c\, \pi\, r^2 \times \int_{0}^{\pi/2} \left[\cos\left(\frac{\pi}{2}\frac{\theta}{\theta_\infty}\right)\right]^{2/(\gamma-1)} \sin\theta\, d\theta$$

For a Mach number 4.45 flow with $\gamma = 1.33$, we have $\theta_\infty = 69^\circ$ and the integral is 0.08. Letting $\rho_c = 3.5 \times 10^{-10}$ g/cm^3, $u_c \simeq u_e = 7.6 \times 10^5$ cm/sec and using the exit conditions of Table 8 we find $r_c = 140$ m and $w = 5 \times 10^{-6}$ g/cm^2.

We calculate the absorption length due to condensed water assuming that all droplets are less than 10 μm in diameter[*] (Rayleigh region). The absorption cross section per droplet of radius R is:

$$\sigma = \pi R^2 Q_{abs}$$

where Q_{abs} at 10.6 μm is shown in Figure 94. One sees from Figure 94 that $Q_{abs} = 3 \times 10^2 R$ where R is in cm. Adding the contribution of all particle j in a unit volume we obtain the absorption coefficient a

$$a = 3 \times 10^2 \sum_j \pi R_j^3 = \frac{3}{4\pi} \frac{3 \times 10^2}{\rho_c} \sum_j \frac{4\pi}{3} R_j^3 \rho_c$$

$$= 70\, \rho \quad \text{cm}^{-1} \tag{396}$$

where ρ_c = density of water (= 1 g/cm^3) and ρ is the mass concentration of water in g/cm^3.

---

[*] This assumption will give maximum absorption.
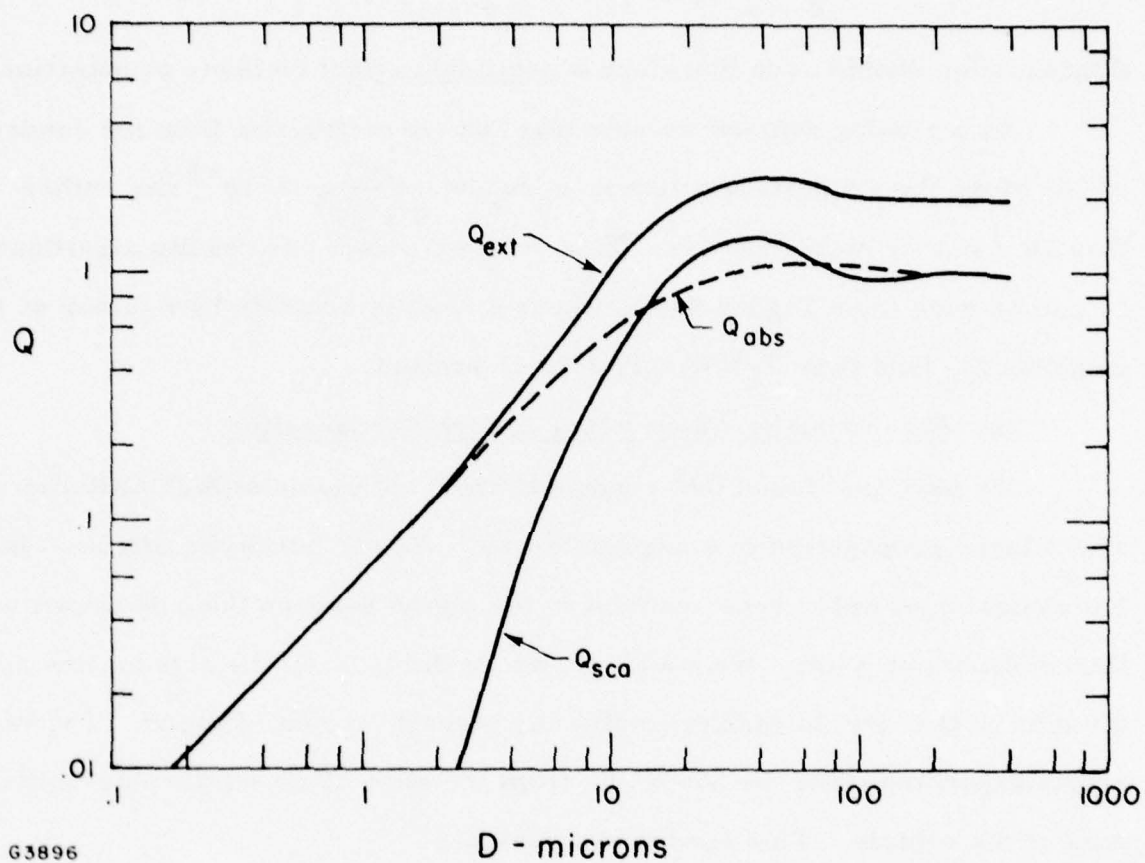
Figure 94   Calculated Mie Efficiency for Water Droplets

G3896

The transmissivity of the condensed part of the plume to a 10.6 μm laser beam traveling along the axis is thus

$$T = e^{-70 \, W} = 1 - 3.5 \times 10^{-4} \simeq 1$$

Condensation should have therefore a negligible effect on laser propagation.

As a closing remark we note than the characteristic time for condensation along the axial stream line is $r_c/u_c \simeq \dfrac{10^4}{8 \times 10^5} \approx 10^{-2}$ sec rather than 10^{-4} sec or stated earlier. This does not effect our results significantly, as can be seen from Figure 93(c), where a shift in ordinate by a factor of 10^2 modifies M_c (and thus T_c) by only a small amount.

(2) Absorption by Water Vapor Before Condensation

We have just found that condensation in the plume at high altitudes will affect laser propagation in a negligible way. We now study the effect on laser transmission of water vapor content in the plume between the exit nozzle and the condensation point. We consider, as we did before, the stream line along the axis of the vehicle which contains the largest amount of vapor. The vapor starts expanding when the Mach line from the edge of the nozzle intersects the axis of the vehicle. This occurs at a distance.

$$L = R \, M_e$$

We thus have $T = T_e$ and $\rho = \rho_e$ for $x < L$. For $x > L$ we approximate the flow field by

$$\rho(x) = \rho_e \frac{L^2}{(x - L)^2 + L^2} \tag{397}$$

and use the isentropic relation (394) to calculate T and p. We can then calculate absorption due to high temperature lines of H_2O by use of Eq. (397). We have calculated the transmission through the plume given by

154

$$T = \left[\exp - \int_0^{x_c} \alpha \, dx \right]$$

in the following two cases.

(a) Frozen Vibration, Frozen Chemistry

Let the absorption coefficient $\alpha = \alpha_e$ at the exit nozzle. Then at a location x the absorption coefficient is

$$\alpha(x) = \alpha_e \left(\frac{P(x)}{P_e} \right)^2 \left(\frac{T_e}{T(x)} \right)^3 = \alpha_e \left(\frac{\rho}{\rho_e} \right)^{3-\gamma}$$

We have

$$\int_0^{x_c} \alpha \, dx = \int_0^{L} \alpha_e \, dx + \int_L^{x_c} \alpha \, dx$$

$$= \alpha_e L + \alpha_e L \int_1^{x_c/L} \frac{d(x/L)}{[(x/L - 1)^2 + 1]^{3-\gamma}} \simeq 2 \alpha_e L$$

where in the last step we made $x_c \to \infty$ and assumed $3 - \gamma = 1.5$.

(b) Equilibrium Vibration, Frozen Chemistry

$$\int \alpha \, dx = \alpha_e L + \frac{\alpha_e L}{2[1 - \exp(-\theta/T_e)]} \int_{T_c/T_e}^{1} dt \sqrt{\frac{t}{1-t}} \, t^{1-\gamma} \exp\left[-\frac{\epsilon}{kT_e}(t^{1-\gamma} - 1) \right]$$

$$\times \left[1 - \exp(-\theta t^{1-\gamma}) \right]$$

Numerical integration of the integral for $T_c \ll T_e$, $\gamma = 1.33$ and $T_e = 3000^\circ K$ yields a value of 0.78.

$$\int \alpha \, dx = \alpha_e L \left\{ 1 + \frac{0.78}{2(1 - \exp - \theta/T_e)} \right\} = 1.88 \, \alpha_e L$$

The above result is for all practical purposes, the same as for frozen vibration.

155

We evaluate the absorption for the P(20) line of CO_2. We have

$$L = R M_e = \sqrt{\frac{1.5 \times 10^4}{\pi}} \times 4.5 = 300 \text{ cm}$$

$$a_e = \frac{5.6 \times 10^7}{(3000)^3} \times (0.06)^2 \times \exp\left(-\frac{3330}{3000}\right)\left(1 - \exp -\frac{2890}{3000}\right) = 1.5 \times 10^{-6} \text{ cm}^{-1}$$

Thus $a_e L = 4.5 \times 10^{-4}$ and absorption by water vapor is negligible.

d. Absorption and Condensation in Lower Altitude Plumes

At low altitudes the external pressure prevents the jet of vapor from expanding freely and cooling of the jet arises from entrainment of and mixing with the ambient air. The cooling of the jet and possible condensation depends on a) the amount of air entrained, b) the ambient temperature, and c) on the degree of recombination of the partially dissociated water vapor.

We have used a three dimensional axisymmetric computer code which numerically solves mass, momentum, enthalpy and species conservation equations using turbulent diffusivity and finite rate chemistry. The results of two runs at 20 km altitude (p = 0.06) and sea level (p = 1 atm) were made and will be discussed.

(1) Condensation of Water Vapor in Plumes

Before presenting results of the computer runs, we first discuss the possibility of condensation in the plume and show from general energy considerations that condensation is unlikely to occur if the air temperature is larger than $\simeq 230^\circ K$.

Consider a mass m_p of plume material that entrains a much larger mass m_a of air. Assume that the exit pressure is the same as the ambient pressure p_0. Conservation of momentum and energy yields

156

$$m_p u_e = (m_a + m_p) u \tag{398}$$

$$m_p (h_e + \tfrac{1}{2} u_e^2) + m_a h_a (T_o) = m_p h_p (T) + m_a h_a (T) + \tfrac{1}{2} (m_p + m_a) u^2. \tag{399}$$

We assumed in the above that the air was at rest and that the vehicle velocity is much less than u_e, so that the relative velocity of the plume with respect to the air is u_e. T_o is the ambient temperature and T is the temperature of the final mixture. Eliminating u between Eqs. (398) and (399) yields

$$h_e + \tfrac{1}{2} u_e^2 - h_p (T) = \left(\frac{1 - \psi_p}{\psi_p} \right) \frac{\mu_a}{\mu_p} C_{pa} \Delta T + \tfrac{1}{2} u_e^2 \frac{\psi_p}{\psi_p + (1 - \psi_p) \frac{\mu_a}{\mu_p}} \tag{400}$$

where $\Delta T = T - T_o$ is the temperature rise of the air, C_{pa} is the specific heat of air, ψ_p is the molar concentration of the plume constituents in the mixture, and μ_a and μ_p are the molecular weights of air and plume material respectively. For mixtures in which $T \simeq T_o$ we can neglect $h_p (T)$ as compared to the stagnation enthalpy $h_e + \tfrac{1}{2} u_e^2$, and, as we shall see later, we can neglect the second term on the right hand side of Eq. (400). We therefore have

$$h_s = h_e + \tfrac{1}{2} u_e^2 = \frac{(1 - \psi_p)}{\psi_p} \frac{\mu_a}{\mu_p} C_{pa} \Delta T$$

Assuming that recombination is complete and $\psi_p \ll 1$, we have

$$p_{H_2O} = \frac{\mu_a}{\mu_{H_2O}} \frac{C_{pa} \Delta T}{h_s} P_o \tag{401}$$

Condensation will occur only when

$$p_{H_2O} \gtrsim P_{sat} \tag{402}$$

157

Where p_{sat} is given by Eq. (395)

$$p_{sat} = B e^{-\theta/T} \begin{cases} B = 4 \times 10^7 \text{ atm} \\ \theta = 6170^{\circ}K \end{cases} \tag{403}$$

We write $T = T_o + \Delta T$ with $\Delta T \ll T_p$ and expand the exponent in Eq. (394). We look for conditions under which inequality (402) is just satisfied. This will yield the temperature T and concentration ψ_p at which condensation may (if the time scale is long enough) just occur. Using Eqs. (401) and (394), Equality (402) gives

$$y e^{-y} = \mu_{H_2O} \frac{h_s B}{\mu_a C_{pa}} \frac{\theta}{T_o^2} \frac{e^{-\theta/T_o}}{p_o} \tag{404}$$

where we defined $\Delta T \theta/T_o^2 = y$. Now, the left hand side of Eq. (398) has a maximum at $y = 1$ of $e^{-1} = 0.37$. If T_o is so large as to make the right hand side of (404) larger than 0.37 then there is no solution and condensation will not occur. We thus write the condition for any condensation to occur as

$$\frac{\mu_{H_2O} h_s B}{\mu_a C_{pa}} \frac{\theta}{T_o^2} \frac{e^{-\theta/T_o}}{p_o} < 0.37 \tag{405}$$

We discuss the range of validity of Ineq. (405), or rather Eq. (404) from which it was derived. We assumed that h_s represents the stagnation enthalpy of the plume. If the chemistry is slow (i.e., recombination is incomplete) and radiation losses are important, one should subtract from h_s the amount of energy remaining in dissociation and the energy per unit mass lost by radiation. In order to take into account the dissociation remaining, the right hand side of Eq. (404) should be multiplied by $1/f$ where f is the fraction of H_2O ($f = 1$ if recombination is complete). The computer runs

158

that we have made at p = 0.06 atm indicate that less than 25% of the initial enthalpy of dissociation remains when a significant amount of air has been entrained. Also, under the times of interest (t < 0.1 sec) we have found that losses by radiation are insignificant.

The air temperature for which inequality (405) is satisfied is shown in Figure 95. In order to plot the boundaries in Figure 95 we used T_e = 3000°K, u_e = 7.6×10^5 cm/sec, h_s = 5.3×10^4 J/g, C_{pa} = 1 J/g$^{\circ}$K, μ_a/μ_{H_2O} = $29/18$ = 1.6. Several boundaries are indicated in Figure 95, corresponding to enthalpy available to heat the gas being 100%, 50%, or 20% of the initial stagnation enthalpy.

The temperature rise of the air when condensation occurs is ΔT = $y\, T_o^2/\theta$ where y is the solution of Eq. (404). The maximum rise in temperature corresponds to the maximum value of y, namely y = 1. Therefore,

$$(\Delta T)_{max} \simeq \frac{T_o^2}{\theta} \frac{(200)^2}{6170} = 6^{\circ}K$$

The partial pressure of H_2O at condensation is also a maximum when y = 1. From Figure 95 one would expect condensation to occur in a small altitude range around 12 km where p_o = 0.2 atm, T_o = 220°K. The concentration of condensed and uncondensed water under the above conditions would be

$$\rho = (\rho_{air})_{STP} \frac{273}{T} \frac{18g}{29g} \times B \exp(-\theta/T)$$

$$= 1.2 \times 10^{-3} \frac{273}{226} \times \frac{1}{1.6} \times 4 \times 10^7 \exp - (6170/226)$$

$$= 5 \times 10^{-8} \text{ g/cm}^3.$$

The absorption coefficient at 10.6 μm due to condensed water is given by Eq. (396) and will be at the most 3.5×10^{-6} cm^{-1}. We can neglect the

159
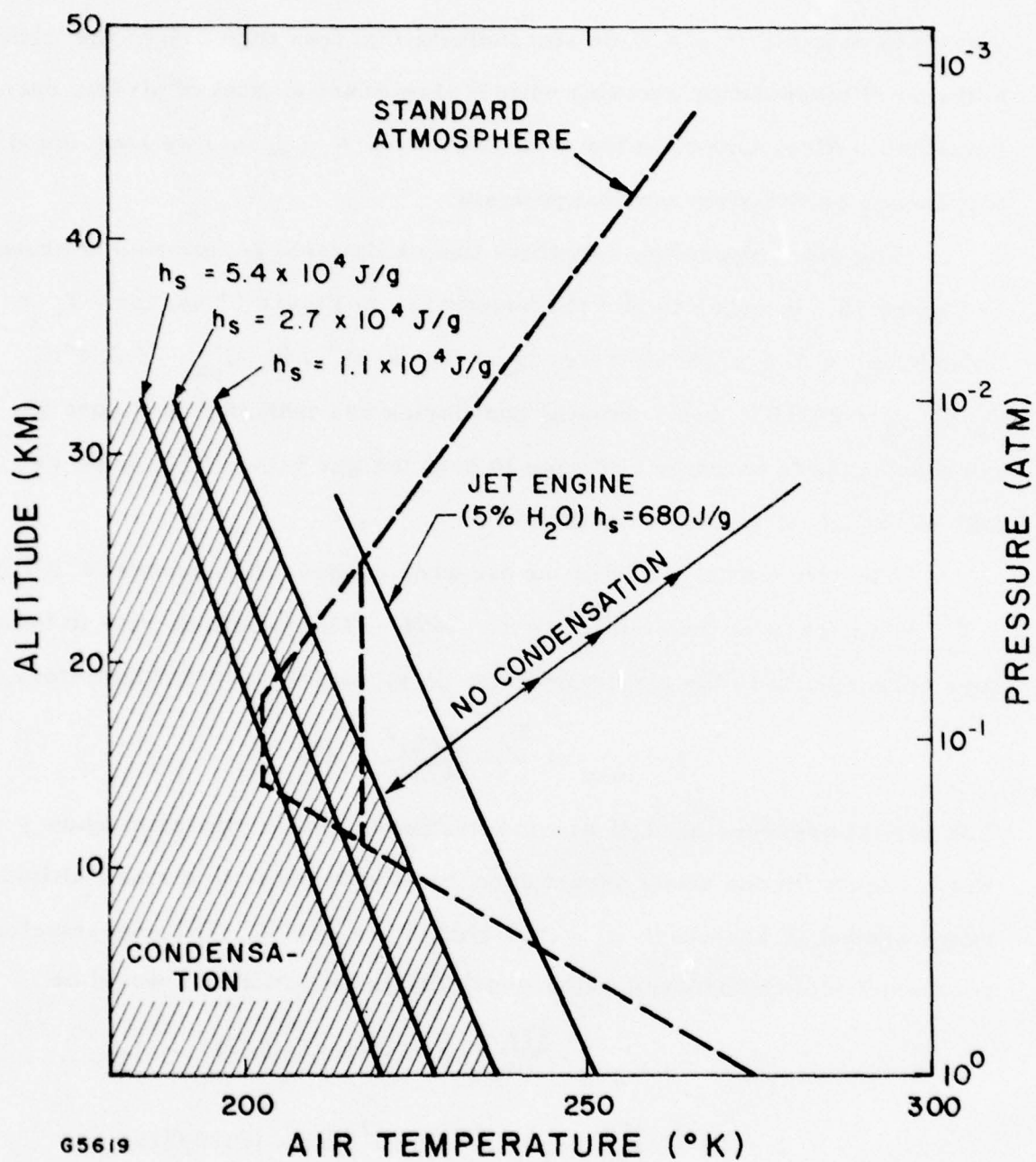
Figure 95   Map for Plume Condensation vs Altitude

160

effect of condensed water on laser propagation, therefore, unless we are dealing with path lengths through condensed zones in excess of 1 km. We can now show that the neglect of the second term on the right hand side of Eq. (400) as compared to the first one was justified. Since $\psi_p \ll$ the neglect of the second term on the right hand side of Eq. (400) is justified if

$$\psi_p^2 = \left(\frac{P_{H_2O}}{P_{air}}\right)^2 \ll 2\left(\frac{\mu_a}{\mu_p}\right)^2 \frac{C_{pa}\,\Delta T}{u_e^2} \tag{406}$$

we have

$$\left(\frac{P_{H_2O}}{P_{air}}\right)^2 \simeq \left(\frac{4 \times 10^7\, e^{-6170/230}}{0.2}\right)^2 = 2 \times 10^{-7}$$

while

$$2\left(\frac{\mu_a}{\mu_p}\right)^2 \frac{C_{pa}\,\Delta T}{u_e} = 2 \times (1.6)^2 \times \frac{10^7 \times 6}{(8 \times 10^5)^2} = 5 \times 10^{-4}$$

Inequality (406) is therefore well satisfied.

(2) Plume at 20 km Altitude

The results of the three dimensional code for a plume with the exit conditions given by the first line of Table 10 are shown in Figure 96. The ambient air temperature is T_o. The contours of constant H_2O concentration are found to follow the contours of constant temperature as is to be expected. The computer run was lengthy and the results of 5 hours computation on a CDC 3174 led to a down stream distance of 80 exit diameters (x = 100 meters). Contours beyond this distance were extrapolated.

The temperature and concentration of H_2O along the axis of the plume are shown in Figure 97. Since the self broadening of H_2O is (roughly) five times larger than broadening due to collisions with air molecules, [32] we compute the absorption coefficient as follows:

(32) Burch, D., Singleton, E., and Williams, D., Appl. Optics 1, 359 (1962).

161
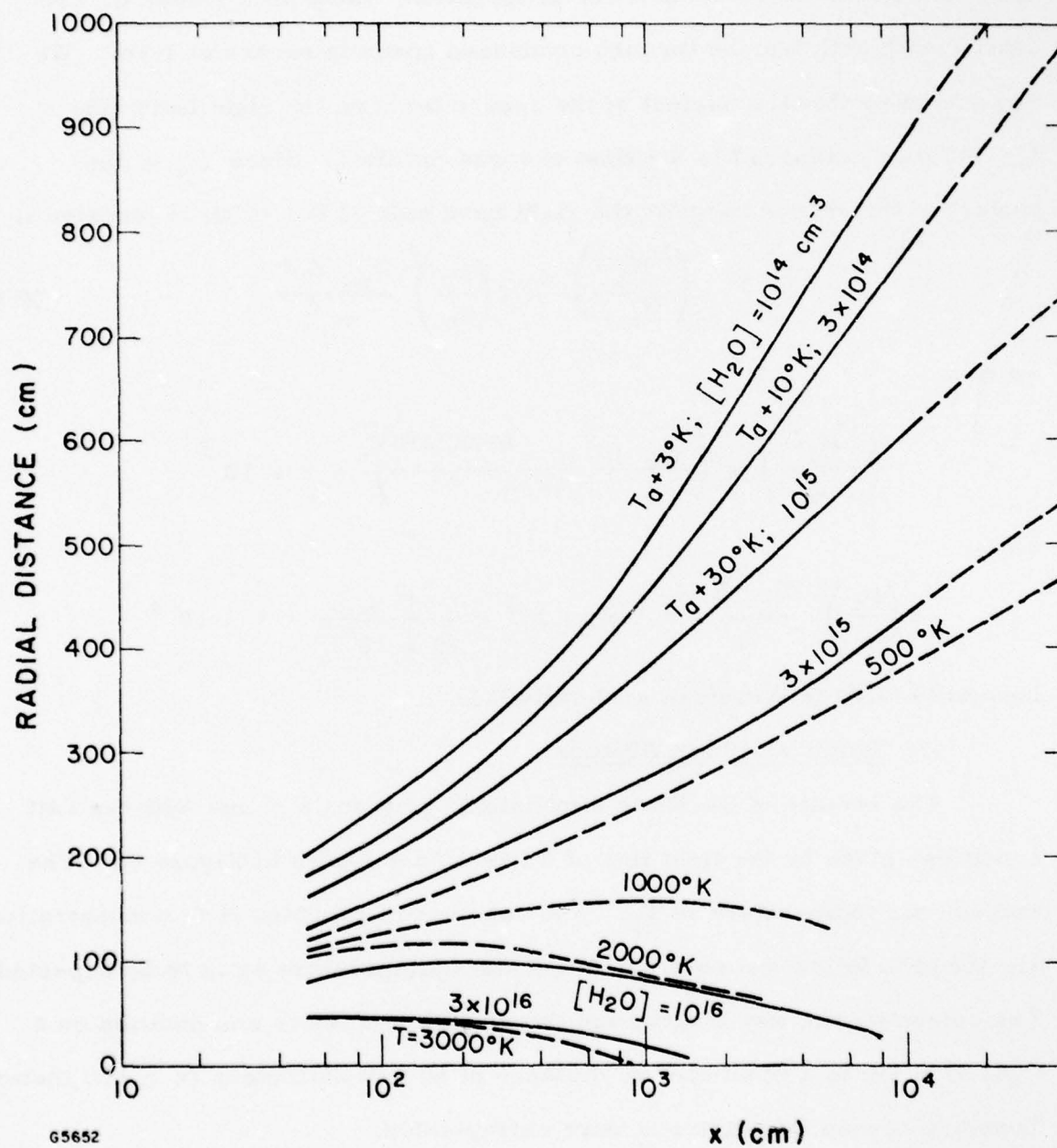
Figure 96   Plume Profile at 20 km Altitude

162
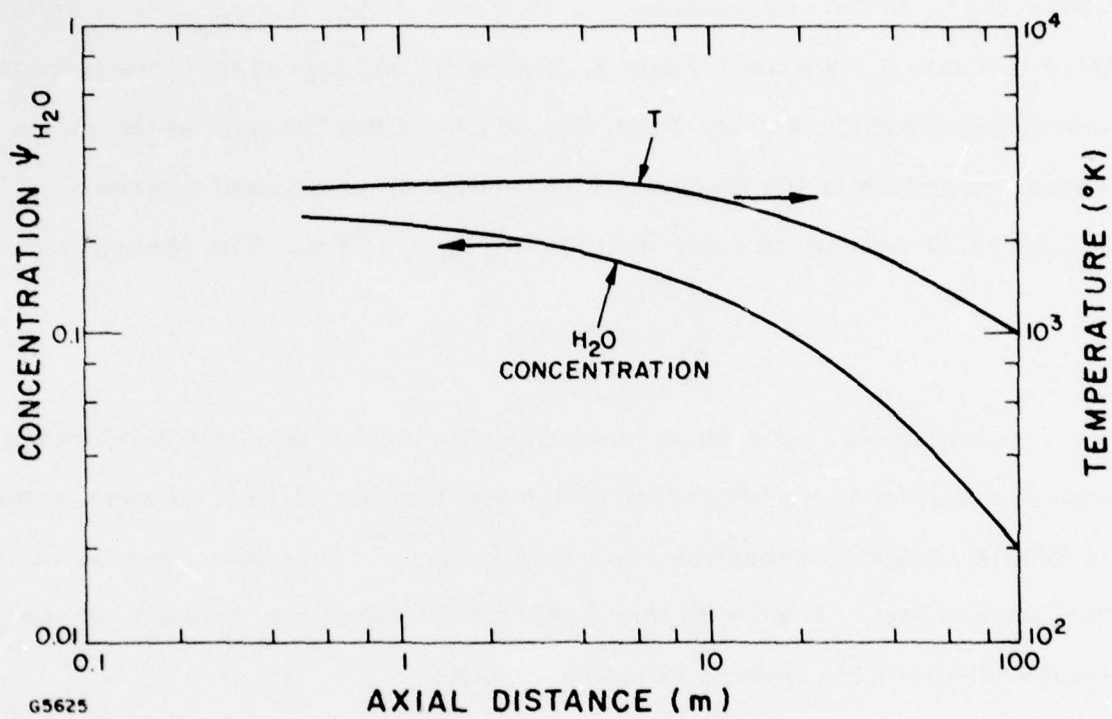
Figure 97   Temperature and H_2O Concentration Atoms Axis
at 10 km Altitude

$$\alpha \left(p_o, \ T, \ \psi_{H_2O} \right) = \alpha \left(p_o, \ T, \ \psi_{H_2O} = 1 \right) \psi_{H_2O} \left[\psi_{H_2O} + \frac{1 - \psi_{H_2O}}{5} \right] \quad (407)$$

where ψ_{H_2O} is the concentration of H_2O and $\alpha \left(p_o, \ T, \ \psi_{H_2O} = 1 \right)$ is tabulated in Table 2. We used Table 9, Figure 97 and Eq. (407) to evaluate the absorption coefficient to the P(20) line of CO_2 along the axis of the plume where absorption is the largest. The absorption coefficient is shown in Figure 98 as well as its integral up to $\psi_{H_2O} = 100$ m. The absorption

$$\int_0^{100} \alpha \ dx = 4 \times 10^{-4}$$

i.e., is negligible. One should keep in mind that we used the McClatchey tape to compute water vapor absorption and that broad-band measurements at $2000^\circ K$ indicate absorption 100 times larger[28] than that given by the McClatchey tape. Even with this factor of 100 taken into account, absorption over a length of 100 meters of plume is small.

In spite of the fact that we have calculated a very small absorption coefficient, absorption may still be significant if the laser is directed straight up the axis of the vehicle and has to traverse the whole length of the plume which may be quite long. One could eliminate these very long paths by requiring a small tilt ($\sim 1-5^\circ$) of the vehicle with respect to the laser beam. Also, the presence of a transverse wind, which usually exists at high altitudes, will cause a bending of the plume and shorten the path length. We consider below the effect of such a transverse wind.

Assume that the axial plume velocity is U and that the transverse wind velocity is W. Consider a unit axial length of plume material. The equation of motion for the transverse velocity V of this element of plume is:

164

G5626
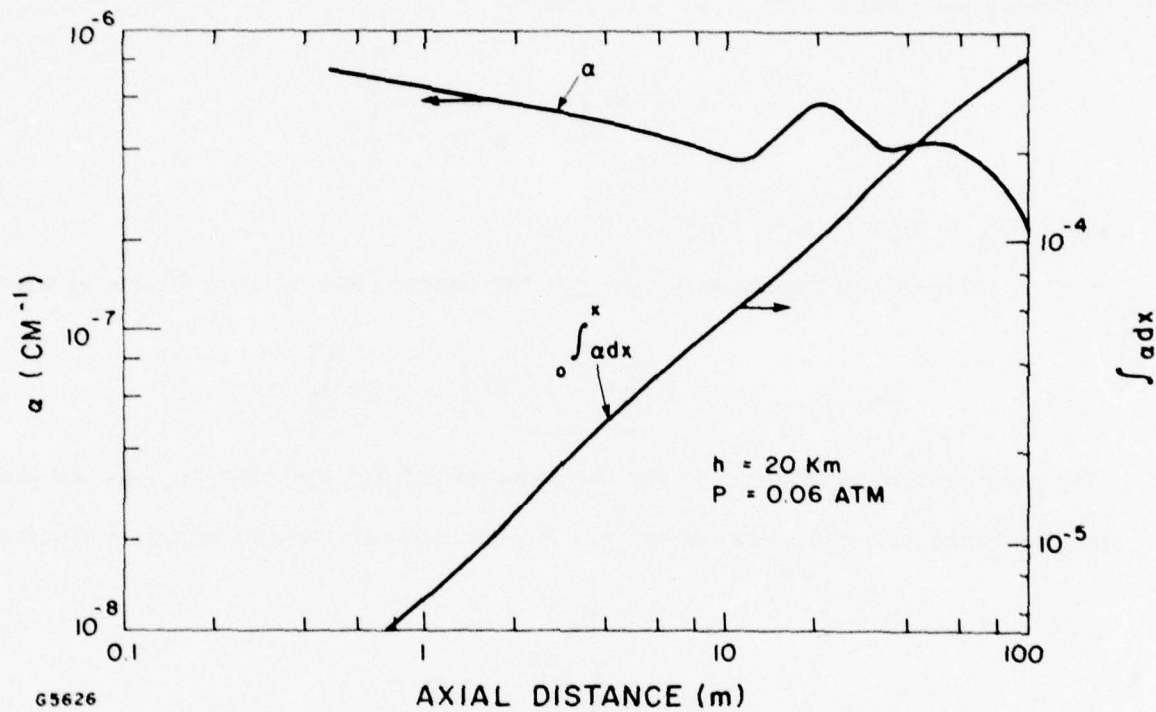
Figure 98   Absorption by 20 km Altitude Plume for Axial Path

165

$$\pi \ \rho_p \ \frac{D^2}{4} \ \frac{dV}{dt} \ = \ C \ \rho_a \ (V \ - \ W)^2 \ \frac{D}{2}$$

where C is a drag coefficient of order 1. Integration from 0 to t, with the boundary condition V (t = 0) = 0, yields

$$V \ = \ W \left[1 \ - \ \frac{1}{1 + \dfrac{t}{t_o}} \right]$$

where $t_o = \rho_p \ \pi \ D/(2 \ C \ W \rho_a)$.

Integrating once again, we get the transverse y coordinate of the

$$y \ = \ W \left[t \ - \ t_o \ \ln \left(1 \ + \ \frac{t}{t_o} \right) \right] \tag{408}$$

We have plotted in Figure 99 the velocity of a fluid element on axis as given by the computer run, versus time. A good approximation to this velocity is

$$u \ = \ u_e \qquad t \ < \ \tau$$
$$u \ = \ u_e \left(\frac{\tau}{t} \right)^a \qquad t \ > \ \tau \tag{409}$$

where $u_e = 7.6 \times 10^5$ cm sec, $\tau = 5.5 \times 10^{-4}$ sec, a = 0.43.

Integration over time yields the axial position

$$x \ = \ u_e \qquad t \ < \ \tau$$
$$x \ = \ \frac{u_e}{1 \ - \ a} \left[- \ a \ \tau \ + \ t \left(\frac{\tau}{t} \right)^a \right] \qquad t \ \gtrless \ \tau \tag{410}$$

Using the above expressions for x and y we have plotted in Figure 100 the position of a laser beam with respect to the plume when the laser beam is pointed straight up the axis of the vehicle and the plume is submitted to a cross-wind of velocity W = 10^3 cm/sec. We chose in the numerical calculations D = 120 cm, $\rho_a = 8 \times 10^{-5}$ g/cc, $\rho_p = \rho_e = 2.8 \times 10^{-6}$ g/cm^3,

166
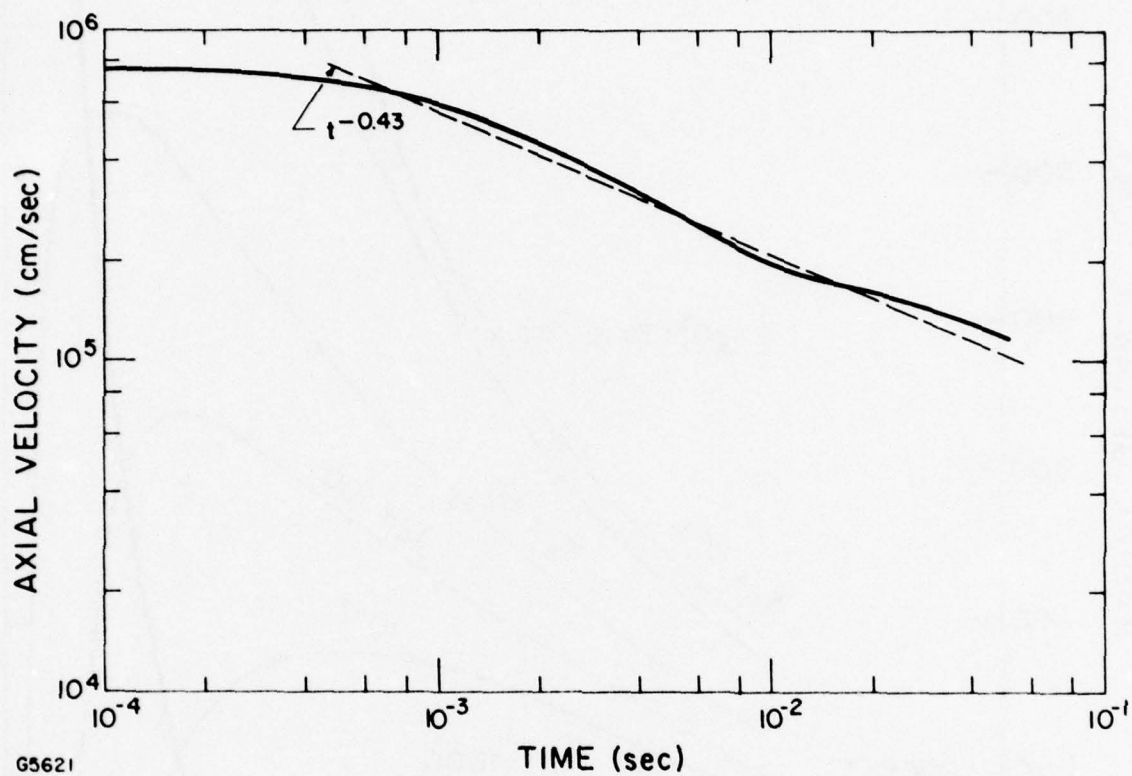
Figure 99   Velocity Along Axis of Plume at 20 km Altitude
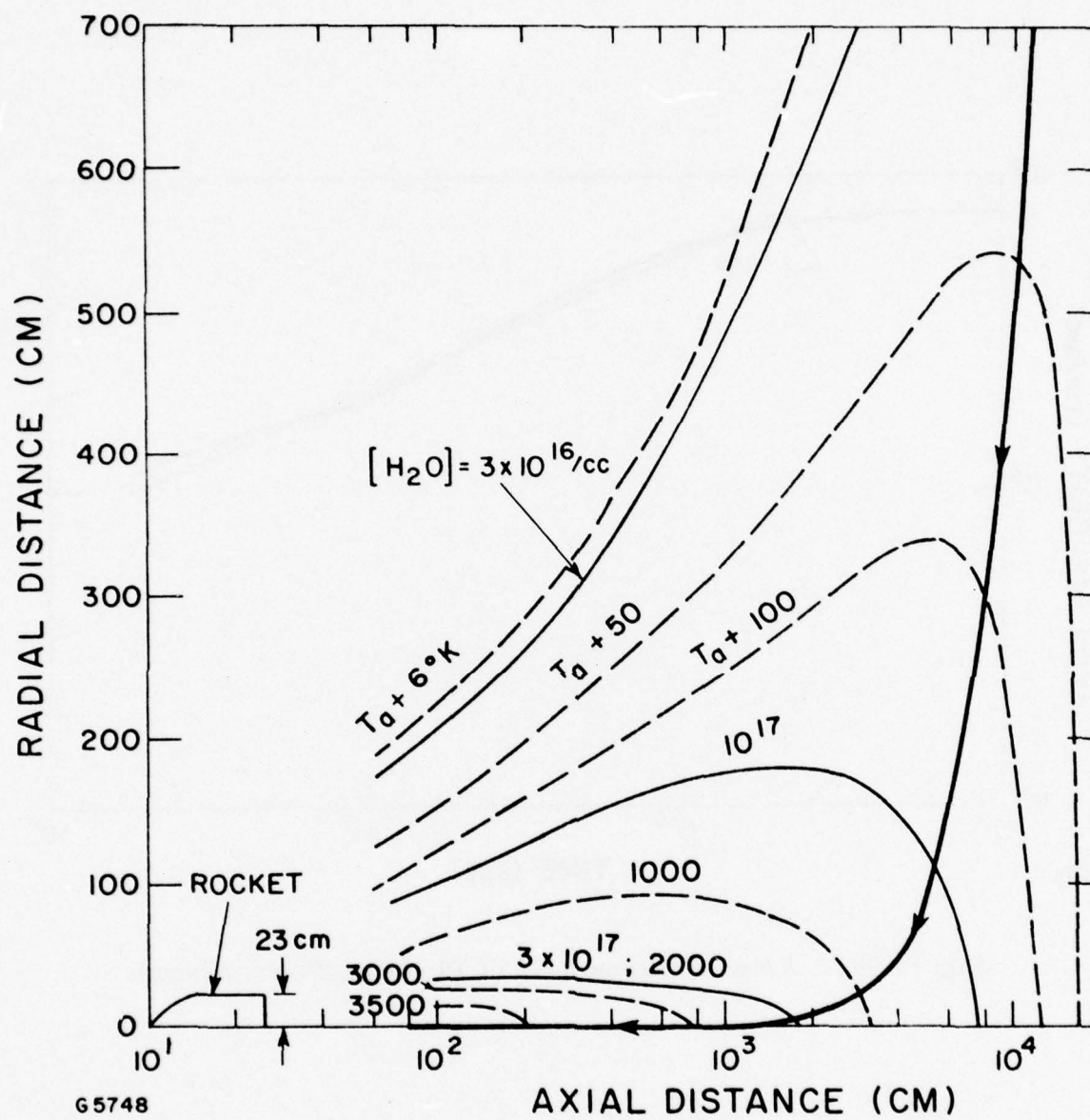
Figure 100   Plume Profile at Sea Level

168

$C = 1$, resulting in $t_o = 6.6 \times 10^{-3}$ sec. The laser beam under such conditions traverses only a section of plume 300-400 meters long. The absorption would be at most 8×10^{-4} if we use the results of Figure 98.

(3) Plume at Sea Level

Finite rate chemistry could not be included in the plume entrainment program at low altitudes because the chemistry is too fast and the axial step size required in order to follow accurately the chemistry would require excessively long computer times. We therefore ran the program using frozen chemistry. Evaluation of the reaction rate at sea level, however, shows that the chemistry must be near equilibrium. We therefore used the temperature and concentration profiles furnished by the frozen chemistry run and then modified these profiles by calculating the equilibrium concentrations of various constituents, keeping the total enthalpy constant.

The exit composition of the plume was as follows: $\psi_H = 0.25$, $\psi_{OH} = 0.15$, $\psi_{H_2} = 0.15$, $\psi_O = 0.12$, $\psi_{O_2} = 0.06$ and $\psi_{H_2O} = 0.23$. Other parameters can be found in the second line of Table 3. The enthalpy of recombination of the vapor components at $3500^\circ K$ to form one mole of H_2O was calculated from the JANAF tabulations[33] to be 74.13 Kcal. Similarly at $298^\circ K$, the enthalpy of recombination was calculated to be 73.4 Kcal/mole of H_2O. It is reasonable to assume that the enthalpy of reaction should be fairly constant over the whole range of temperature encountered. For final temperatures below $2000^\circ K$ practically all of the plume material should be recombined into H_2O. The plume program that we used allows for cooling and heating of all components at constant total enthalpy but with frozen chemistry we took the temperature given by the plume program and raised it by an amount

---

(33) JANAF Thermomechanical Tables, Second Edition, U.S. National Bureau of Standards NBS-37, Government Printing Office (1971).

$$\Delta T = \frac{73.4 \, x}{x \, Cp \, (H_2O) + (1 - x) \, Cp \, (air)} \times 10^3 \qquad (411)$$

where x is the fraction of recombined H_2O in the final mixture, and Cp is the specific heat in cal/mole $^\circ$K [Cp $(H_2O) \simeq$ 13 cal/mole $^\circ$K, Cp (air) $\simeq$ 7 cal/mole $^\circ$K]. Equation (411) should be accurate for $T + \Delta T < 2000^\circ$K. At higher temperatures we used air tables and the Mollier diagram (Figure 91) for water vapor since partial dissociation has to be included.

Temperature and water vapor concentration profiles of the low altitude plume are shown in Figure 100. The temperature and water vapor concentration along the axis is shown in Figure 101. Absorption by water vapor for an axial path length was calculated following the procedure outlined in the previous section and is shown in Figure 102. The integrated absorption for an axial path length extending 100 meters from the exit nozzle of the vehicle is found to be 4%. Longer path lengths do not lead to much larger absorption because of the rapid decrease in temperature. The effect of a 10 m/sec cross wind on absorption was considered and is shown in Figure 100. It sould reduce absorption only slightly since most of this absorption occurs in the first 40 meters of plume and the plume is appreciably bent by the wind only beyond 40 m. Basing oneself on the H_2O absorption lines tabulated by McClatchey[29] one would not expect the absorption by the plume to be significant at sea level. The broadband measurements of Ludwig et al.[28] indicate that absorption could be as much as 100 times higher, leading to catastrophic absorption by the plume at sea level. High resolution measurements of H_2O absorption in the region of the CO_2 lines is needed before any firm conclusions can be drawn. If the laser beam is incident at an angle of

170
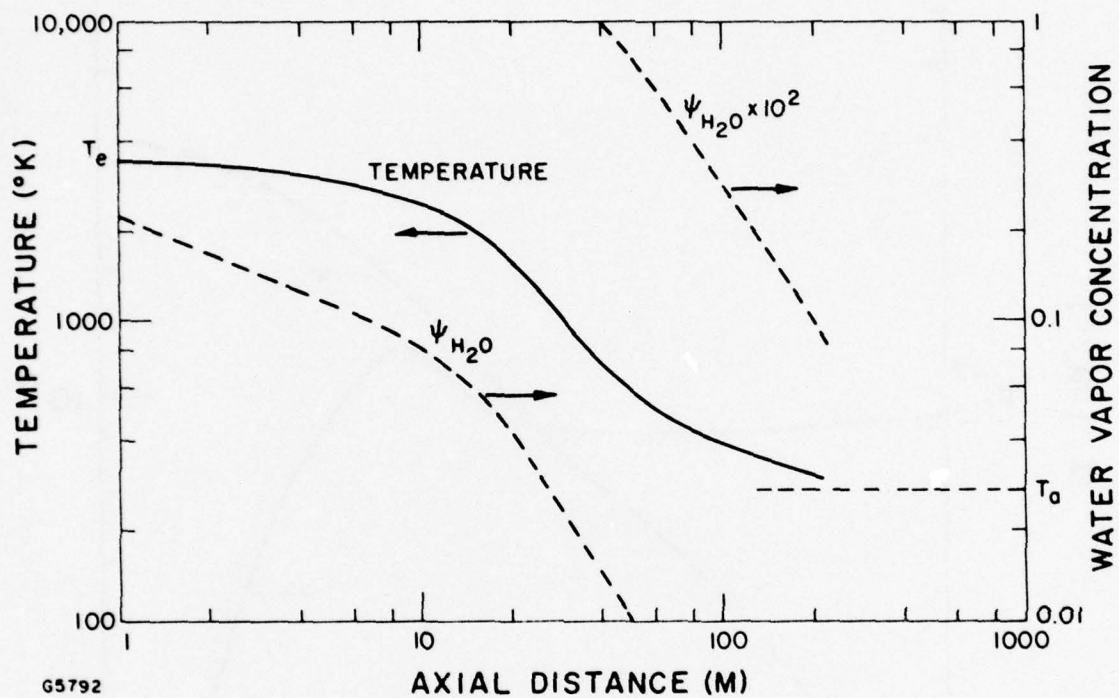
Figure 101   Temperature and H_2O Concentration Along Axis of
Plume at Sea Level

171
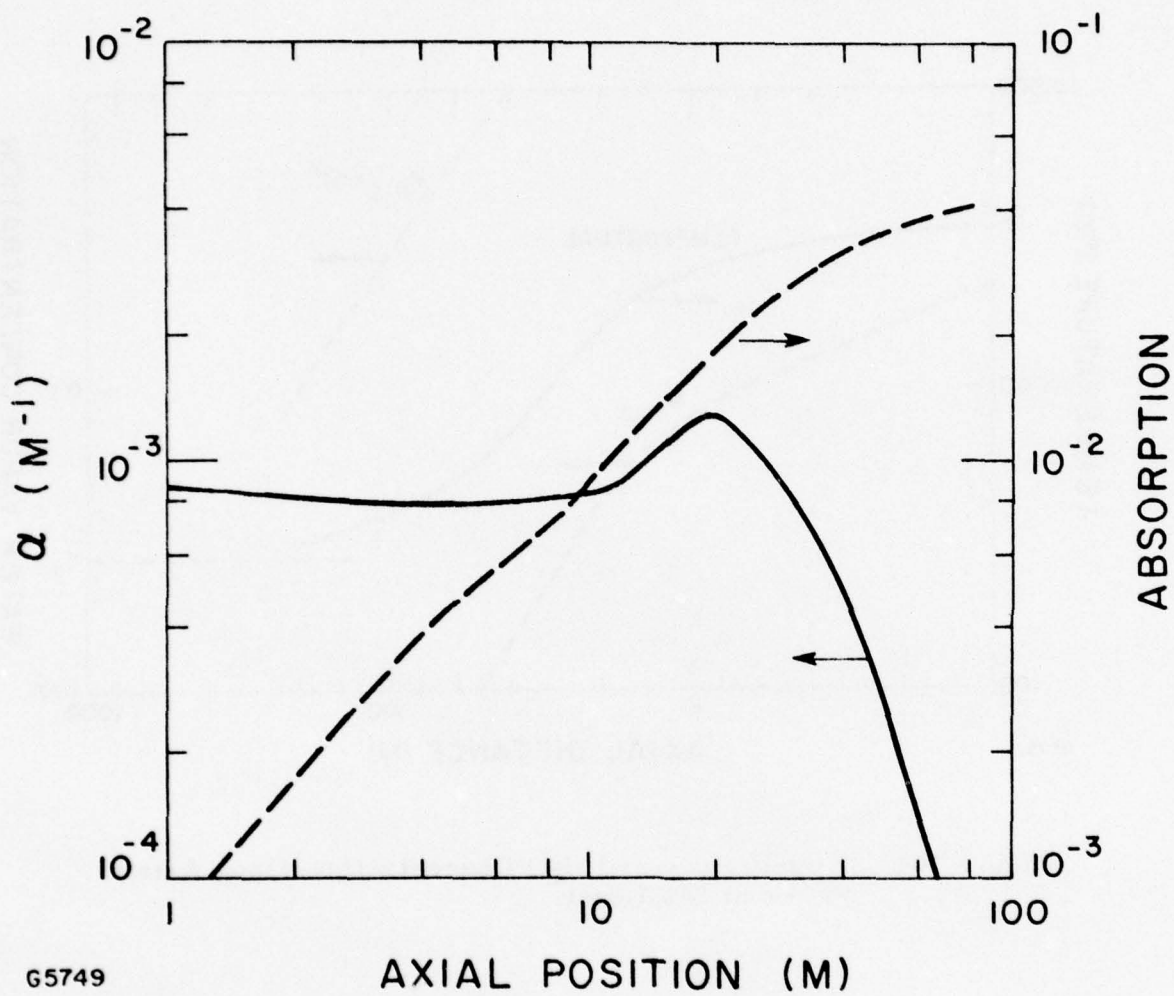
Figure 102   Absorption by Plume at Sea Level for Axial Path

G5749

172

10° with the axis the absorption can be reduced by a factor of 5 to 10, but the absorption, following the measurements of Ref. 28, would still be significant ($\simeq 50\%$).

e. Summary and Conclusions

We have looked at condensation and absorption of CO_2 radiation in water vapor plumes at different altitudes. In the high altitude case the plume was found to exapnd and cool leading to condensation when the temperature was $150^{\circ}K$ ($50^{\circ}K$ below the saturation temperature). Absorption by the condensed H_2O was found to be negligible ($\simeq 10^{-4}$) and absorption by the vapor was also very small. (5×10^{-4} on axis). For intermediate and low altitude plumes where the plume does not expand freely but mixes with the surrounding air it was found that condensation should not occur, except possibly for a small altitude region near 10 km altitude if the ambient temperature is below $\simeq 220^{\circ}K$ (the exact temperature depends on the amount of enthalpy stored in dissociated plume products that have not recombined). Even if the condesation were to occur, the condensed water content would be $\simeq 5 \times 10^{-8}$ g/cm^3, i.e., too small to produce significant absorption.

A three dimensional axisymmetric plume computer code was used to compute temperature and H_2O concentration profiles in water vapor plumes at 20 km altitude and at sea level. Using these profiles we estimated that the effect of H_2O absorption on the P(20) CO_2 laser line propagation. Absorption was found to be negligible at 20 km, (4×10^{-4}) and small at sea level (4%), if one used the H_2O lines tabulated by McClatchey in Ref. 29. Measurements on emissivity of H_2O flame products indicated[28] an absorption 100 times larger than those quoted above, leading us to believe there may well be catastrophic absorption in sea level plumes. The measurements of Ref. 28 are broadband, however, and high resolution transmissivity measurements at the exact location of the CO_2 lines are needed before definite conclusions may be drawn.

173

5. IGNITION OF AIR BREAKDOWN WAVES

Under the high laser fluxes considered, solid aerosols in the atmosphere can heat up, vaporize and act as initiation centers for air breakdown waves. These waves are of two types, subsonic laser supported deflagration waves[34, 35] (LSA waves) that are semi-transparent to the laser beam and laser supported detonation waves[36] (LSD waves) that are supersonic and totally absorbing to the laser beam. The second type of waves are of particular concern since they spread in a plane perpendicular to the beam at a velocity

$$v = \sqrt[3]{\frac{(\gamma^2-1)\,I}{2\,\rho_o}} = 1.1 \times 10^3\,I^{1/3}\ cm/sec$$

where I is in W/cm^2 and the numerical coefficient obtains at sea level. Letting $I = 10^7\ W/cm^2$, one finds that, after 10 μsec, for each particle having ignited an LSD wave, a 17 cm^2 section of the beam will be blocked out. The formation of air breakdown waves will require, however, that the particle igniting the wave have a size larger than a threshold size. There will also be a delay time before ignition occurs. Ignition of air

(34) Bunkin, F., Konov, V.I., Prokhorov, A.M., and Fedorov, V.B., Zherf Pis. Red 9, 609 (1969) (English translation JETP Letters, 9, 371 (1969).

(35) Raizer, P., Yu, Zhetp Pis. Red 11, 195 (1969) (English translation JETP Letters 11, 120 (1970).

(36) Raizer, P., Yu, Zhetp (USSR) 48, 1508 (1965) (English translation, Soviet Physics JETP 21, 1009 (1965).

174

breakdown waves is a complex subject and is the subject of continuing experimental investigation. [37]

We present in Section VI. 5. a a brief survey of high altitude aersol distributions and properties. In Section VI. 5. b we look at the microphysics of an aerosol in a laser beam. We study absorption due to breakdown of the aerosol vapor and perform a scaling with altitude of this absorption. The effect of vapor absorption is found to be negligible. We next look at the time scales required for vaporization, breakdown and initiation of laser supported absorption waves. Breakdown times scale inversely with pressure. Basing ourselves on breakdown times for the most pessimistic assumption where all the laser heating goes into cascade ionization of the electrons, we calculate initiation times that at high altitude are much longer than the laser pulse times considered for a pulsed device.

We present in Section V. 6 the threshold versus altitude for maintaining LSD waves, once ignited. The calculations are based on Raizer theory and closely model the previous work done by Nielsen and Canavan. [38] The threshold decreases with increasing beam size and decreases with increasing altitude up to a certain altitude where it reaches a minimum. For a beam size of 1 meter this minimum is less than 10^5 W/cm^2, and is well below the laser fluxes that we are considering. Thus the long onset time for breakdown off particles mentioned above is essential in order to obtain pulsed laser propagation at the intensities required.

(37) Junge, C., Chagnon, C., and Manson, J., of Meteor, 18, 81, (1961).

(38) Nielsen, P., and Canavan, G., "Laser Absorption Waves In The Atmosphere" in Laser Interaction and Related Plasma Phenomena, Vol. 3A., Schwarz, H., and Bora, H., editors, Plenum Press (1973).

175

a. Aerosol Concentration In The Atmosphere

A review of the concentration, size distribution and composition
of aerosols in the atmosphere up to 30 km altitude can be found in Junge's
paper (Ref. 37) and is summarized below. Aerosols below the tropopause
(h < 10 km) have a lifetime of a few days because they are washed down by
rain. They are composed of insoluble dust and various salts. Above the
tropopause the aerosols are either of atmospheric origin or of cosmic origin.
The particles larger than 1 μm are entirely of cosmic origin because of
their short residence time. Chemical analysis show that stratospheric
aerosols contain iron, sulfur and silicon.

The fall velocity vs altitude for particles of different radius r is
shown in Figure 103, and the residence time in Figure 104. The size dis-
tribution is shown in Figure 105.

Figure 105 shows that from r = 0.1 to 10 μm, one has $\frac{dn}{d\log r} \propto r^{-2}$,
i.e., the number of particles within a constant relative interval $\Delta r/r$ varies
as r^{-2}. The concentration of particles larger than 0.1 μm is shown in
Figure 106 and is $\leq$ 0.1 cm^{-3}.

Basing himself on the fall velocity of particles in the stratosphere
and on the fact that the tropopause acts as a sink for particles, Junge showed
that most of the aerosol particle above the tropopuase must be of atmospheric
origin. These particles, that are now believed to be solutions of H_2SO_4 in
water, present no problem to laser propagation because they will vaporize
at very low temperatures and can not trigger laser supported absorption
waves at the fluxes which we are considering (I < 10^7 W/cm^2).

The particles that we are concerned with are the dust particles of
extra-atmospheric origin of size 10 μm or larger. They are so few in

176
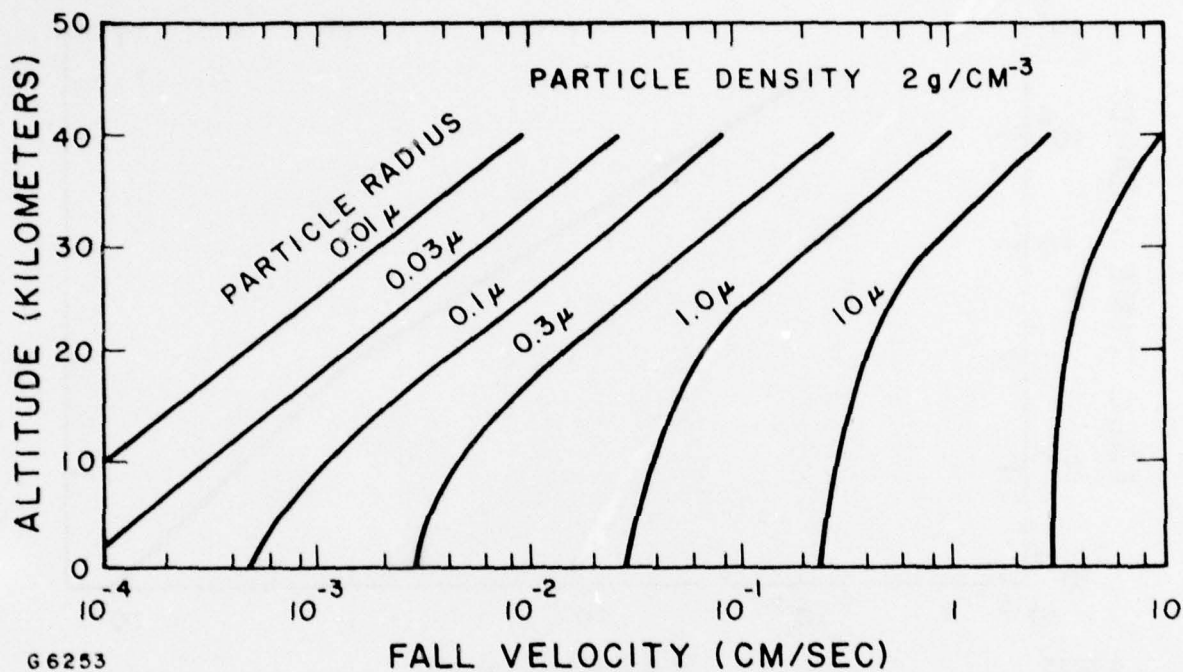
Figure 103   Fall Velocity of Spherical Particles of Density 2 g per cm³ as a Function of Particle Radius and Altitude Calculated from the Stokes-Cunningham Formula
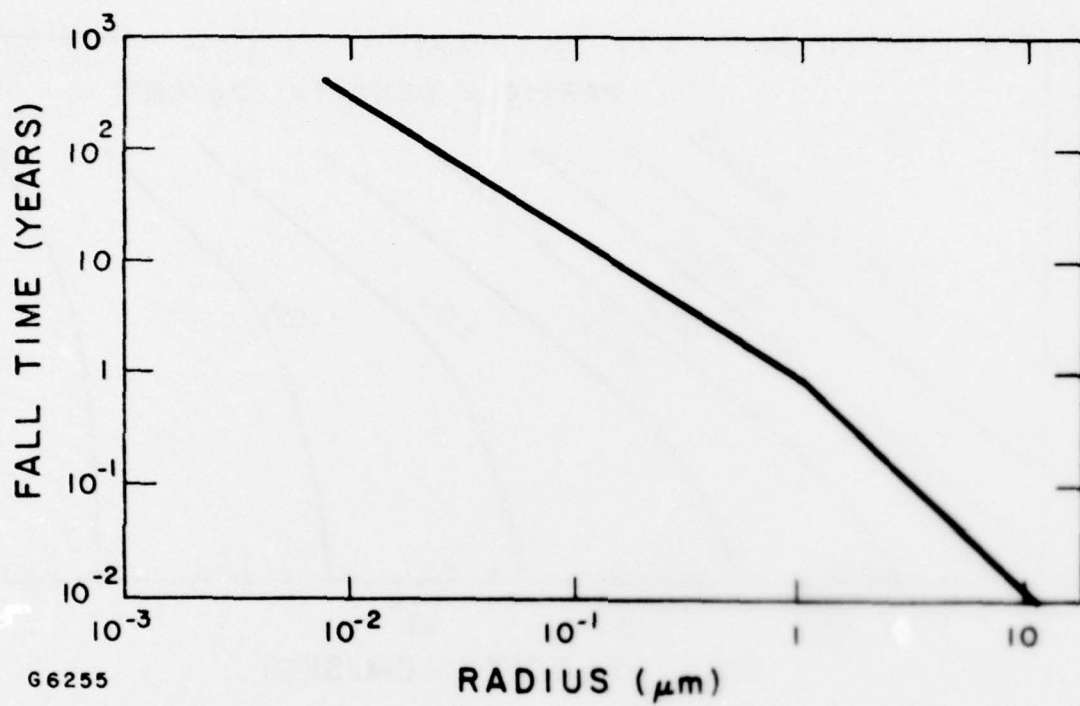
Figure 104   Residence Time of Aerosols in the Stratosphere
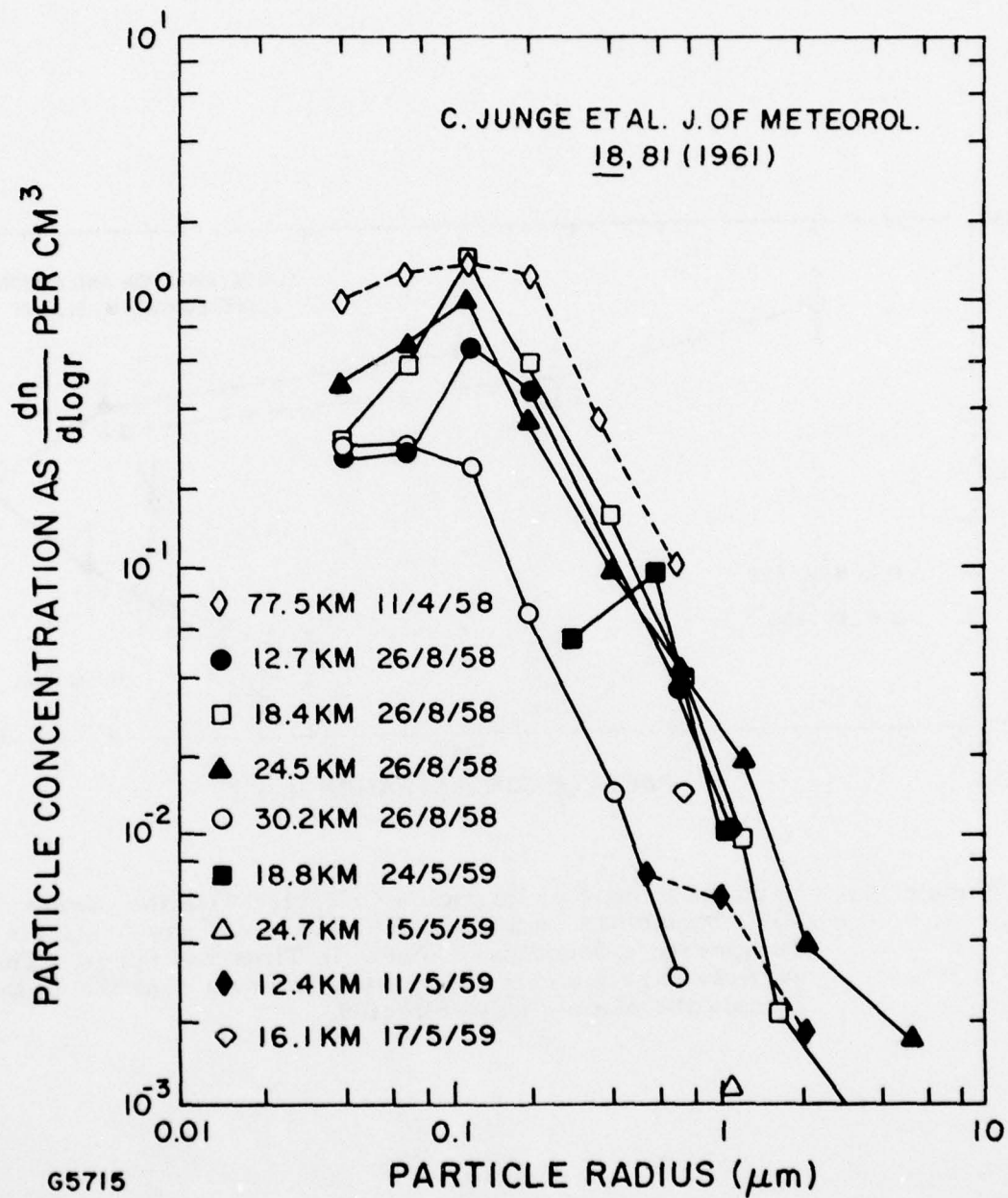
Figure 105   Compilation of all Size-Distribution Data Determined
             from Samples Collected as Indicated.   The numbers
             given after the altitude refer to the stage of the Casella
             impactor on which the sample was collected.

179
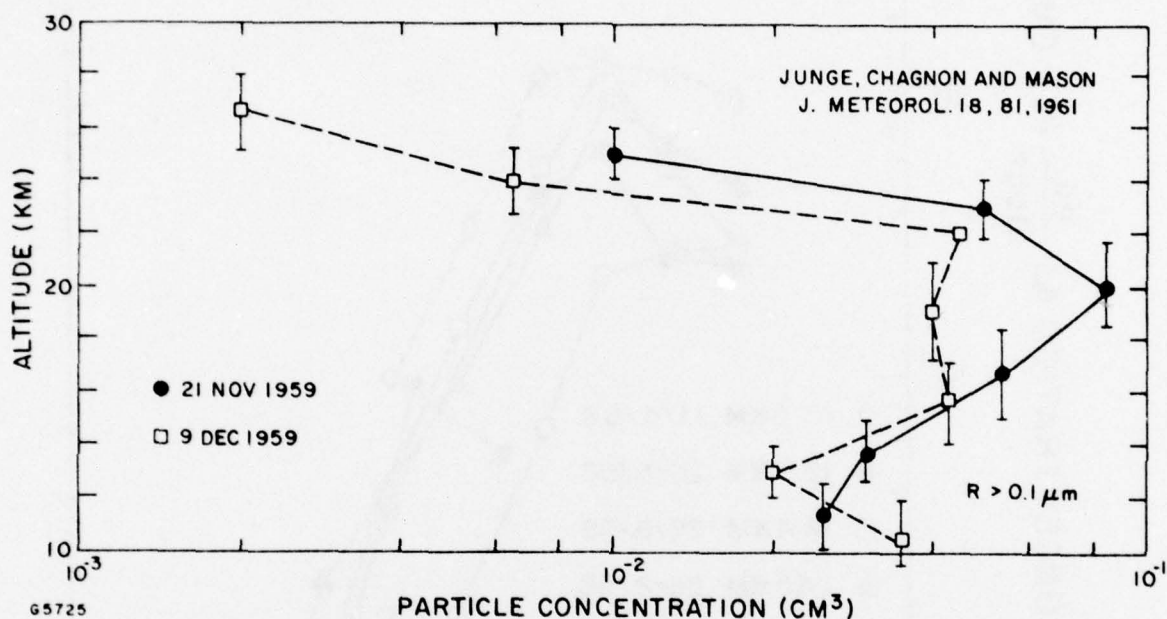
Figure 106   Vertical Profile of Particles Collected with the General
              Mills Impactors on 9 December 1959, and the Available
              Temperature Soundings Closest in Time and Space.   The
              verticle bars indicate the altitude interval over which the
              sample the sample was collected.

180

number that their distribution in size and altitude is unknown. Junge presents data for 10 μm particle at only two altitudes 18.4 and 24.5 km. Since these particles are presumed of extra atmospheric origin, in order to derive the concentration vs altitude, we use the continuity equation $\nabla \cdot n\vec{u} = 0$. This tells us that $n \propto 1/u$ and since u is constant up to 35 km (see Figure 103), we must take n = const. for Z < 35 km. Above 35 km the fall velocity increases since the flow surrounding a falling particle of radius 10 μm or less becomes free molecular and we take n to vary as $e^{-Z/h}$, where h is the scale height (h $\simeq$ 8 km). Assuming that the distribution in size of large particles follows the same law as the small ones, we estimate*

$$n(r > 10 \ \mu m) \simeq \quad 10^{-5} \ cm^{-3} \qquad\qquad 15 < Z < 35 \ km$$

$$n(r > 10 \ \mu m) \simeq \quad 10^{-5} \ e^{-\left(\frac{Z-35}{8}\right)} cm^{-3} \quad Z > 35 \ km \tag{412}$$

Basing ourselves on the previous considerations, we can expect that the number of particles greater than 1 μm in a beam of length 10 km between 15 and 25 km and cross section 1 m^2 will be $(0.1)\left(\frac{0.1 \ \mu m}{1 \ \mu m}\right)^2 \times 10^6 \ cm \times 10^4 \ cm^2 = 10^7$. Similarly for r > 10 μm we find this number to be 10^5.

---

*Note added in proof. More recent measurements (Science, 191, 1270 (1976)) have just come to our attention which indicates that the number of particles larger than 10 μm is $\simeq 10^{-9}$ to 10^{-10} cm^{-3}, i.e., more than four orders of magnitude below those given by Eq. (412) and used in this report. The particles in the range 1 to 10 μm would mainly be spherical Al_2O_3 from rocket exhaust and those above 10 μm, would be extra terrestrial origin.

b. Breakdown Induced by Aerosols

(1) Evaporation and Breakdown of an Aerosol Particle

Analysis[39] of experimental studies of Avco[40] and elsewhere[41, 42] show that particles that initiate air breakdown waves do so by vaporizing with subsequent breakdown in the vapor phase (Al_2O_3, C) and by driving strong shocks in air ($CaCO_3$, H_2O). These conclusions were drawn from the fact that the threshold depends on particle size, and that particles that vaporize at low temperatures have very high thresholds (H_2O). Small particles need high fluxes in order to vaporize since heating is volumetric, while cooling by heat conduction with the air varies as r, the asymptotic temperature reached varying therefore as r^2.

Basing ourselves on sea level measurements of the effect of aerosols on air breakdown, we can derive some simple scaling relations with altitude.

Once a particle has vaporized, the volume occupied by the vapor is

$$V \simeq \frac{4\pi r^3}{3} = \frac{4\pi r_o^3}{3} \frac{\rho_{sol}}{\rho_{air}} \frac{T_v}{T_{air}} \approx 8 \times 10^4 \, r_o^3 \, p^{-1}$$

where r_o = initial radius of <u>solid</u> particle, T_v = vaporization temperature and p = the pressure in atmospheres. In the last step we assumed T_v = $3000^\circ K$, ρ_{sol} = 2 and that the molecular mass of the vapor was the same as air. The 1/p dependence comes from the variation of air density with pressure.

(39) "Propagation Through Atmospheric Aerosols," Semi-Annual Technical Report, AERL, July, 1975.

(40) Schlier, R., Pirri, A., and Reilly, D., "Air Breakdown Studies, Avco Report AFWL-TR-72-74, February, 1973.

(41) Hall, B., Maher, W., and Wei, P., "An Investigation of Laser Supported Detonation Waves," Boeing Report AFWL-TR-73-28, June, 1973.

(42) See Lincoln Laboratory Optics Research Reports for the period 1970-1973.

The vapor will heat up due to inverse bremsstrahlung absorption, but will transfer heat to the surrounding air by heat conduction. The heat conductivity of air varies as $K(T) = K_o T^a$ where $a = 0.8$. The heat lost by a sphere of radius r at temperature T due to conduction to the surrounding air is

$$\phi_L = \frac{4\pi r\, KT}{a+1} \propto p^{-1/3} r_o$$

The absorption of laser energy on the other hand is:

$$\phi_{abs} = a'\, n_e\, n_N\, I_{laser} \times \frac{4\pi}{3} r^3$$

where $a' =$ inverse Bremsstrahlung absorption factor and n_e and n_N are the concentrations of electrons and neutrals respectively. Assume T_v independent of altitude (pressure), then $n_N \propto p$. Initially, we assume $T_e = T_v$ (this will __not__ be true at high fluxes or when most of the gas is dissociated) and that the electron concentrated is in equilibrium with T_e. We will have $n_e \approx A\, n_N^{1/2}\, e^{-\epsilon_I/2kT} \propto p^{1/2}$ where $\epsilon_I =$ ionization potential, and A is a factor depending weakly on T. We thus get

$$\phi_{abs} \propto I_{laser}\, p^{3/2}\, p^{-1} \propto I_{laser}\, p^{1/2}\, r_o^3$$

Equating ϕ_{abs} with ϕ_L, we see that $I_{laser} \propto r_o^{-2}\, p^{-1/3 - 1/2} = p^{-5/6}\, r_o^{-2}$

Figure 107 presents curves of marginal stability for an Al_2O_3 aerosol which has a boiling temperature of 4000^oK and an electron concentration in the vapor phase, for $T_v = 4000^oK$, $P_{sat} = 1$ atm, of 8×10^{14} part/cc. To the right of each curve the vapor tends to cool down. To the left of each curve the vapor will heat up.
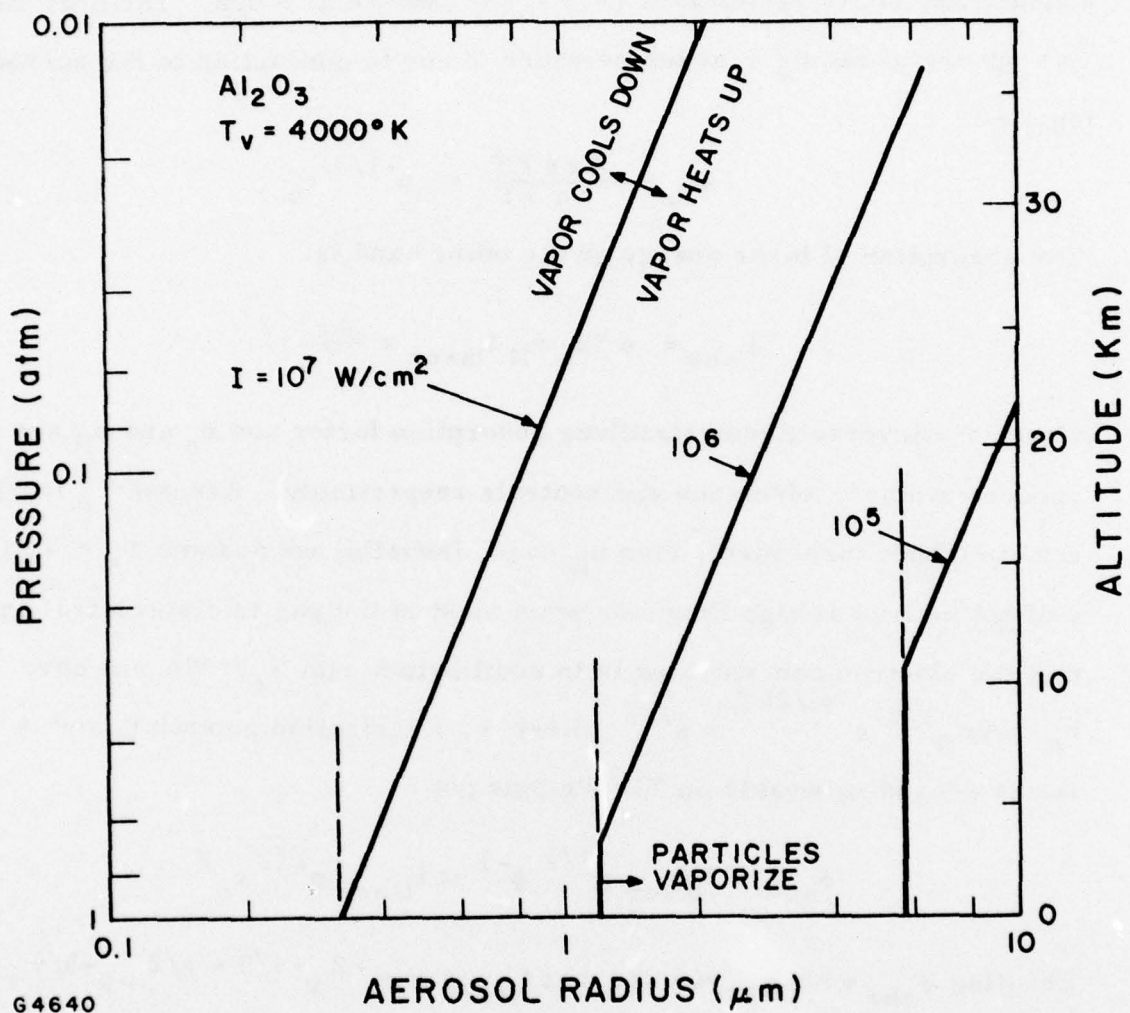
Figure 107   Stability Boundaries for Aerosol Vapor

The intersection of a constant I line with the dashed boundary at the bottom of the figure corresponds to the smallest aerosol particle that will vaporize under the given flux.

We can make an estimate on the effect of aerosols on laser propagation under the following assumptions:

a) At a given I all particles with $r > r_c$ given by Figure 107 vaporize and the vapor expands and heats to $17,000^\circ K$ temperature of maximum absorption[43] where the vapor is practically totally ionized.

b) We assume that no detonation wave forms and that no deflagration wave propagates through air.

c) We use the distribution of particle sizes of Figure 105 for $h > 10$ km with concentration given by Figure 106 up to 20 km and by Eq. (412) above. For $h > 10$ km, we use the distributions and concentrations under the above assumption tabulated by McClatchy[29] corresponding to a 5 km haze. We find an absorption coefficient for the vapor

$$k = 0.25 \times p^2 \ cm^{-1}$$

and an absorption cross section per particle

$$\sigma \ (r_o) = 6 \times 10^{-7} \ r_o^{\ 3} \ p \ cm^2$$

where r_o is expressed in μm. Integrating over the particle distribution of Figure 106 from r_c to 10 μm, we calculate the absorption length shown in Figure 108. This figure shows that

(43) Raizer, Yu., Soviet Physics JETP 31, 1148 (1970).

185
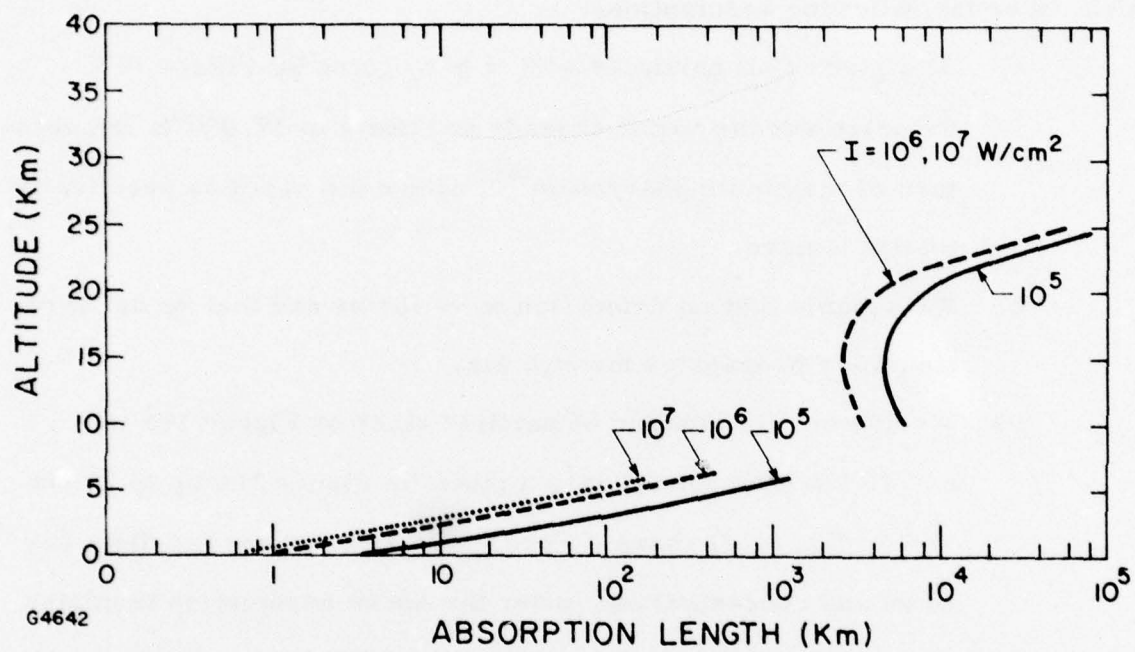
Figure 108   Absorption by Aerosols in the Atmosphere After Breakdown
of the Vapor

absorption by aerosols is only important at sea level. If the laser is situated at a mountain top one can completely neglect the attenuation, due to the aerosol vapor itself.

(2) Time Scales Involved

The time it takes an AI_2O_3 aerosol to heat up, melt and vaporize is shown in Figure 109. The relevant parameter, $I \times t$, which is proportional to the energy deposited in the particle, is the abscissa and the radius of the particle is the ordinate. Under a given flux I, only particles above a given radius will either heat up to T, melt or vaporize because of heat losses to the surrounding air. This radius is given by the intersect of the horizontal dashed lines with the appropriate full curve. Figure 109 shows that for $I = 10^7$ W/cm^2 the minimum time for vaporization to occur is 0.8 μsec (for r = 0.3 μm). This time becomes 8 μsec, and 80 μsec for $I = 10^6$ and 10^5 W/cm^2, respectively. The times for complete vaproization to occur are twenty times longer.

We now look at breakdown in the vapor bubble. The electron distribution function (which determines T_e and ionization rate) is determined by a balance between Joule Heating and elastic and inelastic collisional losses. Since the elastic collision frequency is less than the laser frequency, both heating and cooling rates are linear with pressure[44] and the electron distribution function will therefore depend only on I_{laser}. We expect that the vapor will break down at a threshold I_{th} independent of altitude. The time to breakdown should however scale as $1/p$.

---

(44) This statement is only correct if we neglect the effect of pressure on the degree of dissociation.

187
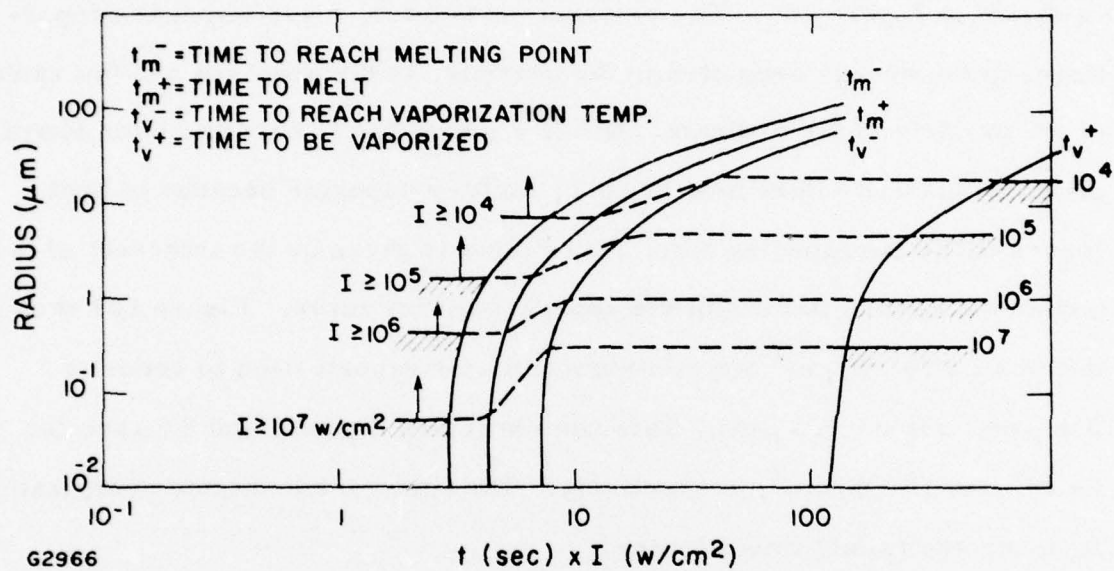
Figure 109   Time Map for $Al_2 O_3$

We derive an estimate of the breakdown time by assuming this time to be ten avalanche breakdown times (i.e., enhancement of the electron density by 10^4) and assuming that <u>all</u> the Joule heating goes into ionization. Using an elastic cross section of 10^{-15} cm^2 and an ionization potential of 13eV and, assuming the vapor at temperature $T_v(^OK)$ to be at the ambient pressure p, we find

$$\tau_{Breakdown} = \frac{6 (T_v/4000)}{(I/10^7) T_e^{1/2} p} \quad \mu sec \tag{413}$$

where T_e is the electron temperature in eV, I is in W/cm^2 and p is in atmospheres. The breakdown time is plotted in Figure 110. For $I = 10^6$ W/cm^2, $p = 1$, $T_e = 1$ eV, we find that $\tau_{Br} = 60$ μsec and will very probably be <u>longer</u> than the laser pulse duration. Note that Eq. (413) gives a lower bound on the breakdown time since any inelastic process will result in gas heating and lengthen the breakdown time.
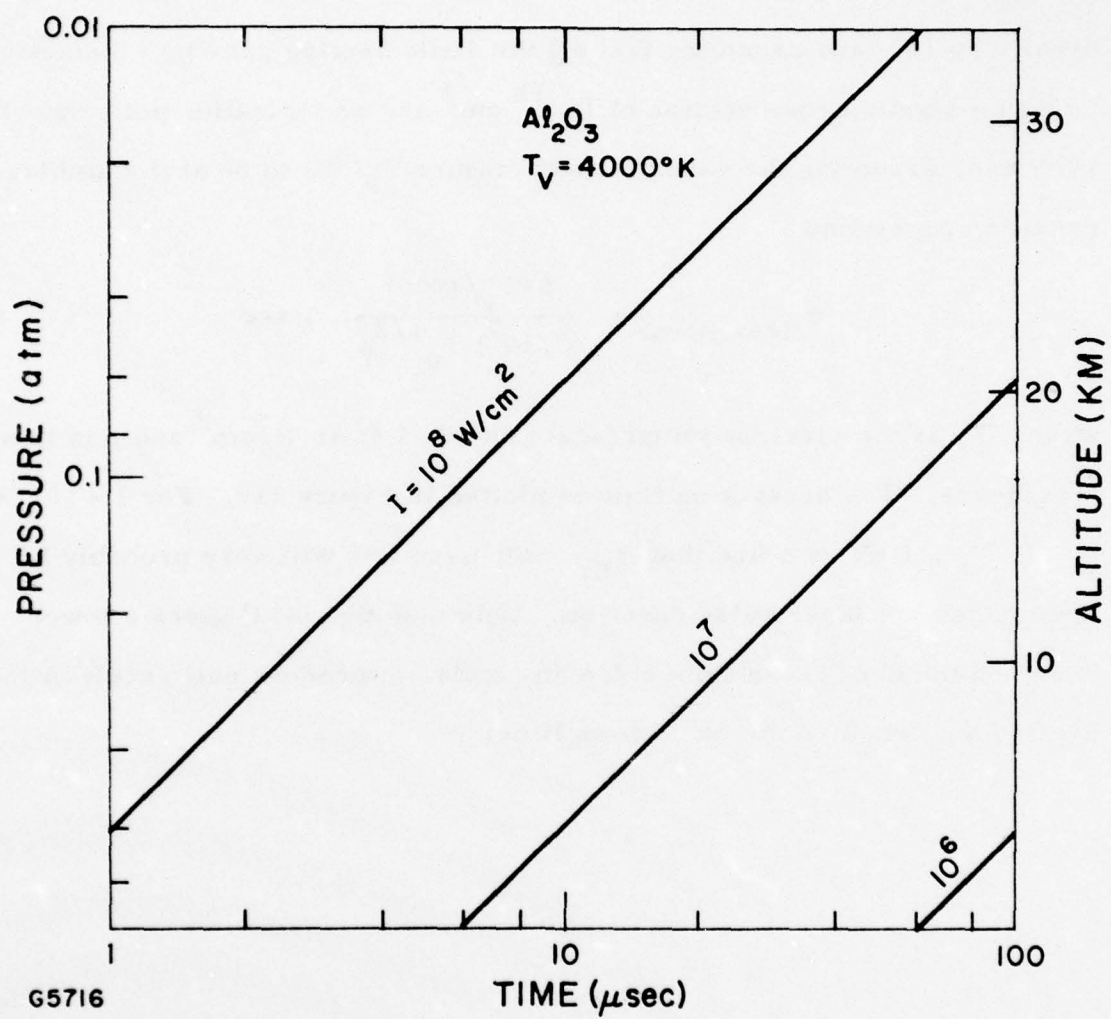
Figure 110   Minimum Breakdown Time for Aerosol Vapor

6. MAINTENANCE OF LASER SUPPORTED ABSORPTION WAVES

Once the aerosol vapor has broken down, the breakdown front will move into the surrounding air, initiating an air breakdown wave. A good understanding of the initiation mechanism and the dependence of threshold flux on pressure is at present lacking.

Subsonic laser supported absorption waves ignited off solid targets were maintained at fluxes as low as 4×10^4 W/cm^2 with a beam area of 0.5 cm^2 and the threshold was found[45] to vary as $r^{-1.6}$. Studies of ignition of laser supported detonation waves off aerosols were made at AERL,[40] and Lincoln Laboratories[42] and give a threshold at sea level of $\simeq 1.5 \times 10^7$ W/cm^2. Computer simulations at Livermore,[46] on the other hand, give a threshold of 3×10^6 W/cm^2.[†] The detonation wave behavior down to the fluxes quoted above were found to agree well with the Raizer detonation wave theory.[36] The Raizer theory assumes a) complete absorption of the laser radiation by the air, b) that the air can be treated as a fluid with constant γ ($\gamma \simeq 1.17$ for $10,000 < T < 20,000^{\circ}$K) and c) that the wave obeys the Chapman Jouguet conditions under equilibrium conditions. Calculations of the absorption length at the Chapman Jouguet point show that at sea level, for fluxes below 10^7 W/cm^2, the absorption length is <u>larger</u> <u>than 1 cm, i.e., much larger than the beam diameter in all the experiments</u>

[†]This low threshold may be explained by the fact that inelastic collisions between electrons and molecules were neglected, resulting in electron temperature much higher than heavy particle temperature. At low fluxes (3×10^6 W/cm^2) where the gas is not completely dissociated departure from LTE is not expected to occur.

(45) Smith, D. C. and Fowler, M., Appl. Phys. Lett. <u>22</u>, 500 (1973).

(46) Edwards, A., Ferriter, N., Fleck, J. and Winslow, A., "A Theoretical Description of the Interaction of a Pulsed Laser and a Target in a Laser Environment," Lawrence Livermore Laboratory, UCRL-51489, November 1973.

quoted above. This indicated that the threshold for maintaining detonation waves is determined by conditions in an absorption zone that may be far from equilibrium. In order to explain the data and correctly predict the threshold for maintaining LSD waves one must look at the structure of the detonation waves. An analytic approach was attempted at Lawrence Livermore Laboratory by Ferriter and Winslow[47] and a computer model was developed at the Air Force Weapons Laboratory by Stamm and Nielsen[48] in order to study the threshold, but none of their results should be given, in our opinion, much credibility, since their treatments are too simplistic.

The initiation threshold of detonation waves at 10.6 μm versus pressure was measured by Hall, et al.,[41] who ignited the waves off various surfaces in a chamber, the inside pressure of which could be varied. They found that the threshold either increased or remained constant as one decreased the pressure from 1 to 10^{-2} atm. In no case were they able to ignite a detonation wave at fluxes below 6×10^6 W/cm^2. At low pressures the sharpness of the front was lost and it was difficult for the experimentators to ascertain whether they had truly ignited a detonation wave. Their laser pulse lasted only 10 μsec and it is not clear whether longer pulses would have resulted in a lower threshold.

The altitude dependence of threshold for maintaining detonation waves was studied by Nielsen and Canavan.[38] They based their calculations on

---

(47) Ferriter, N. and Winslow, A., "Calculated Intensity Threshold for the Maintenance of Laser Supported Detonation Waves with Various Electron Densities," Lawrence Livermore Laboratory, UCRL-51606.

(48) Stamm, M. and Nielsen, P., AIAA J. 13, 205 (1975).

Raizer's Theory which takes into account the lateral expansion of the gas behind the front. If ℓ is the absorption length at the Chapman Jouguet point and R is the radius of the beam, then the flux necessary to maintain the wave following Raizer is increased by a factor $(1 + \ell/R)$ over the flux required to maintain the wave if R were infinite. The threshold flux required to maintain a detonation wave at a given altitude is the minimum of value of I' defined by

$$I' = I (1 + \ell/R)$$

where ℓ is a function of I. We extended the calculations of Nielsen and Canavan, which were done for $R \leq 1$ cm, to larger beam radii. The results are shown in Figure 111. A discussion of the equations used to derive the threshold flux is given in the appendix. At low altitudes, in the linear portion of the graph, our R = 1 cm curve is a factor of 1.5 below the same curve given by Nielsen and Canavan, a consequence of the different choice of numerical coefficient used. The important point to be made here is that the threshold for maintaining detonation waves at high altitudes and large beam radii is very low. For example, with a beam radius of 10 m one would be able to maintain detonation waves at an altitude of 15 km with a laser flux as low as 4×10^4 W/cm^2. Whether such detonation waves can be ignited, however, is open to question. The curves drawn in Figure 111 were terminated at the low density side, wherever ℓ became equal to R.

The dashed lines in Figure 111 represent the beam intensity required to drive a Chapman Jouguet detonation wave with a given absorption length ℓ. The derivation of these curves is explained in the Appendix.

193
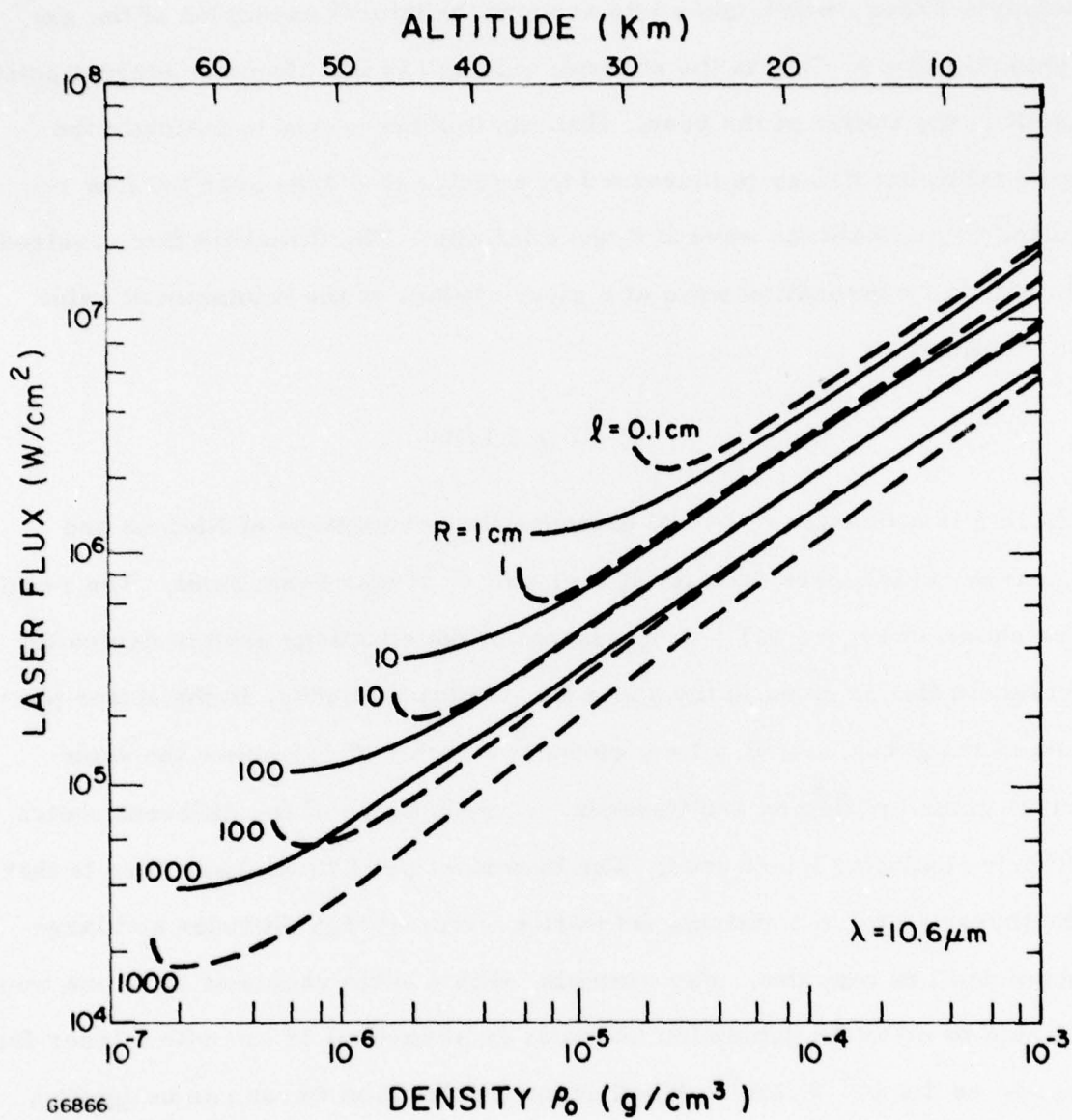
Figure 111   Scaling of LSD Maintenance Threshold on Beam Size (R) and Density (ρ_o); $\lambda = 10.6 \mu m$

One would think, using Nielsen and Canavan's criterion, that by going to larger and larger beams one could maintain detonation waves at arbitrarily low fluxes. Radiation losses from the laser heated region will prevent this from occurring. If one defines $\tau_H = \ell/u$ as the heating time (where $u \simeq D/2$ is the velocity of the fluid with respect to the shock), one must require that the radiative decay time at the Chapman Jouguet point be much longer than the heating time.

We used the values of radiation from hot air calculated by Kivel[49] to compare the radiative losses during the heating time to the energy content of the fluid at the Chapman Jouguet condition. Details of this study are given in the Appendix and the results are presented in Figure 112. In this figure we plotted the intensity required to maintain a detonation wave of a given absorption length as a function of density (altitude). Radiative losses corresponding to 20% and 100% of the energy absorbed by the gas are shown ($\eta = 0.2$ and 1 curves). Since the fluid mechanical losses at threshold, following the criterion of Nielson and Canavan, are roughly 20% of the absorbed energy, radiative losses should dominate fluid dynamic losses in the region to the left and below the $\eta = 0.2$ curve. Radiative losses were calculated assuming the plasma is optically thin to its own radiation. This assumption is only true on the portion of the curve to the left of the minimum, i.e., at an altitude $h > 22$ km for the $\eta = 0.2$ curve. We expect radiative losses to be important at fluxes below 3×10^6 W/cm^2 and altitudes above 22 km. A proper account of these losses, however, can only be made by looking at the detailed <u>structure</u> of the detonation wave, which is beyond the scope of the present study.

(49) Kivel, B., "Radiation from Hot Air," AERL Research Report RR-79, October 1959.
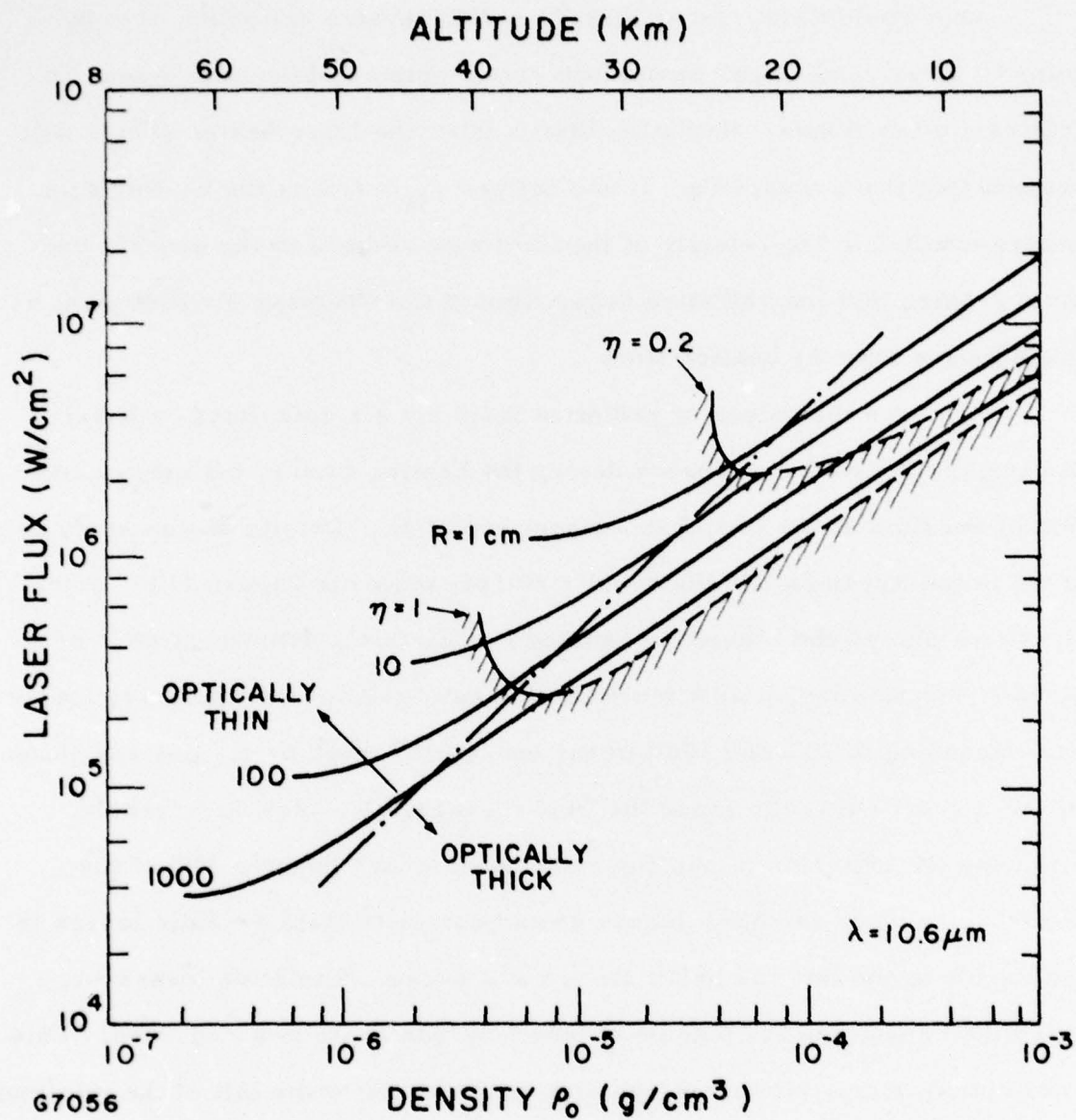
Figure 112   Radiative Losses in Detonation Waves

a. Conclusion

We have found that aerosols in the atmosphere should have a negligible effect on laser beam propagation at fluxes $< 10^7$ W/cm^2, if a) one operates a few kilometers above ground level (i.e., on a mountain) so as to avoid hazy conditions and b) aerosols do not drive laser supported absorption waves in the atmosphere. Basing ourselves on a very simple model of breakdown, we find a delay for breakdown given by Eq. (412) that is longer than the pulse durations that are presently being considered.

7. PROPAGATION THROUGH CLOUDS

The presence of condensed water in the path of the laser will cause an attenuation of the laser beam by scattering and absorption. We estimate these effects in this section. A review of particle concentrations and size distributions in various type clouds and fogs was performed in Ref. 39, and we summarize the result below. The size distribution is presented in Figure 113. The propagation of the laser beam is governed by the equation

$$\frac{dI}{dt} = [\sum_j \pi r_j^2 \, Q_{ext} \, (r_j)] \, I \tag{414}$$

where the sum extends over all particles j of radius r_j in a unit volume and where the extinction coefficient at 10.6 μm for water (sum of scattering + absorption) is given by Figure 114. One sees from this figure that $Q_{ext} \propto r$ for r < 10 μm. Figure 113 shows that most particles in clouds and hazes have a size < 10 μm. The summation in Eq. (414) can then be carried out leading to the simple relation for the sum of the absorption + scattering coefficient

$$\alpha = 70 \, \rho \qquad cm^{-1} \tag{415}$$

where ρ is the mass density in g/cm^3 of condensed water. Equation (415) is valid for water at λ = 10.6 μm. Extinction at other wavelengths can be obtained using Mie Theory[50] and the complex index of refraction of water[51] or ice.[52] The complex index of water and ice over the wavelengths range 1 to 20 μm is shown in Figures 115 and 116.

(50) Van der Hulst, Light Scattering by Small Particles, John Wiley and Sons Publishing, N.Y. (1957).

(51) Centano, M., J. Opt. Soc. Amer. 31, 244 (1941).

(52) Ockman, N., Advances in Physics 7, 199 (1958)
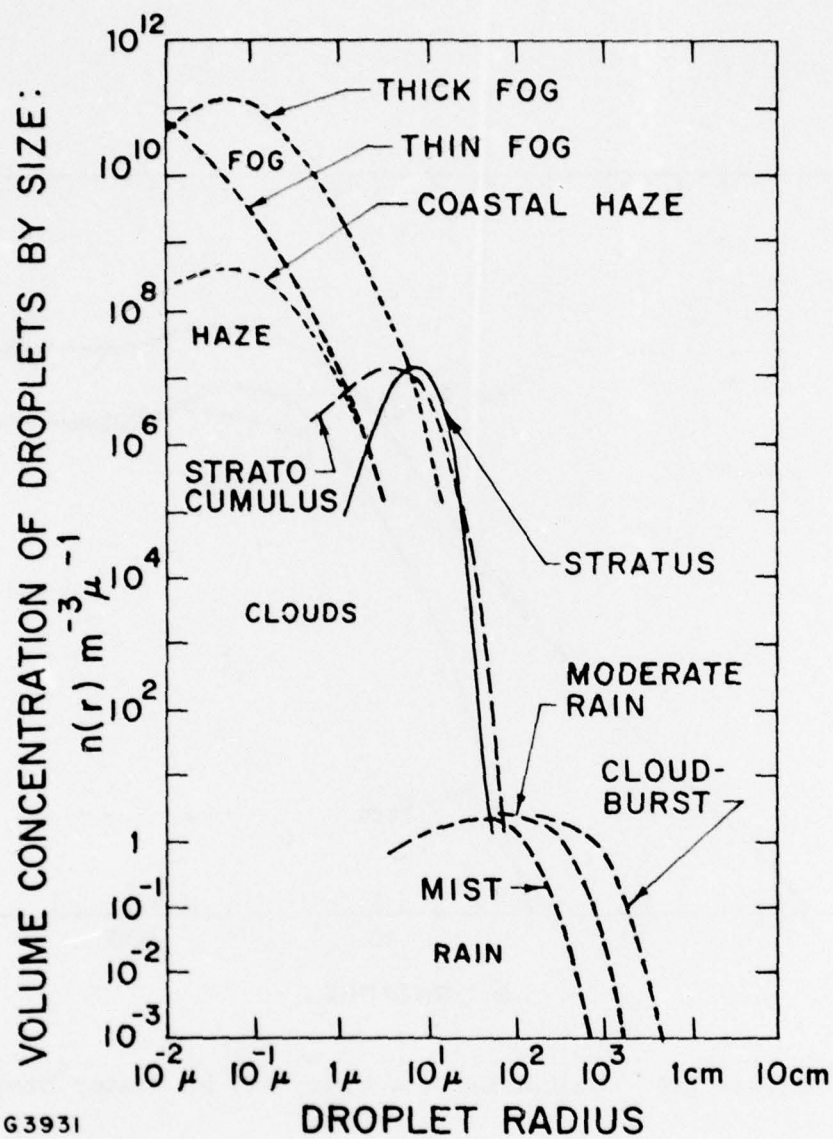
Figure 113   Measured Water Aerosol Distribution Functions

G3931

199
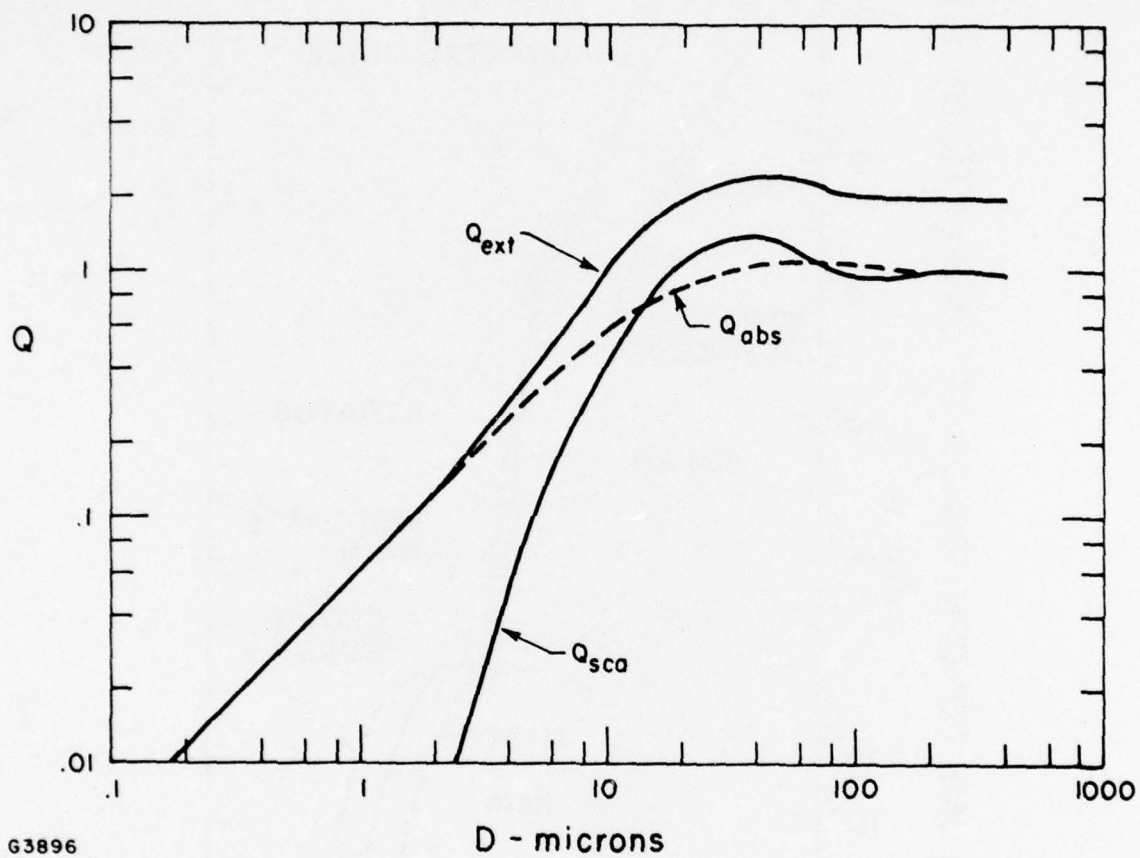
Figure 114   Calculated Mie Efficiency for Water Droplets

G3896
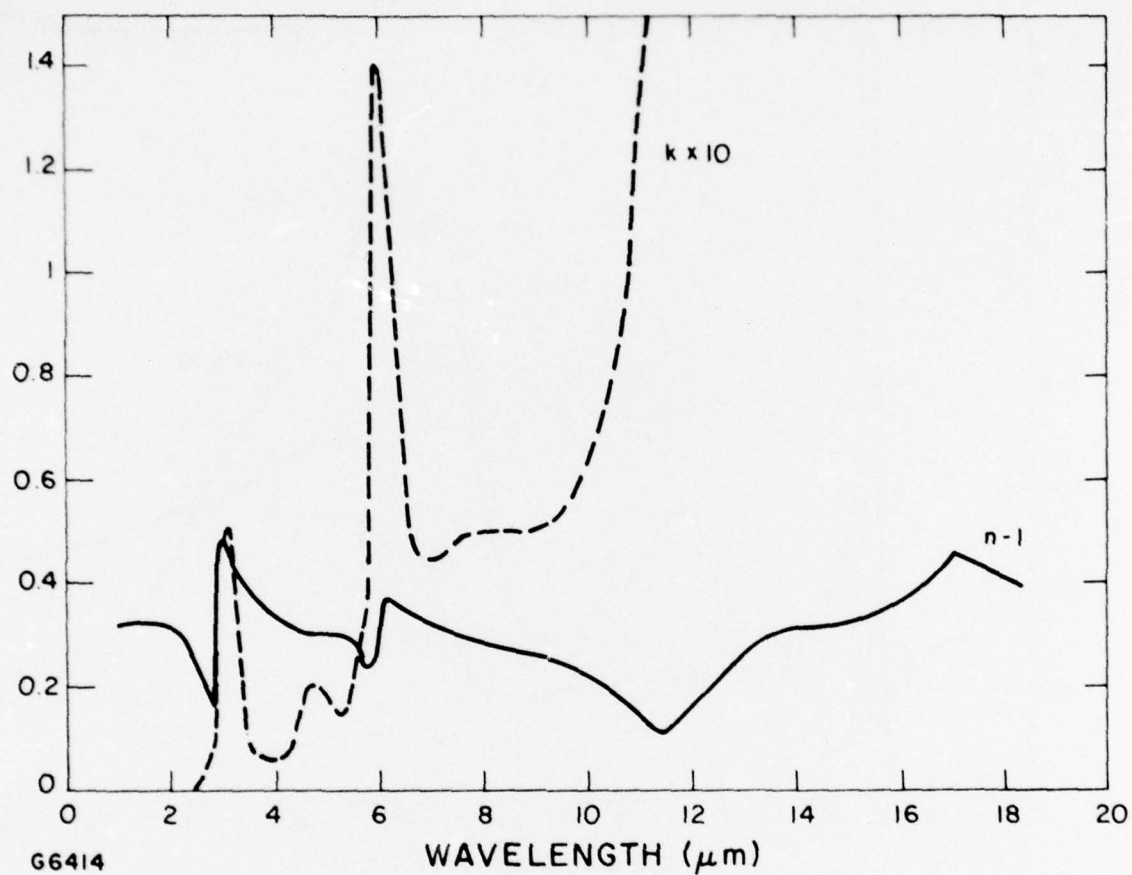
Figure 115   Complex Index of Refraction n − ik of Water in the 1-10 μm Range
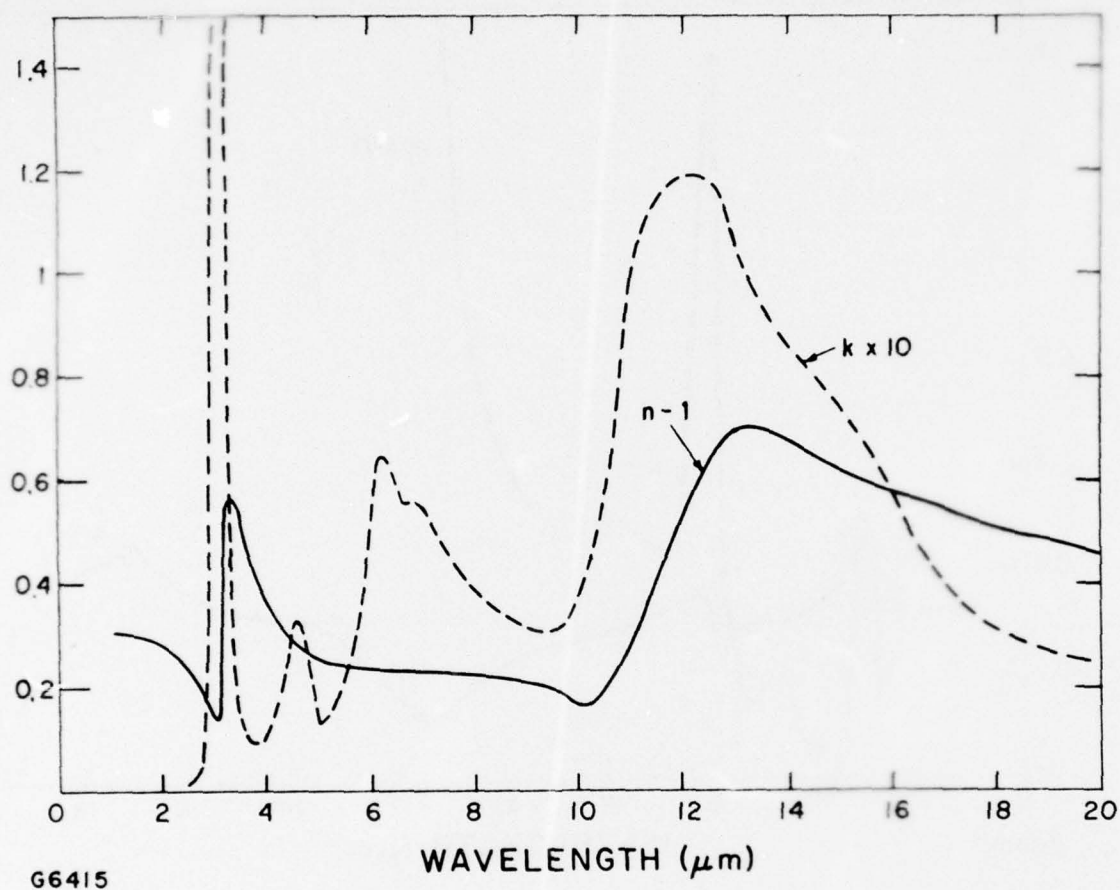
Figure 116   Complex Index of Refraction of Ice in the 1-20 μm Range

We reproduce in Table 11 the data on sizes and water content of clouds and fogs that was compiled in Ref. 39.

The meaning of R_1, R_2 and N in Table 11 becomes apparent when one refers to Figure 117.

If one excludes thick fog and cumulus clouds one estimates a water content of 10^{-7} g/cm^3 or less, which means that a laser beam at 10.6 μm will propagate a distance of $\simeq$ 1 km through clouds and fogs before suffering appreciable attenuation.

Cloud structure having a vertical extent of 1 km or more will cause significant attenuation of the laser beam and this precludes the use of laser propulsion on most cloudy days. Attenuation of the beam will be lower if one operated in the vicinity of 9 and 4 μm due to the smaller absorptance of water and ice. There is no gain however, in operating much below 4 μm because of the increased importance of scattering laser which scale as λ^{-4} and will dominate over absorption losses.
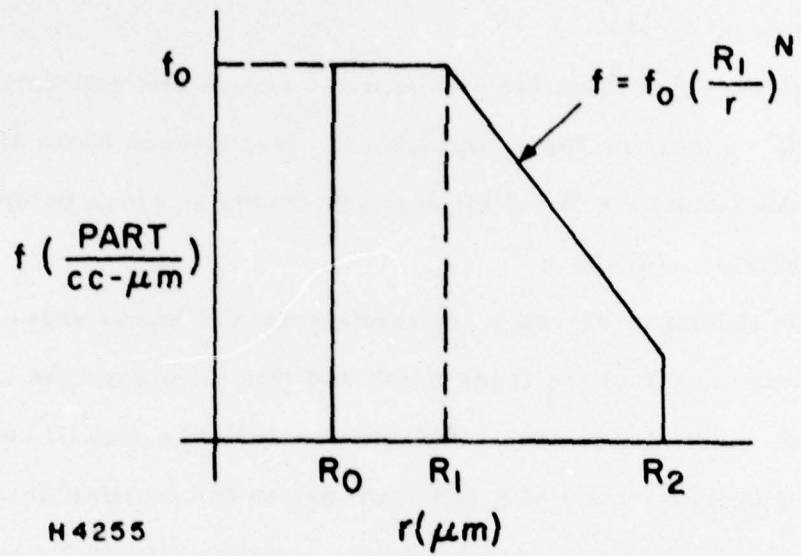
Figure 117   Aerosol Distribution Function

H4255

204

TABLE 11. WATER AEROSOL DATA

Aerosol Class	N	R_1 (μm)	R_2 (μm)	ρ (g/cm^3)
Thick Fog	2	10^{-1}	10	4×10^{-7}
Thin Fog	2	2×10^{-2}	1	6×10^{-11}
Coast Haze	2	2×10^{-1}	2	2×10^{-8}
Stratus	3	10^{-1}	20	4×10^{-7}
Strato Cumulus	3	5	20	10^{-7}
Mist	4	100	800	1.6×10^{-9}
Strato Cumulus	4	7	20	10^{-7}
Fair Weather Cumulus	>6	7	15	10^{-7}
Cloud Burst	4	800	3000	2.3×10^{-6}
Cumulus Congestus	5	17	50	2.5×10^{-6}
Moderate Rain	4	300	2×10^3	6×10^{-8}

VII. ECONOMICS

The advantage of laser propulsion as a means of obtaining direct launch to geosynchronous orbit (GSO) lies in two facts: high volume through-put and cost savings. The first is implicit in the use of a high power laser for a launch whose duration is ~ 200 seconds. A preliminary outline of the second will be given in this section.

Pricing will be in 1976 dollars. We note that each item addressed here will require detailed analysis in future work.

The system cost required is broken into the following main components:

A. CAPITAL COST:

Laser (closed cycle, air breathing)
Power Plant (peaking 6 GW)
Beam control system

B. OPERATING COST:

Fuel cost
Maintenance
Propellant
Vehicle cost

1. CAPITAL COST

a. Laser

Since the major capital component is likely to be the laser array, we will consider the carbon dioxide laser using the pulsed electric closed-cycle air breathing system to maximize efficiency (over 20% efficiency of conversion is obtained).

207

Systems studies[53,54] of laser scaling at AERL result in an effective
capital cost of 60c per watt, for pulsed CO_2 lasers. In the present system we
require a 10^9 watt final beam aiming at the vehicle. Allowing for atmospheric
transmission loss (20%) and pointing and tracking system loss (9%), we re-
quire a beam at the laser exit of 1374 MW. Using a three stage MOPA
system with 10:1 branching ratio, this power is reached using 1111 1.4 MW
units, which will be stacked in a phased array, shown schematically in
Figure 118. The laser capital cost is estimated at $M933.

b. Power plant

Estimating the electrical cost for a system of this type may be done
either by taking the capital cost for the power plant required and including
it in the capital amortization, or by adding the purchased cost of electricity
(at 4c per kwh to the operating cost. If nuclear or hydroelectric power is
used then amortization of the capital cost is the major cost of the power.
We therefore treat the power plants as a capital investment. Taking the
capital cost of generating equipment at 17¢ per watt, a standard power
plant[55] capable of peaking at 6 GW is estimated at $M1020.

c. Beam control system

In the present design a phased array of lasers is used to provide a
correctible beam. Conceptually, phase corrections can be applied to this
beam either before or after the final amplifier stage. Two large mirrors
are required: a chandel, at which the laser beams are combined into a
single coherent phase-corrected beam, and a steerable beam director,
which aims the beam at the target rocket engine (Figure 119). A pointing

(53) Neacy, W., 1976, private communication.
(54) Feinberg, R. and Roos, J., 1976, private communication.
(55) Boston Ediston Inc., 1975, private communication.
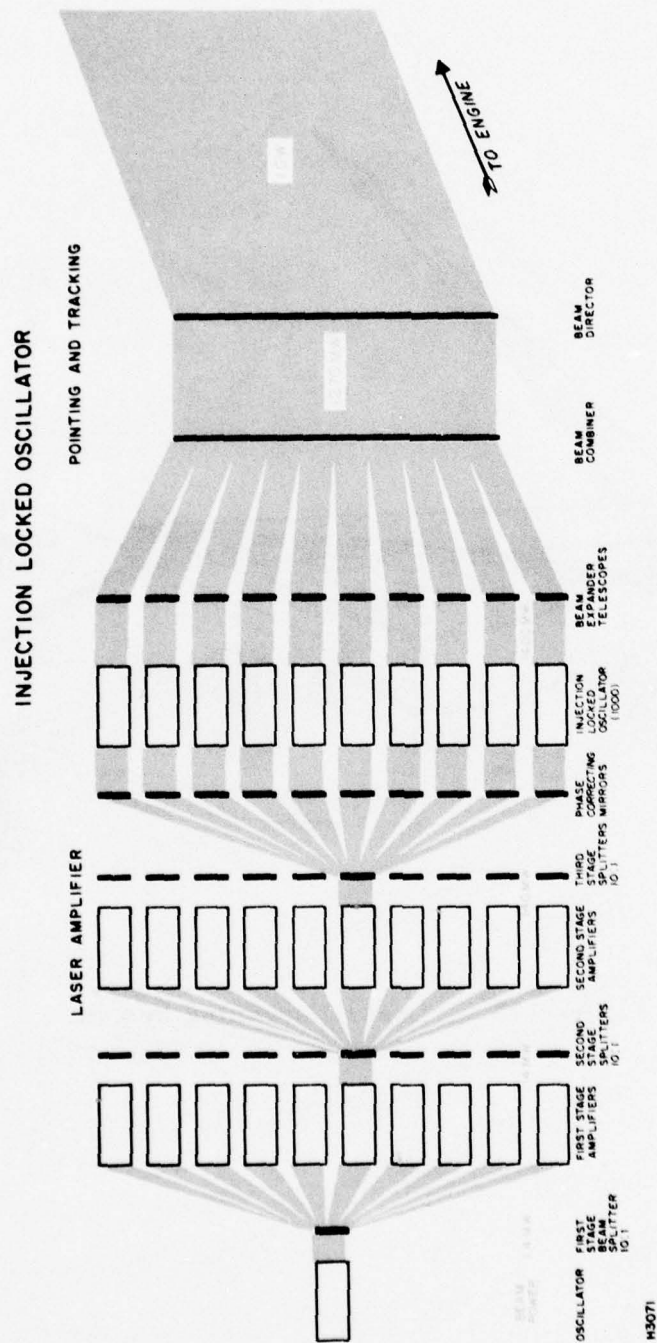
Figure 118   Laser Amplifier System

BEAM DIRECTOR

CHANDEL
BEAM COMBINER
& PHASE CORRECTOR
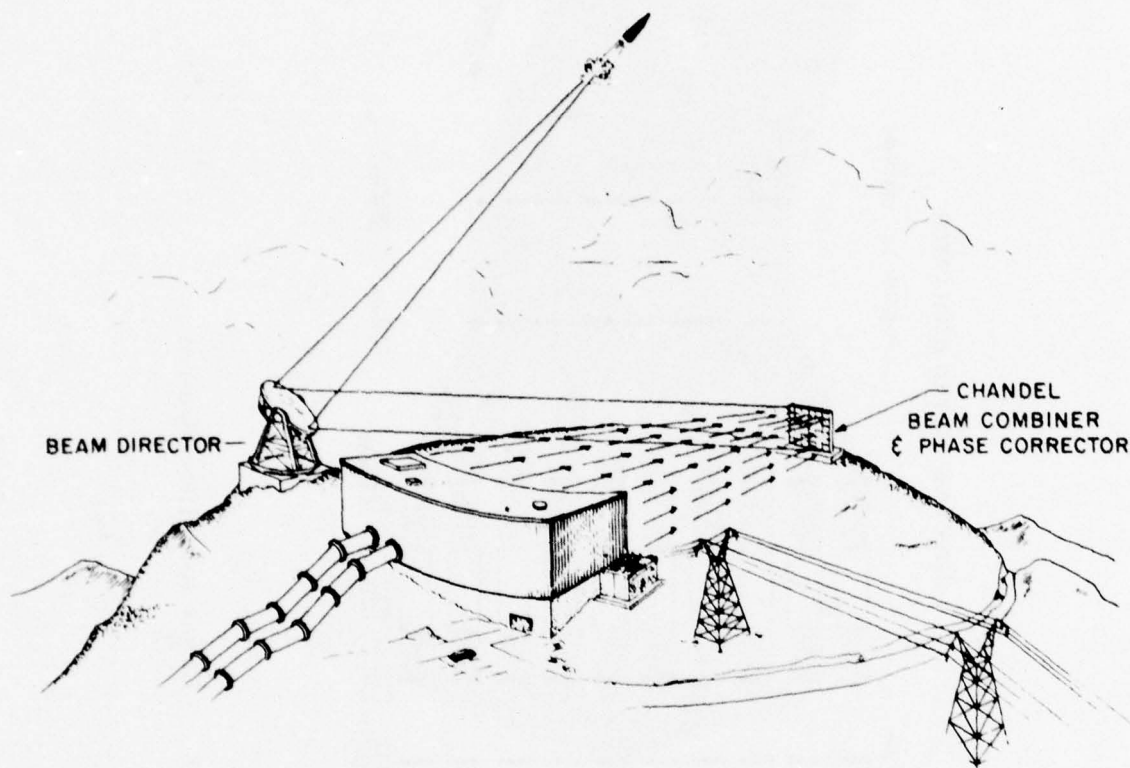
G5763

Figure 119   Laser Launching System

210

and tracking system controls the beam direction. This system is estimated at $M200.

2. OPERATING COST

The costs will be normalized to that required for launch of 1 ton to GSO.

a. Fuel

The laser system operates on the fuel JP-4, the combustion products of which provide the lasing gas mixture. For the launch duration of 256 sec required for the standard case of insertion of 1 ton into geo-synchronous transfer ellipse, we require 40 tons of JP-4, costing $4000.

b. Propellant

Possible propellents and costs[56] are listed in Table 12.

TABLE 12. PROPELLANT COST

Propellant (liquid)	Cost (1976) $ per ton liquid
Ammonia	198
Argon	876
Hydrogen	2750
Methane	4940
Nitrogen	70
Oxygen	62
Water	0

In the present case we take liquid nitrogen as propellant, and obtain the cost for launch of 1 ton to GSO as $350.

(56) Air Products Inc., 1975, private communication.

211

c. Maintenance

The major consumable in the capital equipment is the capacitors used in the power conditioning circuit for the laser supply. These are estimated to be good for 4×10^4 launches, yielding a cost of $2000 per launch. Other maintenance is allowed at $500 per launch.

d. Vehicle Cost

The vehicle is to be kept as simple as possible, and in one elementary form consists of a reinforced block of ice surmounted by the payload, (Figure 120). Guidance is then performed by the laser beam, the flux density of which is varied across the rocket base to provide torques for guidance. In another form liquid fuel is injected into the engine cavity through a porous plate, and there evaporated and subsequently heated. In this case also the concept of steering the rocket engine by varying the laser beam on the ground may apply.

We note that omitting on-board guidance systems would render extremely low rocket cost feasible. However, a considerable systems analysis will be required before a reliable cost figure can be estimated for the engine. The uncertainties of vehicle price suggest that it should be left as a parameter in the final estimate of cost versus usage.

3. SUMMARY

LASER PROPULSION COST ESTIMATE

CAPITAL COST

1111	1.4	MW lasers at 60 c/w	$ 932M
		Electron beam	
		Pulse forming network	
		Cavity optics	
		Gas generation system (closed)	
		P & T loss 9%	
		Atmospheric loss 20%	

212

1 TON
PAYLOAD

5.4 TON
SOLID PROPELLANT

8 km/sec

THRUST
NORMAL TO
BASE

SHOCK ABSORPTION
(OPTIONAL)

ABLATIVE CASE
& 1-D SKIRT LINER
0.5 TON STRUCTURE

SLIDING 1-D SKIRT

NONSYMETRICAL
OFF AXIS LASER
BEAM GENERATES
CONTROL TORQUE

$10 \ \mu sec, \ 2 \times 10^7$ WATTS/cm^2
6 MJOULE, 160pps

G 6275
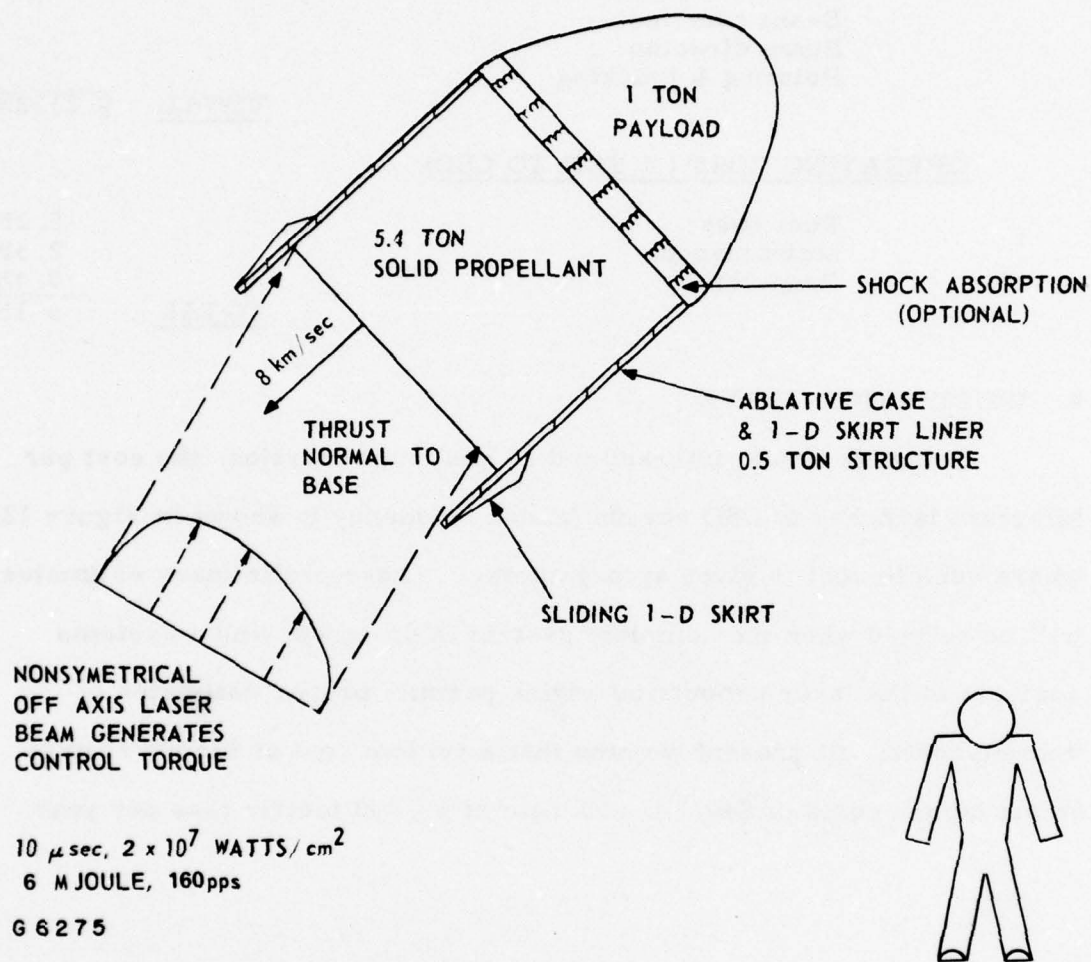
Figure 120   LSD Wave Rocket Engine

213

1 PEAKING POWER PLANT, 6 GW	$ 1020M
1 BEAM CONTROL SYSTEM	$ 200M

Phase corrector
Beam combiner
Beam director
Pointing & tracking

TOTAL $ 2152M

OPERATING COST [1 TON TO GSO]

Fuel cost	5. 2K
Maintenance	2. 5K
Propellant	0. 4K
TOTAL	8 1K

4. UTILIZATION CURVE

Using 8% annual interest and 20 year amortization, the cost per
kilogram launched to GSO versus launch frequency is shown in Figure 121,
where vehicle cost is given as parameter. These preliminary estimates
will be refined when the complete system is designed, and a systems
analysis of the laser propulsion engine permits proper estimates of
vehicle costs. At present we note that a vehicle cost of $25000 results
in net launch costs of $40/kg, at a rate of 10, 000 metric tons per year.
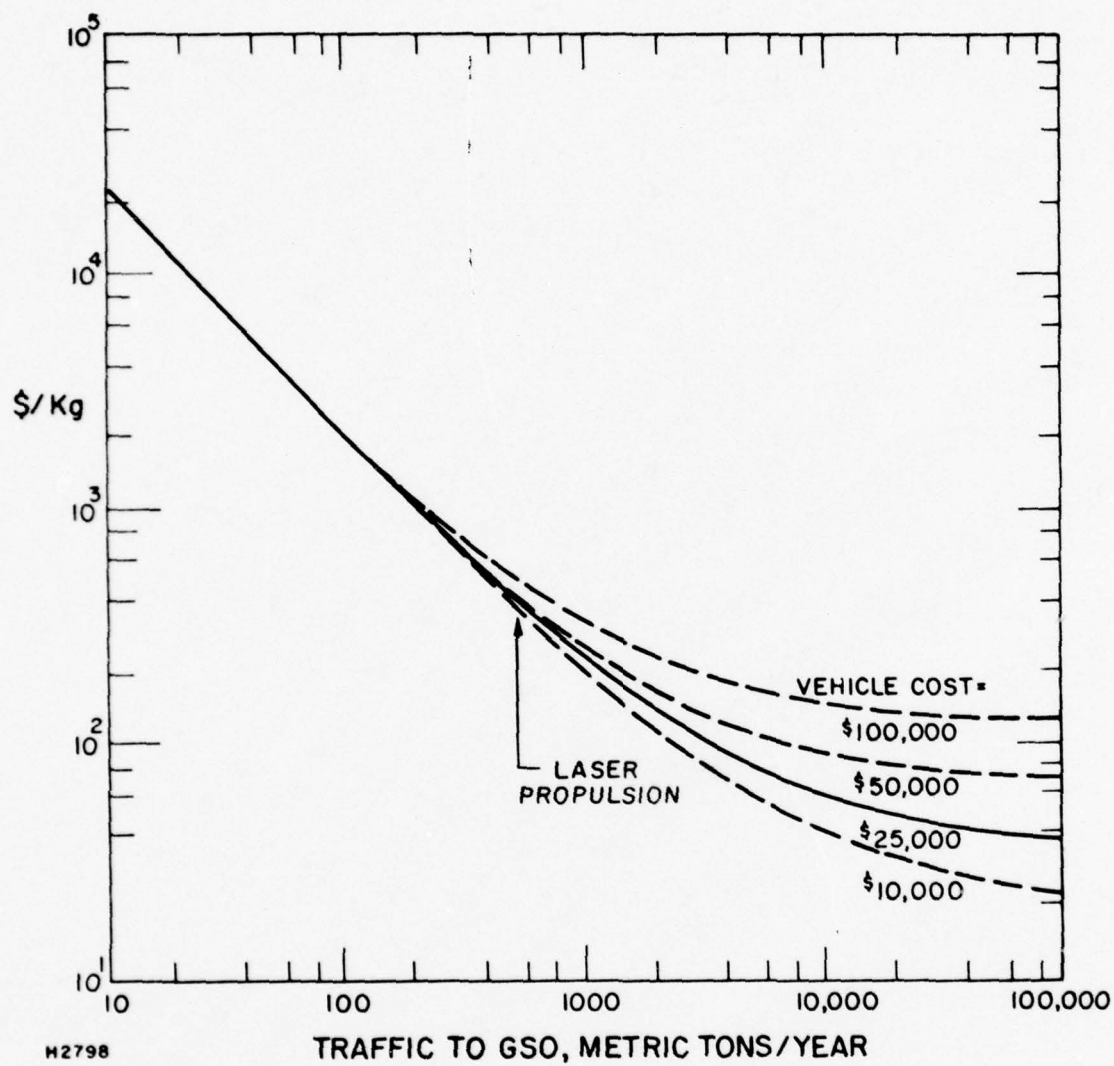
Figure 121   Transportation Cost for 1 Ton for Geosynchronous Orbit

215

VIII. CONCLUSION

An investigation of the potential and possible methods of laser propulsion has been completed. We summarize the results obtained to date.

Trajectory analysis identifies the optimal mission as insertion of a 1 ton (brennschluss weight) vehicle into a GEO transfer trajectory. The first 10^3 km would be powered by the ground laser station. Volume on the order of 10^5 ton/yr is feasible.

The laser required, allowing for propagation losses, would be $\sim 1.4 \times 10^9$ watt. We envisage a stacked array of phase-locked, repetitively pulsed air-breathing CO_2 EDL's. These can be arranged either as a phase-locked oscillator or an oscillator amplifier. Net efficiency anticipated is 20%.

A beam combiner (chandel) reflects the beam onto the beam director, which is a 20m diameter steerable mirror. Laser location on a mountain top ($\sim 10,000$ feet altitude) virtually eliminates atmospheric H_2O absorption. CO_2 net absorption is reduced to $\sim 10\%$ by the bleaching effect, and blooming correspondingly reduced. Use of phase correcting mirrors will give a 2 meter spot at 10^3 km, as required for the rocket engine.

Examination of various possible laser propulsion rocket engines leads us to select the double-pulse laser supported detonation wave (LSD) engine; an initial laser pulse evaporates a selected distribution of propellant, and a second pulse produces an LSD wave which heats the propellant uniformly

217

to a temperature on the order of 1 eV. The propellant then expands out of the engine. Engine efficiencies near 50% are predicted.

Preliminary analysis shows that launch of $\sim 10^4$ tons per year to geo-synchronous (maximum), at a cost of \$20/lb, should be feasible.

We conclude that laser propulsion offers a promising alternative method for economically conveying large amounts of material in units of $\sim 2/3$ ton (allowing for chemical kick-stage) to GEO. Construction and proof-testing of the laser propulsion engine on the largest pulsed lasers available is required as the next step.

REFERENCES

VOLUME I

1. Raizer, Y.P., "Heating of a Gas by a Powerful Light Pulse," Sov. Phys. JETP 21, 1009 (1965).

2. Edwards, A., Ferriter, N., Fleck, Jr. J.A., and Winslow, A.M., "A Theoretical Description of the Interaction of a Pulsed Laser and a Target in an Air Environment," Lawrence Livermore Laboratory, Rept. UCRL - 51489 (1973).

3. Boni, A.A., and Su, F.Y., "Theoretical Study of Laser Target Interactions," Science Applications Inc., Rept. SAI77-567LJ (1977).

VOLUME II

4. Summerfield, M., "The Liquid Propellant Rocket Engine in Princeton Aeronautical Paperbacks," Number 1, Liquid Propellant Rockets, Princeton University Press (1960).

5. Raizer, Yu. P. (1965) "Heating of a Gas by a Powerful Light Pulse," Soviet JETP, 21, No. 5, 1009.

6. D.H. Douglas-Hamilton, AERL private communication, (1976).

7. Wu, P., and Pirri, A.N., AIAA J. 14, No. 3, 390 (1976).

8. Jacob, J., and Mani, S., "Thermal Instability in High Pressure Laser Discharges," (1975).

9. Wilkins, R.L., "Theoretical Evaluation of Chemical Propellants," Prentice-Hall, Inc., Englewood Cliffs, N.J. (1963) p. 181.

10. Ferriso, C., et al., "High Temperature Infrared Emission and Absorption Studies," General Dynamics/Astronautics. Scientific Report AE61-0910, (1961).

11. Wood, A.D., Camac, M., and Gerry, A.E., Appl. Optics 10, 1877 (1971).

12. Avizonis, P.V., Butts, R., and Hegge, B., Appl. Optics 14, 1911 (1975).

13. Adiks, T., Arefyev, V., and Dianovklokov, V., Sov. JQE 5, 481 (1975).

14.   Valley, S. L., "Atmospheric Temperature, Density, Pressure and Moisture." Handbook of Geophysics and Space Environments, AFCRL, Office of Aerospace Res., U.S.A.F. 1965.

15.   Hermann, J., private communication.

16.   Lewis, P. F., and Trainor, D. W., AERL AMP 422 (Nov. 1974).

17.   Douglas-Hamilton, D.H. and Lowder, R.S., "AERL CO_2 Laser Kinetics Handbook," 1974.

18.   J. Herrmann, D.P., Greenwood, P. Kafalas. "Anticipated Propagation Conditions for High Energy Lasers at White Sands Missile Range," Contract DAAH01-75-C-1272.

19.   J. Herrmann, Private Communication.

20.   Alan Phillips, S.A.I., private communication.

21.   This theoretical estimate is quoted in the experimental paper by Bignell et al., next reference.

22.   Bignell, K., Saiedy, F., and Sheppard, P., J. Opt. Soc. Am. 53, 466 (1963).

23.   Roach, W., and Goody, R., Quart. J. Roy. Meteorol. Soc. (London) 84, 319 (1958).

24.   Roberts, R., Selby, J., and Biberman, L., Appl. Optics 15, 2085 (1976).

25.   Adiks, T., Aref'ev, V., and Dianov-Klokov, V.; Sov. J. Quant. Electron 5, 481 (1975).

26.   Burch, D., "Investigation of the Absorption of Infrared Radiation by Atmospheric Gases," Semi-Annual Technical Report, Aeronutronic Division, Philco Ford Corporation, Report U-4784 (January 1971).

27.   McCoy, J., Rensch, D., and Long, R., Appl. Opt. 8, 1471 (1969).

28.   Ludwig, C., Ferriso, L., and Abeyta, C., J. Quant. Spectr. and Rad. Transfer.

29.   McClatchey, R.A., et al., "AFCRL Atmospheric Absorption Line Parameters Compilation," Air Force Cambridge Research Laboratory, AFCRL-TR-73-0096, January 1973.

30.   Goody, R., Atmospheric Radiation, Vol. I Theoretical Basis, Oxford University Press (1964), p. 115.

31. H. Ashkenas af., Sherman in Rarefied Gasdynamics, J.H., de Leeuw Academic Press, New York (1966) Vol. 2, p. 84, F. Albini, AIAA J. 1535 (1965), F. Boynton, AIAA J., 5, 1703 (1967).

32. Burch, D., Singleton, E., and Williams, D., Appl. Optics 1, 359 (1962).

33. JANAF Thermomechanical Tables, Second Edition, U.S. National Bureau of Standards NBS-37, Government Printing Office (1971).

34. Bunkin, F., Konov, V.I., Prokhorov, A.M., and Fedorov, V.B., Zherf Pis. Red 9, 609 (1969) (English translation JETP Letters, 9, 371 (1969).

35. Raizer, P., Yu, Zhetp Pis. Red 11, 195 (1969) (English translation JETP Letters 11, 120 (1970).

36. Raizer, P., Yu, Zhetp (USSR) 48, 1508 (1965) (English translation, Soviet Physics JETP 21, 1009 (1965).

37. Junge, C., Chagnon, C., and Manson, J. of Meteor, 18, 81, (1961).

38. Nielsen, P., and Canavan, G., "Laser Absorption Waves in the Atmosphere," in Laser Interaction and Related Plasma Phenomena, Vol. 3A., Schwarz, H., and Hora, H., editors, Plenum Press (1973).

39. "Propagation through Atmospheric Aerosols," Semi-Annual Technical Report, AERL, July, 1975.

40. Schlier, R., Pirri, A., and Reilly, D., "Air Breakdown Studies, Avco Report AFWL-TR-72-74, February, 1973.

41. Hall, B., Maher, W., and Wei, P., "An Investigation of Laser Supported Detonation Waves," Boeing Report AFWL-TR-73-28, June, 1973.

42. See Lincoln Laboratory Optics Research Reports for the period 1970-1973.

43. Raizer, Yu., Soviet Physics JETP 31, 1148 (1970).

44. This statement is only correct if we neglect the effect of pressure on the degree of dissociation.

45. Smith, D.C., and Fowler, M., Appl. Phys. Lett. 22, 500 (1973).

46. Edwards, A., Ferriter, N., Fleck, J. and Winslow, A., "A Theoretical Description of the Interaction of a Pulsed Laser and a Target in a Laser Environment," Lawrence Livermore Laboratory, UCRL-51489, November 1973.

47.   Ferriter, N., and Winslow, A., "Calculated Intensity Threshold for the Maintenance of Laser Supported Detonation Waves with Various Electron Densities," Lawrence Livermore Laboratory, UCRL-51606.

48.   Stamm, M., and Nielsen, P., AIAA J. 13, 205 (1975).

49.   Kivel, B., "Radiation from Hot Air," AERL Research Report RR-79, October 1959.

50.   Van der Hulst, "Light Scattering by Small Particles," John Wiley and Sons Publishing, N.Y. (1957).

51.   Centano, M., J. Opt. Soc. Amer. 31, 244 (1941).

52.   Ockman, N., "Advances in Physics 7, 199 (1958).

53.   Neacy, W., 1976, private communication.

54.   Feinberg, R. and Roos, J., 1976, private communication.

55.   Boston Edison Inc., 1975, private communication.

56.   Air Products Inc., 1975, private communication.

APPENDIX A

ASTRODYNAMIC FUNDAMENTALS

This Appendix provides a very brief review of elementary astro-
dynamics, together with a derivation of the expressions for mission
velocity, etc., which are used in Section II of this report. It is based
primarily on class notes from Course 16.41, a graduate course in the
Department of Aeronautics at M.I.T., taught by one of the authors of
this report (P.K. Chapman). To facilitate comparison with the literature,
conventional units are used in this Appendix, except that specific results
used in the next are also given in the units of Table 1.

Law of Newtonian Gravitation: Two bodies of masses m_1, m_2,
located exert forces on each other given by

$$\underline{F}_1 = Gm_1 m_2 \underline{R} R^{-3} = m_1 \underline{\ddot{R}}_1 \tag{A-1a}$$

$$\underline{F}_2 = -\underline{F}_1 = m_2 \underline{\ddot{R}}_2 \tag{A-1b}$$

where $G = 6.67 \times 10^{-11} \text{N-m}^2/\text{kg}^2$

$$\underline{R} = \underline{R}_2 - \underline{R}_1$$

Then

$$\underline{\ddot{R}} = \underline{\ddot{R}}_2 - \underline{\ddot{R}}_1 = -Gm_1 R^{-3}\underline{R} - Gm_2 R^{-3}\underline{R}$$
$$= \mu R^{-3}\underline{R} \tag{A-2}$$

where $\mu = G(m_1 + m_2)$

223

The equation of relative motion of the two bodies is thus

$$\underline{R} + \mu R^{-3}\underline{R} = 0 \tag{A-3}$$

In what follows, unless otherwise stated one of the bodies will be the Earth and the second body will be a satellite, of so much smaller mass that we may take

$$\mu = Gm_{\oplus}$$

and regard $\ddot{\underline{R}}$ as the inertial rather than relative acceleration of the satellite (sine the gravitational attraction of the satellite does not move the Earth much). In this case, $\underline{R}$ is the geocentric position vector of the satellite.

Circular Orbits: One possible solution of the equation of motion (A-3), and the simplest possible case, is a circular orbit about the Earth, in which the centripetal acceleration of the satellite equals the gravitational acceleration:

$$v_c^2/R = \Omega^2 R = \mu/R^2 \tag{A-4}$$

where v_c is the orbital velocity, R is the (constant) orbital radius, Ω is the orbital angular velocity. Thus

$$v_c^2 = \mu/R \tag{A-5}$$

$$\Omega^2 = \mu/R^3 \tag{A-6}$$

From the last equation, the periods of two circular orbits of radii R_1 and R_2 are related by

$$T_1/T_2 = \left[R_1/R_2\right]^{3/2} \tag{A-7}$$

For very low orbit, with $R = R_o = 6378$ km, the radius of the Earth,

the acceleration is equal to the surface gravitational acceleration,
$g_o = 9.81$ m/sec^2, so that Eq. (A-4) gives

$$v_o = \gamma(g_o R_o) = 7.91 \text{ km/sec} \tag{A-8}$$

$$\Omega_o = \gamma(g_o/R_o) = \text{Schuler frequency} \tag{A-9}$$

The period of a very low orbit is thus the Schuler period, 84.4 min.
In general, the values of parameters for other orbits may be expressed in
terms of the low-orbit values; e.g., the radius of a geosynchronous
(24-hour) orbit is given by Eq. (A-7) as

$$R_a = T_s/T_o{}^{2/3} R_o = \frac{24 \times 60}{84,4}{}^{2/3} R_o = 6.63 R_o = 42270 \text{ km} \tag{A-10}$$

Radial Escape: Another very simple case is that of escape from
a radius R_1 to infinity, along a geocentric radius. The equation of motion
(A-3) gives

$$\ddot{R} = \frac{d}{dR}\left(\frac{1}{2}v^2\right) = -\mu/R^2$$

$$\tag{A-11}$$

or

$$v_1^2 - v_2^2 = 2\mu\left[\frac{1}{R_1} - \frac{1}{R_2}\right]$$

The minimum velocity at R_1 which is required to escape is given
by this with $v_2 = 0$, $R_2 = \infty$:

$$v_1^2 = 2\mu/R_1$$
$$= 2v_c^2 \tag{A-12}$$

from Eq. (A-5). The velocity required to escape from any point is thus
$\sqrt{2}$ times the circular velocity at that point. In particular, the velocity

225

required to escape from the surface of the Earth (neglecting aerodynamic drag, etc.) is

$$v_e = \sqrt{2} \ v_o = \sqrt{(2g_o R_o} \equiv 11.18 \ \text{km/sec} \qquad (A-13)$$

In the units of Table 1, Eq. (A-12) reads

$$v_1^2 = \frac{2}{r_1} = \frac{2}{1 + y_1} \qquad (A-12a)$$

More General Orbits: If we take the vector product of $\underline{R}$ with the equation of motion (A-3) we find

$$\underline{R} \times (\underline{\ddot{R}} + \mu \ R^{-3} \ \underline{R}) = \underline{R} \times \underline{\ddot{R}} = \frac{d}{dt} (R \times \dot{R}) \qquad (A-14)$$

since $\underline{R} \times \underline{R} = 0$ and $\underline{\dot{R}} \times \underline{R} = 0$. Thus the vector

$$h = \underline{R} \times \underline{\dot{R}} = \text{constant} \qquad (A-15)$$

When multiplied by the mass of the satellite, this vector gives the orbital angular momentum of the satellite: Eq. (A-15) is a statement of angular momentum conservation. Since

$$\underline{R} \cdot \underline{h} = \underline{R} . \ (\underline{R} \times \underline{\dot{R}}) = (\underline{R} \times \underline{R}) \cdot \underline{\dot{R}} = 0 \qquad (A-16)$$

the motion takes place in the plane normal to $\underline{h}$.

If now we take the vector product of h with Eq. (A-3), we obtain

$$
\begin{aligned}
\underline{\ddot{R}} \times \underline{h} &= \frac{d}{dt} (\underline{\dot{R}} \times \underline{h}) \ \text{(since } \underline{h} \ \text{constant)} \\
&= -\mu R^{-3} (\underline{R} \times \underline{h}) \\
&= -\mu R^{-3} [(R \times \dot{R})] \\
&= \mu R^{-3} [\ \underline{R}^2 \underline{R} - (\underline{R}.\underline{\dot{R}})\underline{R}]
\end{aligned}
\qquad (A-17)
$$

226

Now

$$\frac{d}{dt} \frac{1}{R} = \frac{d}{dt} (\underline{R}.\underline{R})^{1/2}$$

$$= - (\underline{R}.\underline{R})^{-3/2} \underline{R}.\underline{\dot{R}} \tag{A-18}$$

$$= - R^{-3} \underline{R}.\underline{\dot{R}}$$

so that Eq. (A-17) may be written

$$\frac{d}{dt} (\underline{\dot{R}} \times \underline{h}) = \mu \left[\frac{1}{R} \underline{\dot{R}} + \underline{R} \frac{d}{dt} \left(\frac{1}{R} \right) \right] \tag{A-19}$$

$$= \mu \frac{d}{dt} (\underline{R}/R)$$

Integration yields

$$\underline{\dot{R}} \times \underline{h} = \mu [\underline{R}/R + \underline{e}] \tag{A-20}$$

where $\underline{e}$ is a vector constant of integration. Taking the scalar product of $\underline{R}$ with this equation gives

$$R.(\dot{R} \times h) = (\underline{R} \times \underline{\dot{R}}).\underline{h} = h^2$$

$$= \mu[R + \underline{R}.e] \tag{A-21}$$

$$= \mu R(1 + e \cos f)$$

where f is the angle between $\underline{R}$ and $\underline{e}$. The equation of the orbit is thus

$$R = \frac{h^2/\mu}{1 + e \cos f} \tag{A-22}$$

This is the polar equation of a conic section, with origin at the focus. The type of conic section depends on the value of the constant e, as follows:

Circle: $e = 0$ Parabola: $e = 1$

Ellipse: $0 < e > 1$ Hyperbola: $e > 1$

Properties of Elliptic Orbit: From the definition (A-15)

$$h = R\dot{R} \sin \gamma = R \dot{R}_\perp \tag{A-23}$$

where γ is the angle between the velocity and the radius vector and $R_\perp$ is the component of velocity perpendlar to the radius vector; but, as the radius vector sweeps through the angle f, the perpendicular component of velocity of the tip is

$$\dot{R}_\perp = R \dot{f} \tag{A-24}$$

so that

$$h = R^2 \dot{f} = 2 \dot{A} \tag{A-25}$$

where $\dot{A}$ is the rate at which the radius vector sweeps out area in the ellipse. The area rate is thus a constant: this is Kepler's second law of planetary motion.

It is clear from Eq. (A-22) that R is a minimum when f = 0, so that f is the geocentric angle away from the direction of the point of closest approach to Earth in the orbit, which is called perigee. The point of maximum distance from Earth, called apogee, occurs when $f = 180^\circ$. From Figure A-1 and Eq. (A-22); the sum of perigee and apogee radii is

$$R_p + R_a = 2a = \frac{h^2}{\mu} \left(\frac{1}{1+e} + \frac{1}{1-e} \right)$$

$$= \frac{2h^2}{\mu(1-e^2)} \tag{A-26}$$
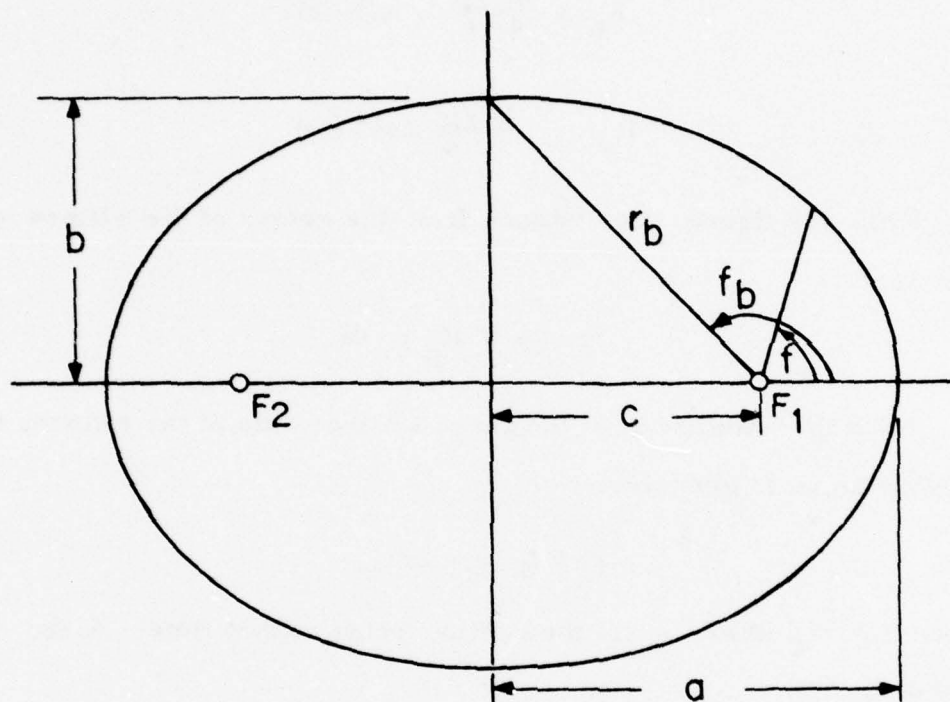
H2554

Figure A-1   Elliptic Orbit Nomenclature

Thus

$$h^2 = \mu a(1 - e^2)$$ (A-27)

and

$$R_p = \frac{h^2/\mu}{1 + e} = a(1 - e)$$ (A-28)

$$R_a = \frac{h^2/\mu}{1 - e} = a(1 + e)$$ (A-29)

From the figure, the distance from the center of the ellipse to a focus is

$$c = a - R_p = ea$$ (A-30)

When the satellite is at the tip of a minor axis of the ellipse, the geocentric angle is given by

$$\cos f_b = -c/r_b$$ (A-31)

from the figure, where r_b is the radius vector at that time. Also, from Eq. (A-22),

$$r_b = \frac{h^2/\mu}{1 - ec/r_b}$$

or

$$\begin{aligned} r_b^2 &= (h^2/\mu + ec)^2 = [a(1 - e^2) + e^2 a]^2 = a^2 \\ &= c^2 + b^2 = e^2 a^2 + b^2 \end{aligned}$$ (A-32)

Thus the eccentricity e is given in terms of the semi-major and semi-minor axes of the ellipse by

$$e^2 = 1 - b^2/a^2$$ (A-33)

230

The area of an ellipse is πab. If the period of the orbit is T, the rate at which area is swept out is

$$\frac{\pi ab}{T} = \frac{1}{2} h \tag{A-34}$$

from (A-25). The period of the orbit is thus given by

$$T = \frac{2\pi ab}{h} = \frac{2\pi a^2 \sqrt{(1-e^2)}}{\sqrt{(\mu a(1-e^2))}} = 2\pi a^{3/2}/\sqrt{\mu} \tag{A-35}$$

and depends only on the semi-major axis. Thus all orbits having the same maximum diameter have the same period.

To obtain an expression for velocity in the orbit, return to the equation of motion (A-3) and take the scalar product with $\dot{\underline{R}}$:

$$\underline{R} . \ddot{\underline{R}} = \frac{1}{2} \frac{d}{dt} (\dot{\underline{R}} . \dot{\underline{R}}) = \frac{d}{dt} \left(\frac{1}{2} v^2 \right)$$

$$= -\mu R^{-3} \underline{R} . \dot{\underline{R}} \tag{A-36}$$

$$= \mu \frac{d}{dt} \left(\frac{1}{R} \right)$$

the last step being from Eq. (A-18). Integration gives

$$\frac{1}{2} v^2 = \frac{\mu}{R} + C \tag{A-37}$$

where the integration constant C may be obtained from conditions at perigee, where the velocity is $v_p = R_p \dot{f}$ (being perpendicular to the radius there). Thus,

$$C = \frac{1}{2} v_p^2 - \mu/R_p$$

$$= \frac{1}{2} (R_p \dot{f})^2 - \mu/R_p$$

231

$$= \frac{1}{2}\left(h/R_p\right)^2 - \mu/R_p \qquad \text{(from (A-25)}$$

(A-38)

$$= \frac{\mu a(1-e^2)}{2a^2(1-e)^2} - \frac{\mu}{a(1-e)} \quad \text{(from A-27), (A-28)}$$

$$= -\frac{\mu}{2a}$$

so that, finally, Eq. (A-37) reads

$$v^2 = \mu\left(\frac{2}{R} - \frac{1}{a}\right) \qquad\qquad \text{(A-39)}$$

This very useful expression is sometimes known as the vis-viva integral. Note that velocity in an orbit at a given radius depends only on the semi-major axis of the orbit. In particular, if the semi-major axis is infinite, so that the vehicle is on an escape orbit Eq. (A-39) reduces to

$$v^2 = \frac{2\mu}{R} \qquad\qquad \text{(A-40)}$$

which is the same form found for radial escape (Eq. (A-12). Thus escape velocity from any point is independent of the direction in which the vehicle is projected.

Transfer Ellipse to Geosynchronous Orbit

If a transfer ellipse with apogee at geosynchronous altitude (A-10) is required, the vis viva integral (A-39) can be used directly to give the required injection velocity only if the perigee altitude (and hence the semi-major axis) is specified. However, from Eq. (A-15), the magnitude of the orbital angular momentum h at any point is equal to the orbit radius times the component of orbital velocity perpendicular to the orbit radius. From the geometry of Figure A-2, just at burnout we thus have

$$h = v_1 R_1 \sin(\gamma - \delta_1) \qquad\qquad \text{(A-41)}$$

232
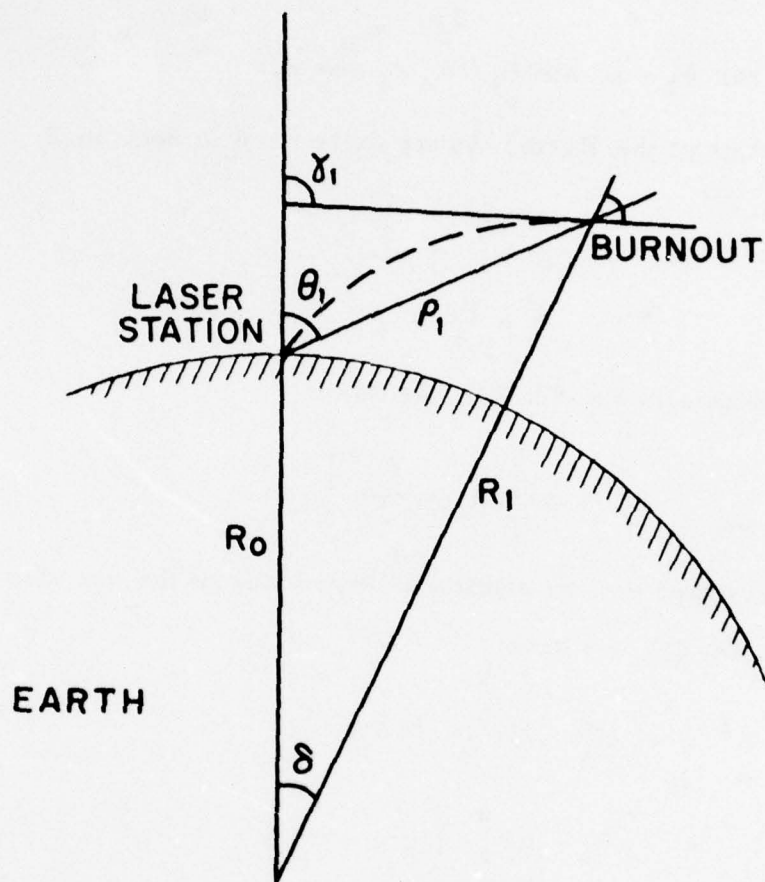
H2553

Figure A-2   Geometry of Burnout

233

where γ_1 is the flight path angle at burnout, relative to the local vertical at the laser station, and δ_1 is the geocentric angle traversed during boost. Clearly

$$\tan \delta_1 = \rho_1 \sin \Theta_1 / (R_o \rho_1 \cos \Theta_1) \qquad (A-42)$$

where R_o is the radius of the Earth. In the units used in Section II, this gives Eq. (108).

From Eq. (A-29)

$$e = \frac{Ra}{a} - 1 \qquad (A-43)$$

and, if we substitute this in Eq. (A-27), we find

$$h^2 = \mu \left[2R_a - \frac{R_a^2}{a} \right] \qquad (A-44)$$

The semi-major axis may now be eliminated by means of the vis viva integral. With Eq. (A-41), we have

$$
\begin{aligned}
h^2 &= v_1^2 R_1^2 \sin^2(\gamma_1 - \delta_1) \\
&= 2\mu R_a - \mu R_a^2 \left(\frac{2}{R_1} - \frac{v_1^2}{\mu} \right) \\
&= 2\mu R_a^2 \left(\frac{1}{R_a} - \frac{1}{R_1} \right) v_1^2 R_a^2
\end{aligned}
\qquad (A-45)
$$

whence, finally

$$v_1^2 = 2\mu \left(\frac{1}{R_1} - \frac{1}{R_a} \right) \bigg/ \left(1 - \frac{R_1^2}{R_a} \sin^2 (\gamma_1 - \delta_1) \right)$$

which gives the mission velocity Eq. (107) for a transfer ellipse to GSO.

Circularization ΔV

Finally, we calculate the ΔV required to circularize a coplanar transfer ellipse to GSO at geosynchronous altitude. The expression (110)

234

for the velocity at apogee in the transfer orbit is obtained directly by noting that $a = 2(R_p R_a)$, so that Eq. (A-39) gives

$$v_a^2 = 2\mu \left(\frac{1}{R_a} - \frac{1}{R_p R_a} = \frac{2\mu R_p}{R_a(R_p R_a)} \right) \tag{A-46}$$

For the applications in Section II, where the perigee radius is not directly known, a more useful expression is found by equating the orbital angular momentum to that at burnout, given by Eq. (A-41)

$$h = v_a R_a = v_1 R_1 \sin(\gamma_1 - \delta) \tag{A-47}$$

so

$$v_a = v_1 \frac{R_1}{R_a} \sin(\gamma_1 - \delta_1) \tag{A-48}$$

The circular velocity at synchronous altitude is given by (A-5) as

$$v_c = \sqrt{\frac{2}{R_a}} \tag{A-49}$$

so that the ΔV required of the circularization kick stage is

$$\Delta V_k = \sqrt{\frac{2}{R_a}} - v_1 \frac{R_1}{R_a} \sin(\gamma_1 - \delta_1) \tag{A-50}$$

which is equivalent to Eq. (172)

Notice that, if Eq. (A-48) is used in Eq. (A-45), one obtains

$$\frac{1}{2} v_1^2 - \frac{\mu}{R_1} = \frac{1}{2} v_a^2 - \frac{\mu}{R_a} \tag{A-51}$$

which states that the sum of kinetic and gravitational potential energy of the vehicle at injection to the transfer ellipse is equal to that at apogee. Thus, Eq. (A-45) could have been obtained simply from energy conservation.

APPENDIX B

PRELIMINARY SYSTEM CONCEPT

1. AEROSOL INJECTION

The detonation-wave laser propulsion (LP) engine requires a uniform distribution of propellant gas in the chamber before the laser supported detonation wave travels through it. This distribution may be prepared by expansion of gas evaporated from a condensed phase using a preliminary laser pulse; it may also be prepared by electric-arc induced heating of a condensed propellant layer. In this Appendix we discuss a third method, the generation of an aerosol whose mean density equals that required in the propellant.

If an aerosol is generated and ejected into the vacuum from the engine feedplate, then provided the particles do not evaporate too rapidly in the interpulse period, when the main laser pulse arrives the aerosol will be evaporated extremely rapidly. The released gas, expanding in all directions from each droplet, will provide a uniform gaseous propellant. The laser pulse, having propagated (by evaporating the droplets) through the aerosol to the end plate, will then strike a detonation wave which will travel back through the propellant gas, thus heating it to the required levels. We will examine aerosol evaporation, generation and distribution.

2. AEROSOL EVAPORATION

The behaviour of a droplet in a vacuum is predicted from first principles by calculating the energy loss rate due to evaporation and allowing for the effect of the consequent temperature decrease on the evaporation rate, using the Clapeyron equation. The rate of change of radius r will be

$$\frac{dr}{dt} = -\frac{1}{4} \frac{n\,\bar{c}\,M}{\rho\,n_o} \qquad (B-1)$$

where $\bar{c}$ is local soundspeed, M molecular weight, ρ droplet density and n_o Avogadro's number. The local gas density n near the droplet may be taken as that causing the vapour pressure (obtained from Clapeyron's equation), so that:

$$n = n' \cdot \left(\frac{T'}{T}\right)\left(\frac{P_o}{760}\right) \frac{e^{-LM/RT}}{\sqrt{T}} \qquad (B-2)$$

where n' is Loschmidt's number, $T' = 273^o K$, $p_o = 5.67 \times 10^9$ for H_2O, and L is the droplet vaporization latent heat. Since the heat loss rate will be

$$\frac{dq}{dt} = \frac{4}{3}\pi r^3 \rho\, C_p \frac{dT}{dt} = L \cdot 4\pi\rho r^2 \frac{dr}{dt} \qquad (B-2a)$$

where C_p is the droplet specific heat, we obtain

$$T_1 - T = \frac{3L}{C_p} \ell n \left(\frac{r_1}{r}\right) \qquad (B-3)$$

where T_1 and r_1 are the initial values of temperature and radius. Combining Eqs. (B-1), (B-2) and (B-2a) we obtain the differential equation for the droplet temperature as:

$$\frac{dT}{dt} = -\frac{3\,AL}{r_1 C_p T} \cdot e^{\frac{C_p}{3L}(T_1-T) - LM/RT} \qquad (B-4)$$

where A is a numerical constant; $A = 1.25 \times 10^9$ cm^{o}K/sec for H_2O. Supposing that T is limited to (relatively) small excursions, Eq. (B-4) can then be integrated and yields an expression for droplet radius:

$$r = r_1 \left[1 + \left(\frac{LM}{RT_1} - \frac{C_p T_1}{3L} \right) \cdot \frac{3AL}{r_1 C_p T_1^2} \ e^{-LM/RT_1} t \right]^{-1/(3L^2 M/RC_p T_1^2 - 1)} \qquad (B-5)$$

The fractional mass loss is then

$$\frac{\Delta m}{m} = 1 - \left(\frac{r}{r_1} \right)^3 . \qquad (B-5a)$$

We note that if the droplet undergoes a phase change and freezes, which will happen if a suitable crystallizing nucleus is present, since the droplet will become supercooled very soon after its exposure to the vacuum, then the fractional radius change required to induce freezing will be:

$$\frac{r_2}{r_1} = \left(1 + \frac{L'\rho'}{L\rho} \right)^{\frac{1}{3}} \qquad (B-6)$$

where L' is the latent heat and ρ' the density of ice. Consequently $\sim 5\%$ of the radius is lost in the phase change for the freezing of H_2O droplets.

Combining this with Eqs. (B-5) and (B-5a) gives the fractional mass loss as function of initial radius for various times after exposure to the vacuum. This is shown in Figure B-1, where the values of $\Delta m/m$ are shown for both frozen and supercooled droplets.

For a typical pulsed laser engine design, the interpulse period would be 10 msec. It is probable that droplets remain supercooled for this period. We observe that for droplets larger than 20 μm in diameter, less than 10% of the mass would be lost to evaporation in this period. Thus if an aerosol of this type could be created in vacuo, it would exist for long enough to be used.

239

Figure B-1 Water Droplet Injected into Vacuum:
Mass Fraction Lost in Time t
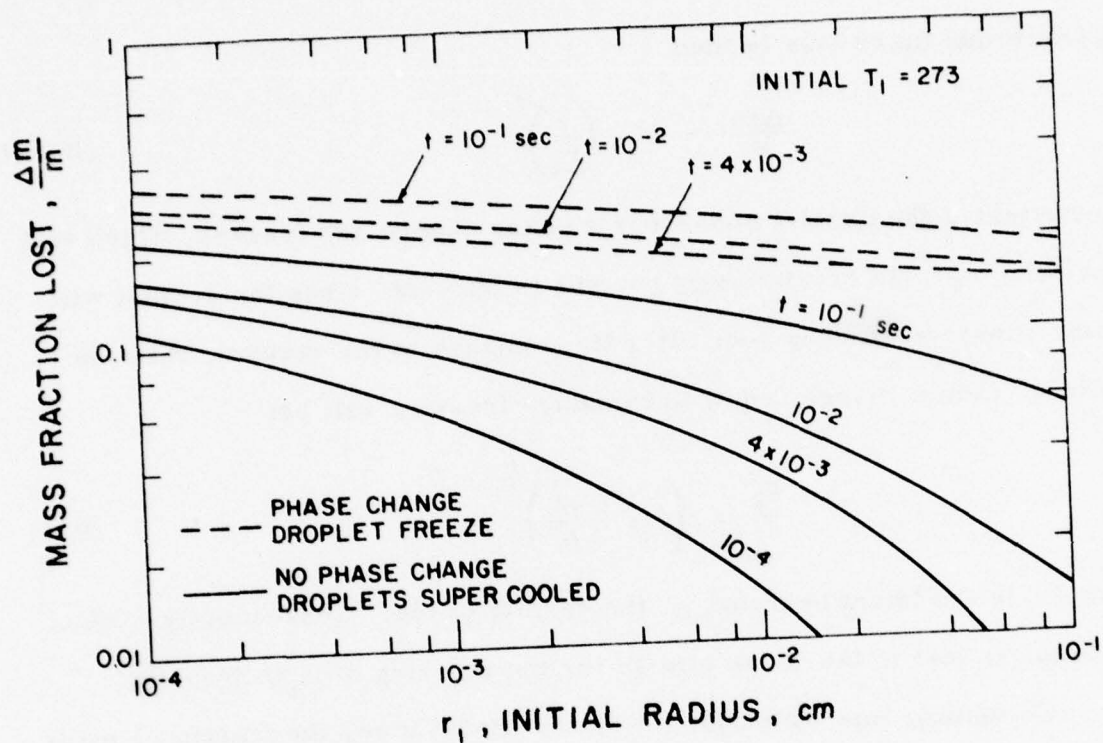
$$\frac{r}{r_I} = \left[1 + \left\{\frac{LM}{RT_I} - \frac{C_pT_I}{3L}\right\} \cdot \frac{3AL}{r_I C_pT_I^{\,2}} \cdot e^{-LM/RT_I \cdot t}\right]^{1/\left[1 - 3L^2 M/RC_pT_I^{\,2}\right]}$$

$$\left.\frac{\Delta m}{m}\right|_{\substack{\text{SUPER}\\\text{COOLED}}} = 1 - \left\{\frac{r}{r_I}\right\}^3 \qquad\qquad \left.\frac{\Delta m}{m}\right|_{\substack{\text{PHASE}\\\text{CHANGE}}} = 1 - \left\{0.950\,\frac{r}{r_I}\right\}^3$$

G5564

240

3. AEROSOL PRODUCTION AND DISTRIBUTION

Whereas the stability of an aerosol in vacuo appears to be satisfactory for our purposes, its production and distribution is more problematical. The main difficulty is that although aerosols can be produced in air by inducing a Rayleigh instability at the interface of a liquid stream or film and a gas, in a vacuum this is impossible. We are therefore forced to use the Rayleigh jet instability. We note that alternate methods, such as generation of droplets by high electric fields, while theoretically possible,[1,2] do not permit a large decrease in droplet radius over that produced by the jet instability. A useful rule of thumb concerning the latter is that the mean droplet diameter is roughly twice the jet diameter.[3] Since we require droplets with diameters near the laser wavelength of 10 μm, at which Mie absorption (which corresponds to the maximum absorption efficiency per unit mass) will become important, this implies that we require an aerosol plate with a very large number of very small holes, through which the liquid is forced by a high pressure difference. The velocity of the emergent droplets will then be $u = \sqrt{p/\rho}$, where p is the stagnation pressure. For a continuously operating droplet source, we require that the droplets travel a distance during the interpulse phase equal to that traversed by the detonation wave during the main laser pulse. Thus the detonation chamber length is

$$d = u \, \tau_i = V \, \tau_p$$

(1) Peskin, R. L. and Raco, R. J., Drop Size from a Liquid Jet in a Longitudinal Electric Field, Technical notes, AIAA Journal, 2, 781, (1964).

(2) Lapple, C. E., Electrostatic Phenomena with Particulates, Adv. in Chem. Eng. 8, 1 (1970), (A. P. New York).

(3) Hidy, G. M. and Brock, J. R., The Dynamics of Aerocolloidal Systems, Pergamon, 1970.

where τ_i and τ_p are the interpulse and laser pulse durations, and V is the detonation wave velocity. The latter is given by

$$V = V_o \left[\frac{\phi}{\rho_c} \right]^{\frac{1}{3}}$$

where

$$V_o = \left[2(\gamma^2 - 1) \right]^{\frac{1}{3}} = 1.24$$

for H_2O vapor, ρ_c is the aerosol mass density, and ϕ is laser flux density. Now the aerosol density must be

$$\rho_c = \frac{\dot{m} \tau_i}{u \tau_i A_c}$$

where the mass flow $\dot{m} = A_j u \rho$; A_c is chamber area and A_j is combined droplet jet area. Consequently

$$\rho_c = \frac{A_j}{A_c} \cdot \rho \, . \tag{B-7}$$

The density needed in the detonation chamber must be at least enough to provide a Mie absorption length less than the chamber length. The Mie absorption length[4] for H_2O at 10.6 μm may be written

$$L_{Mie} = \frac{4.44 \times 10^{-3}}{\rho_c} \text{ cm.}$$

Since we require

$$L_{Mie} \leq d, \text{ then } \frac{4.4 \times 10^{-3}}{\rho_c} \leq \tau_p V_o \left[\frac{\phi}{\rho_c} \right]^{\frac{1}{3}}$$

(4) Reilly, J. P. et al., Multiple Pulse Propagation in Fog, Rain and Dust at 10.6 μm, Interim Report, 30 Sept. 1975 to 1 April 1976. Contract No. N00173-76-C-0059 (ONR).

or

$$\rho_c \geq \left[4.4 \times 10^{-3}/(\tau_p V_o \phi^{\frac{1}{3}}) \right]^{\frac{3}{2}} .$$

(B-8)

$$\rho_c \geq 2.36 \times 10^{-4} \text{ g cm}^{-3}, \text{ for } \tau_p \approx 20 \ \mu\text{sec and } \phi \sim 10^7 \text{ W/cm}^2$$

Then the open fraction of the aerosol plate must be

$$\frac{A_j}{A_c} > 2.36 \times 10^{-4} .$$

Thus considering 10 μm diameter jet holes, which will produce droplets at the upper limit of acceptable diameter, we note using Eq. (B-7) that we will require more than 300 such holes per square centimeter of detonation chamber aerosol plate. This is a considerable engineering problem.

Let us ignore for a moment the exact mechanism of droplet formation. It should be noted that large droplets will be shattered very rapidly by the laser pulse,[4] thus producing smaller particles whose Mie absorption efficiency will be much higher. For fluxes $\phi \geq 10^7$, explosive vaporization and shattering will occur in particles with radius $r \geq 10 \ \mu$m, and in a time scale on the order of the sound travel time across the droplet[4] (about 1 μsec for $r > 10 \ \mu$m droplets). It is thus imaginable that we distribute larger aerosol particles and allow the natural shattering process to provide us with an efficiently absorbing aerosol of Mie droplets. Then the number of aerosol-generating holes is relaxed. We take the above numbers for the case of a large pulsed laser, and obtain $\tau_p = 20 \ \mu$sec, $\tau_i = 4 \times 10^{-3}$ sec. Then taking the flux as 10^7 W/cm^2, lower limit of surface breakdown, we have $d = V\tau_p$, $V = V_o (\phi/\rho_c)^{1/3}$; taking $\rho_c = 2.36 \times 10^{-4}$, as above, then $V = 9.31 \times 10^5 \approx 10^6$ cm/sec, and $d = 18.6$ cm. Then the velocity u is

243

$$u = \frac{\tau_p}{\tau_i} V = 5 \times 10^3,$$

which implies a stagnation pressure $p = \rho_u^{\ 2} = 25$ atm, or 355 psi. The mass flow $\dot{m} = A_j u \rho$ is then 1.18 g/sec. For a 500 kW laser the peak power is 10^8 W. Area of the aerosol plate should therefore be ~ 10 cm^2 in order to get 10^7 W/cm^2, so the total mass flow will be 11.8 g/sec, and the enthalpy per gram will be 4.24×10^4 J.

The stagnation pressure (355 psi) is lower by a factor of 5 than the pressure usually used for producing unstable jets that generate fine aerosols. We note that a further possibility would be to produce a sufficiently fine aerosol with the conventional stagnation pressure (~ 1500 psi). The droplets would, in this case, be traveling away from the plate at more than twice the required velocity. They could be decelerated by changing the droplets and using properly arranged electric fields. This arrangement, however, would greatly improve the complexity of the laser feed. It appears preferable to find ways of producing aerosols (e.g., by colliding jets) using the stagnation pressure above (355 psi). Experimental work is needed to determine:

1) Whether adequately fine aerosols can be produced at this stagnation pressure.

2) Whether the laser beam will efficiently shatter oversized droplets, thus producing a medium which will absorb it efficiently.

While it is possible that electrostatic aerosol production or ultrasonic jet disintegration could be used to produce the small droplets needed, it appears at present as though alternate methods of producing the required propellant distribution will be easier to handle and cheaper to produce.

APPENDIX B

REFERENCES

1. Peskin, R. L. and Raco, R. J., Drop Size from a Liquid Jet in a Longitudinal Electric Field, Technical notes, AIAA Journal, 2, 781, (1964).

2. Lapple, C. E., Electrostatic Phenomena with Particulates, Adv. in Chem. Eng. 8, 1, (1970), (A. P. New York).

3. Hidy, G. M. and Brock, J. R., The Dynamics of Aerocolloidal Systems, Pergamon, 1970.

4. Reilly, J. P. et al., Multiple Pulse Propagation in Fog, Rain and Dust at 10.6 μm, Interim Report, 30 Sept. 1975 to 1 April 1976. Contract No. N00173-76-C-0059 (ONR).

APPENDIX C

THERMODYNAMIC PROPERTIES OF SELECTED PROPELLANTS

The available thermal energy for conversion to kinetic energy and ultimately to specific impulse is most conveniently observed for a specific gas on a Mollier Chart. This chart provides the functional form of h (p, T, ϕ) and s (p, T, ϕ) where h is the enthalpy, s is the entropy, p is the pressure, T is the temperature, and ϕ is a measure of the "chemical" state of the gas, i.e., whether it is dissociated or ionized, etc. For a simple system thermodynamic variables (h, s) are a function of only two variables p and T. At elevated temperatures ϕ may be considered as a compressibility factor. Steady propulsion system are most conveniently described by pressure and temperature. Unsteady (or pulsed) systems naturally favor the use of two different thermodynamic variables - the specific internal energy and the density.

1. H_2O

Water is one of our most common chemical compounds. We recognize water in its solid state as ice, in its liquid state, and of course in its gaseous state as steam. Much is known about water at these low temperatures ($\leq 1000°K$) since it has played such a big part in steam generators as well as many other technological applications. For our laser propulsion applications we require high-temperature properties of H_2O at sub- and super-atmospheric pressure levels.

In order to underline the fact that H_2O exhibits rather unique behavior we first describe the variation of the ratio of specific heats γ with T ($°K$) and

247

p (atm). At very low temperatures $\gamma = 4/3$ which is typical for a polyatomic gas, however as the temperature increases there is very little range where γ may be approximated to be a constant.

Figure C-1 shows $\gamma = \gamma \, (p, T)$ for both equilibrium and frozen chemistry as computed at AERL using an equilibrium chemistry code. The increase of γ between $2000^{\circ}K$ and $3000^{\circ}K$ is a result of the dissociation of H_2O since dissociation essentially makes the gas more diatomic - or at very high temperatures more monatomic. This behavior can be seen in Figures C-2 to C-4 where we display the composition of H_2O at 1, 10, and 50 atm.

The Mollier Chart for H_2O is given in Figure C-5 where we have the pressure and temperature on the enthalpy-entropy plane. Note that the dashed lines correspond to the compressibility factor

$$Z = 0.2196 \, \frac{p \text{ (atm)}}{\rho \text{ (gm/cm}^3) \, T \, (^{\circ}K)} \tag{C-1}$$

from Z, p, and T we can compute $\dot{\rho}$ for any position on the chart.

2. OXYGEN, O_2

In Figure C-6 we show the Mollier Chart for oxygen. We note immediately that in the temperature and pressure range of the chart (same as that for H_2O) there is less available enthalpy. Furthermore, at first glance the efficiencies of constant entropy expansion processes appear to be inferior to H_2O. In general, the shape of the O_2 chart is the same as that of H_2O. This statement can not be made for N_2.

3. NITROGEN, N_2

In Figure C-7 we display the nitrogen Mollier Chart. The general shape of this chart is different from that of H_2O and O_2. Note the region at high pressures which is not very influenced by dissociation effects. This
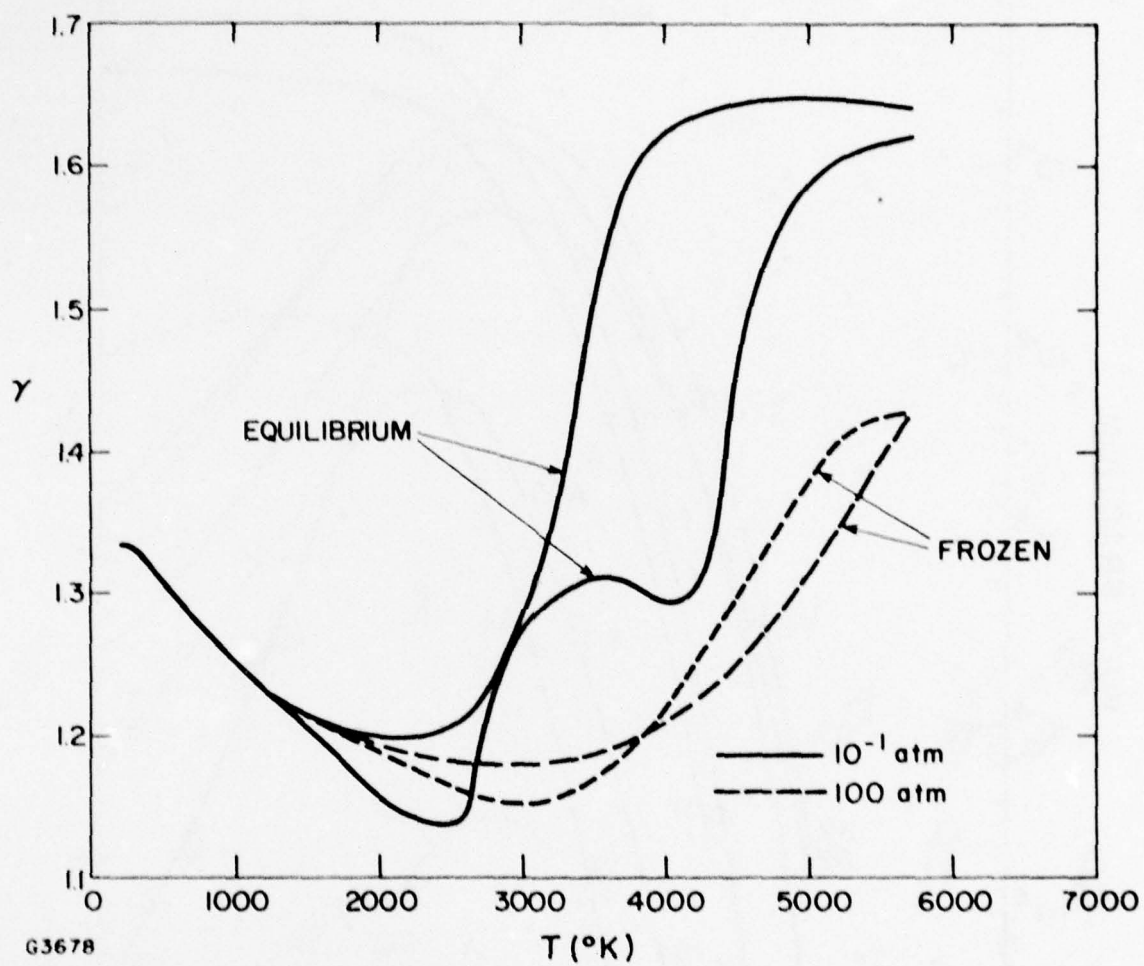
248

Figure C-1   Calculated Variation of γ for H_2O under Frozen and
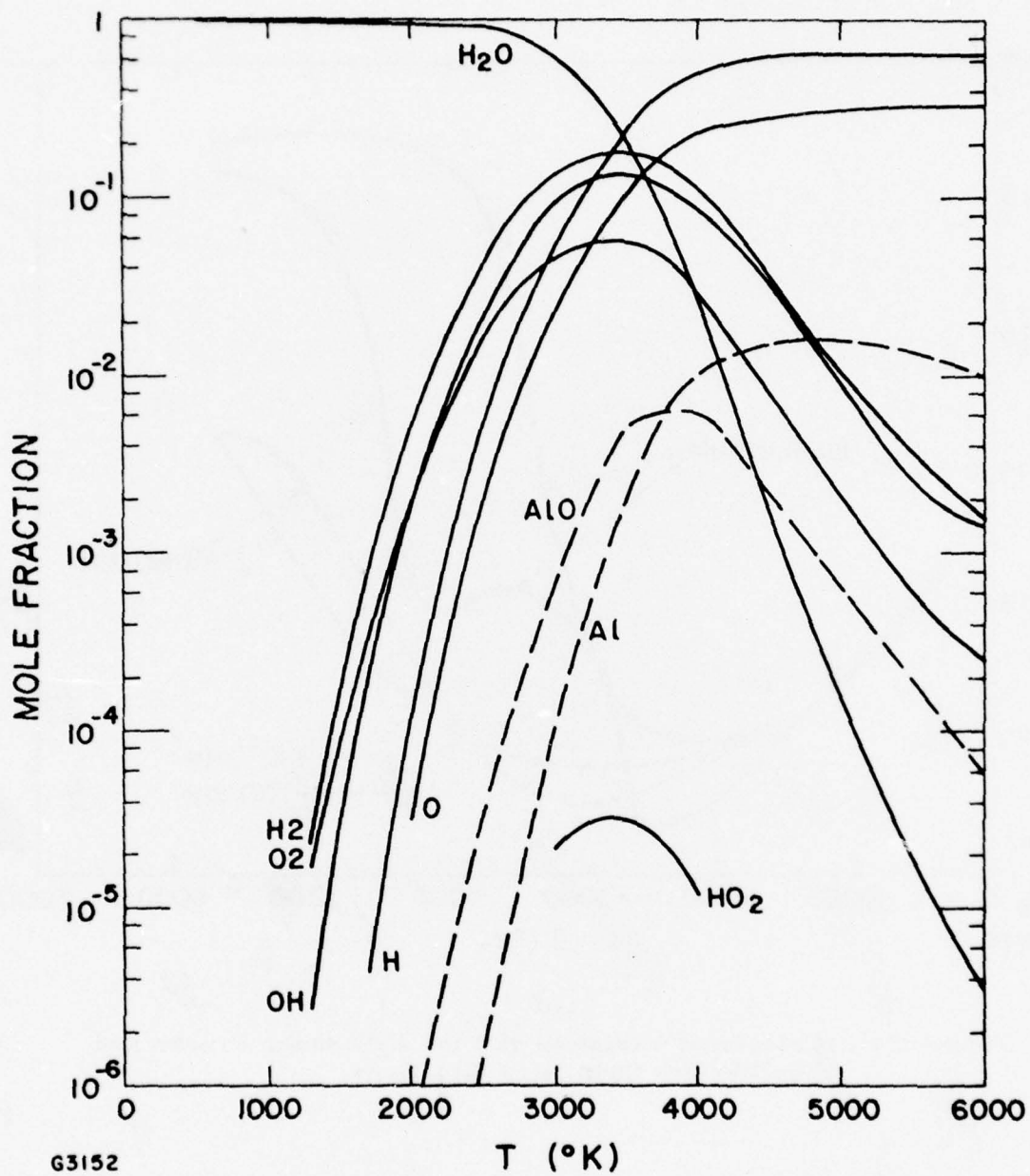Equilibrium Chemistry Situations

G3678

249

Figure C-2 H_2O Composition at 1 atm

G3152

250

MOLE FRACTION

H_2O

ALO

Al

OH

H

H2

O2

O

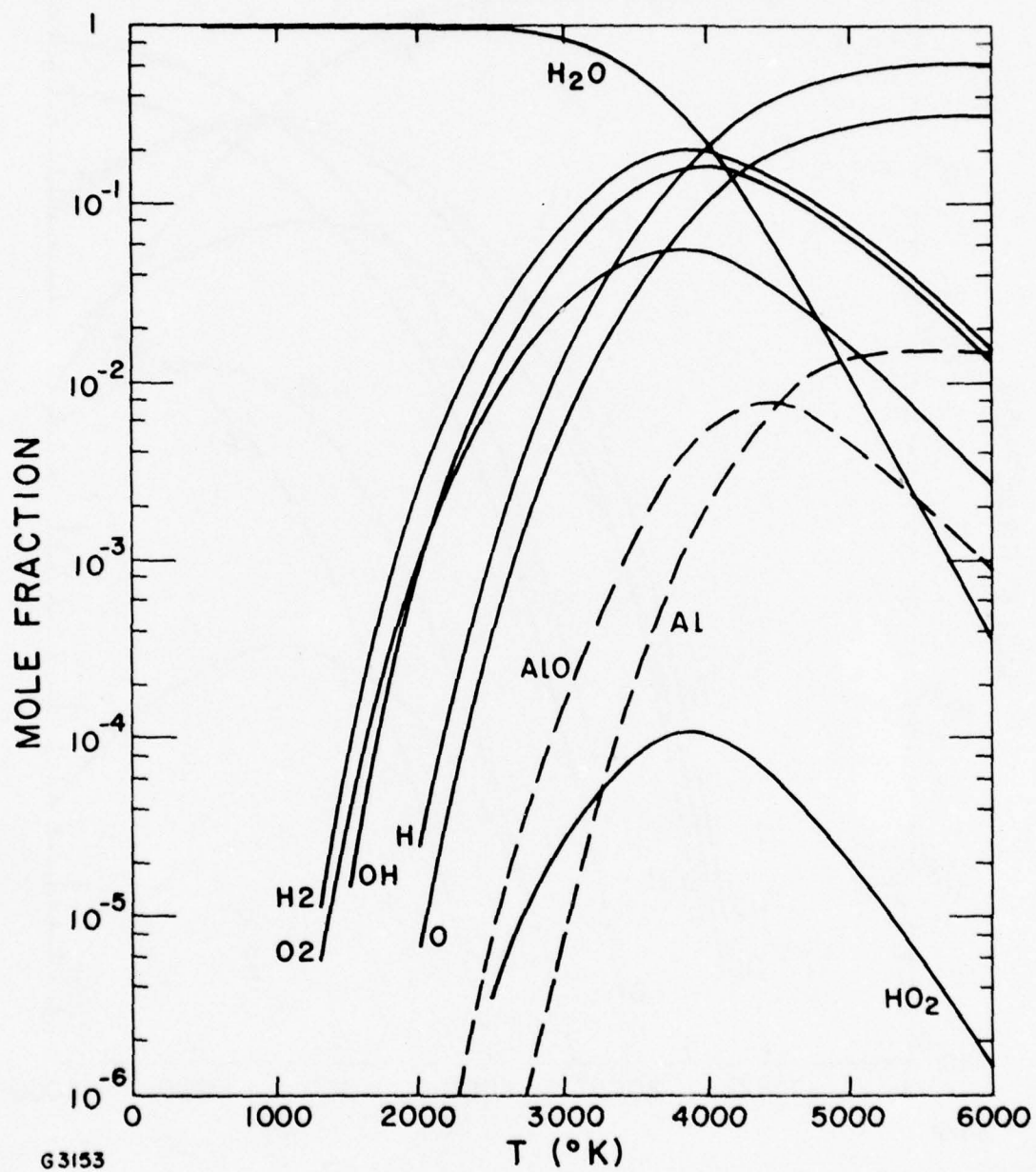HO_2

T (°K)

G3153

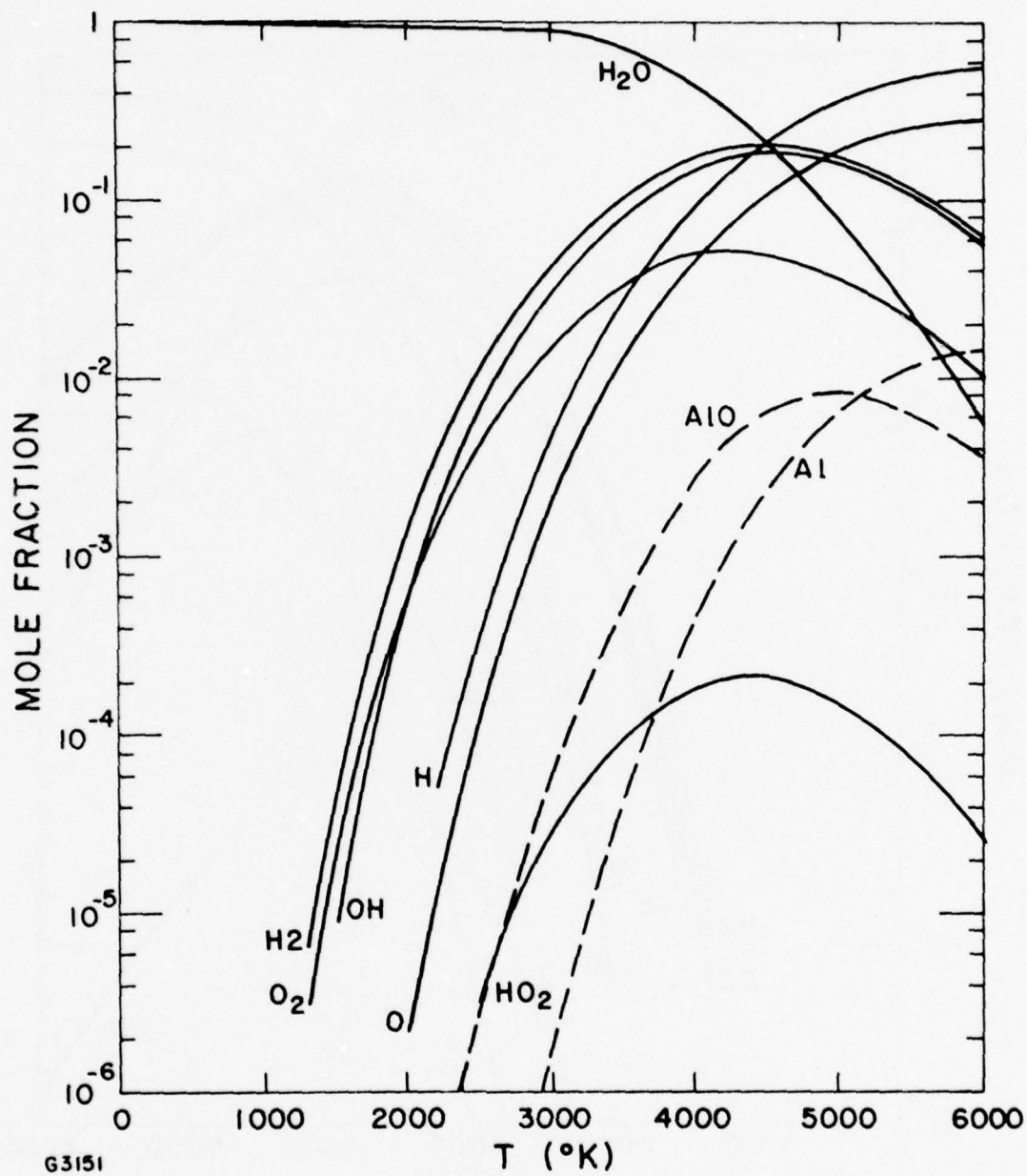Figure C-3 H_2O Composition at 10 atm

251

Figure C-4 H_2O Composition at 50 atm
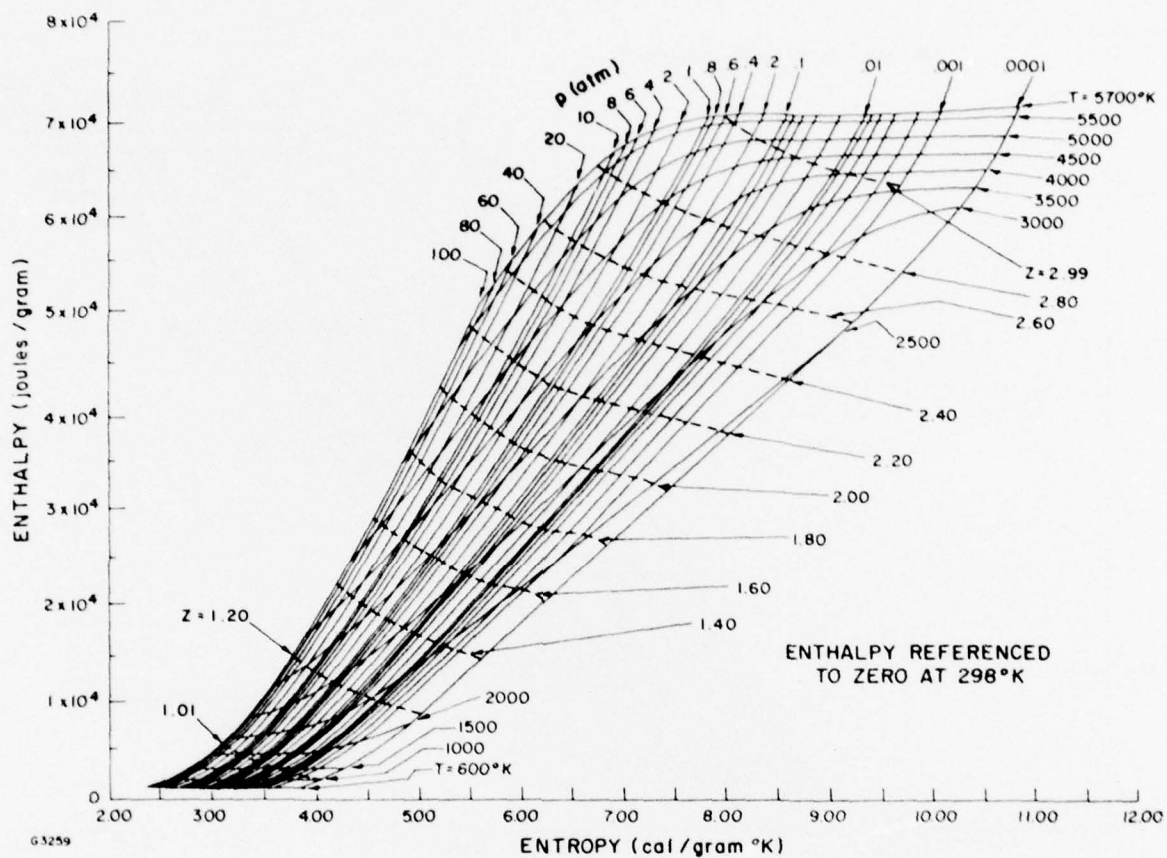
G3151

252

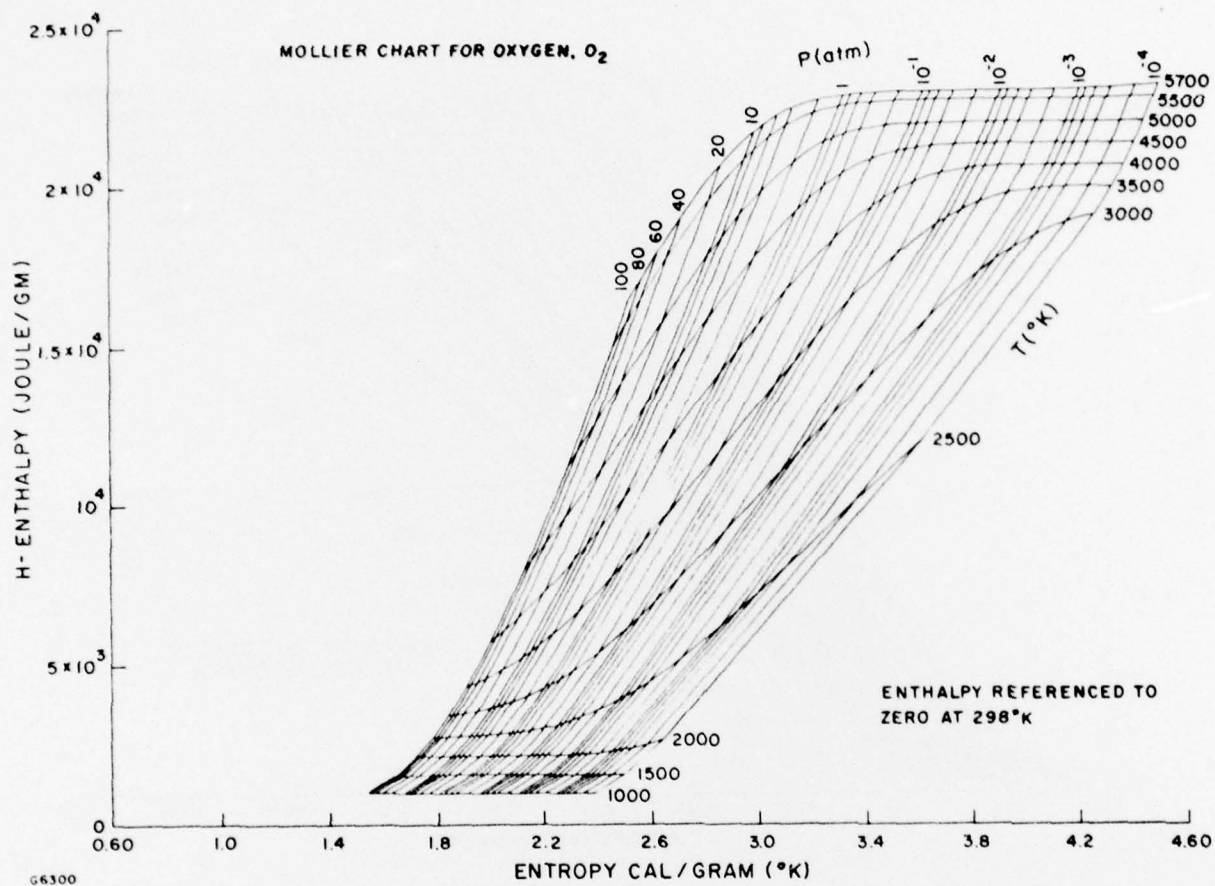Figure C-5   Mollier Chart for H_2O (p, T, Z)

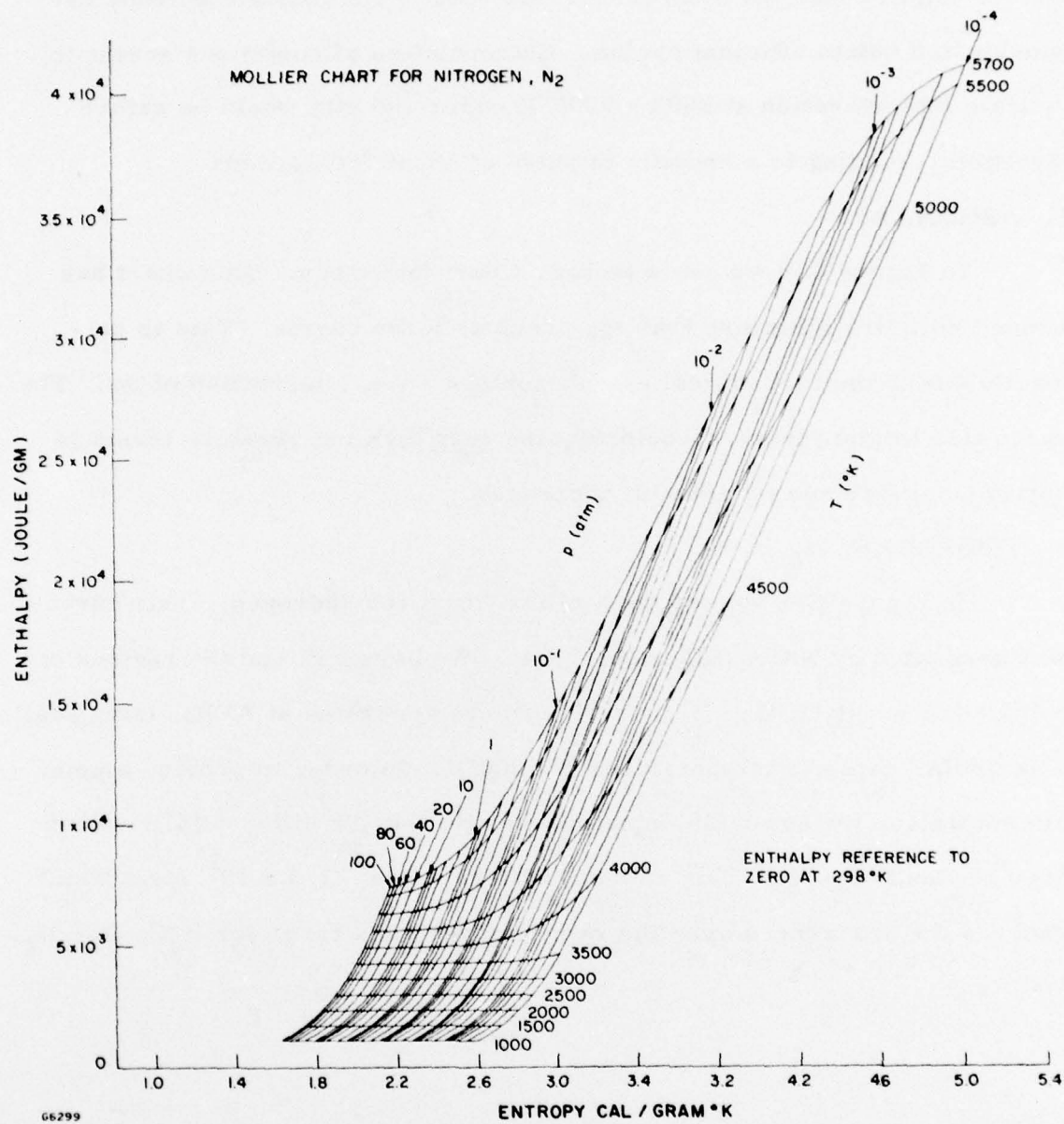Figure C-6   Mollier Chart for O_2

254

Figure C-7   Mollier Chart for N_2

feature implies that one can recover this energy via constant entropy expansion and obtain efficient cycles. Extrapolation of conditions seems to indicate that operation at 8000 - 9000°K under 100 atm would be rather favorable - leading to a specific impulse of about 750 seconds.

4. ARGON, Ar

In Figure C-8 we see a Mollier Chart for Argon. This chart has a much simpler structure than the previous three charts. This is primarily due to the lack of real gas phenomena - i.e., ionization of Ar. The chart also implies that we would require _very_ high temperature levels to obtain laser-propulsion enthalpy increases.

5. HYDROGEN, H_2

In Figure C-9 we see the Mollier Chart for hydrogen. This curve was generated by NASA (SP-3002, 1964). We have outlined the regions of calculation for H_2O, O_2, N_2, Ar which were generated at AERL using available JANAF tapes to temperatures of 6000°K. In order to provide a point of comparison for available enthalpy, we cite the Δh differential between 1000°K about 6000°K. This enthalpy difference is 1.5 x 10^5 J/gm which exceeds the differences over the same temperature range for H_2O, O_2, N_2, and Ar.

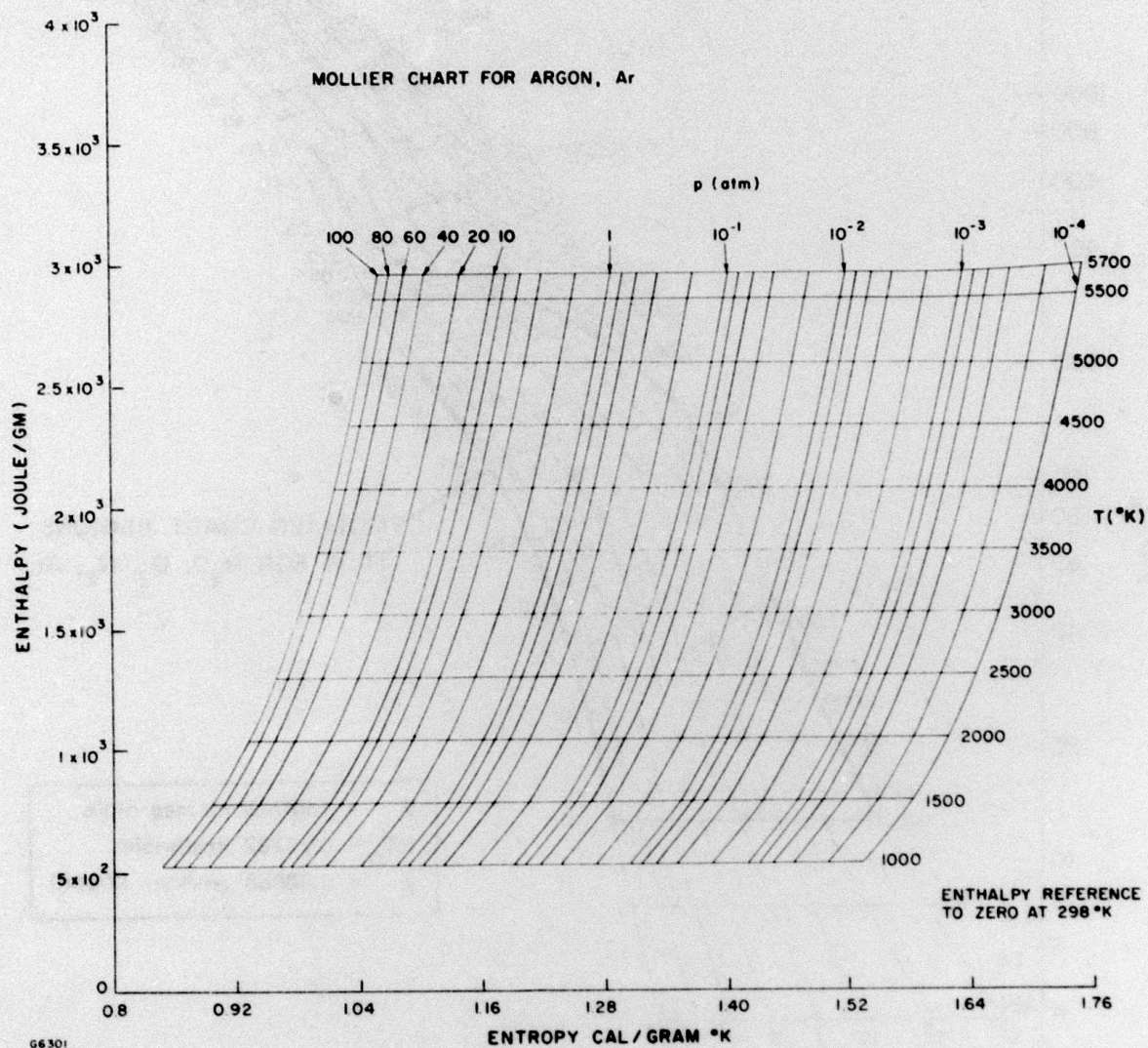Figure C-8   Mollier Chart for Ar

Figure C-9   Mollier Chart for H_2

258

APPENDIX D

CALCULATION OF THE MAINTENANCE THRESHOLD OF
DETONATION WAVES IN AIR

We start from the following equations:

$$\frac{1}{\ell} = \frac{A \rho^2 x^2}{T^{3/2}} \tag{D-1}$$

$$\frac{x^2}{1 - x} = \frac{B T^{3/2} e^{-\theta/T}}{\rho} \tag{D-2}$$

$$I = \beta \rho e^{3/2} (1 + \ell/R) \tag{D-3}$$

$$e = C \left(\frac{T}{10,000}\right)^{1.5} \left(\frac{\rho_s}{\rho}\right)^{0.12} \tag{D-4}$$

where ℓ = absorption length in the plasma (cm), R = radius of the beam, ρ, T and x are the density (g/cm^3), temperature $(^{\circ}K)$ energy per unit mass (erg/g), and fractional ionization at the Chapman Jouguet point. Equation (D-1) gives the absorption length due to electron inverse bremmstrahlung. At λ = 10.6 μm the coefficient A is:

$$A = 2 \times 10^{16} \left[\ell n \left(\frac{T}{10,000}\right)^{3/2} + 0.57\right] \tag{D-5}$$

Equation (D-2) is an approximate Saha equation for air with $B = 10^{-7}$ and $\theta = 160,000^{\circ}K$ (13.6 eV). Equation (D-3) can be derived from Raizer's theory[1] and relates conditions at the Chapman Jouguet point to the laser flux. The coefficient $\beta = (\gamma - 1)^{1/2} (\gamma + 1)/(2\gamma^{1/2}) \simeq 0.4$, where γ is the

---

(1) Raizer, Yu., Soviet Physics JETP 21, 1009 (1965).

effective coefficient of the adiabat ($\gamma \simeq 1.17$). Equation (D-4) is the energy equation of state for air[2] with $c = 2.8 \times 10^{11}$ in cgs units and with ρ_s the standard density (1.3×10^{-3} g/cm^3). Note that Eq. (D-4) implies $\gamma = 1.24$, so that our choice of $\gamma = 1.17$ in the evaluation of β is not completely consistent with Eq. (D-4).

System (D-1) through (D-4) represents 4 equations with 6 unknowns, ρ, ℓ, T, X, e and I. If we fix ρ we can eliminate x, T and e and evaluate I as a function of ℓ. We then seek the minimum of I when ℓ is varied. This is essentially the procedure used by Nielson and Canavan[3] in order to determine the maintenance threshold. The resulting threshold is plotted in Figure 111. At low altitude and long absorption lengths inverse bremmstrahlung absorption due to electron collisions with <u>neutrals</u> rather than ions is predominant and we took these into account by modifying the coefficient A.

$$A = 2 \times 10^{16} \left[\ell n \left(\frac{T}{10,000} \right)^{3/2} + 0.57 \right] + \frac{1.2 \times 10^3}{x} T^{2.8}$$

The last term is due to electron collisions with O and N atoms. For T = 10,000°K both terms are of same magnitude when the degree of ionization is 1%. The inclusion of electron neutral collisions has the effect of reducing the threshold flux by a factor of 1.5 at sea level for R = 1,000 cm. The effect at smaller beam radii and higher altitudes was found to be neglibible.

Simple analytic results can be derived when the degree of ionization is small, i.e., $x \ll 1$. Eliminating x between Eqs. (D-1) and (D-2), we get

$$T = \frac{\theta}{\ell n \, (AB \, \rho \, \ell)} \tag{D-6}$$

---

(2) Zel'dovich, Ya. and Raizer, Yu., Vol. I of <u>Physics of Shock Waves and High Temperature Hydrodynamic Phenomena</u>, Academic Press, N.Y. (1966), 1, 209.

(3) Nielson, P. and Canavan, G., "Laser Absorption Waves in the Atmosphere", in <u>Laser Interaction and Related Plasma Phenomena</u>, Vol. 3A (H. Hora and H. Schwarz, Editors) Plenum Press, N.Y. (1973), p. 177.

Inserting this value for T into Eqs. (D-3) and (D-4) and eliminating e between the two we get:

$$I = \beta e^{3/2} \rho^{0.82} \left(\frac{\theta}{\ell n \ AB \ \rho \ell} \right)^{9/4} \left(1 + \frac{\ell}{R} \right) \qquad (D-7)$$

Taking the derivative of (D-7) with respect to ℓ, neglecting the variation of A with T (or ℓ), we get the implicit equation from which ℓ can be calculated in order to find the threshold flux.

$$\ell = \frac{9}{4} \ \frac{R}{\ell n \ (AB \ \rho\ell) - 9/4} \qquad (D-8)$$

The solution to Eq. (D-8) is shown in Figure D-1 as a function of ρ for various values of R. One sees from this figure that ℓ/R varies in the narrow range 0.13 to 0.36 when ρ varies over 4 orders of magnitude and L varies for 1 cm to 100 cm. The straight portion of the threshold curves in Figure 111 is therefore well approximated by setting $\ell/R = 0.2$ in Eq. (D-3) and the slope of the curves $I(\rho)$ is 0.82. The separation between the curves corresponding to different beam radii is due to the factor $[\ell n \ (AB \ \rho\ell)]^{-9/4} \simeq [\ell n \ (0.2 \ AB \ \rho \ R)]^{-9/4}$.

It is of interest to compute the laser flux at a given altitude required to drive a detonation wave with a given absorption length ℓ. In order to do this, one solves the set of Eqs. (D-1) through (D-4) with Eq. (D-3) replaced by

$$I = \beta \rho \ e^{3/2} \qquad (D-9)$$

Curves $I(\rho)$ corresponding to constant values of ℓ are plotted in the overlay to Figure 111.

An analytic representation for the straight portion of the constant ℓ curves, when $x \ll 1$, is given by:
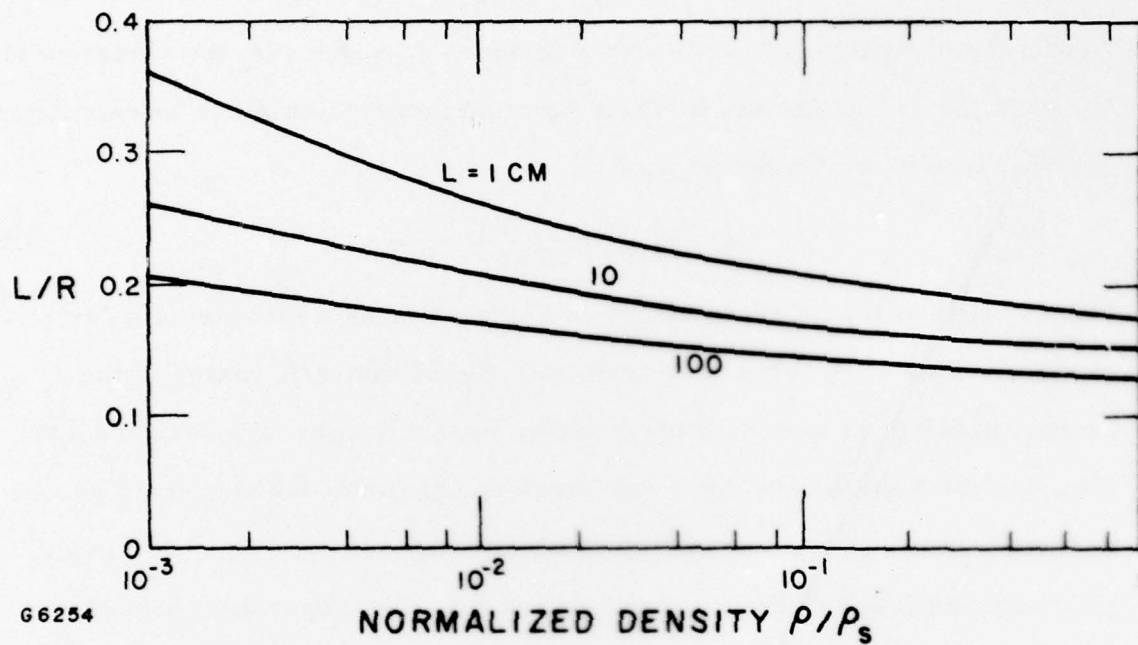
261

Figure D-1   Ratio of Absorption Length to Beam Radius at Threshold

$$I = 1.41 \times 10^7 \; \frac{(\rho_o/\rho_s)^{0.82}}{\left[1 + 6.5 \times 10^{-2} \; \ln\left(\frac{\rho_o}{\rho_s}\right) \ell \right]^{9/4}} \; W/cm^2$$

where ρ_s = standard density and ρ_o = upstream density ($\approx \frac{\gamma}{\gamma + 1} \rho$).

The constant ℓ curves have a minimum, and terminate on the low density side with a vertical slope. The reason the curves terminate is that the solution to Eqs. (D-1) and (D-2) is double valued in T, the lower value of T being the stable solution. The low altitude limit corresponds to the convergence of the two solutions given by the condition $(\partial \rho/\partial T)_\ell = 0$ or $(\partial \rho/\partial I)_\ell = 0$, i.e., the curves terminate with vertical slope in the overlay. The minimum density or maximum altitude at which a detonation wave with a given absorption length can be maintained is obtained by eliminating x between Eqs. (D-1) and (D-2), which leads to

$$\rho = \frac{e^{\theta/T}}{A \; \rho \; B} + \frac{T^{3/4}}{(A\ell)^{1/2}}$$

and writing that $(\partial \rho/\partial T)_\ell = 0$. This leads to the additional equation

$$e^{\theta/T} = \frac{3}{4} \; T^{3/4} \; \frac{(A\ell)^{1/4} \; B}{\rho} \tag{D-10}$$

Combining Eq. (D-10) with Eqs. (D-1) and (D-2) one can solve from T, x and ρ at the maximum altitude as a function of ℓ.

The maintenance threshold that we derived and that is shown in Figure 111 does not include the effect of radiative losses. We now study these losses in order to ascertain how important these may be in determining the threshold. Figure D-2, taken from Ref. 4 shows the energy radiated, ω, per unit volume of hot air at density ρ and temperature T. In

---

(4) Kivel, B., "Radiation from Hot Air and Stagnation Heating," RR-79, Avco Everett Research Laboratory, Inc., October 1959.
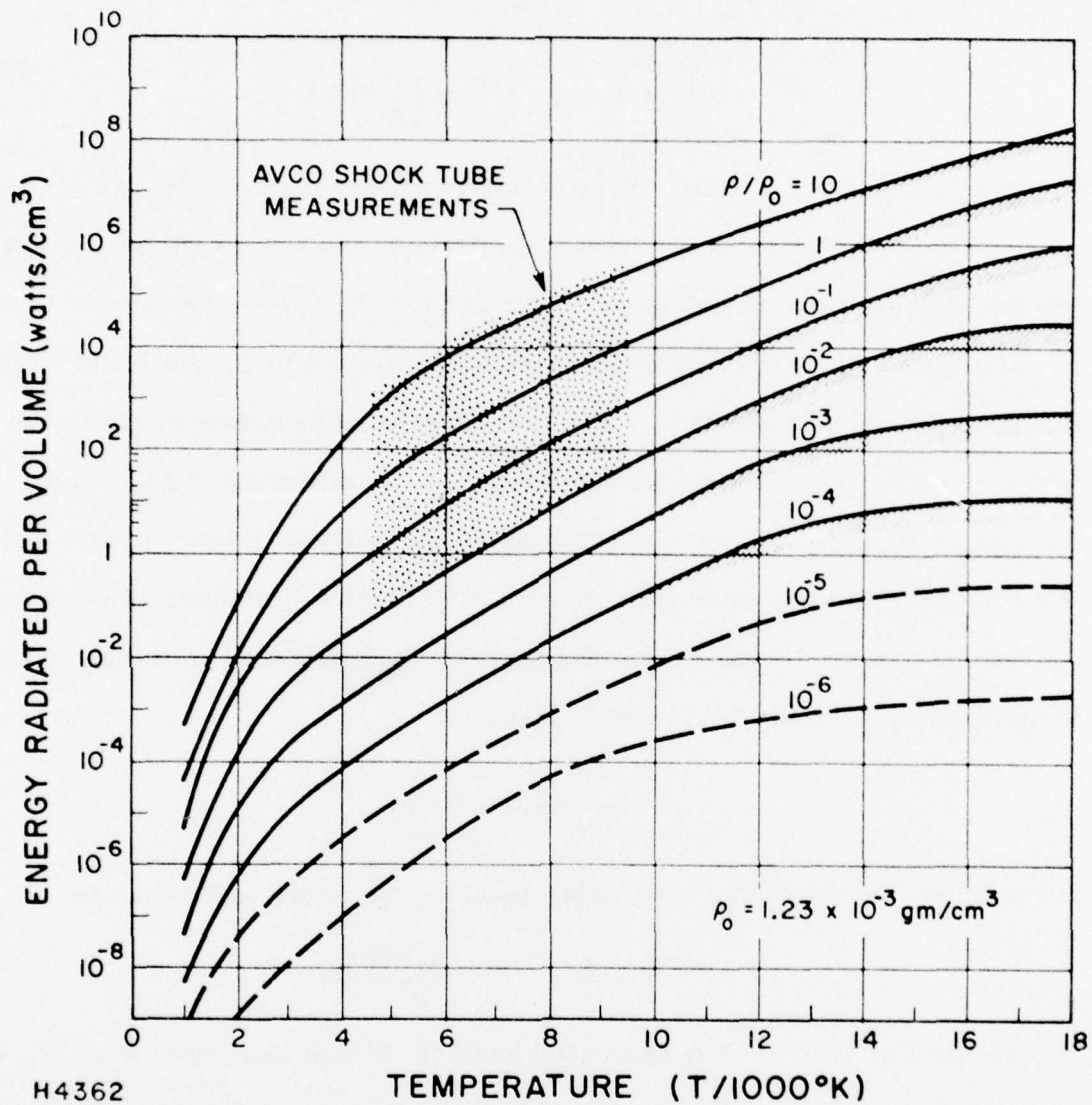
Figure D-2   Total Emitted Radiation Energy per Unit Volume of High
Temperature Air in Full Equilibrium as a Function of
Temperature for Constant Values of the Density

264

the temperature range 8-12, 000°K and density range $(\rho/\rho_s) = 1$ to 10^{-3} we approximate the curves by

$$\omega = 10^{12} \left(\frac{\rho}{\rho_s}\right)\left(\frac{T}{10,000}\right)^{10} \text{erg/(cm}^3 \text{ sec)} \tag{D-11}$$

where ρ_s is the standard density.

We require, for radiative losses to be negligible, that the amount radiated per unit mass during the residence time of the flux in the absorption zone be much smaller than the energy per unit mass stored in kinetic, dissociation and ionization energy. This requirement can be written as

$$\frac{(\omega/\rho) \times (\ell/u)}{e} = \eta \ll 1 \tag{D-12}$$

where e is given by Eq. (D-4), (ℓ/u) is the residence time, and the velocity u of the fluid with respect to the shock is given by, [1]

$$u \simeq \frac{D}{2} = \frac{1}{2} \left(\frac{2(\gamma^2 - 1) I}{\rho_o}\right)^{1/3} \tag{D-13}$$

with use of Eqs. (D-4), (D-6), (D-7), (D-11) and (D-13), in Eq. (D-12) becomes

$$\ell(\text{cm}) \ll 52 \left[1 + 6.5 \times 10^{-2} \ell n\left(\frac{\rho_o}{\rho_s} \ell\right)\right]^{7.75} \left(\frac{\rho_o}{\rho_s}\right)^{-0.18} \tag{D-14}$$

We have plotted in Figure D-3 the absorption length ℓ vs normalized density ρ_o/ρ_s for which a constant fraction η of the absorbed energy is radiated during the time ρ/u. The results can be plotted in a form similar to that used by Nielson and Canavan by expressing ℓ as a function of I and ρ through Eq. (D-7). This is shown in Figure 112 where, as dashed curves corresponding to $\eta = 0.2$ and $\eta = 1$.
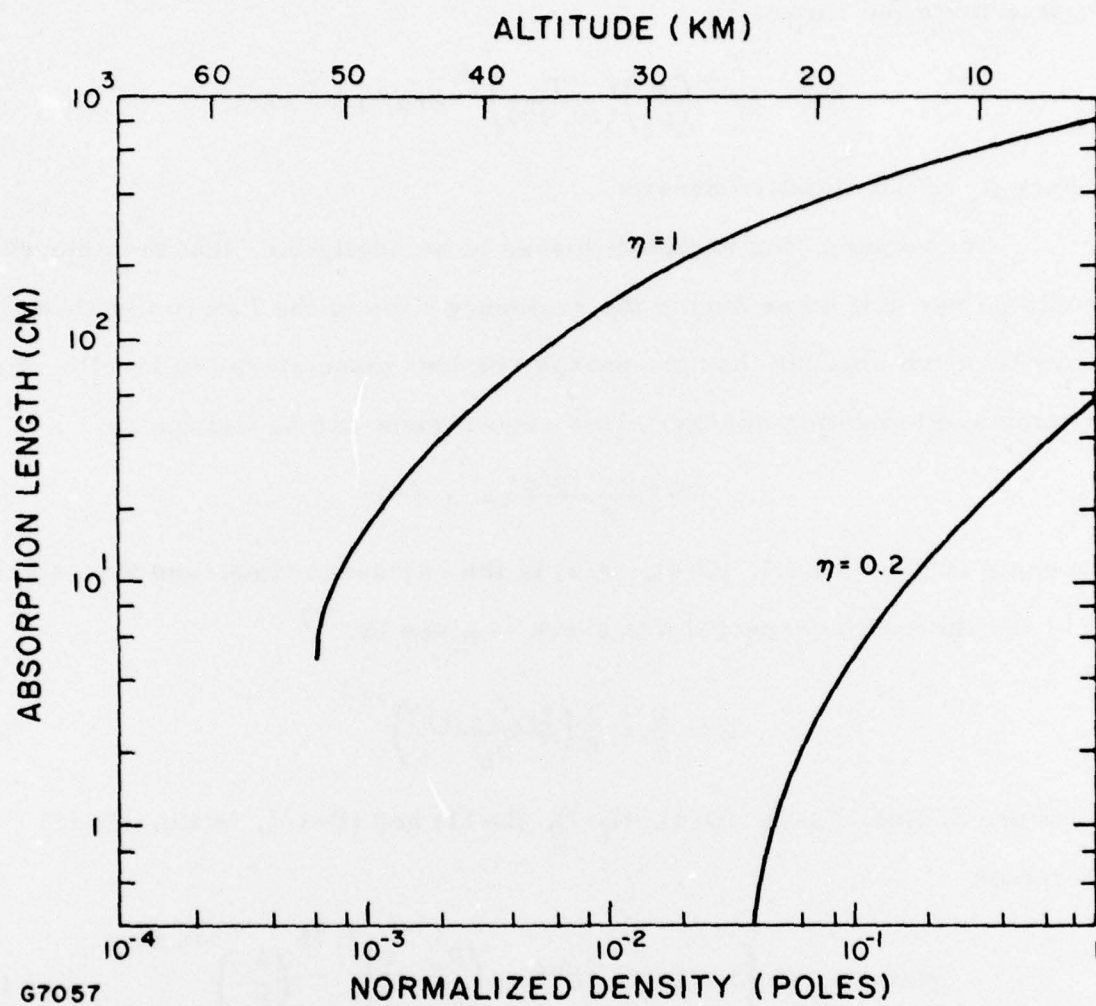
265

Figure D-3   Radiative Losses in Detonation Wave

G7057

APPENDIX D

REFERENCES

1. Raizer, Yu., Soviet Physics JETP 21, 1009 (1965).

2. Zel'dovich, Ya. and Raizer, Yu., Vol. I of Physics of Shock Waves and High Temperature Hydrodynamic Phenomena, Academic Press, N.Y. (1966), 1, 209.

3. Nielsen, P. and Canavan, G., "Laser Absorption Waves in the Atmosphere", in Laser Interaction and Related Plasma Phenomena, Vol. 3A, p. 177 (H. Hora and H. Schwartz, Editors), Plenum Press, N.Y. (1973).

4. Kivel, B., "Radiation from Hot Air and Stagnation Heating", RR-79, Avco Everett Research Laboratory, Inc., October 1959.